

**Centre for Green Energy and Vehicle Innovation
Faculty of Engineering and Information Technology
Centre for Clean Energy Technology
Faculty of Science**

**Graphene and Metal Oxide Nanomaterials
for High-performance Supercapacitors**

A Thesis Presented in Fulfillment of the Requirement for the

Degree of

Doctor of Philosophy

By

Yiying Wei, B. E.

University of Technology Sydney

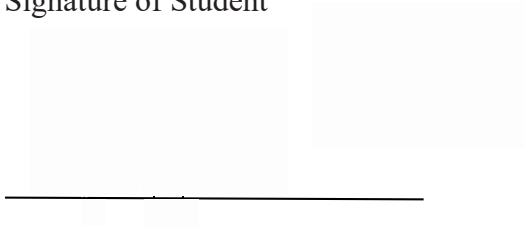
August 2015

CERTIFICATE OF ORIGINAL AUTHORSHIP

I certify that the work in this thesis has not previously been submitted for a degree nor has been submitted as part of requirements for a degree except as fully acknowledged within the text.

I also certify that the thesis has been written by me. Any help that I have received in my research work and the preparation of the thesis itself has been acknowledged. In addition, I certify that all information sources and literature used are indicated in the thesis.

Signature of Student



August 2015

ACKNOWLEDGEMENTS

First, I would like to express my sincere gratitude to my supervisors, Prof. Jianguo Zhu and Prof. Guoxiu Wang, who have been guiding and supporting me wholeheartedly through rigorous but fruitful supervision and financial funding for over four years since I started my research career in 2011. Dr. Jane Yao is also gratefully acknowledged for all the administrative assistance and lab management. Thanks are also due to Laurence Stonard, the manager of UTS workshop, who helped me fabricate all the devices I designed.

Special thanks are given to all my colleagues in the research team at the Centre for Green Energy and Vehicle Innovation and Centre for Clean Energy Technology for all the valuable discussions, kind co-operation and assistance. It is a pleasure to have worked with all of you and I really appreciate everyone's efforts in creating an intimate atmosphere for the research work.

I am also grateful for the assistance and patience of A/Prof. Youguang Guo and Dr. Zhiwei Lin, who always gave me the advice and discussion about the technic issues. Relevant training in the research facilities from Dr. Ronald Shimmon, Dr. Linda Xiao, and all the MAU staff are much appreciated as well.

Deep gratitude is to be expressed to my parents and my relatives, who have been caring and sustaining me over these years. Without your continuous support, I could not have finalized my PhD study and become a mature and responsible person.

LIST OF PUBLICATION

1. **Yiyang Wei**, Bing Sun, Dawei Su, Jianguo Zhu and Guoxiu Wang. "3D Free-Standing NiCo₂O₄@graphene Foam for High-performance Supercapacitors." *Advanced Functional Materials*, submitted, 2015. (Impact factor: 11.8)
2. **Yiyang Wei**, Shuangqiang Chen, Dawei Su, Bing Sun, Jianguo Zhu, and Guoxiu Wang. "3D mesoporous hybrid NiCo₂O₄@graphene nanoarchitectures as electrode materials for supercapacitors with enhanced performances." *Journal of Materials Chemistry A* 2, no. 21 (2014): 8103-8109. (Impact factor: 7.4)
3. **Yiyang Wei**, Jianguo Zhu, and Guoxiu Wang. "High-Specific-Capacitance Supercapacitor Based on Vanadium Oxide Nanoribbon." (2014). *Applied Superconductivity, IEEE Transactions on*, 2014, 24, (5), 1-4. (Impact factor: 1.2)
4. **Yiyang Wei**, Guoxiu Wang, Jianguo Zhu, "Synthesis and Characterization of Vanadium Oxide Nanotubes as Electrode Materials for Electrochemical Capacitors", *ECS Transactions* 58 (2014) 61-67.
5. **Yiyang Wei**, Shuangqiang Chen, Jianguo Zhu and Guoxiu Wang, "Synthesis and Characterization of Nanoporous NaMn₂O₄ electrode Material for Sodium-Ion Battery", 17th International Meeting on Lithium Batteries in Como, Italy, June 10 to 14, 2014.
6. Chen, Shuangqiang, Yufei Zhao, Bing Sun, Zhimin Ao, Xiuqiang Xie, **Yiyang Wei**, and Guoxiu Wang. "Microwave-assisted synthesis of mesoporous Co₃O₄ nanoflakes for applications in lithium ion batteries and oxygen evolution reactions." *ACS applied materials & interfaces* 7, no. 5 (2015): 3306-3313. (Impact factor: 6.7)

RECEIVED AWARDS

2015 UTS FEIT HDR Publications Award

2014 UTS FEIT HDR Publications Award

TABLE OF CONTENTS

CERTIFICATE OF ORIGINAL AUTHORSHIP.....	I
ACKNOWLEDGEMENTS.....	II
LIST OF PUBLICATION.....	III
RECEIVED AWARDS.....	IV
TABLE OF CONTENTS.....	V
LIST OF SYMBOLS AND ABBREVIATIONS.....	VIII
LIST OF FIGURES.....	X
LIST OF TABLES.....	XXI
ABSTRACT.....	XXII
Chapter 1. INTRODUCTION.....	1
1.1. Research Aims and Objectives.....	1
1.2. Background and Significance.....	2
1.3. Thesis Outline.....	9
Chapter 2. Literature Review.....	11
2.1. Energy Storage Technologies.....	11
2.1.1. Supercapacitors.....	11
2.1.2. Battery.....	15
2.1.3. Flywheel.....	19
2.1.4. Superconductive Magnetic Energy Storage.....	21
2.2. Supercapacitor Metrics and Parameters.....	21
2.2.1. Electrode Surface Area.....	22
2.2.2. Electrode Area-specific Capacitance.....	22
2.2.3. Gravimetric Capacitance of Carbon Electrode.....	22
2.2.4. Volumetric Specific Capacitance.....	22
2.2.5. Impedance.....	23
2.2.6. Power Density.....	23
2.2.7. Energy Density.....	23
2.3. Supercapacitor Modelling.....	23
2.3.1. Physical Model.....	23
2.3.2. Mathematic Model.....	29
2.3.3. Pore Impedance Model.....	32

2.3.4.	Circuit Model with Pore Impedance Model.....	35
2.4.	Electrode materials for supercapacitor	41
2.4.1.	Carbon nanotube	41
2.4.2.	Graphene-based electrode	47
2.4.3.	Unzipped CNTs.....	60
2.4.4.	Vanadium Oxide.....	64
2.5.	Summary	71
Chapter 3.	Experimental Methods.....	77
3.1.	Materials synthesis	77
3.1.1.	Hydrothermal method	77
3.1.2.	Freeze drying.....	81
3.1.3.	Vacuum filtration	86
3.1.4.	<i>In-situ</i> self-assembly.....	89
3.2.	Physical and morphological characterization	91
3.2.1.	X-ray Diffractometry (XRD)	91
3.2.2.	Scanning electron microscopy (SEM).....	92
3.2.3.	Transmission Electron Microscopy (TEM).....	93
3.2.4.	Thermogravimetric Analysis (TGA)	94
3.2.5.	Brunauer-Emmett-Teller (BET) Surface Area and Barrett-Joyner-Halenda (BJH) Pore Size and Volume Analysis	94
3.3.	Electrode fabrication and electrochemical characterization.....	95
3.3.1.	Electrode fabrication.....	95
3.3.2.	Electrochemical testing.....	96
3.3.2.1.	Cyclic voltammetry (CV).....	96
3.3.2.2.	Galvanostatic Charge/Discharge (DC).....	97
3.3.2.3.	Electrochemical Impedance Spectroscopy	98
3.4.	Summary	98
Chapter 4.	Synthesis and Characterization of Vanadium Oxide Nanotubes as Electrode Materials for Electrochemical Capacitors.....	99
4.1.	Introduction	99
4.2.	Experimental	100
4.3.	Results and discussion	102
4.4.	Summary	106

Chapter 5. High-Specific-Capacitance Supercapacitor Based on Vanadium Oxide Nanoribbon	107
5.1. Introduction	107
5.2. Experimental	109
5.3. Results and discussion	111
5.4. Summary	115
Chapter 6. 3D Mesoporous Hybrid NiCo ₂ O ₄ @graphene Nanoarchitectures as Electrode Materials for Supercapacitors with Enhanced Performances	117
6.1. Introduction	117
6.2. Experimental	119
6.2.1. Fabrication of graphene – polyurethane (PU) sponges	119
6.2.2. Preparation of NiCo ₂ O ₄ @graphene nanoarchitectures	119
6.2.3. Materials characterization	120
6.2.4. Electrochemical testing.....	120
6.3. Results and Discussion	121
6.4. Summary	132
Chapter 7. A High-Rigid Binder-Free 3D Free-Standing NiCo ₂ O ₄ @graphene Foam Fabricated by Controllable Freeze Casting for High-performance Supercapacitors	134
7.1. Introduction	134
7.2. Experimental	139
7.2.1. Fabrication of 3D NiCo ₂ O ₄ @graphene Precursor	139
7.2.2. Fabrication of 3D NiCo ₂ O ₄ @graphene Foam	139
7.2.3. Material Characterization	140
7.2.4. Electrochemical testing.....	140
7.3. Results and Discussion	141
7.4. Summary	157
Chapter 8. Conclusion and Future Work	159
8.1. General Conclusion	159
8.2. Future Work.....	161
REFERENCES	163

LIST OF SYMBOLS AND ABBREVIATIONS

Abbreviation	Full name
1D	One-dimensional
3D	Three Dimension
ALD	Atomic layer deposition
BET	Brunauer–Emmett–Teller
CAES	Compressed air energy storage
CFC	Controllable freeze casting
CMG	Chemically modified graphene
CNHs	Carbon nanohorns
CNTs	Carbon nanotubes
CPE	Constant phase element
DLCs	Double layer capacitors
EDLCs	Electrochemical double layer capacitors
ESR	Equivalent series resistance
ESSs	Energy storage systems
EVs	Electric vehicles
FES	Flywheel energy storage
FESEM	Field-emission scanning electron microscopy
GONPs	Graphene oxide nanoplatelets
HEVs	Hybrid electric vehicles
ICE	Internal combustion engine
LPCVD	Low-pressure chemical vapor deposition
MWNTs	Multi-walled carbon nanotubes
OHP	Outer Helmholtz Plane
PEI	polyethyleneimine
PHEVs	Plug-in hybrid electric vehicles
PVDC	Poly vinylidene chloride
SEM	Scanning electron microscopy
SMES	Superconductive magnetic energy storage
SWNTs	Single-walled nanotubes

TEM	Transmission electron microscopy
TMAOH	Tetramethyl ammonium
VN	Vanadium nitride

LIST OF FIGURES

Figure 2-1 The schematic of the electrolytic capacitor designed by Becker and Ferry. ¹⁰⁰	12
Figure 2-2 The schematic of the electrolytic capacitor designed by SOHIO. ¹⁰¹	12
Figure 2-3 Section view of the positive plate. ¹⁰⁴	17
Figure 2-4 Helmholtz model. ¹⁰⁵	24
Figure 2-5 Potential distribution of Helmholtz model, Gouy-Chapman model and Stern model. ¹⁰⁶	25
Figure 2-6 Grahame model and the charge distribution. ¹⁰⁸	28
Figure 2-7 Bockris, Devanathan and Muller Model: Water dipole model of the double layer at an electrode/electrolyte interface. ¹⁰⁹	28
Figure 2-8 RC network model	29
Figure 2-9 The results of experiment and simulation of RC model. ¹¹¹	30
Figure 2-10 Three RC branches with a voltage-dependent capacitor. ¹¹¹	31
Figure 2-11 The parameters D. A. New's supercapacitor model. ¹¹²	31
Figure 2-12 Equivalent circuit of a pore. ¹¹⁴	32
Figure 2-13 An infinitesimally small section d_z of a pore. ¹¹⁴	33
Figure 2-14 Equivalent circuit of a supercapacitor. ¹¹⁸	35
Figure 2-15 The experimental impedance spectrum and the simulation of standard impedance and generalized impedance model.....	37
Figure 2-16 RC network model.	37
Figure 2-17 RC equivalent circuit of ZARC element. ¹²¹	38
Figure 2-18 RC parameter of the equivalent circuit of ZARC. ¹¹³	38
Figure 2-19 Generalized pore impedance model is represented by a parallel RC circuit	

with the standard pore impedance. ¹²²	39
Figure 2-20 Equivalent impedance model of porous electrode. ¹¹⁸	40
Figure 2-21 Equivalent circuit of ZARC element. ¹¹⁸	40
Figure 2-22 Schematic diagram of the collapse of the aligned low-density as-grown forest (above) to the highly densely packed SWNT solid (below). ⁵⁸	43
Figure 2-23 SEM image of the aligned CNT. ³⁵	45
Figure 2-24 Comparison of different carbon materials as electrodes of supercapacitors. (a) Activated carbon. Activated carbon has a high surface area. However, many of the micropores cannot be accessed by electrolyte ions. (b) Single-walled carbon nanotube (SWCNT) bundles. SWCNTs usually form bundles, limiting their surface area. Only the outmost surface can be accessed by electrolyte ions. (c) Pristine graphene. Graphene nano-sheets are likely to agglomerate through van der Waals interactions during the drying process. It would be difficult for electrolyte ions to access the ultras-small pores, especially for larger ions such as an organic electrolyte or at a high charging rate. (d) Graphene/CNT composite. SWCNTs can serve as a spacer between the graphene nano-sheets to give rise to rapid diffusion pathways for the electrolyte ions. Moreover, they can enhance electrical conduction for the electrons. The CNTs also serve as a binder to hold the graphene nano-sheets together preventing disintegration of the graphene structure into the electrolyte. ⁶⁴	48
Figure 2-25 Scheme for preparing (a) reducedGO electrode and (b) GS-CNTs-9-1 electrode. Note the schematic models of GS-CNT composites with various GS/CNTs ratios; where (c) GO are dispersed in the solution and GS aggregates/stacks are formed after reduction, (d) GO and CNTs coexist in the solution and CNTs act as nanospacers to increase the interlayer space between GS after reduction, avoiding the aggregation issue, (e) excess CNTs attach on the surface of GS resulting in a low exposure of surface area,	

and (f) CNTs are dispersed in the solution and CNTs aggregates are formed in the dry state. ¹²⁵	49
Figure 2-26 Illustration of positively charged PEI-GN and negatively charged MWNT film deposition process on an appropriate substrate.	50
Figure 2-27 Scheme representation of the preparation of self-assembled hierarchical nanostructure comprising graphene and carbon spheres. ¹²⁶	52
Figure 2-28 Cyclic voltammograms (CVs) of supercapacitors constructed with different materials based electrodes in 6MKOH (scan rate of 20 mV s ⁻¹ , electrode mass of 8.2 mg). ¹²⁶	52
Figure 2-29 Illustration of the electrochemical synthesis process of the PPy/GR nanoplatelet electrodes.	53
Figure 2-30 Fabrication of an RG-O and aminated MWNT (RG-O/MWNT) double layer on a substrate. ¹²⁹	53
Figure 2-31 Fabrication of hybrid suspensions of CCG and CNTs. ⁶⁹	55
Figure 2-32 Schematic representation of hybrid LbL multilayer of MWNTs and RGO. ¹³⁰	56
Figure 2-33 Schematic for the assembly of the CNTs/G composite film. ¹³¹	57
Figure 2-34 Schematic depiction for the performance comparison of the conventional stacked geometry (a,b) Vs the „in-plane“ geometry (c,d). ¹³³	58
Figure 2-35 Schematic illustration of the fabrication process for carbon hybrid films. ¹³⁴	59
Figure 2-36 (a) Representation of the gradual unzipping of one wall of a carbon nanotube to form a nanoribbon. Oxygenated sites are not shown. (b) The proposed chemical mechanism of nanotube unzipping. ¹³⁶	61
Figure 2-37 (a) A pristine MWCNT was used as the starting raw material. (b) The	

MWCNT was deposited on a Si substrate and then coated with a PMMA film. (c) The PMMA–MWCNT film was peeled from the Si substrate, turned over and then exposed to an Ar plasma. (d–g) Several possible products were generated after etching for different times: GNRs with CNT cores were obtained after etching for a short time t_1 (d); tri-, bi- and single-layer GNRs were produced after etching for times t_2 , t_3 and t_4 , respectively (t_4 , t_3 , t_2 , t_1 ; e–g). (h) The PMMA was removed to release the GNR. 63

Figure 2-38 Mmechanism for intercalation and unwrapping of MWNT..... 64

Figure 2-39 Schematic diagram of horizontal alumina tube furnace for growth of vanadium oxides.¹⁴³ 66

Figure 2-40 Schematic representation of VN/CNTs nanocomposite synthesis process.¹⁵⁰ 69

Figure 2-41 SEM images of (a) uncoated samples, and samples coated with VOx for (b) 100 ALD cycles, (c) 300 ALD cycles, and (d) 500 ALD cycles.⁷¹ 70

Figure 2-42 Cross-section SEM images of ordered nanotube arrays on different substrates: (a) Ti, (b) Ti_{0.2}V, (c) Ti₃V, and (d) Ti₁₈V by anodization in an electrolyte composed of ethylene glycol with 0.2 M HF at 120 V for 30 minutes. (e) and (f) High magnification cross-section and top-view SEM images of the Ti₁₈V Ti–V oxide nanotubes.⁸⁰ 71

Figure 2-43 An ideal design of the electrode material for next generation supercapacitors, RuO₂·xH₂O nanotubular arrayed electrode. The mesoporous architecture, hydrous nature, and metallic conductivity provide the proton and electron “superhighways” for the extremely rapid charge/discharge processes.⁷⁴ 72

Figure 2-44 The scheme represents the enhanced charge storage process of the prepared electrode.¹⁵⁶ 73

Figure 2-45 (a) Schematic illustration showing conductive wrapping of graphene/MnO₂ to introduce an additional electron transport path (in a discharge cycle). (b) Schematic of

graphene/MnO ₂ /CNT and graphene/MnO ₂ /conducting polymer systems formed by wrapping of GM nanostructures with CNTs or conducting polymers (black, graphene; rose, MnO ₂ ; yellow, CNTs; blue, conducting polymer). ⁸²	75
Figure 2-46 Structural characterization of MnO ₂ /Zn ₂ SnO ₄ / carbon microfibers hybrid composite. (a-d) SEM images of Zn ₂ SnO ₄ nanowires grown radially on the woven carbon microfibers. ¹⁶⁵	76
Figure 3-1 Typical FESEM images of (A, B) bare carbon nanofibers after Te nanowire core removal; (C, D) NiCo-precursor nanorod arrays/ carbon nanofibers hybrid nanostructure; and (E, F) crystalline NiCo ₂ O ₄ nanorod arrays/carbon nanofibers hybrid structure obtained by annealing the NiCo-precursor nanorods/carbon nanofibers at 300 °C for 2 h with a slow heating rate of 0.5 °C min ⁻¹ . ⁸⁹	80
Figure 3-2 Benchtop Manifold Freeze-Dryer marketed by Millrock Technology.....	81
Figure 3-3 The three phase diagram of water.....	82
Figure 3-4 (a-c) Typical top-view (a,b) and side-view (c) SEM images of graphene monolith of 5.10 mg cm ⁻³ . (d) Schematic showing the formation mechanism of the cork-like monolith by freeze casting. When a well-dispersed pr-GO dispersion (the first scheme) is frozen, pr-GO sheets are concentrated at the boundary of ice crystals and then aligned along the growth direction of ice due to the squeezing effect (the second scheme, side-view). As a result, a continuous honeycomb-like network is formed. The network retains its connectivity when the ice is thawed (the third scheme, top-view). The pr-GO sheets are illustrated as slightly corrugated lines in the scheme with the brown representing partially reduced, whereas the black for fully reduced. Photos of the corresponding samples are presented in the insets. Scale bars, 50 mm (a,c) and 10 mm (b). ¹⁵⁶	83
Figure 3-5 (a) Illustration of the fabrication process of the ultralight graphene aerogel (ULGA). (b) Digital images of time-dependent formation process of functionalized	

graphene hydrogel (FGH). ¹⁵⁷	85
Figure 3-6 Diagram of vacuum filtration.....	87
Figure 3-7 Low and high magnification SEM images of (a) and (b) mechanically densified aMEGO and (c) and (d) aligned aMEGO. ¹⁶⁴	88
Figure 3-8 Schematic drawings illustrating the leavening process to prepare rGO foams. ¹⁶⁶	88
Figure 3-9 The proposed self-assembly mechanism for graphene hydrogel formation during the chemical reduction of GO in an aqueous suspension. ¹⁶⁷	89
Figure 3-10 Schematic illustrations of the ternary self-assembly approach to ordered metal oxide graphene nanocomposites. ¹⁶⁸	90
Figure 3-11 An X-ray diffractometer (Siemens D5000 model) in UTS.....	91
Figure 3-12 An FE-SEM facility (Zeiss Supra 55VP) in UTS.	92
Figure 3-13 A commercial TEM setup (JEOL 2011 model).....	93
Figure 3-14 A TGA/DTA Analyzer (SDT 2960 model, TA Instruments) in UTS.....	94
Figure 3-15 A TriStar II Surface Area Analyzer.....	95
Figure 3-16 An electrochemistry workstation (CHI660D model).	97
Figure 4-1 XRD pattern of the as-prepared nanotube with the standard V ₂ O ₅ pattern, (b) Schematic depiction of the nanoribbon structure.....	102
Figure 4-2 The uniform vanadium oxide nanotubes was demonstrated by SEM images (a and b); The detailed information about the nanotubes were shown in the TEM images (c-e).....	103
Figure 4-3 Cyclic voltametric curves of the vanadium oxide nanotubes (a) in 2 M KCl, (b) in 2 M LiCl and (c) in 2 M NaCl at the scan rates of 2 mV s ⁻¹ , 5 mV s ⁻¹ , 10 mV s ⁻¹ , 20 mV s ⁻¹ , and 50 mV s ⁻¹ . (d) Comparison of CV curves in 2 M KCl, 2 M LiCl and 2 M NaCl at the scan rate of 50 mV s ⁻¹	104

Figure 4-4 Measured capacitance of vanadium oxide nanotubes in 2 M KCl, 2 M LiCl and 2 M NaCl at the scan rates of 2 mV s ⁻¹ , 5 mV s ⁻¹ , 10 mV s ⁻¹ , 20 mV s ⁻¹ , and 50 mV s ⁻¹	106
Figure 5-1 (a) XRD pattern of the as-prepared nanoribbon with the standard V ₂ O ₅ pattern, (b) Schematic depiction of the nanoribbon structure.	111
Figure 5-2 (a) SEM images of nanoribbon, (b, c) low- and high-magnification TEM images, respectively. (d) selected area electron diffraction (SAED).	112
Figure 5-3 Cyclic voltametric curves of the vanadium oxide nanoribbon (a) in 2M KCl (b) in 2M NaCl, nanotube at the scan rates of 2 mV s ⁻¹ , 5 mV s ⁻¹ , 10 mV s ⁻¹ , 20 mV s ⁻¹ , and 50 mV s ⁻¹	113
Figure 5-4 The specific capacitance of vanadium oxide nanoribbon in 2M KCl, 2M NaCl at the scan rates of 2 mV s ⁻¹ , 5 mV s ⁻¹ , 10 mV s ⁻¹ , 20 mV s ⁻¹ , 50 mV s ⁻¹	114
Figure 6-1 Synthesis process of NiCo ₂ O ₄ @graphene nanoarchitectures: (A) a piece of PU-sponge and the solution with RGO stabilized using sodium cholate hydrate (SCH); (B) The RGO was coated and anchored onto the PU-sponge assisted by microwave and freeze drying; (C) NiCo ₂ O ₄ precursor nanosheets grown on RGO-PU-sponges; (D) 3D mesoporous hybrid NiCo ₂ O ₄ @graphene nanoarchitectures. (E) Crystallized NiCo ₂ O ₄ nanosheets with mesopores.	121
Figure 6-2 The SEM images of the (A, B) PU-sponge, showing macroporous structure; (C, D) RGO-PU-sponge, indicating RGO was coated onto PU-sponge.	122
Figure 6-3 SEM images of (A, B) NiCo ₂ O ₄ precursor sheets that grew on the skeleton of RGO-PU-sponge; (C) high magnification SEM image of NiCo ₂ O ₄ precursor with macropores.	123
Figure 6-4 (A) XRD pattern of NiCo ₂ O ₄ @graphene nanoarchitectures. (B) SEM image of foam-like hybrid NiCo ₂ O ₄ @graphene nanoarchitectures with hierarchical pores. (C)	

SEM image of NiCo ₂ O ₄ nanosheets.....	124
Figure 6-5 The SEM images of (A, B) large-size NiCo ₂ O ₄ @graphene obtained by annealing the precursor at 350 °C in air for 2 hours; TEM images of (C) NiCo ₂ O ₄ @graphene nanoarchitectures with macropores, (D) mesopores ranging from 2-5nm.	125
Figure 6-6 (A) TEM image of NiCo ₂ O ₄ @graphene nanosheets, showing the porous architecture. (B) HRTEM images of NiCo ₂ O ₄ @graphene nanosheets. The inset SAED pattern can be fully indexed to polycrystalline NiCo ₂ O ₄ . (C) Lattice resolved HRTEM image of NiCo ₂ O ₄ nanosheets.....	126
Figure 6-7 (A) Nitrogen adsorption/desorption isotherms; (B) pore size distribution of NiCo ₂ O ₄ @ graphene nanoarchitectures.....	127
Figure 6-8 Electrochemical performance of the NiCo ₂ O ₄ @graphene nanoarchitectures. (A) CV curves at the scan rate of 5 mV s ⁻¹ to 200 mV s ⁻¹ ; (B) constant-current charge/discharge profile at the current densities of 1 A g ⁻¹ to 80 A g ⁻¹ ; (C) specific capacitance vs current density; (D) capacity retention vs cycle number up to 10,000 cycles at 10 A g ⁻¹ . All the data are taken in 2.0 M KOH electrolyte.....	128
Figure 6-9 Charging/discharging profile of pure Ni foam at the same current rates of the active material, ranging from 1 to 40 A g ⁻¹	129
Figure 6-10 Electrochemical performance of NiCo ₂ O ₄ @graphene nanoarchitectures and bare NiCo ₂ O ₄ (A) charging/discharging curves at a current density of 10 A g ⁻¹ ; (B) specific capacitances at current densities of 1 to 80 A g ⁻¹ ; (C) capacities retention up to 10000 cycles at 10 A g ⁻¹ ;.....	131
Figure 6-11 Nyquist plots of the a.c. impedance spectra of the porous NiCo ₂ O ₄ @graphene electrode and the bare NiCo ₂ O ₄ electrode in the frequency range from of 100 kHz to 0.01 Hz.....	132
Figure 7-1 Schematic illustration showing the experimental steps of fabricating	

NiCo ₂ O ₄ @graphene foam.	141
Figure 7-2 The schematics of the (a) upper base, (b) bottom base and (c) cylinder tube of the as-designed device. (d) The images of the device (left image), after inserting the plunger (right image).	142
Figure 7-3 The compression test shows that the as-prepared foam has a high-rigid mechanical property. The foam has (a) a diameter of 14 mm and (b) a thickness of about 2 mm. (c) The real-time image of the compressed sample loading with the balance of 100 g. (d) the images of the sample after loading the weights, shows that the foam retained the original structure without collapsing. (e) There is no change in the thickness of the foam after loading the related balance weight.	144
Figure 7-4 The real-time images of the compressed sample loading with the balance of (a) 2 g, (d) 10 g, (g) 20 g and (j) 50 g. (b), (e), (h) and (k) the images of the sample after loading these weights, showing the foam retained the original structure without collapsing. (c), (f), (i) and (l) there is no change in the thickness of the foam after loading the related balance weight.....	145
Figure 7-5 The compression test of the material fabricated without using extra air compress pressure. (a) The size of the foam is smaller than that of filter paper due to the shrink during the freeze drying process. (b) Cross-sectional image of the foam, showing cone-like structure. (c) The foam was loaded with the balance of 20g. (d) and (e) The image of sample after loading the weight, showing the foam suffered structure collapsing.	146
Figure 7-6 (a) SEM images of NiCo ₂ O ₄ precursor foam after freeze drying. (b) Magnified SEM image showing NiCo ₂ O ₄ precursor gown on GO sheets.	147
Figure 7-7 (a) XRD pattern of the NiCo ₂ O ₄ @graphene nanoarchitectures. (b) SEM images of the foam indicating a compressed structure with small-size pores, ranging from	

1-10 um. (c) The magnified SEM image of ROG sheets. (d) Cross-sectional SEM image of the foam which shows plenty of horizontal channels built by NiCo₂O₄@graphene sheets. (e) SEM image of the fully filtered NiCo₂O₄@graphene, indicating the NiCo₂O₄@graphene sheets stacked together without the porous structure and vertical channels. (f) SEM image of the 1 ml NiCo₂O₄@graphene precursor directly freeze dried without filtration, showing random structure and fragile property. 148

Figure 7-8 (a) Image of the material after annealing at 600 °C for 2 hours in pure argon and then 250 °C for 2 hours in air. (b) The SEM images of the foam with vertical channels with respect to the current collector. (c) Magnified SEM image of the foam showing the pore size from 1um to 10 um. (d) Magnified cross-sectional SEM images (Figure 3d) of the foam..... 149

Figure 7-9 (a) Low-magnified and (b) high-magnified SEM images of the fully filtered NiCo₂O₄@graphene. 150

Figure 7-10 (a) TEM image of the NiCo₂O₄@graphene nanosheets of the foam, showing uniform distribution of NiCo₂O₄ on RGO sheet. (b) Magnified TEM image of the NiCo₂O₄ nanoparticles, ranging from 20 - 50 nm. (c) HRTEM image of the NiCo₂O₄ nanoparticle. The lattice spacing of 0.2 nm corresponds to the (4 0 0) lattice planes, the lattice spacing of 0.245 nm corresponds to the (3 1 1) lattice planes and the lattice spacing of 0.4 nm corresponds to the (2 0 0) lattice planes. The inset SAED pattern can be indexed to the diffraction planes of the spinel phase of NiCo₂O₄..... 151

Figure 7-11 Energy dispersive X-ray spectroscopy (EDS) characterization of the 3D free-standing NiCo₂O₄@graphene foam. (a) SEM image of part of the foam; (b) elemental mapping image of the foam; (c-f) EDS Ni, O, Co and C mapping of the region as show in (a). 152

Figure 7-12 EDS spectrum captured for the region shown in Figure 6-11 (a)..... 153

Figure 7-13 N₂ adsorption–desorption isotherms of the 3D NiCo₂O₄@graphene foam. The inset shows the pore size distribution. 153

Figure 7-14 Electrochemical performance of the NiCo₂O₄@graphene foam. (a) CV curves at a scan rate of 5 mV s⁻¹ to 200 mV s⁻¹; (b) constant-current charge/discharge profile at current densities of 2 A g⁻¹ to 80 A g⁻¹; (c) specific capacitance vs. current density; (d) capacity retention vs. cycle number up to 5000 cycles at 10 A g⁻¹. All the data are taken in 2.0 M KOH electrolyte. 154

Figure 7-15 Electrochemical performance of 3D NiCo₂O₄@graphene foam and the fully filtered NiCo₂O₄@graphene (a) Charging/discharging curves at a current density of 10 A g⁻¹; (b) Specific capacitances at current densities of 2 to 80 A g⁻¹; (c) Capacities retention up to 5000 cycles at 10 A g⁻¹..... 156

LIST OF TABLES

Table 2-1 Comparison of the supercapacitor from different companies.....	14
Table 2-2 Comparison of different kind of batteries.....	15
Table 5-1 Comparison of the specific capacitance value of as-prepared vanadium oxide nanoribbon with the reported studies in different electrolyte at the scan rate of 5 mV s^{-1}	115
Table 6-1 Comparison of the electrochemical performance of as-prepared NiCo_2O_4 @graphene with the materials reported in the literatures	132

ABSTRACT

Energy storage systems (ESSs) play a critical role in plenty of applications including renewable energy systems, power systems for electric vehicles (EVs) and hybrid electric vehicles (HEVs), and electrical power grids for improving reliability and overall use of the entire system. Currently, there are several types ESSs dominated the energy storage. Each kind of ESSs has their own operation mechanism, energy efficiency, energy density, power density, cycle life, charge and discharge capability, cost efficiency, operating temperature. The common ESS is based on lead acid battery which stores electrical energy in the form of chemical energy. However, if the batteries are overdischarged or kept at a discharged state, its capability will be irreversibly undermined because the sulfate crystals become larger and more difficult to break up during recharge. Since the first NiCd battery was created by Waldemar Jungner in 1899, even though NiCd battery technologies have experienced a series of evolutionary developments, its demerits are obvious including 1) shorter life cycle; 2) memory effect; 3) toxicity of Cd; 4) lower energy density; and 5) limited negative temperature coefficient. Based on the development of NiCd battery technology, nickel metal hydride (NiMH) batteries was proposed by researchers which possess better performance than NiCd batteries in cycle life, energy density and charge&discharge rates. Lithium ion is the preferred chemistry, having a superior specific energy and power density to nickel metal hydride. More lithium per gram stored in the electrodes contributes to higher energy density and power density. In addition to chemical battery system, researchers recently proposed some new sorts of ESSs including flywheel, compressed air energy storage (CAES), superconductive magnetic energy storage (SMES), etc. All of them can provide super energy density and power density. But they are more or less blocked either in complex mechanical

construction or cooling device.

Supercapacitor has emerged to be an exciting energy storage device, which is able to provide high specific power, charge and discharge up to million times, have long lifetime and broad range of working temperature. Even though supercapacitor has been widely seen as a promising energy storage candidate to replace the traditional chemical batteries, it also suffer its drawback that the low energy density (the energy stored in per unit of volume and weight), high equivalent series resistance (ESR) and its high cost associated with its performance.

Therefore, this PHD thesis project aims to address these drawbacks of supercapacitor by designing different nanotechnologies and fabrication methods to synthesize advance materials with better performance than that of conventional supercapacitor. A Series of designed structures and materials were fabricated by designed methods. All the materials were also investigated by using X-ray diffraction, scanning electron microscopy (SEM), transmission electron microscopy (TEM) observation techniques, Brunauer–Emmett–Teller (BET) surface area measurement and electrochemical testing.

A facile and effective hydrothermal treatment that is able to control the condensation speeds of precursors in the solution along the $\langle 010 \rangle$, $\langle 100 \rangle$ and $\langle 001 \rangle$ directions was designed to fabricate vanadium oxide nanoribbon used for the electrode of supercapacitor. It was achieved by controlling the hydrothermal reaction time and the weight ratio to synthesize the ultralong vanadium oxide nanoribbon with controlled width. It has high specific capacitance of 453 F g^{-1} at the scan rate of 2 mV s^{-1} in 2 M NaCl electrolyte, and it still maintained a high capacitance of 201 F g^{-1} at a higher scan rate of 50 mV s^{-1} , attributing to the easy ion insertion and electronic transport along the a-b plane rather through the layers of the c-axis.

Vanadium oxide nanotubes were synthesized by a revised hydrothermal treatment with high-speed stirring. The preparation involved dissolution of V_2O_5 into H_2O_2 and high-speed stirring (10000 r/min) with hexadecylamine. The product was characterized by scanning electron microscopy, transmission electron microscope, X-ray diffraction and thermogravimetric analysis. The electrochemical properties of the materials as electrodes for electrochemical capacitors were evaluated by cyclic voltammetry in a three electrode system consisting of a saturated calomel electrode as reference electrode, platinum as a counter electrode and the active materials as the working electrode. A high capacitance of 148.5 F g^{-1} was obtained at a scan rate of 2 mV s^{-1} in 2M KCl. The electrode maintained a high capacitance of 105 F g^{-1} at a higher scan rate of 50 mV s^{-1} in 2M KCl electrolyte.

3D mesoporous hybrid $NiCo_2O_4@graphene$ nanoarchitectures were successfully synthesized by a combination of freeze drying and hydrothermal reaction. Field-emission scanning electron microscopy (FESEM) and TEM analyses revealed that $NiCo_2O_4@graphene$ nanostructures consist of a hierarchical mesoporous sheet-on-sheet nanoarchitecture with a high specific surface area of $194 \text{ m}^2 \text{ g}^{-1}$. Ultrathin $NiCo_2O_4$ nanosheets, with a thickness of a few nanometers and mesopores ranging from 2 to 5 nm, were wrapped in graphene nanosheets and formed hybrid nanoarchitectures. When applied as electrode materials in supercapacitors, hybrid $NiCo_2O_4@graphene$ nanosheets exhibited a high capacitance of 778 F g^{-1} at the current density of 1 A g^{-1} , and an excellent cycling performance extending to 10000 cycles at the high current density of 10 A g^{-1} .

We also presented a rational, large-scale and general method, called controllable freeze casting (CFC), to fabricate a high-densely assembled and aligned free-standing $NiCo_2O_4@graphene$ 3D foam by vacuum filtration and air compress pressure assembly method. In the designed method, the amount of water is controllable, therefore controlling

the size and the shape of the ice when the material was introduced into freeze drying system, finally achieving controllable pore size and aligned structure. This free-standing foam retains the intrinsic properties of graphene sheet, such as high surface area and high electrical conductivity. In the foam, the graphene sheets build the high conductive skeletons. And the skeletons with high surface areas support the uniform distribution of NiCo₂O₄ nanoparticles on the graphene sheets. By controlling the amount of water in the precursor, it is possible to fabricate 3D NiCo₂O₄@graphene foams with a wide range of thickness and pore size. This dense NiCo₂O₄@graphene material exhibited a high capacitance of 790 F g⁻¹ at a current density of 2 A g⁻¹, and an excellent cycling performance at a high current density of 10 A g⁻¹. The compression test revealed that the 3D NiCo₂O₄@graphene foam exhibited strong mechanical property which is able to support 20,000 times its own weight without structure collapsing. The novel synthesis method of such 3D foam with excellent properties paves the way to explore the application of lamellar materials like graphene in a self-supporting, metal oxide deposition and 3D foam.

Chapter 1. INTRODUCTION

1.1. Research Aims and Objectives

This PHD thesis project aims to design the supercapacitor with long life, robust energy storage and high power density compared to current supercapacitor. The research focuses on novel structures and materials of the electrode to expand the surface area, optimizing the porous size and structure to improve the ion diffusion, specific capacitance, finally enhance the energy density without degrading the power energy density. The modeling, fabrication and testing of the electrodes were also done in the project. For the material of the electrode, different metal oxides with pseudocapacitance, especially V_2O_5 and $NiCo_2O_4$ were investigated. The first one is that design and fabricate the nanostructures of vanadium oxide as the supercapacitor electrode. The fabrication methods of vanadium oxide with the nanostructures were studied and proposed to synthesize nanotube and nanoribbon structures. Furthermore, to prepare 3D macroporous structure, sponge was used to support the 3D graphene structures. The ways to coat conductive materials including graphene were investigated. Based on the sponge foam, 3D mesoporous and macroporous foam with hybrid ultrathin $NiCo_2O_4$ nanosheets onto large-size graphene skeleton was fabricated by a facile method followed by post annealing treatment. The freeze drying system by using liquid nitrogen was designed to fabricate aligned 3D materials. Vacuum filtration with assistant of air compress pressure was designed to fabricate high-densely assembled and aligned free-standing $NiCo_2O_4@graphene$ 3D foam. Different methods to deposit metal oxides onto the prepared substrate will be proposed and implied to enhance the specific capacitance. The morphologies, electrochemical performance of the materials deposited with different metal oxides and mass of the metal oxides were comparative studied. The as-prepared high performance supercapacitor will

contribute to the many applications particularly the EVs.

1.2. Background and Significance

With increased climate change like global warming, more research concern has focused on minimizing the generation and exhaust of carbons dioxide. These concerns have led to the proliferation of electricity generation using both smart grid and distributed renewable energy resources such as wind, solar, tidal, etc. However, the intermittent nature of these renewable resources involves in the issues with system stability, power efficiency and electricity quality. In addition, power grid always experiences the growth of electronic loads and the requirement of supplying stable power with high quality. When a power disturbance like an instant increase of load occurs, the electricity generators are not able to take the rapid response. The ESSs which can convert electricity to another form of energy such as kinetic, chemical or magnetic, are being used to solve the issues of the renewable energy resource. Serving as an energy pool, in power grid, it can also address the continuous variations of the load and stabilize the power supply and demand.

Except the endeavor of generating more green energy, the consuming of energy also gave rise to lots of concerns. Currently, transportation consumption is one of the major and largest fuel consumers. Road vehicles emit significant air-borne pollution, including 18% of America's suspended particulates, 27% of the volatile organic compounds, 28% of Pb, 32% of nitrogen oxides, and 62% of CO.¹ Even though lots of solutions to improve the combustion rate of internal combustion engine (ICE) have been proposed and utilized in traditional vehicles, emission reductions and fuel-economy gains have been offset by more people, more cars, more vehicle miles traveled and larger light-duty vehicles. Transportation electrification is therefore seen as an effective way to substantially reduce the overall use of hydrocarbons.² Differing from traditional vehicles powered by ICE, the

technology innovations focused on more efficient vehicle configurations which have been presented in many researches and commercial automotive such as EVs,³ HEVs,⁴⁻¹⁵ plug-in hybrid electric vehicles (PHEVs),^{12, 16-32} and fuel-cell vehicles.^{5, 33, 34}

As a critical part of these new vehicle configurations, energy storage system is able to provide the power demand from electric motor and absorb the energy generated by regenerative braking, which is far fewer emissions and fuel consumption possibly about 30% less than that of the ICE-powered vehicles. The electrified vehicle with pure electric energy storage system that is capable of storing energy from power grid can achieve zero emissions of greenhouse gas such as hydrocarbon, carbon monoxide, and nitrogen oxides.

Currently, the electrochemical batteries have experienced great improvements in the energy density, environment tolerance and lifetime etc. Among the various types of electrochemical batteries, Li-ion battery, since the release of the first commercial Li-ion battery in 1991, shows a continued progression that has improved the performance and reliability. The cycle life in full discharge reaches to 1500-2000 cycles. The specific energy density is greater than 100 Wh kg^{-1} achieving from 150 to 250 Wh kg^{-1} ; the corresponding volumetric energy density is from 250 to 620 Wh l^{-1} ; and specific power reaches to about 1500 W kg^{-1} . Moreover, the operating temperature of Li-ion battery is also enhanced widely from -20°C to 60°C .^{1, 35}

However these batteries with faradaic reaction are limited by their chemical reactions associated with the limited cycleability, lifetime and the ability of quick charge and discharge. Electrochemical double layer capacitors (EDLCs), which are able to provide high specific power, be charged and discharge up to million times, and have long lifetime and broad range of working temperature, has attracted more and more attentions from researchers. The mechanism that EDLCs storage energy is similar to that of the

electrostatic capacitor: the charge forms on the parallel layers separated by an insulator. With the unlike charges on the electrodes, the electric energy then is stored in the electric field between the anode and cathode. Even though supercapacitor has been widely seen as a promising energy storage candidate to replace the traditional chemical batteries, it also suffer its drawback that the low energy density, high ESR and its high cost associated with its performance. The ability to fabricate the supercapacitor with high power and energy density, long life and robust performance has given rise to intense research activity on the study of carbon materials and transit metal oxides. Various carbon-based materials, including activated carbons, tangled carbon nanotube and aligned carbon nanotube, have been widely used as the electrodes of supercapacitor.

Activated carbon has earned its status in EDLC capacitor electrode materials due to its cost effectiveness and the large specific surface area that has the ability to accumulate a large number of charges.³⁶ Even though activated carbon has huge surface area³⁶⁻⁴⁰ which is more than $2000 \text{ m}^2 \text{ g}^{-1}$,^{36, 41, 42} the power density and energy density were limited by its widely varying pore sizes. The specific power of the electrode consisting of activated carbon is just $0.5\text{-}5 \text{ kW kg}^{-1}$, which leads to low specific energy densities ranging from 0.5 to 10 Wh kg^{-1} and the mass-specific capacitances is usually less than 200 F g^{-1} .^{42, 43} This results from that the active carbon always has the irregular pore size distribution ranging from 20 \AA micropores and 500 \AA micropores. Most of the surface area resides in micropores which are incapable of supporting an electrical double layer. The remaining surface area can be accessed as the ions migrate into the pores, accompanied by an increasing electrolyte resistance.⁴⁴ Therefore, the micropores ($<2 \text{ nm}$) of activated carbon are difficult to be completely wet with electrolyte. Hence, an undesired decrease in capacitance is evident at high current density due to the resistance of the diffusion and transport of electrolyte ions in inner-pores.³⁶ Elzbieta gave the rough theoretical estimate

that the ideal attainable capacitance should be 250F g^{-1} .³⁹ However, the practical capacitance is just a few tens of farad per gram. In addition, the addition of a binder^{39, 43, 45-48} is necessary in the synthesis of the electrode to adhere the activated carbons into together. The binder material inevitably blocks the ion accessing the pore of the electrode and degrades the electrical conductivity, additionally leads to high ion diffusion resistance.⁴⁹

Owing to these drawbacks mentioned above of activated carbon, carbon nanotubes (CNTs) including single-walled and multi-walled carbon nanotubes (SWNTs and MWNTs) are replacing the roles of activated carbon in the supercapacitor electrodes. Currently, CNTs are attractive materials for the electrodes of supercapacitor owing to their superb characteristics of electrical,⁵⁰⁻⁵⁴ mechanical low mass density,^{55, 56} low resistivity and large surface area.^{44, 57-59} Some electrodes consisting of tangled CNTs^{57, 60-62} have achieved more excellent performance than activated carbon. However, it is difficult to maintain high permeability and porosity of the tangled CNTs film. The random network of CNTs also involves in binder to bind the single SWNT or MWNT together to form the thin film. Moreover, the acid-treated process introduced in the preparation of CNTs inevitably degrades the intrinsic properties of single CNT. Another drawback of CNTs-based electrode is that the contact resistance between the CNTs and the metal current collector.

With better controllable porous size and lower ion diffusion resistivity, aligned carbon nanotubes make them a most promising candidate for energy storage. There has been a number of effort and development in the studying and fabricating aligned CNTs for the energy storage. The power density of aligned CNTs-based electrode has reached to 13Wh kg^{-1} or 10.4Wh l^{-1} from 3.9Wh kg^{-1} or 3.1Wh l^{-1} , and the power density ranges from

3.50 kW kg⁻¹ to 163 kW kg⁻¹.^{44, 58, 63} Especially, Signorelli *et al.*³⁵ employed the low-pressure chemical vapor deposition (LPCVD) to fabricate the MWNT directly on the aluminum substrates, and the energy densities increases to 35 Wh kg⁻¹ and 37 Wh l⁻¹ which is approximately seven times higher than the energy densities available with commercial activated carbon EDLCs. However, the energy density is not enough to serve in the application requiring high energy like electrical vehicle. Moreover, single walled carbon nanotubes are very likely to stack in bundles. As a result, only the outermost portion of CNTs can function for ion absorption and the inner carbon atoms are all wasted, leading to lower specific capacitance of CNT-based supercapacitors.⁶⁴

Graphene, a one-atom-thick two-dimensional sheet of sp²-hybridized carbon atoms,^{65, 66} is considered as the outstanding electrode material for electrochemical double layer capacitors.^{42, 64, 66-68} Due to its intriguing structure single layer of carbon,⁶⁹ graphene possesses high electric conductivity and mechanical strength, charge carrier mobility,⁴² high specific surface area up to 2675 m² g⁻¹,^{64, 68} which is much larger than that of activated carbon and carbon nanotubes. Moreover the specific capacitance of graphene is able to reach to 21 uF cm⁻², and graphene has the largest theoretical electrochemical double layer capacitance of about 526 F g⁻¹.⁶⁴ It can also provide conduction pathways to a greater area per unit mass than CNTs, which should translate into improved conductivity.⁶⁹ In addition, the supercapacitor based on the graphene film can work in high frequency,⁷⁰ being different from activated carbon and CNTs. However, graphene usually agglomerates together to form the graphite and fail to maintain its intrinsic properties especially the large surface area. Curved graphene and other spacer materials have been employed to separate the graphene to avoid restacking, which finally improved the surface area and the specific capacitance.

However the supercapacitor with only EDLC mechanism is limited by its energy density.^{71, 72} There is a critical need to develop novel supercapacitor electrodes with improved high-energy and remained high-power properties. Another type of supercapacitor with pseudocapacitance is a promising energy storage device to improve the energy density and still maintain the high power density of supercapacitor. Unlike the EDLC's energy storage mechanism that occurs at or near the electrode/electrolyte interfaces, pseudocapacitor involves in the transfer of charges between electrode and the ion in the electrolyte which is a Faradic process. Pseudocapacitive transition-metal oxides are predicted to have a high capacitance for storing electrical charge while also being inexpensive and not harmful to the environment.^{72, 73} Ruthenium oxide (RuO_2) has been intensively studied for pseudocapacitors⁷⁴⁻⁷⁹ because of its intrinsic reversibility of surface redox couples,⁷⁴ theoretical specific capacitance as high as 1358 F g^{-1} and high electrical conductivity ($3 \times 10^2 \text{ } \Omega^{-1} \text{ cm}^{-1}$).⁷⁵ But the high cost and rareness of Ru inhibit the commercialization of the supercapacitor based on RuO_2 . Among broadly available transition metal oxides, vanadium pentoxide is one of the most promising ion insertion materials.⁸⁰ Vanadium pentoxide (V_2O_5) is abundant, relatively inexpensive (\$12 per kg), layered structure⁸⁰ and offers a broad range of oxidation states which will offer the broad range of redox reactions suitable for supercapacitor operation.⁷¹ V^{5+} can be easily reduced leading to mixed valence vanadium oxides in which both V^{5+} and V^{4+} and even V^{3+} ions are observed.⁸¹ In addition to V_2O_5 , MnO_2 is considered another pseudocapactive material for high-performance supercapacitors because of its high theoretical specific capacitance, low-cost, environmental benignity, and natural abundance.^{73, 82} $\text{RuO}_2 \cdot x\text{H}_2\text{O}$ and NiOOH have to be used in strong acidic or alkaline electrolytes which may cause environment pollution; in contrast, MnO_2 can be used in neutral aqueous electrolytes.⁸³ In comparison, NiCo_2O_4 is one of the most promising transition metal oxide for pseudocapacitors due to

its intriguing electronic conductivity, low diffusion resistance to protons/cations, easy electrolyte penetration and electrochemical properties.⁸⁴⁻⁸⁷ In NiCo₂O₄, it is generally regarded that the nickel occupies the octahedral sites and cobalt is distributed over both octahedral and tetrahedral sites, in which the solid-state redox couples Co³⁺/Co²⁺ and Ni³⁺/Ni²⁺ are present.⁸⁴ In order to obtain high specific capacitance from NiCo₂O₄, many studies has been focusing on the optimization of its morphology and incorporating NiCo₂O₄ with conductive materials to synthesize hybrid electrode structure. Wei⁸⁶ *et al.* synthesized spinel nickel cobaltite aerogels with a specific capacitance of 1400 F g⁻¹ at the sweep rate of 25 mV s⁻¹. Yuan *et al.* demonstrated ultrathin mesoporous NiCo₂O₄ nanosheets grew on Ni foam by co-electrodeposition of Ni and Co which has a high specific capacitance of 1450 F g⁻¹ at the current density of 20 A g⁻¹. Furthermore, Zhang *et al.* fabricated mesoporous NiCo₂O₄ nanosheets on Ni foam, Ti foil, stainless-steel foil and flexible graphite paper,^{88, 89} and nanoneedle arrays⁸⁵ on carbon nanofiber exhibiting high capacitance and cycle ability.

However, the poor electric conductivity of the transition metal oxide limits the performance in high power density, cycling, high charge and discharge rate. To improve the electric conductivity of the transition metal oxides, researchers have developed composites in which the transition metal oxide are ex-situ or in-situ combined with highly conductive materials such as graphite,⁹⁰ active carbon,^{91, 92} CNT,⁹³⁻⁹⁶ conducting polymers,^{79, 97} graphene.^{73, 82, 98, 99} The morphology of the fabricated materials is another critical factor that influences the performance of the supercapacitor. Nanorod, nanosheet, nanoflower, nanofoam are synthesized to optimize the ion diffusion path. The shorter diffusion path of ion leads to faster charging and discharging of supercapacitor, and less degradation of specific capacitance with the increased scan rate or current density.

Therefore, it is urge to design novel material synthesis methods and fabricate high-performance materials with controllable structures, excellent conductivity and relative mechanical strength. The supercapacitor with long life, robust energy storage and high power density is then produced, based on the as-prepared high-performance materials.

1.3. Thesis Outline

The thesis is organized as follows:

In Chapter 1, the objective and background of the PHD project are introduced. The research focuses on fabrication of materials with controllable structure to expand the surface area, optimizing the porous size and structure to improve the ion diffusion, specific capacitance, finally enhance the energy density without degrading the power energy density. After that, the significance and background about supercapacitor are presented.

In Chapter 2, the state of art of the energy storage technologies including supercapacitor, battery, flywheel and superconductive magnetic energy storage are studied. The metrics and parameters of supercapacitor are also summarized. The physical and mathematic models of supercapacitor enable the understanding the mechanism of energy storage in supercapacitor. And the precise description and simulation of the behavior of supercapacitor is a necessary for the industry applications. Therefore, the physical and mathematic models of supercapacitor were compared in this chapter. Finally, the chapter classifies the various electrode materials and the fabrication methods for supercapacitor such as carbon nanotube, graphene-based composites, unzipped CNTs and the metal oxides.

In Chapter 3, the methods used to synthesize the active materials are described. The

relative characterization equipment and techniques are reported to investigate the physical and morphological properties of the as-prepared materials. The chapter presents the procedure, electrode fabrication and the electrochemical testing.

In Chapters 4 to 6, the fabrication of vanadium oxide nanoribbon, nanotube and 3D mesoporous hybrid NiCo_2O_4 @graphene nanoarchitectures are described. The products are characterized by using scanning electron microscopy, transmission electron microscope, BET and X-ray. The electrochemical properties of the material as the electrode of electrochemical capacitor were evaluated by cyclic voltammetry in a three electrode system.

Chapter 7 focuses on the fabrication of 3D graphene foam with aligned and compressed structure. It starts with an introduction of the as-designed device used in this project. And then the mechanism of the fabrication method is discussed. The mechanical testing, morphology, physical and electrochemical properties are investigated.

In Chapter 8, the contribution of this PHD project to fabrication and understanding of high-performance supercapacitor is summarized. And the next challenges that we have to fix in the future work are discussed.

Chapter 2. Literature Review

2.1. Energy Storage Technologies

2.1.1. Supercapacitors

The storage of electrical charge on two surfaces has been studied since from the discovery of the Leyden jar in which two electrodes are separated by a layer of glass. It was of major significance for the development of supercapacitors. Although plenty of experimental and theoretical studies about the electrical charging of surfaces were conducted after the invention of the Leyden jar, the charge storage on the surface of capacitors could not have been fully confirmed until the electron was characterized. The charging of the conductive plates will involve generation of excess or deficiency of the density of delocalized electrons of the electrodes. The energy stored in the supercapacitor can be represented by G :

$$G = \frac{1}{2} CV^2 = \frac{1}{2} qV \quad (1.1)$$

where the V is the potential difference between the two electrodes, established by the electrodes accommodating charges $+q$ and $-q$.

The earliest practical use of EDLC (Figure 2-1) was proposed by Becker and Ferry from the General Electric Company, which was patented in 1957.¹⁰⁰ The patent claimed the charges were stored at the double layer between the porous carbon material and the aqueous electrolyte which exhibited high capacitance. The Standard Oil Company, Cleveland, Ohio (SOHIO) is the first company to use activated carbon as the electrodes for their supercapacitors (Figure 2-2). In the patent claimed by SOHIO in 1970,

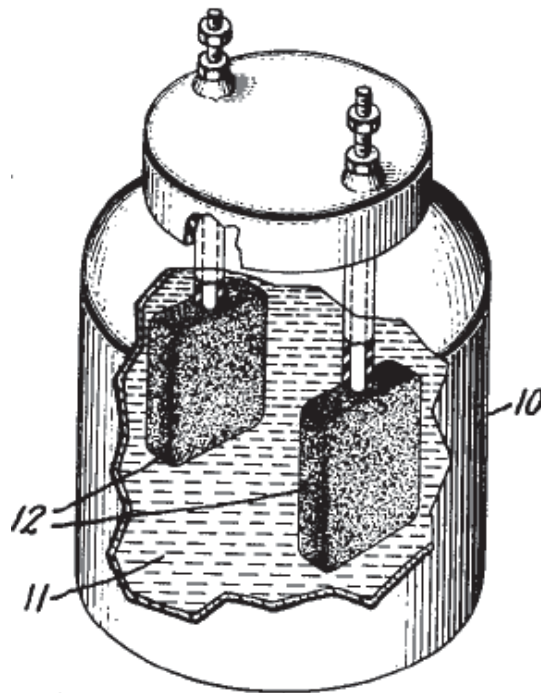


Figure 2-1 The schematic of the electrolytic capacitor designed by Becker and Ferry.¹⁰⁰

the specific surface of the activated carbon which was used to mix with electrolyte reached to $1500 \text{ m}^2 \text{ g}^{-1}$.¹⁰¹ In contrast to a much lower specific capacitance achieved by Becker's supercapacitor, the high surface area of activated carbon used by SOHIO contributed to a high specific capacitance of 200 farads per cubic inch of total capacitor volume. What is more important, the past technology invented in this patent prevents the carbon electrode from cracking and breaking during charging and discharging.

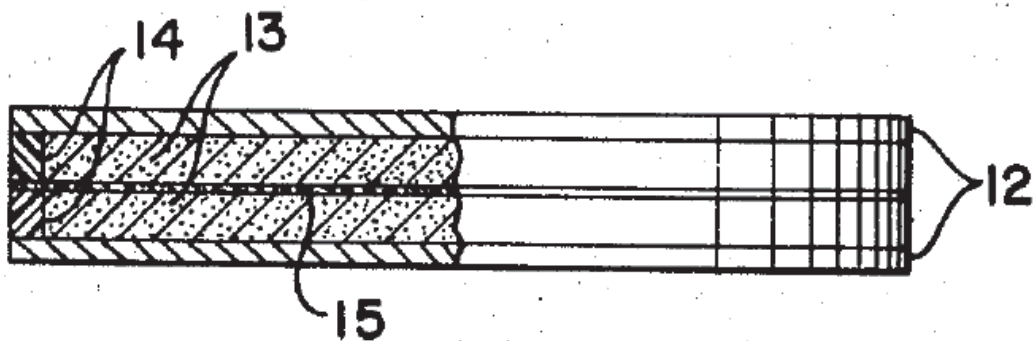


Figure 2-2 The schematic of the electrolytic capacitor designed by SOHIO.¹⁰¹

Another type of supercapacitor with different energy storage principle to EDLC was developed by Conway from 1980s, which was called pseudocapacitor.¹⁰² It involves in a sequence of reversible redox processes in which the chemical and associated electrode potentials increase with the degree of charge. There are two kinds of pseudocapacitor: one of them is based on the faradaic pseudocapacitance of two-dimensional (2D) or quasi 2D materials; another one involves the oxidation/reduction in the microporous transition metal hydrous oxides like RuO₂, IrO₂ and other oxide mixtures.¹⁰² Owing to the reversible charging and discharging with the redox reaction, pseudocapacitor is able to approach large specific capacitance and multiple cyclability over 100, 000 cycles.

Nowadays, a number of companies around the world design and manufacture commercial supercapacitors including EDLCs and pseudocapacitors. The use of activated carbon or metal oxide materials with large surface area has led to the commercial manufacture of high-capacitance supercapacitor. Maxwell in USA is one of the major manufacturers which produce supercapacitors. As shown in the Table 2-1, the supercapacitors produced by Maxwell are able to operate at a high voltage of 2.7 V, with various capacitance from 650 F to 3000 F. Nesscap, established in 1998, designed and produced a range of large-size supercapacitor to satisfy various requirements from different application. It also markets supercapacitor modules such as specifically designed for internal combustion engines in cold temperature. In addition, Nesscap is one of the first companies which market small and medium-sized pseudocapacitors. These pseudocapacitor cells have capacitances from 50 F to 300 F with operating voltage of 2.3 V, which are able to store approximately twice the energy of a typical EDLC of the same size and weight. What's more important, the cost per unit of energy of producing a pseudocapacitor is lower than that of an EDLC. Cap-XX in Australia focuses on making thin and flat supercapacitors with high power and energy density.

Table 2-1 Comparison of the supercapacitor from different companies.

Device	System type	V rated	Capacity(F)	Resistance (mOhm)	Wh/Kg	kW/kg (95%)	kW/kg, Impedance Match Specific Power	Weight (kg)
Maxwell	Activated Carbon/acetonitrile/Activated Carbon	2.7	650	0.8	4.1	6.8	14	0.16
Maxwell	Activated Carbon/acetonitrile/Activated Carbon	2.7	1200	0.58	4.7	5.8	12	0.26
Maxwell	Activated Carbon/acetonitrile/Activated Carbon	2.7	1500	0.47	5.4	6.6	14	0.28
Maxwell	Activated Carbon/acetonitrile/Activated Carbon	2.7	2000	0.35	5.6	6.9	14	0.36
Maxwell	Activated Carbon/acetonitrile/Activated Carbon	2.7	3000	0.29	6	5.9	12	0.51
Nippon Chemicon	--	2.5	350	6.5	4.4	--	--	0.09
Nippon Chemicon	--	2.5	700	4	4.7	--	--	0.15
Nippon Chemicon	--	2.5	1400	2.4	4.6	--	--	0.28
Nippon Chemicon	--	2.5	2300	1.2	4.3	--	--	0.47
Nesscap	Activated Carbon/acetonitrile/Activated Carbon	2.7	650	0.6	3.2	7.1	14.8	0.205
Nesscap	Activated Carbon/acetonitrile/Activated Carbon	2.7	1200	0.48	4.3	6.5	13.5	0.28
Nesscap	Activated Carbon/acetonitrile/Activated Carbon	2.7	1600	0.41	4.8	6.3	13.2	0.335
Nesscap	Activated Carbon/acetonitrile/Activated Carbon	2.7	2000	0.33	5.1	6.7	14.1	0.39
Nesscap	LiCoO2 /LiMn2O4/Propylene carbonate /Activated Carbon	2.3	120	<27	5.87			0.015
Nesscap	LiCoO2 /LiMn2O4/Propylene carbonate /Activated Carbon	2.3	300	<18	8.73			0.0252
Nesscap	LiCoO2 /LiMn2O4/Propylene carbonate /Activated Carbon	2.3	10000	0.4	8.65			0.85

2.1.2. Battery

Currently, the electrochemical batteries have experienced great improvements in the energy density, environment tolerance and lifetime. Among the various types of electrochemical batteries, Li-ion battery, since the release of the first commercial Li-ion battery in 1991, shows a continued progression that has improved the performance and reliability. The cycle life in full discharge reaches 1500-2000 cycles. The specific energy density is greater than 100 Wh kg^{-1} achieving from 150 to 250 Wh kg^{-1} ; the corresponding volumetric energy density is from 250 to 620 Wh l^{-1} ; and specific power reaches about 1500 W kg^{-1} . Moreover, the operating temperature of the Li-ion battery is also enhanced widely from -20°C to 60°C .^{1,35}

Batteries store energy in the form of chemical energy. The one way conversion efficiency is about 85 to 90%. A typical battery cell has a chemical electrolyte between positive and negative electrode plates with insulating separators. The two groups of electrode plates are connected to two external terminals mounted on a casing. The cell stores electrochemical energy at a low electrical potential which is involved in electrochemical reactions. The battery rating is stated in terms of the average voltage during discharge and ampere hour (Ah) capacity it can deliver before the voltage drops below the specified limit. The product of the voltage and Ah gives the energy rating in

Table 2-2 Comparison of different kind of batteries.

Battery types	Cell Voltage (V)	Properties
Lead acid	2.0	Least cost
Nickel cadmium	1.2	Memory effect
Nickel metal hydride	1.2	Temperature sensitive
Lithium ion	3.6	Safe, high energy density
Lithium polymer	3.0	Contains metallic lithium
Zinc air	1.2	Requires continues air management

watt hours (Wh) that the battery can deliver to a load from the fully charged condition.

The state of charge (SOC) of the battery at any time is defined as:

$$\text{SOC} = \frac{\text{Ah capacity remaining in the battery}}{\text{Rated Ah capacity}} \quad (1.2)$$

There are many types of rechargeable batteries. The commonly used ones are:

- Lead-acid (Pb-acid)
- Nickel-cadmium (NiCd)
- Nickel-metal hydride (NiMH)
- Lithium-ion (Li-ion)
- Lithium-polymer (Li-poly)
- Zinc-air

2.1.2.1. Lead-acid battery

Lead-acid battery is the most common type of rechargeable battery used today because of its maturity and high performance over cost ratio, though it has the least energy density by weight and volume. The lead acid battery stores electrical energy in the form of chemical energy. When it discharges energy, the battery releases its stored chemical energy into an electrical circuit. In addition, the electrochemical reaction in this battery is reversible. The charging and discharging of the lead-acid cell can be described by the chemical reaction,¹⁰³ where the cell's positive active material (lead dioxide-PbO₂) and its negative active material (sponge lead-Pb) both react with the sulfuric acid electrolyte to form lead sulfate (PbSO₄) and water.¹⁰⁴

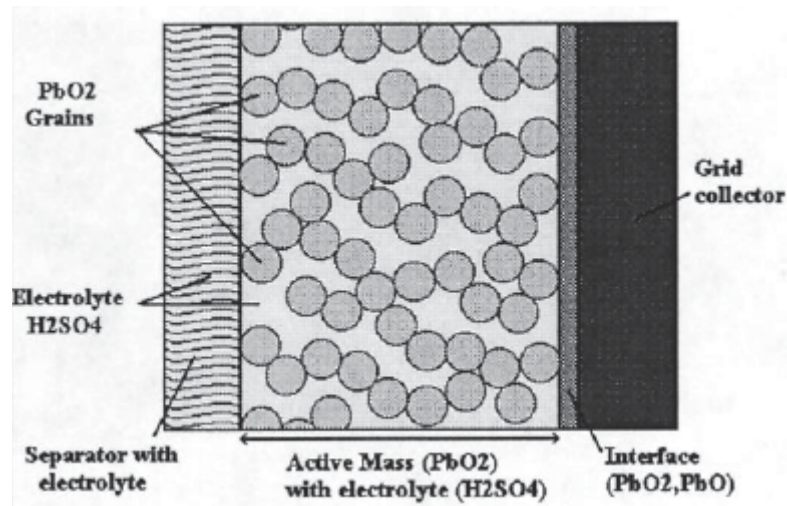


Figure 2-3 Section view of the positive plate. ¹⁰⁴



The author presented the discharge and charge process through the inner mechanism prospective.¹⁰³ During discharge, lead sulfate is produced on both electrodes. If the batteries are over-discharged or kept at a discharged state, the sulfate crystals become larger and are more difficult to break up during recharge. In addition, the large lead sulfite crystals disjoin the active material from the collector plates. Due to the production of hydrogen at the positive electrode, lead acid batteries suffer from water loss during overcharge.² Distilled water is sometimes added to flooded lead acid batteries to mitigate this problem. Maintenance-free versions use a valve to minimize the water loss by allowing hydrogen and oxygen recombination. Current collectors in lead acid batteries are made of lead, leading to the low energy density (in watt hours per kilogram). Furthermore, the lead is prone to corrosion when exposed to the sulfuric acid electrolyte.

2.1.2.2. Nickel-cadmium (NiCd) battery

Since the first NiCd battery was created by Waldemar Jungner in 1899, NiCd battery

technologies have experienced a series of evolutionary developments in the positive and negative electrodes, and the separators. Each of these generations has a number of major cell design factors which show a continued progression toward optimum values that have enhanced performance and reliability with concomitant improvements in useable energy density.

Currently, the positive electrode of Nickel-cadmium battery is made of cadmium and the negative electrode is nickel hydroxide. The two electrodes are separated by nylon separators and placed in potassium hydroxide electrolyte in a stainless steel casing. With a sealed cell and half the weight of the conventional Pb-acid, the NiCd battery has been used to power most rechargeable consumer applications; it has a longer deep-cycle life and is more temperature tolerant than the Pb-acid battery.

NiCd batteries have a higher energy density and longer cycle life than lead acid batteries but are inferior to NiMH batteries. Other disadvantages of NiCd batteries compared to NiMH include the following: 1) shorter life cycle; 2) more memory effect; 3) toxicity of Cd that requires a complex recycling procedure; 4) lower energy density; and 5) flat discharge curve and negative temperature coefficient that may cause thermal runaway in voltage-controlled charging.

2.1.2.3. Nickel-metal hydride battery

Because of the defects of NiCd batteries mentioned above, nickel metal hydride (NiMH) batteries possess better prominence than NiCd batteries in cycle life, energy density and charge/discharge rates. NiMH batteries use nickel oxyhydroxide for the positive electrode and metallic cadmium for the negative electrode. In fact, the nickel-metal hydride battery is an extension of the NiCd technology and offers an improvement in energy density over NiCd. The major construction difference is that the anode is made of a metal hydride.

This eliminates the environmental concerns of cadmium. Another performance improvement is that it has a negligible memory effect.

However, NiMH is less capable of delivering high peak power, has a high self-discharge rate, and is susceptible to damage due to overcharging. Compared to NiCd, NiMH is expensive at present although the price is expected to drop significantly in the future.

2.1.2.4. Lithium-ion battery

Lithium ion is a preferred chemistry which has superior specific energy than nickel metal hydride. Lithium polymer, a development of lithium technology, promises to further improve on these values. In the Li-ion battery, lithium moves from one electrode to the other and back again, depending on whether the battery is being charged or discharged. Essential points of development involve better materials (storing more lithium per gram, especially in the cathode) and better engineered products (with less void space and lighter packaging).

Lithium-ion battery is a new development, which offers three times the energy density over that of Pb-acid. Such a large improvement in energy density comes from lithium's low atomic weight of 6.9 vs. 207 for lead. Moreover, Li-ion has a higher cell voltage, 3.5V vs. 2V for Pb-acid and 1.2V for other electrochemistries. This requires fewer cells in series for a given battery voltage, thus reducing the manufacturing cost.

2.1.3. Flywheel

Flywheel stores kinetic energy in a rotating inertia. It has been commonly used as a mechanical device for equalizing the speed of rotation. Flywheel energy storage (FES) works by accelerating a rotor (flywheel) to a very high speed and maintaining the energy in the system as rotational energy. When energy is extracted from the system, the

flywheel's rotational speed is reduced as a consequence of the principle of energy conservation; adding energy to the system correspondingly results in an increase in the speed of the flywheel. Most FES systems use electricity to accelerate and decelerate the flywheel, but devices that directly use mechanical energy are being developed.

Advanced FES systems have rotors made of high strength carbon-composite filaments, suspended by magnetic bearings, and spinning at speeds from 20,000 to over 50,000 rpm in a vacuum enclosure. Such flywheels can come up to speed in a matter of minutes-much quicker than some other forms of energy storage. The round trip conversion efficiency of a large FES can approach 90%, much higher than that of a battery. The energy stored in a flywheel is limited by the mechanical stresses due to the centrifugal forces at high speeds. Modern FES can achieve five times the energy density of the currently available batteries.

The energy stored in a flywheel having the moment of inertia J and rotating at an angular speed ω is given by the following:

$$E = \frac{1}{2} J \omega^2 \quad (1.4)$$

The centrifugal force in the rotor material of density ρ at radius r is given by $\rho(r\omega)^2$, which is supported by the hoop stress in the rotor rim. Because of the linear velocity $v = 2\pi r\omega$, the maximum centrifugal stress in the rotor is proportional to the square of the outer tip velocity. The allowable stress in the material places an upper limit on the rotor tip speed. Therefore, a smaller rotor can run at a higher speed. The thin rim type rotor has a high inertia to weight ratio and stores more energy per kilogram weight. For such a rotor with inner radius R_1 and outer radius R_2 , the maximum energy that can be stored for an

allowable rotor tip velocity is

$$E_{\max} = K_1 v^2 \left[1 + \left(\frac{R_1}{R_2} \right) \right] \quad (1.5)$$

where K_1 is the proportionality constant.

2.1.4. Superconductive Magnetic Energy Storage

Superconducting magnetic energy storage (SMES) is new type of energy storage system which consists of superconducting magnet and power regulator system.¹⁰⁵ SMES is able to quickly provide the active and reactive power almost instantaneously which improves the dynamic characteristics of power network. In addition, high power output is always available in a very short time. The primary function of the SMES is to insulate the network from high-frequency power fluctuations thereby acting as a shock absorber.¹⁰⁶ It stores the energy in magnetic fields:

$$E = \frac{1}{2} Li^2 \quad (1.6)$$

However, in order to maintain the energy storage function of SMES, it has to cool the temperature below the superconducting critical temperature. High temperature superconductors SMES is becoming practical owing to the advanced cooling system. Also, the efficiency is able to reach to 95% and the maximum system now is 5000 MWh with life time up to 30 years. However, the scale-size of the SMES is usually very large which is inevitable to increase the total cost of the system. A large-size of cooling system is also necessary to maintain the function of the system.

2.2. Supercapacitor Metrics and Parameters

The basic measures of supercapacitor performance are the electrode surface area, the electrode area-specific differential capacitance, the electrode volumetric capacitance, the

frequency behavior of the impedance, the shape of the cyclic voltammetry trajectory, and the ESR which is reflected in the power density of the device.^{35, 41}

2.2.1. Electrode Surface Area

The electrode surface area is usually measured by the BET method, which relates the weight of a monolayer of gas adsorbed on the accessible surface of the carbon electrode to the surface area of a uniform monolayer of the gas. The measured result is known as the BET surface area with the units of square meter per gram.

2.2.2. Electrode Area-specific Capacitance

The electrode area-specific capacitance in units of farad per square centimeter, commonly known as the differential capacitance or intrinsic capacitance, C_d , is the incremental capacitance (dQ/dV) of 1 cm² of the BET measured surface area of the carbon. It is a function of both the measurement frequency and bias voltage. The frequency dependence arises because of the different transit times of ions penetrating the different pore sizes in the carbon. The voltage dependence is due to the nonlinear relationship between the charge in the Helmholtz layer and the potential between the solid electrode and the bulk of the electrolyte.

2.2.3. Gravimetric Capacitance of Carbon Electrode

Assuming that the entire BET surface area is accessible to the ionic charge, the gravimetric specific capacitance can be approximately calculated by the product of C_d and the BET surface area.

2.2.4. Volumetric Specific Capacitance

Volumetric Specific Capacitance is the capacitance of 1 cm³ of electrode volume. It is

able to reflect the density of pores as well as the area specific capacitance. It allows a relative measure of the physical size of an electrode at specific rating current density.

2.2.5. Impedance

The impedance data of a supercapacitor represent its various behaviors from capacitor to resistor with the change of frequency. Nyquist diagram is generally used to plot the impedance against the frequency. The cyclic voltammetry is also used to describe the reaction on the surface of the electrode when the voltage across the electrodes changes at a fixed scan rate.

2.2.6. Power Density

Power density is able to scale the power in units kW kg^{-1} or kW l^{-1} of electrode material. It focuses on the amount of power the supercapacitor discharged, based on the weight or volume of the active material of the electrode. As a practical matter, the power density provides a comparative measure of the pulsed power capability of a supercapacitor.

2.2.7. Energy Density

Energy Density providing a useful comparative measure of the capability of a supercapacitor was a common-cited parameter. It represents the capability of a supercapacitor which stores energy in per kilogram or per liter in the units Wh kg^{-1} or Wh l^{-1} .

2.3. Supercapacitor Modelling

2.3.1. Physical Model

The precise description and simulation of the behavior of supercapacitor is a necessary

prerequisite for each application. In this section, the physical model is first analyzed. Through the understanding of the physical properties, the mathematical equation is deduced to represent the physical model which can be simulated by an equivalent circuit.

2.3.1.1. Helmholtz Model

In 1853, Helmholtz proposed the first model of double layer capacitors (DLCs) which described the properties of the interface between the electronic conductor and the electrolyte. Unlike the traditional parallel capacitor, the electrons are stored at the

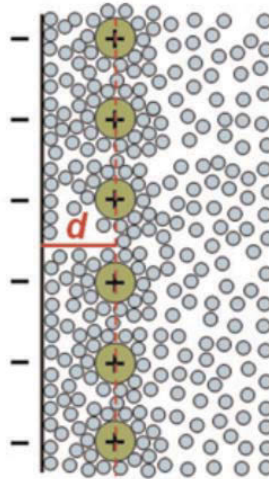


Figure 2-4 Helmholtz model.¹⁰⁵

surface of electrodes as shown in Figure 2-4. The charge formed on the electrode is balanced in solution by an equal but oppositely charged amount of ions.¹⁰⁷ Two capacitors are therefore constructed at the anode and cathode respectively. As known, the capacitance of a capacitor can be obtained through:

$$C = \frac{\epsilon_0 \epsilon_1 A}{4\pi d} \tag{1.6}$$

Therefore, the total capacitance of an EDLC is

$$C_{total} = \frac{1}{2} C \tag{1.7}$$

In Helmholtz model, due to the new structure that opposite charge accumulated on the surface of electrode and electrolyte, the distance d is quite short being limited by the ionic radius. This molecule-scaled distance contributes to large capacitance which can be up to thousands of Farads. The line drawn through the center of such ions at a minimum distance from the electrolyte surface marks the boundary known as the ‘Outer Helmholtz Plane’ (OHP). The region within this plane Helmholtz called the electrical double layer.

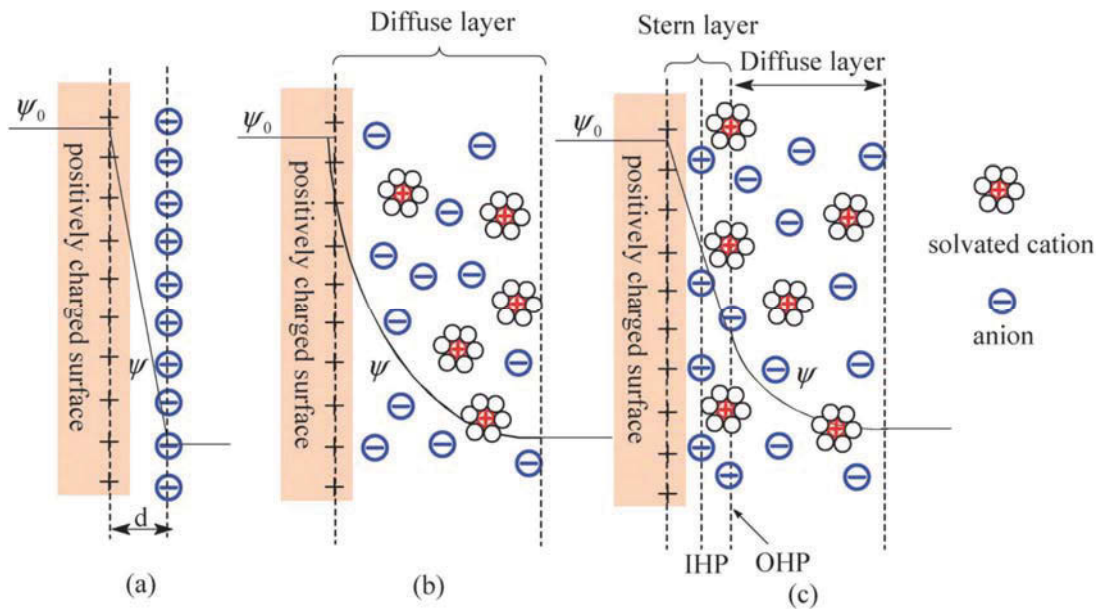


Figure 2-5 Potential distribution of Helmholtz model, Gouy-Chapman model and Stern model.¹⁰⁶

With the generation of a double layer with anions and cations, a potential difference occurs across the interface, forming an electric field gradient across the charge separation layer. In the Helmholtz model, it is assumed that all the ions within the electrolyte are attracted at each OHP. This assumption means two electric field jumps occur at the two OHP, and the electric field in the electrolyte is static, no change as shown in Figure 2-5.

2.3.1.2. Gouy-Chapman Model

Gouy and Chapman introduced the random thermal motion in the electrolyte to describe features of DLCs.¹⁰⁸ The thermal motion accounts for the concept that the electrolyte ions are not completely situated at the OHP. This means there are charges randomly moving in the electrolyte and the thickness of the OHP is not rigidly stable. They pointed out that it is not a rigid Helmholtz double layer, but a diffuse double layer in the DLCs. Unlike the Helmholtz model's assumption, the charge density decreases with the distance from the boundary of electrode and electrolyte. Therefore, the potential from the electrode to the electrolyte is gradually changing with the distance between electrode and the position in the electrolyte as shown in Figure 2-5. However, in the Gouy-Chapman model, they saw the ions in the electrolyte as individual points without radius. The capacitance theoretically calculated from the model provided by Gouy and Chapman is therefore higher than that experimentally measuring. G. M. Torrie and J. P. Valleau¹⁰⁹ compared the Monte Carlo calculation results of the charge distribution and potential of the diffuse layer with that of the Gouy-Chapman model, and found that the Gouy-Chapman model greatly overestimates the surface potential even at quite low surface charges and electrolyte concentrations.

2.3.1.3. Stern Model

In 1924, Stern pointed out that the DLC construction has the combinational features of Gouy-Chapman and Helmholtz. As he described, the DLCs have ions of electrolyte situated at the electrodes and the diffuse distribution as Gouy and Chapman presented.¹⁰⁸ Stern assumed the charge in the electrolyte on the solution side resided partially in a compact layer (the Helmholtz charge), and the remainder of the charge resides in a diffuse region (as in the Gouy-Chapman models) in the solution. In the Stern

$\frac{1}{C} = \frac{1}{C_H} + \frac{1}{C_G}$ Model, the total capacitance of the DLC is determined by the combination

of the Helmholtz Capacitor and Gouy-Chapman capacitor. The total capacitance formed on one of the electrodes is therefore shown as:

$$(1.8)$$

From the formula and analysis, we can see that Helmholtz Capacitor and Gouy-Chapman capacitor work in a serial model which means the capacitor with smaller capacitance will dominate the whole performance of DLC. Therefore in his model, he successfully explained that the overall performance will depend on the C_G in low dilute solutions and zero charge.

2.3.1.4. Grahame Model

A further improvement of the DLC model is made by Grahame, showing more detail about the region near the electrode. Grahame suggested that some special molecules may penetrate into the closest region to electrode, which will cause the change of potential from the electrode to the solution. These special molecules include the ions without solvation shell or which lost their shell. When approaching the electrode surface, strongly solvated cations cannot shed their solvation sheath and, hence, cannot reach the surface of the metal. Therefore they are not affected by specific adsorption forces, which act efficiently only at very short distance. On the contrary, weakly solvated anions easily shed their solvation sheath, so that they can approach the metal surface very closely and can be adsorbed.¹¹⁰ After they penetrate the region, in contrast to the two regions described by Stern, three regions are formed with two planes. The first region is from the surface of the electrode to the center of the specific adsorbed ions which is the first plane: the inner Helmholtz plane. The area between inner and outer Helmholtz plane is the second region. In the third region, it is the diffuse part which all sorts of ions can access.

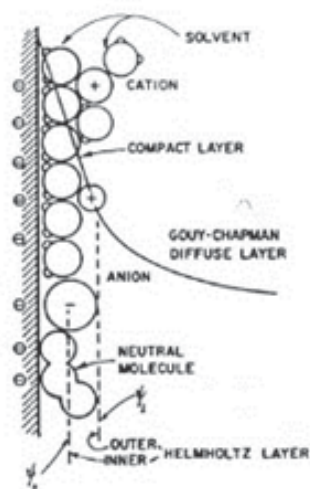


Figure 2-6 Grahame model and the charge distribution.¹⁰⁸

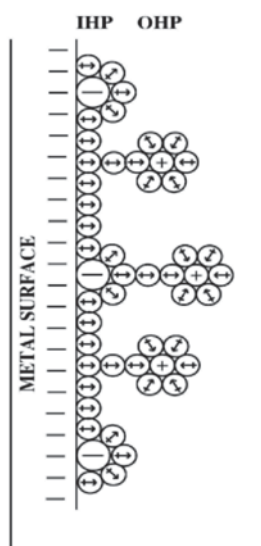


Figure 2-7 Bockris, Devanathan and Muller Model: Water dipole model of the double layer at an electrode/electrolyte interface.¹⁰⁹

2.3.1.5. Bockris, Devanathan and Muller Model

Bockris, Devanathan and Muller took into account solvent impact in the interface between electrode and solution. In their model, the solvent molecules together with the specifically adsorbed ions occupy the closest approach to the electrode, as shown in Figure 2-7.¹¹¹

2.3.2. Mathematic Model

To describe the terminal behavior of the DLC for power electronics applications, the equivalent mathematic model of DLC is necessary. Modeling the dynamical behavior of electrochemical power sources is an important issue in simulation of automotive power systems, photovoltaic systems, electric and hybrid vehicles. Furthermore, battery monitoring and battery management systems require dynamic battery models, which are continuously adapted to the battery behavior observed.¹¹² The model has to demonstrate the status of DLC in various conditions from charging or discharging profile to the dependence on ambient temperature. Based on Interface physical model of supercapacitor, several mathematic models have been constructed.

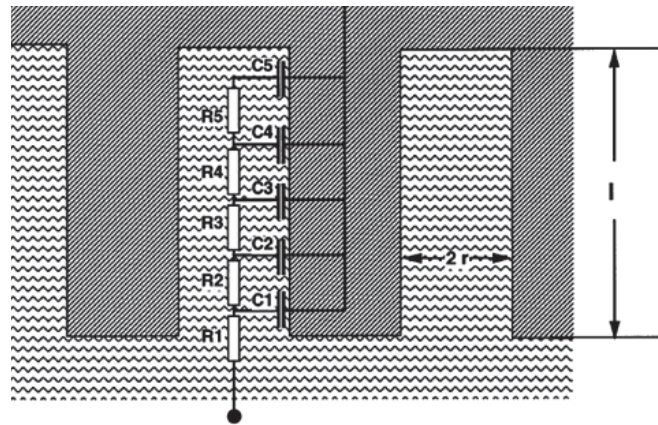


Figure 2-8 RC network model

2.3.2.1.1. RC Model

First, based on the electrochemistry principle of the interface between two materials in different phases, the performance of a supercapacitor can be modeled as an RC circuit network, as shown in Figure 2-8. The resistivity that forms the double layer can be represented by the resistive element. The capacitive element represents the capacitance forming on the Helmholtz layer and the diffuse layer when the voltage is supplied across

the electrodes.

2.3.2.1.2. Three RC Branches with a Voltage-dependent Capacitor

However, the simple resistive and capacitive model (series RC circuit) is insufficient to accurately describe the feature of a supercapacitor during its working status. As shown in the Figure 2-9,¹¹³ the curve of charging of supercapacitor is nonlinear, not a linear rise, following a burst peak after charging. When the charging source is removed, the potential between the two electrodes, slightly decrease. It does not have the ability to stay at the same voltage value. The slight drop means there should be the existence of a second distribution of the charge. After discharging, the measured voltage is lower than that of the simulation, with a slight recovery trend through the lowest voltage.

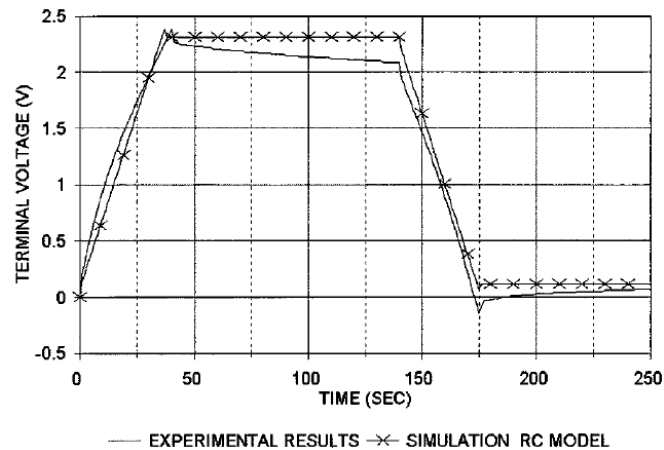


Figure 2-9 The results of experiment and simulation of RC model.¹¹¹

Obviously, the simulation result of a simple RC network model cannot accurately demonstrate the real behavior of a supercapacitor.

Luis Zubieta, and Richard Bonert¹¹³ proposed an equivalent circuit model consists of three RC branches, one of them with a voltage-dependent capacitance that described the performance of the supercapacitor in charging and discharging status. As shown in Figure 2-10, in addition to the element R_i , C_{i0} , the immediate branch has a capacitor charged with

the terminal voltage across the electrodes. It represents the change of the capacitance caused by interfacial tension change with different voltage added on the electrode. The delayed branch, with parameters R_d and C_d dominates the terminal behavior in the range of minutes. The long-term branch consists of parameters R_l and C_l determining the behavior for times longer than 10 mins. The R_{lea} represents the leakage resistor due to the existence of self-discharge in the supercapacitor.

D. A. New¹¹⁴ modeled the supercapacitors' performance from rapid charging or discharging (short-term storage) to long-term storage (in days), and conducted relevant experiments to test the profile of supercapacitors in various conditions, represented the measurement solution for supercapacitors (Figure 2-11). As the representation of D.A.

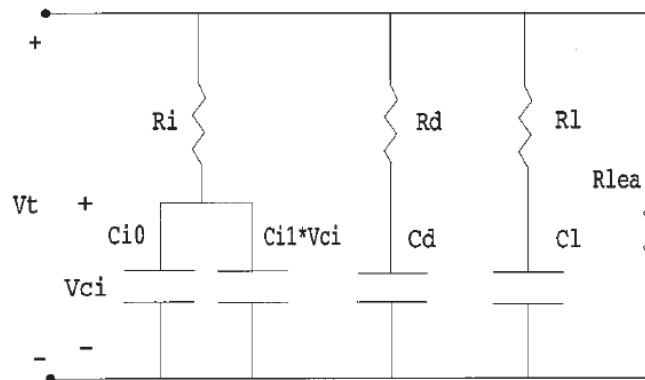
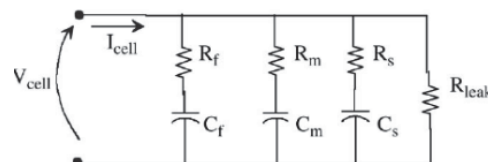


Figure 2-10 Three RC branches with a voltage-dependent capacitor.¹¹¹



Fast branch		Medium branch		Slow branch		Leakage	
R_f	0.68 m Ω	R_m	0.8 Ω	R_s	2.9 Ω	R_{lk}	3 k Ω
C_f	2600 F	C_m	250 F	C_s	560 F		
t_f	1.768 s	t_m	200 s	t_s	1624 s		

Figure 2-11 The parameters D. A. New's supercapacitor model.¹¹²

New's experiments, the model designed by Luis Zubieta is just suitable to the short-time

charging/discharging as required for EVs. However, the experiment data about the long-term application needs more validation to determine the parameter of leakage resistance. The validated data can be used to develop the complex models which could contribute to accurately describe the behavior for extended period usage such as in an automotive system.

2.3.3. Pore Impedance Model

The basic supercapacitor model composing ideal capacitors and resistances insufficiently describes its dynamic behavior. Interleaved RC network should satisfy the requirement for the model of supercapacitor in many applications.^{113 114} However, the calculation of

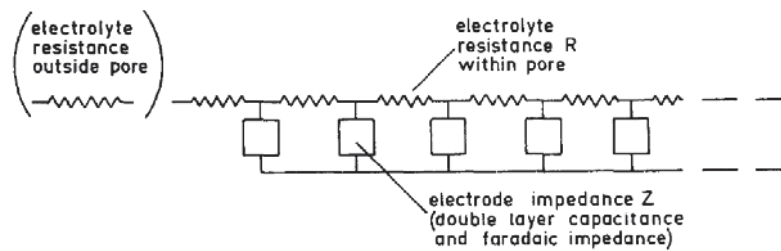


Figure 2-12 Equivalent circuit of a pore.¹¹⁴

the parameters for the model circuit is extremely challenging and usually imprecise. The reason is that these parameters have a strong influence on each other and, thus, it is nearly impossible to determine more than five or six independent parameters in an efficient way.¹¹⁵ Using the analysis of the potential and current distribution within each pore of the electrode is a promising means to describe the dynamical behavior of a supercapacitor.

In 1964, the first model of the concept of pore impedance is introduced by Levie,¹¹⁶ who modeled a small amplitude voltage applied to the orifice of a pore. The proposed model is that for a pore; the impedance consists of an electrolyte resistance outside the pore. A series electrolyte resistance within the pore and the electrode impedance are shown in

Figure 2-12.

For small amplitudes, the impedance Z is dependent on the angular frequency only. The equivalent circuit of an infinitesimal section d_z of a pore is shown as Figure 2-13. When

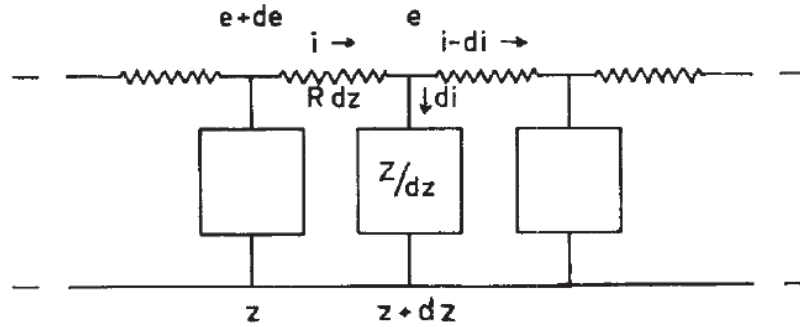


Figure 2-13 An infinitesimally small section d_z of a pore.¹¹⁴

small amplitude is applied across the pore, the distribution of current and potential is as shown in Figure 2-13.

For the infinitesimal section d_z , the electrolyte resistance d_{rz} and interfacial impedance d_{zz} are given by the equations as below:

$$d_{rz} = R_0 dz = [\rho / (\pi r^2)] dz \quad (1.9)$$

$$d_{zz} = Z_0 dz = Z_{IF} / (2\pi r dz) \quad (1.10)$$

Moreover, the Figure 2-13 also shows the schematic of the transmission-line model of Levie, in which, Z_0 is the impedance of the electrolyte-electrode interface per unit pore length, R_0 is the ohmic resistance of the pore per unit pore length and Z_{IF} is the interfacial impedance per surface unit in ohm m^{-2} , the resistivity of the electrolyte is ρ ohm-cm.

Levie gave the impedance of a single pore with length l :

$$Z_p = \sqrt{R_0 Z_0} \cot \operatorname{anh}(l \sqrt{R_0 / Z_0}) \quad (1.11)$$

Levie also defined the penetration depth as:

$$\lambda \equiv \frac{\sqrt{|Z_0| R_0}}{R \cos(\frac{1}{2}\varphi)} \quad (1.12)$$

Though the forgoing analysis, the pore impedance is able to demonstrate the inner distribution of current and potential in a pore.

For holistic electrode with n pores, radius r and length l , the total experimental electrode impedance can be obtained from the impedance of single pore Z_p .¹¹⁷

$$Z_{\text{exp}} = \frac{Z_p}{n} \quad (1.13)$$

$$Z_{\text{exp}} = \frac{(\rho Z_{IF})^{1/2}}{\sqrt{2\pi n r^{3/2}}} \coth\left(l \sqrt{\frac{2\rho}{r Z_{IF}}}\right) \quad (1.14)$$

In 2002, E. Karden *et al.*¹¹² gave more detail about the penetration depth which is impacted by the signal frequency:

$$\lambda = \sqrt{\frac{k_{el}\pi a^2}{2\omega c_{dl} 2\pi a}} = \frac{1}{2} \sqrt{\frac{k_{el}a}{\omega c_{dl}}} \sim \omega^{-1/2} \quad (1.15)$$

$$\frac{Z}{Z^*} = R_0 = R_{el} l = \frac{l}{k_{el}\pi a^2} \quad (1.16)$$

in which k_{el} is the electrolyte conductivity, C_{dl} is the specific double layer capacitance, a is pore radius, l is pore length. λ is used to represent the depth the ion of electrolyte penetrates the pore of electrode under different signals. In addition, a constant-phase behavior when the frequency reached to a high section was observed in the spectrum plot.

An analytic expression of porous impedance was given:¹¹⁸

$$Z_p = \sqrt{\frac{R_{el}}{j\omega C_{dl}}} \coth \sqrt{j\omega R_{el} C_{dl}} \quad (1.17)$$

When $\omega \rightarrow \infty$ or $\omega \rightarrow 0$, we can get the approximated value of Z_p in high or low frequency respectively:

$$Z_p(\omega \rightarrow \infty) = \sqrt{\frac{R_{el}}{j\omega C_{dl}}} \quad (1.18)$$

$$Z_p(\omega \rightarrow 0) = \frac{R_{el}}{3} + \frac{1}{j\omega C_{dl}} \quad (1.19)$$

The equation in high frequency described the Warburg region of porous electrode with a

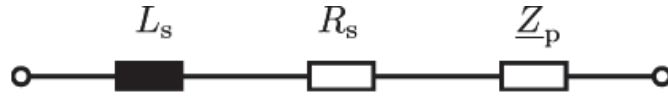


Figure 2-14 Equivalent circuit of a supercapacitor.¹¹⁸

constant phase angle 45° . In 2000, R. Kotz *et al.*¹¹⁹ proposed an improved model in which the capacitance expression $j\omega$ is replaced by a constant phase element (CPE) expression $(j\omega)^r$ with $0 < r \leq 1$:

$$Z_{pg} = \sqrt{\frac{R_{el}}{(j\omega)^r C_{dl}}} \coth \sqrt{(j\omega)^r R_{el} C_{dl}} \quad (1.20)$$

In the model, $r=1$ represents an ideal capacitor with no frequency dependence, $r=0.5$ describes the branch with 45° phase angle, $r=0$ corresponds to pure resistance.

2.3.4. Circuit Model with Pore Impedance Model

With the consideration of pore size, pore length and the signal frequency, the impedance model can accurately demonstrate the dynamic behavior of supercapacitor. Connecting with a series resistor R_s that represents the resistance of the metal electrode and the electrolyte, a conductor L_s that represents the stray inductance of the supercapacitor and the pore impedance model Z_p , the equivalent circuit as shown in Figure 2-14 has been a

predominant model used in the applications.^{115 118 120 121 122}

Oliver Bohlen *et al.*¹¹⁸ demonstrated the experiment results for the standard model of supercapacitor with the pore impedance model proposed by Leive¹¹⁶ and improved by E.Karden.¹¹²

$$Z_{ZDLC, std} = R_s + j\omega L_s + \sqrt{\frac{R_{el}}{j\omega C_{dl}}} \coth \sqrt{j\omega C_{dl} R_{el}} \quad (1.21)$$

and the generalized model with the CPE element in the pore impedance model of EDLC:

$$Z_{ZDLC} = R_s + j\omega L_s + \sqrt{\frac{R_{el}}{(j\omega)^\gamma C_{dl}}} \coth \sqrt{(j\omega)^\gamma C_{dl} R_{el}} \quad (1.22)$$

The simulation and measured results are shown as below (Figure 2-15). The Nyquist plot shows that both the standard model and generalized model of supercapacitor are approximately matched with the measured result of the impedance spectrum. The 45° phase angle to the real axis was also represented in the plot. However, as shown in the two figures, even though in the high frequency above 1Hz, the standard model is able to accurately describe the behavior of a supercapacitor. The trend becomes vertical which deviates from the real behavior of a supercapacitor if the frequency decreases to below 1 Hz of a low frequency range. Fortunately, the generalized model has the capability to track the measured spectrum of a commercial supercapacitor over the complete frequency range. The better performance of the generalized model resulted from the CPE which

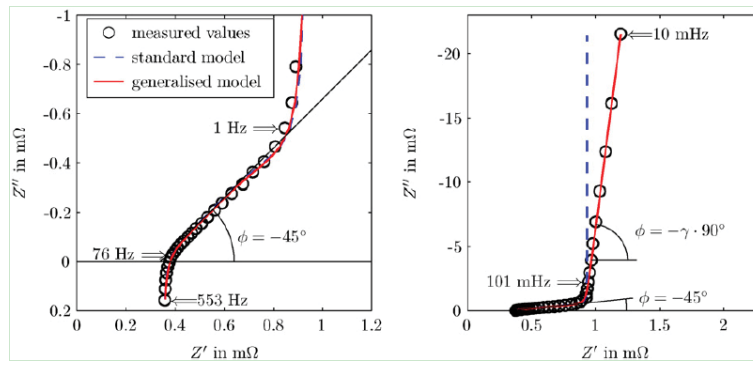


Figure 2-15 The experimental impedance spectrum and the simulation of standard impedance and generalized impedance model

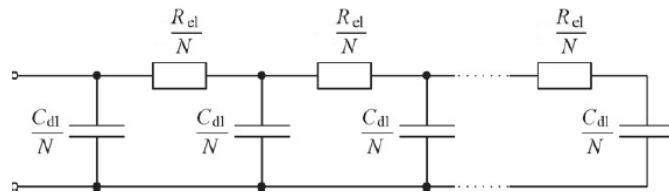


Figure 2-16 RC network model.

models the interfacial impedance of the electrode.

The pore impedance of the electrode with the CPE is able to describe the behavior of the supercapacitor. However it is difficult to directly apply this mode to simulation because it cannot simply be replaced by the common electrical element like the resistor, capacitor and inductor. As the initial idea of Levie, the standard pore impedance can be represented by an unlimited ladder network with N resistors and capacitors. This kind of circuit mode will lead to large networks and inefficiency with respect to computation time. Appropriate approximations by means of RC circuits or RC ladder network topologies therefore have to be found first (Figure 2-16).

The basic idea for the representation of a ZARC element, employed to model a depressed, capacitive semicircle in the complex plane which can be used to describe the character of the pore impedance model is proposed by S. Buller *et al.*,¹²³ as shown in Figure 2-17.

Nonlinear RCs determined by the parameters of the ZARC element were connected in series. With an increasing number of RC circuits, the approximation of the ZARC elements becomes more and more precise. However, the computation time increases with rise in the RC number.

A transform of the standard model was given by S. Buller *et al.*,¹¹⁵ in which two independent parameters (C, τ) was used to replace the unknown parameters in the standard model, as shown below.

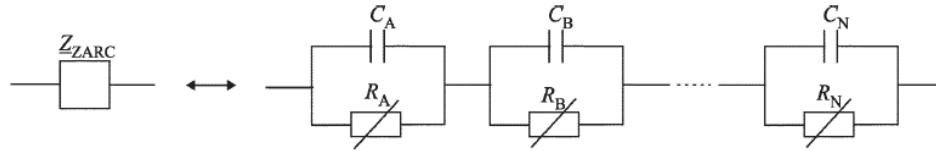


Figure 2-17 RC equivalent circuit of ZARC element.¹²¹

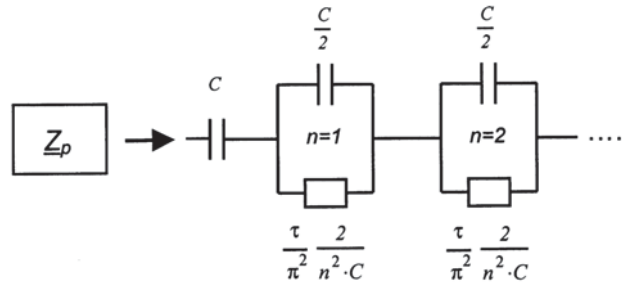


Figure 2-18 RC parameter of the equivalent circuit of ZARC.¹¹³

$$Z_p(j\omega) = \frac{\tau \cdot \coth(\sqrt{j\omega\tau})}{C \cdot \sqrt{j\omega\tau}} \quad (1.23)$$

Based on the circuit model as shown in Figure 2-18, a large number of impedance measurements were performed in different operation conditions (different voltage and temperature) to construct a lookup table for the parameters C, τ, R_i . They showed a way that transforms the model in the frequency domain to the time domain, so that the

transformed model can be used in simulation tools like Matab/Simulink.

Due to the transformation, the total RC model which is able to describe the behavior of pore model was obtained as shown in Figure 2-18. The corresponding parameters of the model are also given through the mathematical transform. In their experiment report, the models consisting of ten RC circuits already show very good agreement with the measured impedance.

A compromise circuit mode is obtained by adding a single parallel RC circuit in series with the network that represents the standard pore impedance (Figure 2-19). The parameters of R_x and C_x are calculated from the impedance parameters C_{dl} and γ by equating the real part of the RC-circuit at its characteristic angular frequency $f_x = R_x C_x$ with the difference of the real parts of the standard and the general pore model.¹²⁴ Through

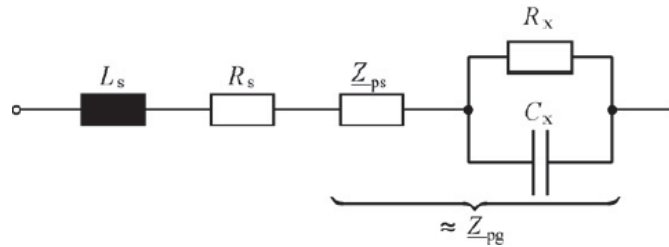


Figure 2-19 Generalized pore impedance model is represented by a parallel RC circuit with the standard pore impedance.¹²²

the calculation, we can get the parameters of the additional circuit:

$$R_x = \frac{2 \cos(\gamma\pi / 2)}{\omega_x^\gamma} \quad (1.24)$$

$$C_x = \frac{1}{\omega_x R_x} \quad (1.28)$$

A CPE and a ZARC network connected in series were used to represent impedance model of porous electrode.¹²⁰ For one ZARC element, a resistor and a CPE were connected in

parallel as shown in Figure 2-20. In order to simulate the character of the ZARC element, three R-C parallel circuits connected in series were used to approximate the ZARC element, as shown in Figure 2-21.

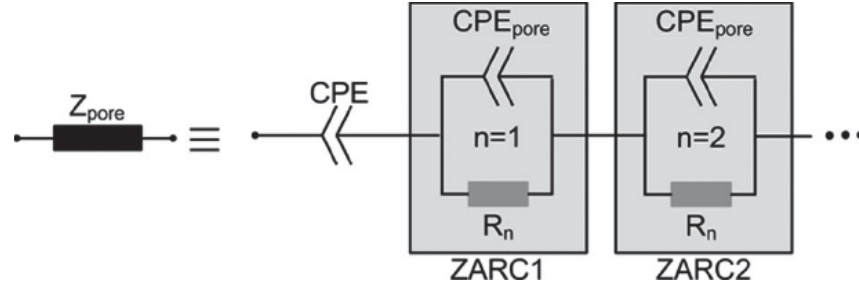


Figure 2-20 Equivalent impedance model of porous electrode.¹¹⁸

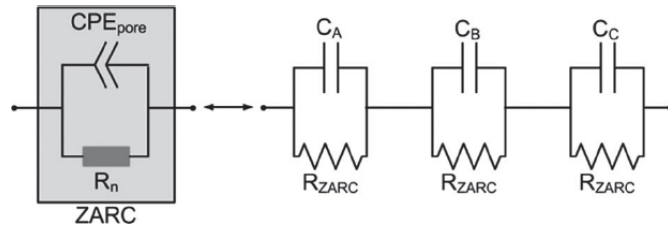


Figure 2-21 Equivalent circuit of ZARC element.¹¹⁸

In the circuit, an adjusting parameter $f(d)$ was used to adjust the capacitance of C_B and C_C which makes the impedance of the three RC circuit form the same depressed semicircle as the ZARC impedance plot in the complex plane. Finally, the parameters of the model are represented as below:

$$\begin{aligned}
 C_A &= \frac{1}{\omega_{ch_ZARC} \cdot R_n / 3} \\
 C_B &= \frac{C_A}{f(d)} \\
 C_C &= C_A \cdot f(d)
 \end{aligned}
 \tag{1.29}$$

With

$$f(d) = \frac{-2 + \sqrt{4 - \beta}}{\beta}, \beta = \frac{3 \sin(d\pi / 2)}{1 + \cos(d\pi / 2)} + 1$$

$$R_{ZARC} = \frac{R_n}{3} = \frac{2R_e}{3n^2\pi^2}$$

2.4. Electrode materials for supercapacitor

Electrode materials play a crucial role in determining the electrochemical performance of a supercapacitor. Nowadays, most of the researchers focus on the synthesis of environmentally friendly materials for supercapacitors with increased energy and power density. Among these investigations, porous carbon materials, conducting polymers and transition metal oxides are promising candidates for supercapacitor electrode materials. Porous carbon materials, such as activated carbons, carbon nanotubes, and mesoporous carbons, have been widely studied due to their stable physicochemical properties, high surface area, good conductivity, low cost and long cycle life.

2.4.1. Carbon nanotube

The first idea that uses nanotubes as the electrodes of a supercapacitor is proposed by Chunming Niu in 2001.⁴⁴ In the proposal, Niu employed the commercial catalytically grown carbon nanotubes as the original material. In the commercial nanotubes, the individual nanotubes entangle together and therefore they are formed as bundles with individual nanotubes arranged semiparallel to each other. Hence, the disassemble process is necessary to disperse the entangled nanotubes. In the method proposed by Niu *et al.*, the entangled nanotubes was firstly treated in nitric acid, then the oxygenate functions are introduced onto the surface of nanotube to disassemble the nanotube aggregates. The functionalized hydrophilic nanotubes are dispersed in the water, followed by filtration and the reassembly of the individualized carbon nanotubes into an interconnected,

entangled, free standing structure.

Combining a nickel foil as the charge collector with the produced nanotube sheet, Niu showed that they get a power density of 8 kW kg^{-1} and an energy density of 0.56 Wh kg^{-1} . For the electrode, the power density is 163 kW kg^{-1} and energy density is 12.6 Wh l^{-1} or 15.7 Wh kg^{-1} . After the Nitric acid treatment, the BET surface area increased from 250 to $430 \text{ m}^2 \text{ g}^{-1}$. In the electrolyte with 38 wt.% H_2SO_4 , the maximum specific capacitance reached to 113 F g^{-1} (90 F cc^{-1}). Due to the introduced oxygen functions, the solid electrode can be self-adhesive without any binder. The binder-free feature contributes to the device being free of contaminant which would otherwise degrade the performance of the electrode.

To achieve a high energy density and power density of supercapacitors with the SWNTs electrodes, An *et al.*⁶³ investigated the key factors that determine the performance of the supercapacitor such as the composition of the binder, annealing temperature and type of current collector. The SWNTs were fabricated by using DC arc discharge under 100 torr pressure. To synthesize the electrode, they introduced the ploy (vinylidene chloride) (PVDC) as a binder. After the comparison of the specific capacitance and ESR of different weight percentages of SWNTs and binder, the electrode with 70 wt.-% randomly entangled and cross-linked SWNTs and 30 wt.-% was chosen in the further investigation. With the increasing of temperature, the average pore diameter decreased to a lower pore sizes of 30-50Å, while there is a significant increase in the specific surface area. The specific surface area increased to $357 \text{ m}^2 \text{ g}^{-1}$ at 1000°C. Moreover, the number of smaller pores which are suitable to absorb the ion of electrolyte increased and reached the maximum amount at 1000°C. Through the mixture with PVDC binder and heat treatment, the electrode differential capacitance was about 50 uF cm^{-2} . The cell, fabricated with two

SWNT electrodes separated by a thin polymer (Celgard) in 7.5 M KOH aqueous solution as the electrolyte, achieved a maximum specific capacitance of 180 F g^{-1} with a larger power density of 20 kW kg^{-1} and an energy density of 6.5 Wh kg^{-1} .

In the paper, An. *et al.* pointed out the hydrated ions in the electrolyte possess the diameter in the range of 6-7.6 Å, the minimum effective size of the pore therefore should be greater than 15 Å. In general, if the pore size is less than 15 Å, the performance is inferior due to higher ion diffusion barriers. Whereas, in macropores, if the pore size is greater than 50 Å, the pore will not contribute to the capacitance because of the loosely bound to the surface of the layer.

In 2006, Futab *et al.*⁵⁸ proposed a single-walled carbon nanotube (SWNT) solid that

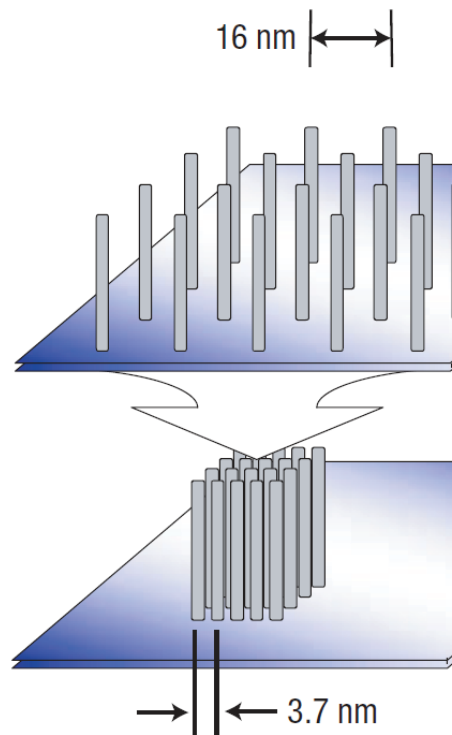


Figure 2-22 Schematic diagram of the collapse of the aligned low-density as-grown forest (above) to the highly densely packed SWNT solid (below).⁵⁸

possessed aligned formation, high mass density and retained the intrinsic properties of

individual SWNT. The SWNT solid was obtained by using the zipping effect of liquid to draw nanotubes together. Through their approach, a longer vertically aligned SWNT was obtained directly from the substrate. Without damage to the nanotube, a solid with high mass density was achieved from the aligned low-density as-grown forest (above) to the highly densely packed SWNT solid (below), as shown in Figure 2-22.

The EDLC, consisting of the SWNT solid electrodes sandwiched between Pt sheets and Pt meshes and the tetraethylammonium tetrafluoroborate (Et_4NBF_4)/propylene carbonate electrolyte, achieved the specific capacitance of 80 F g^{-1} and energy density of 69.4 Wh kg^{-1} for a three-electrode cell charged at 2.5 V. The power density of an EDLC with a 100 μm thick SWNT solid were calculated as 43.3 kW kg^{-1} .

In the collapse, the alignment of the original as-grown forest is critical to get the well-ordered packing of tubes and contracture. If the original forest is not sufficiently aligned, the van der Waals forces will be different in various areas during the liquid-induced collapse process. In the research, they also pointed out that the aligned SWNT solid has less impendence for ion diffusion than the activated carbon electrode. For activated carbon, thicker electrodes possess higher ion diffusion barriers in the inner region of the electrode, resulting in higher internal resistance and inferior high-power performance. However, thick electrodes are advantageous to increase the energy density because in such cells the active material can occupy high ratios of the volume and weight.

Signorelli *et al.*³⁵ employed the low-pressure chemical vapor deposition (LPCVD) to fabricate the multiwalled carbon nanotube (MWNT) directly on a variety of substrates. The conducting substrate electrode materials can be aluminum, tungsten and platinum. The substrate was polished on one side by using either a rough sandpaper procedure or a more fine chemical mechanical procedure. Once the substrate was prepared, the

generation of underlayer and the catalyst were deposited on the cleaned substrate by introduction to the electron beam evaporator. Iron is then deposited on the top layer of the aluminum oxide of the deposition of Al substrate. After being coating with catalyst, the CNTs were fabricated on the Al substrate during the vapor deposition.

Through the nanotubes fabrication, Signorelli achieved the maximum nanotube density of 4×10^{11} CNT cm^{-2} . The electrode is composed of nanotubes having an average diameter 6.5nm with an average spacing between nanotube centers of 10 nm (Figure 2-23). As Signorelli's assumption, the ion accessible surface area of the triple wall nanotube is $450 \text{ m}^2 \text{ g}^{-1}$, and the length of the nanotube active layer is 200 μm with three walls. The EDLC with aligned CNTs possesses specific capacitance of 50 uF cm^{-2} . The energy densities

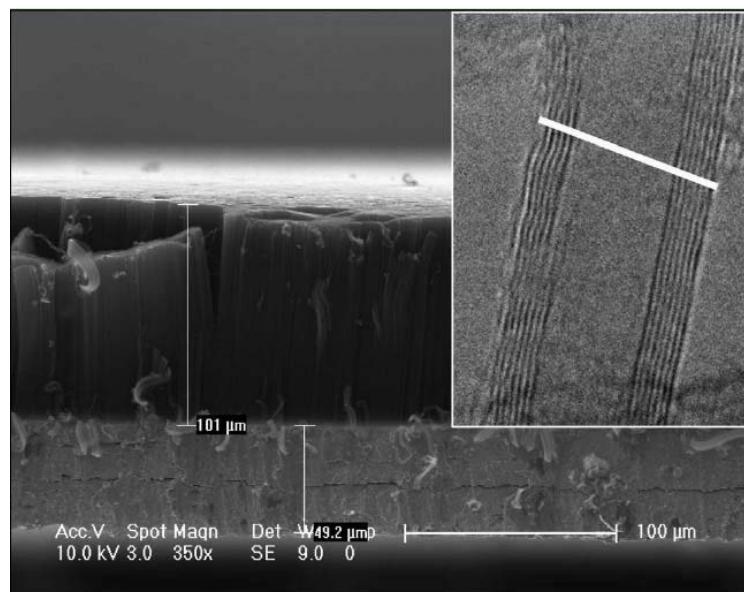


Figure 2-23 SEM image of the aligned CNT.³⁵

reaches to 21 Wh kg^{-2} and 22 Wh l^{-2} when the cell is charged at 2.7 V. The cell can work up to 3.5 V, providing energy densities up to 35 Wh kg^{-2} and 37 Wh l^{-2} in the higher molarity electrolyte. The differential capacitance increases to 50 uF cm^{-2} . The measurement data shows that the energy density of aligned CNT-based EDLC is potentially up to seven times that of commercial activated carbon-based EDLCs.

Hiralal *et al.*⁵⁷ demonstrates a hierarchical structure of the electrode of supercapacitor that achieved high power density by the SWNTs and high energy density by carbon nanohorns (CNHs). In their work, the CNHs were used to fill the pores in a random network of SWNTs, which contributes to an enhanced surface area and maintains high permeability and porosity. The combination results in the enhancement of energy density and the decrease of the internal resistance, without degrading the lifetime of the supercapacitor.

The SWNT thin film was obtained by using a vacuum filtration method and then they were removed from the polyethylene terephthalate substrate. After the SWNT film was ready, it was dispersed in the deionized water with 1 wt% sodium dodecyl sulfate. Following the dispersal process, the vacuum filtration and a short annealing process were executed. Finally, due to the intimate van der Waals contact, the individual SWNT bonded together to form the thin film. In addition, the CHNs were produced by arc discharge in liquid nitrogen as described by Hiralal. After the discharge, the CNHs were collected, dried, and subsequently dispersed in de-ionised water and drop cast onto the SWNT film. For the electrode combined by SWNTs and CNHs, the CNHs drop-casted on the SWNTs network have about 100 nm diameter agglomerates and pore sizes of 0.427 nm. The nanocarbon powder with horn opening width 3-5nm and the radius of curvature 1-2 nm, provides a large surface area of about 1025 m² g⁻¹.

The EDLC used the nano films combined with SWNTs and CNHs as the electrode, separated by a mixed ester cellulose paper soaking in 1 M sulfuric acid. It achieved a power density of 3.50 kW kg⁻¹, and energy density of 6.03 Wh kg⁻¹. The electrodes consisting of SWNTs and CNHs, possess high surface area, porosity and permeability, which contribute to the energy conversion and storage. Moreover, it is free of binder which results in low ESR.

Without using the supporting metal current collector, a novel metal oxide/carbon nanotube substrate (CNT-S) was first introduced to be the electrode of the lithium battery. In the work, Marschilok⁶⁰ provided two methods to prepare the electrodes: the first using material deposited on the CNT substrate after isolation; the second method using direct integration during material synthesis. For the first method named particle deposition method, the conductive additives and the CNTs were prepared respectively before forming a metal oxide/CNT-S electrode. For the substrate integration method, the second method, the CNTs were introduced to the process when the conductive additives were synthesized. The amount of the material loading results in different morphology of the electrode. As the demonstration of the work, the second method achieved viable discharge performance without additional binder for the electrode, and enhanced the penetration of the active materials. Compared with the foil current collector, the specific capacity of CNT-S electrodes was increased by 20-60%. The CNT-S electrodes also exhibited long life time due to the elimination of metal foil that currently experiences grid corrosion.

2.4.2. Graphene-based electrode

Using the chemically modified graphene (CMG) as the material of the electrode for a supercapacitor was firstly proposed by Stoller.¹²⁵ The CMGs were synthesized from reducing the graphene oxide sheets suspended in water. Hydrazine hydrate was used to reduce the graphene oxide and reduced graphene sheets then agglomerate into particles with diameter of 15-25 μ m. The N₂ absorption BET measurement demonstrated the surface area of the agglomerated graphene is 705 m² g⁻¹. The specific capacitance reached to 135 F g⁻¹ and 99 F g⁻¹ in aqueous and organic electrolyte, respectively. However, because the graphene sheets agglomerated to graphene particles, it means the inter graphene sheets can't be accessed by the ions of the electrolyte and only the sheets at the

surface can contribute to the forming of DLC.

Compared to the method where graphene sheets are reduced in aqueous solution at high temperature, a gas-based hydrazine reduction at room temperature was reported by Wang *et al.*¹²⁶ In this method, the reducing agent hydrazine (80wt% water solution) was heated to vapor and saturated in a vacuum desiccator. The graphene oxide prepared by Hummer's method was reduced by the hydrazine in the form of gas in the vacuum desiccator. Via this method, they prepared the reduced graphene sheets with a low degree of agglomeration. Wang *et al.* achieved a maximum specific capacitance of 205 F g⁻¹ in

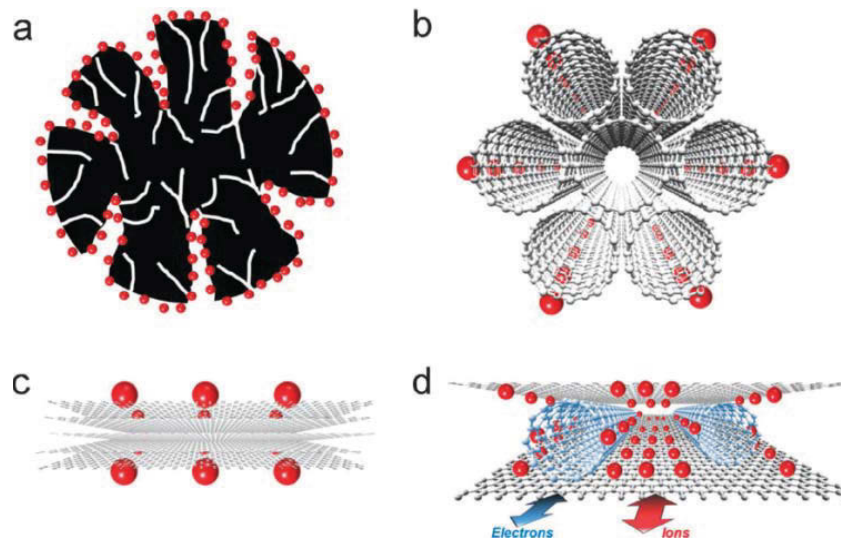


Figure 2-24 Comparison of different carbon materials as electrodes of supercapacitors. (a) Activated carbon. Activated carbon has a high surface area. However, many of the micropores cannot be accessed by electrolyte ions. (b) Single-walled carbon nanotube (SWCNT) bundles. SWCNTs usually form bundles, limiting their surface area. Only the outmost surface can be accessed by electrolyte ions. (c) Pristine graphene. Graphene nano-sheets are likely to agglomerate through van der Waals interactions during the drying process. It would be difficult for electrolyte ions to access the ultras-small pores, especially for larger ions such as an organic electrolyte or at a high charging rate. (d) Graphene/CNT composite. SWCNTs can serve as a spacer between the graphene nano-sheets to give rise to rapid diffusion pathways for the electrolyte ions. Moreover, they can enhance electrical conduction for the electrons. The CNTs also serve as a binder to hold the graphene nano-sheets together preventing disintegration of the graphene structure into the electrolyte.⁶⁴

the aqueous solution. The power density of the electrode was approximately 10 kW kg⁻¹ and the energy density was about 28.5 Wh kg⁻¹.

The agglomeration phenomenon during the preparation of graphene sheets inhibits the

implication of pure graphene in the electrodes of supercapacitors. There has been an increasing and urgent demand for fabricating graphene-based electrodes with low-degree agglomeration.

Qian *et al.*⁶⁴ proposed a new construction: graphene/CNT composite as the electrode material for electrochemical double layer supercapacitors. In the construction, the CNTs were functioned as the spacer materials to separate the graphene sheets and then prevent the agglomeration of graphene sheets. Due the high conductivity, high surface area and superb mechanical properties, CNTs can disperse the graphene stacks to individual

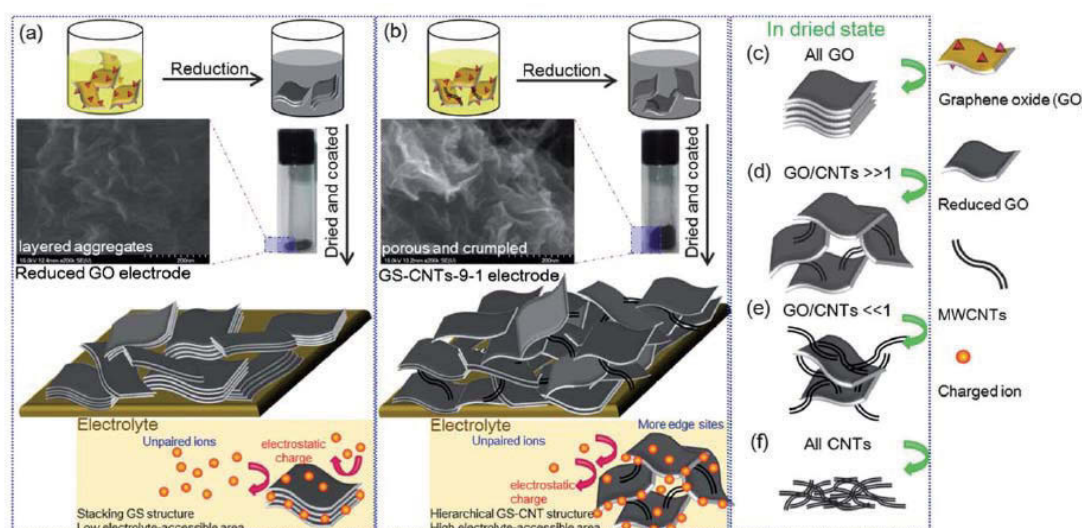


Figure 2-25 Scheme for preparing (a) reducedGO electrode and (b) GS-CNTs-9-1 electrode. Note the schematic models of GS-CNT composites with various GS/CNTs ratios; where (c) GO are dispersed in the solution and GS aggregates/stacks are formed after reduction, (d) GO and CNTs coexist in the solution and CNTs act as nanospacers to increase the interlayer space between GS after reduction, avoiding the aggregation issue, (e) excess CNTs attach on the surface of GS resulting in a low exposure of surface area, and (f) CNTs are dispersed in the solution and CNTs aggregates are formed in the dry state.¹²⁵

graphene sheets and can serve as a connector and binder of the two graphene layers at the end of the CNTs as show in Figure 2-24. With the new construction, the author reported that they got specific capacitances of 290.6 F g⁻¹ in aqueous electrolyte and 201.0 F g⁻¹ in organic electrolytes for a single electrode, and energy density reached 155.6 Wh kg⁻¹ in ionic liquid at room temperature.

Yang *et al.*¹²⁷ used a simple strategy to prevent the irreversible agglomeration of graphene and subsequently advance the utilization of the large surface area of graphene. In their work, 1D CNTs and 2D graphene sheets were combined together to improve the capacitive performance of supercapacitors. As shown in Figure 2-25, the as-prepared graphene oxide and MWCNTs were added into deionized water followed by ultrasonication for 2h. After the heating, stirring of the solution, the composite material was finally obtained by washing and drying the powder filtered from solution. In order to get the optimized performance, the weight ratio of reduced GO/CNTs was also

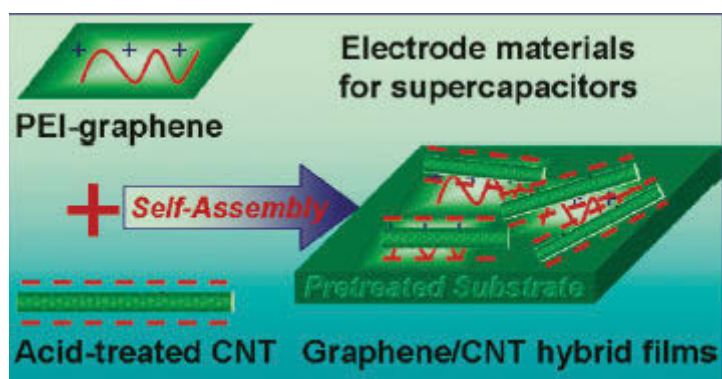


Figure 2-26 Illustration of positively charged PEI-GN and negatively charged MWNT film deposition process on an appropriate substrate.

investigated in their work. They found the composite film with 9:1 weight ratio of graphene and MWCNTs possesses the highest specific capacitance, reaching 326.5 F g^{-1} . Via the intercalation of MWCNTs into graphene layers, the BET surface area of the hybrid film increased from $138.2 \text{ m}^2 \text{ g}^{-1}$ of graphene oxide to $538.9 \text{ m}^2 \text{ g}^{-1}$ after the MWCNTs intercalation. Furthermore, the energy and power densities of this film are achieved at 21.74 Wh kg^{-1} and 78.29 kW kg^{-1} , respectively.

Electrostatic interaction was used to fabricate large-area hybrid films by sequential self-assembly of functionalized graphene sheets and CNTs.⁶⁷ The exfoliated graphene oxide was firstly reduced by hydrazine in the cationic polyethyleneimine (PEI) (Figure 2-26). After

the introduction of the charged PEI chain, the graphene sheets were assembled with acid-oxidized MWCNTs to generate the hybrid film. The self-assembled process involved repeatedly immersing the substrate into aqueous PEI-GN solution and aqueous MWCNT solution prepared acid oxidation. The electrostatic interaction between the negatively charged MWCNTs and positively charged graphene oxide was demonstrated to enable the generation of an interconnected network of both material with aligned nanopores and the maximum utilization of the large surface area of graphene sheet. The network structures with well-defined pores contributed to fast electronic and ionic conducting channels, providing ideal electrodes for energy storage devices. The electrodes based on the hybrid film exhibited a nearly rectangular CV with specific capacitance of 120 F g⁻¹.

Guo *et al.*¹²⁸ reported a hierarchical nanostructure to enhance the performance of a supercapacitor. As shown in Figure 2-27, by using the electrostatic interaction between the positively charged carbon spheres and negatively charged graphene oxide, Guo *et al.* achieved a maximum power density of 15.4 kW kg⁻¹. The hierarchical carbon materials were used as the activated material to fabricate the electrode for the supercapacitor. Compared with the electrodes only consisting of the graphene under the same condition (a specific capacitance of 115 F g⁻¹), the composited electrode possesses higher specific capacitance (a maximum specific capacitance of 198 F g⁻¹) which indicates the carbon spheres have separated the graphene sheets in the electrode. The ERS of the hierarchical electrode is about 1.98 Ω. However,

It did not have the typical rectangular CV as shown in Figure 2-28, which results from the incomplete reduction of graphene oxide. Also, like the activated carbon electrode, the ion diffusion channel is out of control.

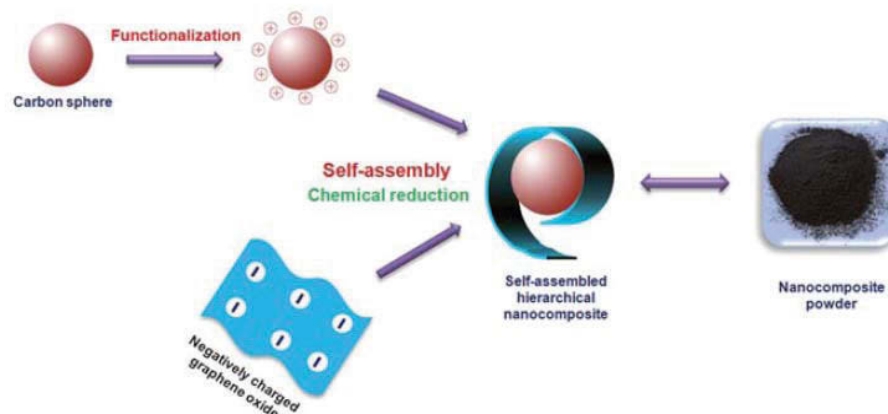


Figure 2-27 Scheme representation of the preparation of self-assembled hierarchical nanostructure comprising graphene and carbon spheres.¹²⁶

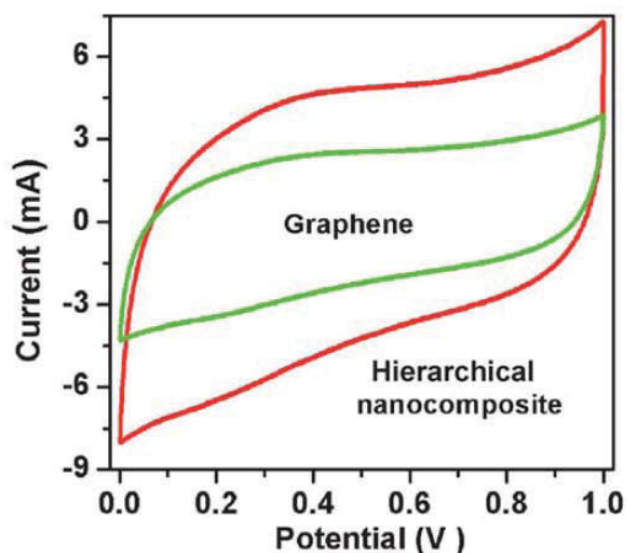


Figure 2-28 Cyclic voltammograms (CVs) of supercapacitors constructed with different materials based electrodes in 6MKOH (scan rate of 20 mV s^{-1} , electrode mass of 8.2 mg).¹²⁶

Peng Si *et al.*¹²⁹ presented a hybrid electrode compositing of polypyrrole and graphene with a high specific capacitance. Electrochemical reduction, rather than chemical reduction, was employed in their work, as shown in Figure 2-29. The composite of polypyrrole/graphene oxide was directly synthesized on the surface of a glassy carbon electrode by using potentiostatic method. After removing the absorbed species, the composite was introduced to CV scanning within the potential window of -1~0 V for

several cycle, followed by the reduction of GO in the composite. The polypyrrole and

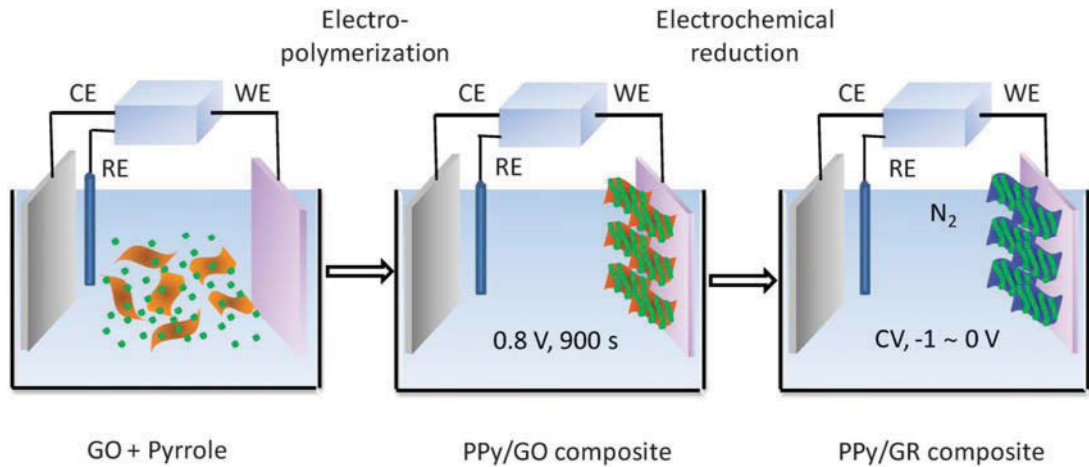


Figure 2-29 Illustration of the electrochemical synthesis process of the PPy/GR nanoplatelet electrodes.

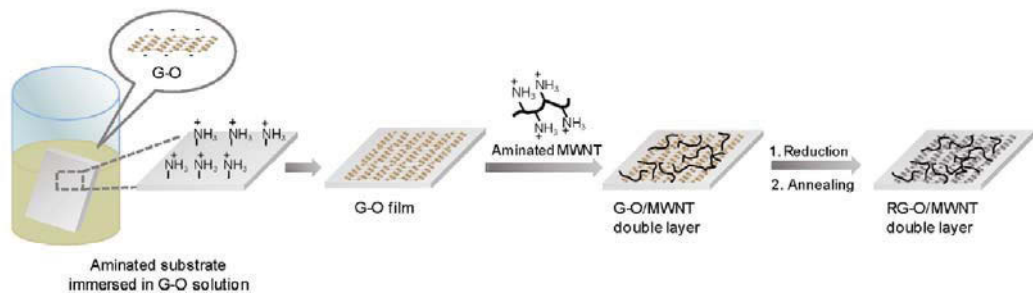


Figure 2-30 Fabrication of an RG-O and aminated MWNT (RG-O/MWNT) double layer on a substrate.¹²⁹

graphene sheets, reduced from polypyrrole and graphene oxide sheets by electrochemical reduction, achieved a large surface area of $136.5 \text{ m}^2 \text{ g}^{-1}$ and a high capacitance of 285 F g^{-1} .

Highly conductive carbon hybrid films using graphene oxide as the carrier was fabricated by Cai *et al.*¹³⁰ The functionalized multiwalled carbon nanotubes with 3-5 wt% hydroxyl groups (MWCNTs-OH) and the graphene oxide nanoplatelets (GONPs) prepared from expanded graphite by hHummers ultrasonic were dispersed in the N-dimethylformamide. The hybrid films with various weight ratios of MWCNTs-OH and GONPs were investigated in their research. They found that a large number of MWCNTs-OH were

well-stacked in the horizontal direction because the carriers GONPs have the two-dimensional structure. The square resistance could be reduced to $1.3 \times 10^{-4} \Omega \text{ sq}^{-1}$ when the weight ratios of MWCNTs-OH/ GONPs reached 5/1.

Electrostatic interaction-induced self-assembly process for fabricating the large-area thin films of graphene/carbon nanotube is proposed.¹³¹ The SiO₂/Si was firstly treated in the toluene solution of 3-aminopropyltriethoxysilane for 30 min; consequently the surface of the substrate has a positive surface charge of 31.32 mV (Figure 2-30). Once the positively charged substrate was obtained, it was immersed in the graphene-oxide (G-O) aqueous suspension which has negative charges. Due to the electrostatic adsorption, the G-O was coated on the surface of the substrate. The G-O coated substrate possessed a highly negative surface charge so that the aminated MWNTs with a positive charge were absorbed on the surface of the G-O coated substrate via electrostatic interaction. After deoxygenation and annealing at 500 °C under an argon atmosphere, the average sheet resistances of the RG-O/MWNT thin film reduced to 103 k $\Omega \text{ sq}^{-1}$. Through this fabrication method, the thin film possesses excellent mechanical strength, expected sheet resistance, uniform structure. However, the author didn't show the influence of weight ratios of the G-O and the MWNT which may dramatically affect the feature of the hybrid film. Also insufficient deoxygenated MWNT will increase the resistance of the hybrid thin film.

First report about dispersing CNTs in anhydrous hydrazine is presented by Vincent *et al.*⁶⁹ in 2009. This dispersing process enables the enhancement of the electrical properties of CNTs since it does not introduce the use of surfactants. To stably disperse the CNTs in hydrazine, N₂H₅⁺ was employed to surround the negatively charges in their method. With the method, they fabricated carbon nanotubes and chemical converted graphene hybrid

nanocomposite for a polymer solar cell, which achieved the sheet resistance $240 \Omega \text{ sq}^{-1}$ with 86% transmittance after chemical doping. Firstly, the graphite oxide was synthesized and then purified by using Hummer's method. Graphite powder is dissolved in deionized water with the assistance of ultrasonication. The CNTs for the hybrid materials were prepared by introducing the hydroxyl and carboxylic moieties by refluxing the CNTs in a mixture of nitric acid and sulfuric acid. The CNTs activated with oxygen functionalities was then filtered and washed repeatedly in the deionized water and ethanol. When the graphite oxide powder and CNTs were ready, both of them were directly dispersed into anhydrous hydrazine. The synthesizing process of the hybrid electrode is shown in Figure 2-31. This low-temperature solution synthesizing the graphene and CNTs technology was easy, inexpensive, massively scalable and compatible with flexible substrates.

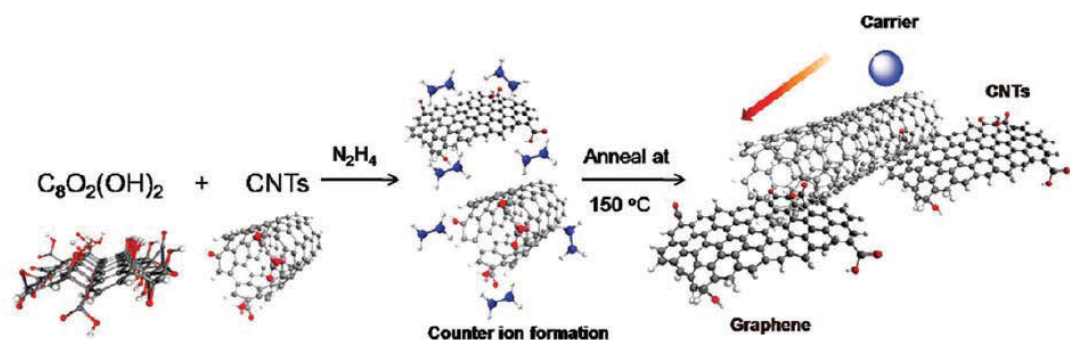


Figure 2-31 Fabrication of hybrid suspensions of CCG and CNTs.⁶⁹

Hong *et al.*¹³² developed a layer by layer assembly method to fabricate the thin film consisting of reduced graphene oxide (RGO) sheets and multiwalled carbon nanotubes, as shown in Figure 2-32. The approach required that the original material RGO was negatively charged and the positive charges were introduced on MWNTs. Once the original materials were charged, the positively charged MWNT-NH₃⁺ was dropped on the hydrophilic-surfaced substrate by using the spin coater spun at 2000 rpm for 30s. Then,

with the same procedure, the RGO solution negatively charged will be spincoated on the surface of the MWNT-NH₃⁺ layer to form the bilayer of MWNT and RGO sheets. Desired number of MWNT and RGO layers can be achieved by repeating the procedures. This method enabled excellent control over the synthesizing of multilayers of MWNT and RGO sheets, which results in excellent optical properties. After high temperature 1000 °C for 30min thermal treatment, a MWNT/RGO film with a thickness of 11 nm and a sheet resistance of 8 kΩ sq⁻¹ with a transparency of 81% was achieved.

A solid-phase layer-stacking approach using ethanol wetting was proposed to fabricate carbon-based thin films in which the carbon nanotube network was assembled with

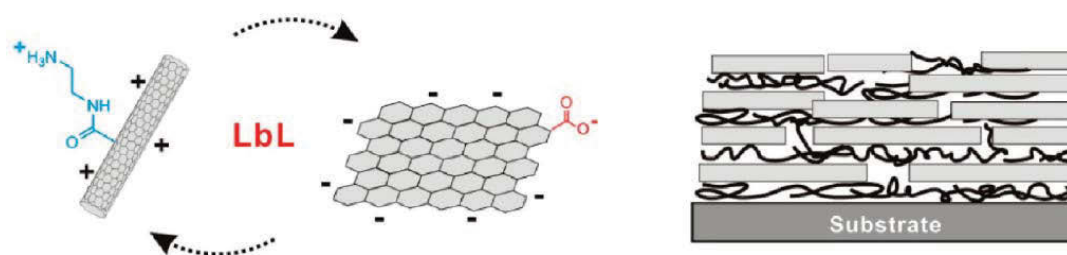


Figure 2-32 Schematic representation of hybrid LbL multilayer of MWNTs and RGO.¹³⁰

graphene.¹³³ A pure CNT network thin film was prepared by using floating catalyst CVD methods. The graphene films were fabricated on a copper foil by the self-catalytic CVD approach. After the CNT and graphene films were ready, they were assembled in the procedure as shown in Figure 2-33. The CNT film dispersed from the grown substrate was gently covered on the surface of the copper foil coated with the as-grown graphene. The ethanol then was dropped on the thin film which contributes excellent adhesion between the CNT film and graphene. After drying out the ethanol, the etching process was used to detach the copper substrate and finally the hybrid film was obtained. The

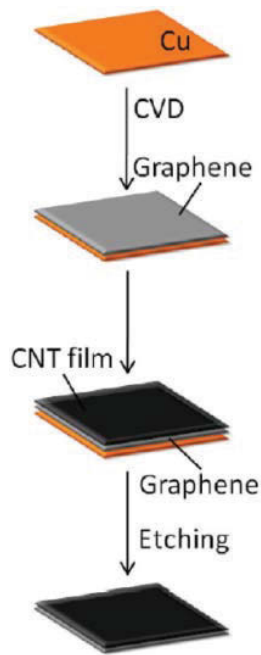


Figure 2-33 Schematic for the assembly of the CNTs/G composite film.¹³¹

previous solution-based processes will inevitably damage the intrinsic properties of CNT and graphene. It is without doubt that the introduction of the oxidation function group and reduction of the CNT and graphene in solution-based processes will sacrifice the performance of CNT and graphene like conductivity, transparency and strength. However, the solid-phase layer stacking method can maintain the structural integrity of CNT and graphene while keeping the intrinsic electrical and mechanical properties. They found the sheet resistance of the directly stacked CNT film into graphene films was reduce to $735 \Omega \text{ sq}^{-1}$.

The bulk production of layered graphene ribbons by using CVD was reported by Jessica *et al.*¹³⁴ The aerosol pyrolysis process in which the mixture solution containing ferrocene, thiophene and ethanol were sprayed into a quartz tube and then heated at 1223 K was employed for one-step production of bulk quantities of graphite ribbons. The graphene nanoribbon, obtained from the method, possesses 20~30 μm in length and 20-300nm in width with small thickness of 2-40 layers. The Nitrogen adsorption measurements

indicated the flat structure of the graphene ribbon. The electron transport of the ribbon is similar to the behavior of metal with straight line for the $I-V$ curves. The resistance of the ribbon dropped to $10.5\text{ K}\Omega$ from $20\text{ K}\Omega$ after the annealing by 1.6 V for 15 min .

A supercapacitors with in-planar structure electrodes consisting of graphene and reduced multilayer graphene oxide (RMGO) were fabricated by Yoo *et al.*,¹³⁵ firstly reported in 2011. The in-planar structure takes full advantage of the large surface area of each graphene layer for energy storage, as shown in Figure 2-34. For the conventional electrodes with stacked graphene layer, when it is charging, the ions have to overcome the barrier formed by the graphene flakes to cross over the graphene sheets to penetrate

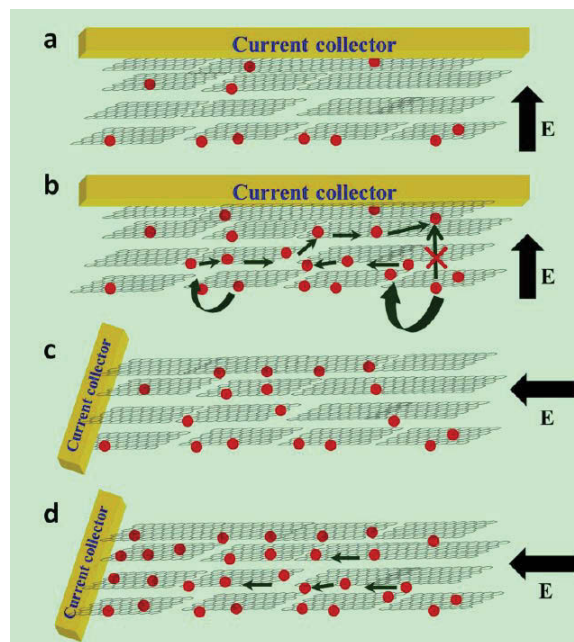


Figure 2-34 Schematic depiction for the performance comparison of the conventional stacked geometry (a,b) Vs the „in-plane“ geometry (c,d).¹³³

into the inner part of the electrode. However, the novel structure allows the ions to fill in the electrode more quickly since there is the same direction of the electric field and the geometry of the electrode. It therefore increases the specific capacity and offers better charge mobility and more effective utilization of the surface of the electrode as opposes

to those of the stacked electrode.

In the work, the authors employed the layer-by-layer assembly method to prepare the graphene oxide films followed by chemical reduction. The method involves charging the quartz substrate by dipping it into a cationic polymer, polyethyleneimine (PEI) followed by rinsing with deionized water. After drying in air, the substrate was immersed in the graphene oxide solution. The controlled dipping and rinsing process was repeated three times to form a GO film. Once the reduction of the GO film was finished, RMGO films with 10 nm thickness were obtained. The specific capacitance of the electrode synthesized by them reached to 394 uF cm^{-2} , energy and power densities were calculated to 8.5 Wh

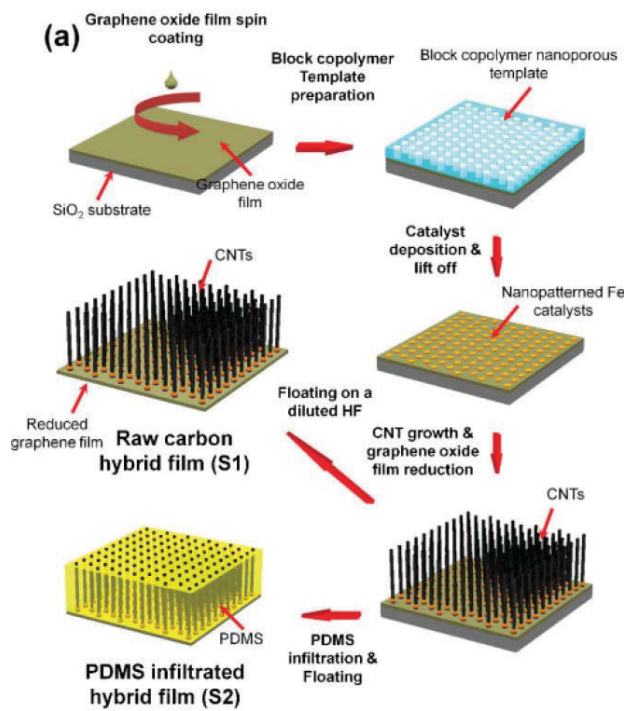


Figure 2-35 Schematic illustration of the fabrication process for carbon hybrid films.¹³⁴

kg^{-1} and 5.7 kW kg^{-1} , respectively.

The authors reported that about 21 layers of graphene existed in the RMGO film with 10 nm, yielding an interlayer spacing of 5 \AA . The interlayer space is enough for the situation

such as $\text{H}_2\text{PO}_4^{1-}$, HPO_4^{2-} and PO_4^{3-} with the diameter of 4.8Å. However, according to the previous studies,^{41, 63} since the sizes of hydrated ions are in the range of $6\pm 7.6\text{Å}$, the minimum effective pore size should be greater than 15Å. It is known that, in general, pore sizes in the range of $30\pm 50\text{Å}$ are required to maximize the capacitance in the double-layer capacitor. In addition, this method can be used in manufacturing a supercapacitor with high capacitance and energy since it is difficult to fabricate the electrode with higher thickness, just only the thin in-planar electrode.

The first simple method that fabricates the hybrid graphene and vertical CNTs films by thermal chemical vapour deposition was proposed by Lee *et al.*¹³⁶ in 2010, in which the graphene oxide was reduced to graphene with the synthesized vertical CNTs. Vertical CNTs were grown from the nanopatterned catalyst array by the CVD method in a direct current plasma atmosphere (Figure 2-35). During CNT growth process, the graphene oxide film coated on the surface of the Si substrate is reduced in the high-temperature atmosphere and, thus, gains electroconductivity. The hybrid film obtained through the method they proposed enables high temperature stability, mechanical compliance as well as excellent field emission performance.

2.4.3. Unzipped CNTs

Most of the CNTs grown by the CVD method are multi-walled CNTs because the single-walled CNTs are difficult to be obtained and not cost effective. Therefore, most of the vertically aligned CNTs employed in supercapacitors, especially in the commercial supercapacitor, are multi-walled CNTs. However, for multi-walled CNTs, only the outer portion of CNTs can be accessed by ions and the inner carbon surface are all wasted, leading to lower specific capacitance of the multi-wall CNTs-based supercapacitors.

Single layer samples of graphene are most often the result of a laborious peeling method, which is neither scalable nor capable of producing uniform depositions.⁶⁹ CNT can be seen as rolling few-layer graphene to form the seamless nanotube. Recently, researchers have proposed different methods to unzip the CNTs to make graphene sheets and nanoribbons. Even though the electrical property of graphene nanoribbon, semiconducting or metallic, are dependent on the width of the nanoribbon and independent of their edge patterns¹³⁷, the diameter of the CNTs, grown by the CVD method, can be controlled by the pattern of the catalyst deposited on the substrate.

Directly unzipping the aligned vertical CNTs to graphene sheets is expected to make

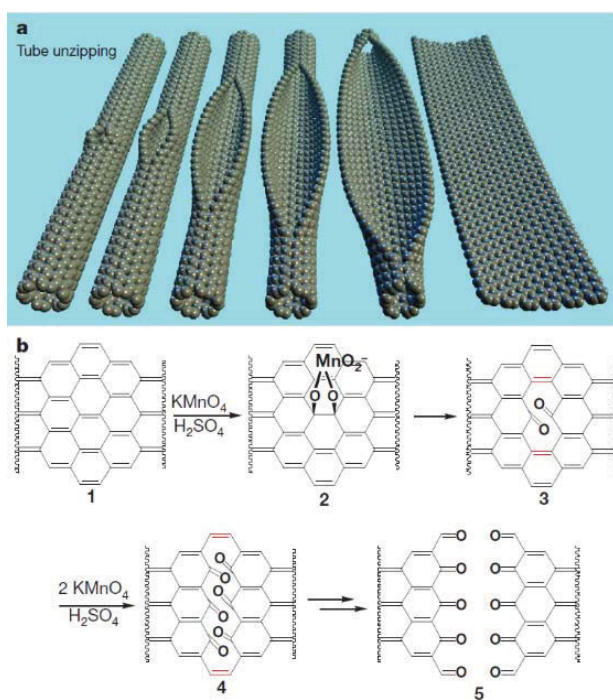


Figure 2-36 (a) Representation of the gradual unzipping of one wall of a carbon nanotube to form a nanoribbon. Oxygenated sites are not shown. (b) The proposed chemical mechanism of nanotube unzipping.¹³⁶

supercapacitors possessing high energy storage capability. To date, graphene, possessing large surface, high conductivity and charge carrier mobility, has spawned intensive researches into fabricating supercapacitor electrodes with graphene. However, most of

the electrodes compositing graphene and conducting materials like CNTs, have uncontrollable pore structure and ion diffusion. Currently, all the graphene is fabricated on the horizon plant, and the employing of the vertical graphene sheet as the electrode has not been reported. If the vertical graphene sheet is successfully used in the electrode, the supercapacitor will possess high energy density and power density due to the intrinsic property of graphene.

Kosynkin *et al.*¹³⁸ reported a simple solution-based technique to make graphene sheets and nanoribbons, as shown in Figure 2-36. In the technique, MWCNTs were firstly treated by concentrated sulphuric acid to obtain suspended MWCNTs, followed by 500 wt% potassium permanganate treatment. The reaction mixture was then stirred at room temperature for 1h and finally heated to 55–70 °C for an additional 1h. The diameter of the original MWCNTs ranges from 40nm to 80nm and the inner diameter of the MWCNTs is approximately 15-20 nm. After chemically unzipping the nanotubes, the width of the nanoribbon reached 100-500 nm. The unzipped nanotubes were poorly conducting because of the existence of the oxygen-containing functionalities on the edge of the nanoribbon. The surface oxidations disrupt the flow of the charge carriers, degrading the conductivity. Aqueous N_2H_4 in the presence of ammonia was used to reduce the unzipped nanotubes with oxygen groups. After chemical reduction or annealing process, the wide nanoribbons restored the electrical conductivity. The sort of nanoribbon possesses metallic property which is suitable to serve as the electrodes of supercapacitors.

A selective etching of CNTs to graphene nanoribbon by using argon plasma is reported by Jiao *et al.*¹³⁹ In the method, the MWCNTs were partly embedded in a poly methyl methacrylate (PMMA) layer as an etching mask (Figure 2-37). The parts that were not covered by the PMMA were etched during the argon plasma process. Finally the graphene

nanoribbons with various widths were obtained after the polymer film was removed by using acetone vapour. The width of the graphene depends on the number of layers of the original MWCNTs and the diameter of the MWCNTs. Furthermore, the duration that the MWCNTs with polymer film were exposed to argon plasma controls the width of the graphene film. The mean diameter of the author's starting MWCNTs was 8 nm. After 10s of Ar plasma etching, about 20% of MWCNTs were unwrapped to single- or few-layer graphene nanoribbon. This method contributes to cleaving CNTs in the longitudinal direction rather than etching along the circumference.

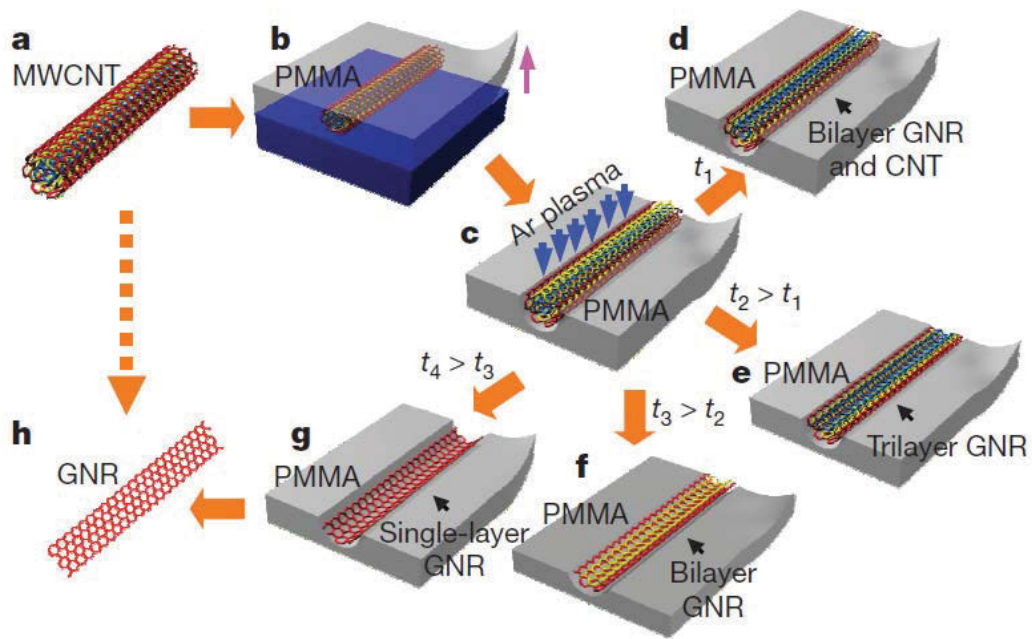


Figure 2-37 (a) A pristine MWCNT was used as the starting raw material. (b) The MWCNT was deposited on a Si substrate and then coated with a PMMA film. (c) The PMMA–MWCNT film was peeled from the Si substrate, turned over and then exposed to an Ar plasma. (d–g) Several possible products were generated after etching for different times: GNRs with CNT cores were obtained after etching for a short time t_1 (d); tri-, bi- and single-layer GNRs were produced after etching for times t_2 , t_3 and t_4 , respectively ($t_4 > t_3 > t_2 > t_1$; e–g). (h) The PMMA was removed to release the GNR.

Abraham *et al.*¹⁴⁰ employed intercalation and ammonia to longitudinally unwrap the MWCNTs. The cointercalant Li and NH_3 was used in the work. The simultaneous intercalation of Li and NH_3 is able to increase the interlayer distance to 6.62 Å which is

enough to break the nanotube walls followed by exfoliation and unwrapping of the nanotube (Figure 2-38). Due to the nanotubes fabricated by CVD being highly crystalline with closed ends, acid purification and hydrothermal procedures were used to open the tips of the nanotubes which contributes to the intercalation of Li-NH₃ complex. This method produced 0~5% of ex-MWCNTs, most of them are damaged, only the outer layers were exfoliated, and partially exfoliated. To effectively unwrap the MWCNTs, several of ratios Li/C were tested. Their results showed that higher amounts of Li results in more exfoliation of nanotubes. They also found that the refluxing of the solution containing Li,

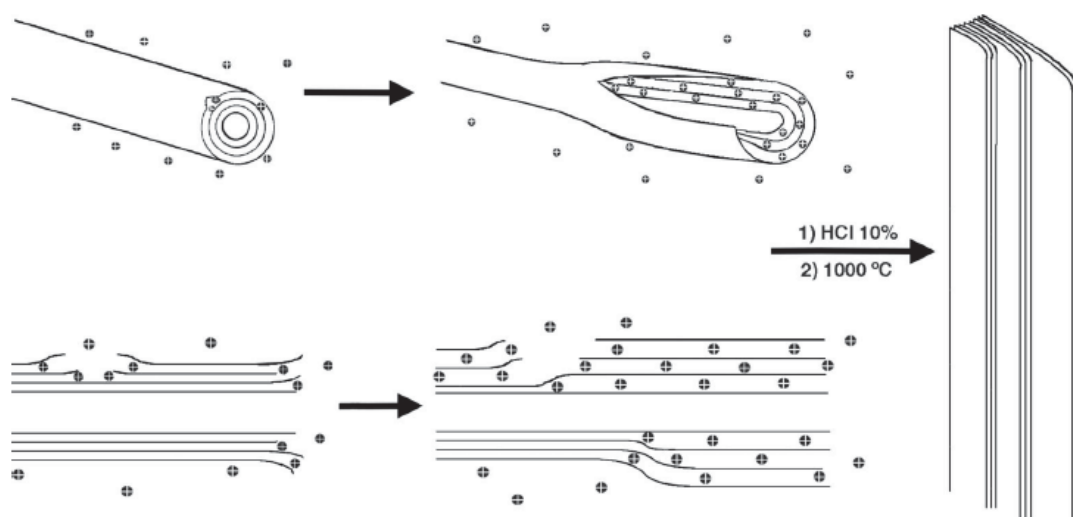


Figure 2-38 Mechanism for intercalation and unwrapping of MWNT.

NH₃ and MWCNTs in 10% HCl contributes more ex-MWCNTs than room temperature stirring. The exothermal reaction between HCl and Li-NH₃ enhanced the further exfoliation of MWCNTs.

2.4.4. Vanadium Oxide

Various carbon-based materials, including activated carbons, tangled carbon nanotube and aligned carbon nanotube, have been widely used as the electrodes of supercapacitors. Even though activated carbon has a huge surface area³⁶⁻⁴⁰ which is more than 1410 m² g⁻¹

¹ reported³⁶ and 2000-3000 m² g⁻¹,^{41, 42} the power density and energy density were limited by its widely varying pore sizes. The specific power of the electrode consisting of activated carbon is just 0.5-5 kW kg⁻¹, which leads to low specific energy densities ranging from 0.5 to 10 Wh kg⁻¹⁴³ and the mass-specific capacitance is usually less than 200 F g⁻¹.⁴² CNTs are attractive materials for the electrodes of supercapacitors owing to their superb characteristics of electrical,⁵⁰⁻⁵⁴ mechanical,^{55, 56} low mass density, low resistivity and large surface area.^{44, 57-59} Some electrodes consisting of tangled CNTs^{57, 60-62} have achieved much better performance than activated carbon. However, it is difficult to maintain high permeability and porosity of the tangled CNTs film. With better controllable pore size and lower ion diffusion resistivity, aligned carbon nanotubes make them a most promising candidate for energy storage. The power density of aligned CNTs-based electrodes has reached to 13 Wh kg⁻¹ or 10.4 Wh l⁻¹ from 3.9 Wh kg⁻¹ or 3.1 Wh l⁻¹, and the power density ranges from 3.50 kW kg⁻¹ to 163 kW kg⁻¹.^{44, 58, 63} Due to the intriguing structure single layer of carbon,⁶⁹ graphene possesses high electric conductivity and mechanical strength, charge carrier mobility,⁴² high specific surface area up to 2675 m² g⁻¹,^{64, 68} which is much larger than that of activated carbon and carbon nanotubes. Moreover the specific capacitance of graphene is able to reach 21 uF cm⁻², and graphene has the largest theoretical electrochemical double layer capacitance of about 526 F g⁻¹.⁶⁴ It can also provide conduction pathways to a greater area per unit mass than CNTs, which should translate into improved conductivity.⁶⁹

However the supercapacitor with only EDLC mechanism is limited by its energy density. There is a critical need to develop novel supercapacitor electrodes with improved high-energy and remained high-power properties. The formation of carbon-transition metal oxide nanocomposites may offer unique benefits for such applications. Among broadly available transition metal oxides, vanadium oxide is one of the most promising ion

insertion materials.⁸⁰ Vanadium oxide is abundant, relatively inexpensive (\$12 per kg), has a layered structure⁸⁰ and offers a broad range of oxidation states which will offer the broad range of redox reactions suitable for supercapacitor operation⁷¹ V^{5+} can be easily reduced leading to mixed valence vanadium oxides in which both V^{5+} and V^{4+} and even V^{3+} ions are observed.⁸¹

However, compared with double-layer capacitors, pseudo-capacitors often suffer from a lower power delivery rate limited by the redox reaction rate and the conductivity of the

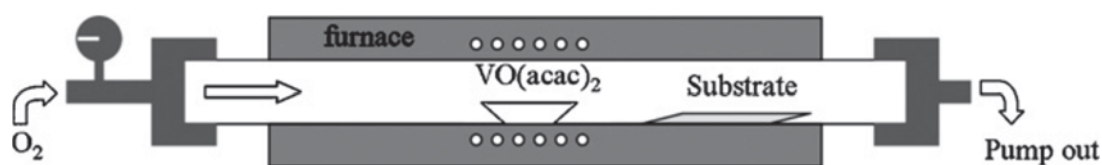


Figure 2-39 Schematic diagram of horizontal alumina tube furnace for growth of vanadium oxides.¹⁴³

redox active species.¹⁴¹ For example, V_2O_5 suffers from low electronic conductivity with high resistivities, limiting the application of the vanadium oxide electrodes in supercapacitors.

Sol-gel synthesis is one of the prevalent methods used to fabricate the V_2O_5 nanotubes.¹⁴²⁻¹⁴⁴ Ammonium meta-vanadate (NH_4VO_3) and acidic ion exchange were firstly resined in water. After the heating at 60 °C, the orange colored sol was prepared. Following the mixture, the V_2O_5 nanofiber was obtained by washing in ethanol and drying at 100 °C. The composite film with V_2O_5 nanofiber was demonstrated to possess high surface area, which facilitates electrochemical charge injection and intercalation.

Chemical vapor deposition (CVD) technology is another method employed to fabricate the V_2O_5 nanostructure film.¹⁴⁵ In their CVD method (Figure 2-39), the vanadyl acetylacetonate ($VO(acac)_2$) powder was used as the vanadium precursor. Vanadyl

acetylacetonate ($\text{VO}(\text{acac})_2$) powder was selected as the vanadium precursor because of its low boiling point. Various morphologies vanadium oxides including V_2O_5 rods, VO_x microspheres and microroblocks were obtained, which depended on the depositing temperature. V_2O_5 rods with a diameter of ~ 250 nm, VO_x microstructure with V^{5+} and V^{4+} cations and VO_2 microblocks were obtained at the depositing temperature of 500, 450–250 and 150 °C, respectively. When the depositing temperature was as high as 500 °C, most of the V^{4+} cations were oxidized to V^{5+} cations and V_2O_5 rods were obtained.

Hydrothermal synthesis of vanadium oxide nanostructures can also be fabricated by heating aqueous V solutions and the related chemical parameters.⁸¹ Tetramethyl ammonium $\text{N}(\text{CH}_3)_4\text{OH}$ (TMAOH) was added into the aqueous solution of decavanadic acid and then the layered compound $\text{TMA}[\text{V}_4\text{O}_{10}]$ is obtained, after hydrothermal heating at 180 °C. In particular, the influence of pH and the temperature of the precursor were investigated. And Mello *et al.* demonstrated that heating V_2O_5 solution with tetramethyl ammonium $\text{N}(\text{CH}_3)_4\text{OH}$ (TMAOH) for instance leads to different layered compounds depending on pH. Hydrothermal synthesis was also used to synthesize platinum and vanadium oxide nanotubes hybrid film.¹⁴⁶ Cui *et al.*¹⁴⁷ synthesized polypyrrole/vanadium oxide nanotubes (PPy/ VO_x -NTs) by using combination of hydrothermal treatment and cationic exchange technique. The hybrid composite was used as the cathode material for rechargeable Li-ion battery.

Anodic deposition of vanadium oxides was proposed to synthesise various nanostructures.^{148, 149} The precursor solution was chosen as 25 mM VO_2SO_4 with 5 mM H_2O_2 . Under the potentiostatic mode of 0.7 V vs. Ag/AgCl, the hydrous vanadium oxide ($\text{VO}_x \cdot y\text{H}_2\text{O}$) was directly deposited on the graphite substrate. After cleaning and drying, the $\text{VO}_x \cdot y\text{H}_2\text{O}$ /graphite electrode was obtained. They found that the success in growing

one-dimensional (1D) vanadium oxide nanowires strongly depends on the deposition variables such as the V^{5+}/V^{4+} ratio (adjusted by H_2O_2 addition) in the $VOSO_4$ solution and the applied current density during anodic deposition. The novel oxide deposit showing a porous three-dimensional network architecture possessed high power characteristics and acceptable specific capacitance ($CS \approx 167 \text{ F g}^{-1}$ at 25 mV s^{-1}) for pseudocapacitor applications.

Ahmad *et al.*¹⁵⁰ investigated the effect of ultrasonics on the formation of vanadium oxide nanotube by using sol-gel reaction method. In the work, crystalline V_2O_5 was firstly dissolved in the water with the ultrasonics. Once the V_2O_5 slurry was prepared, it was mixed with the hexadecylamine solution with acetone. Then vanadium oxide nanotube was fabricated by the hydrothermal method. Ultrasonication did not reduce the particle size and, in fact, enhanced the suspension homogeneity of vanadium oxide with hexadecylamine for better and faster formation of NTs. The ultrasonic treatment for the duration of 15 min produced well developed nanotubes with only a small amount of amorphous or lamellar by-products but for the duration of 30 min it also produced VO_x -NTS with longer length and similar diameter. The ultrasonication also has the benefit of reducing the mixing time from 48h to 24h, and the hydrothermal condition from 7 days to 5 days.

Multi-walled carbon nanotube (MWCNT)-induced vanadium oxide nanosheet composite was synthesized via sol-gel method and subsequent hydrothermal treatment process.¹⁵¹ The MWCNTs were pretreated by mix-acid ($H_2SO_4:HNO_3 = 3:1$) and then dispersed in the distilled water. Once the vanadium peroxide solution was ready, the MWCNTs solution was added to form the composite solution. A rectangular sheet-like nanostructure was obtained by using this method. The high capacity is attributed to the uniform coating

of vanadium oxide onto the MWCNTs network and the high conductivity of MWCNTs. They also demonstrated the presence of MWCNTs pretreated by mixed acid is conducive to the reduction and oriented crystallization of vanadium oxide sol, and then leads to the formation of vanadium oxide nanosheet which is monoclinic crystalline and primarily composed of VO_2 .

The sol-gel method and subsequent hydrothermal treatment process were also employed

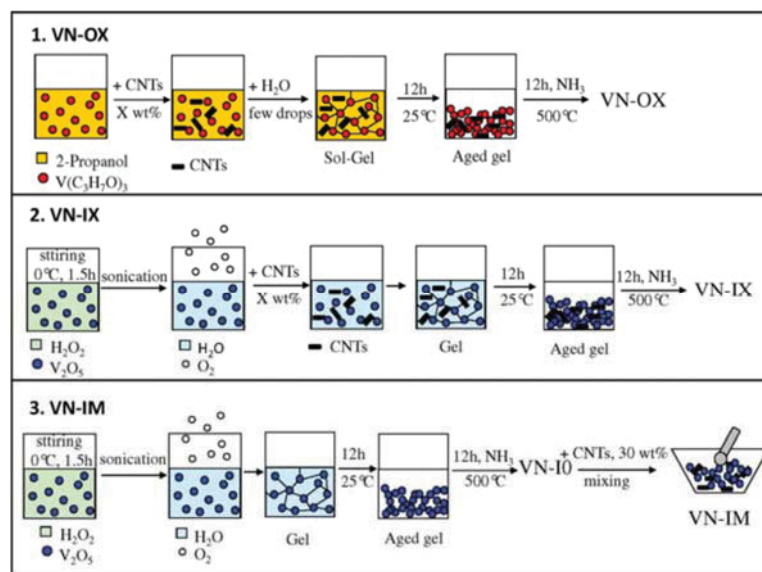


Figure 2-40 Schematic representation of VN/CNTs nanocomposite synthesis process.¹⁵⁰

to synthesize nanostructured vanadium nitride/multiwalled carbon nanotubes (VN/CNTs) composites.¹⁵² The incorporation of CNTs during VN synthesis allows VN/CNTs nanocomposites to be obtained with higher porosity, narrower pore size distribution, better conductivity and improved electrochemical properties compared to VN without CNTs (Figure 2-40). As a consequence, the hybrid electrode results in an enhancement of the energy density at high power.

Sofiane *et al.*⁷¹ uniformly deposited the smooth nanostructured vanadium oxide on the porous multi-walled carbon nanotubes (MWCNTs) electrode. In their work, the

deposition of vanadium oxide on the MWCNTs substrate was achieved by the atomic layer deposition (ALD) method. The average coating thickness increases by 0.1 nm per cycle. After 500 ALD cycles, around 110 nm thickness of vanadium oxide was deposited on the porous MWCNTs substrate (Figure 2-41). By using the MWCNT-vanadium oxide electrode without binder, Sofiane achieved specific capacitance of up to 600 F g⁻¹ of the composite electrode. Due to the high conductivity of the CNT, the ESR of their samples

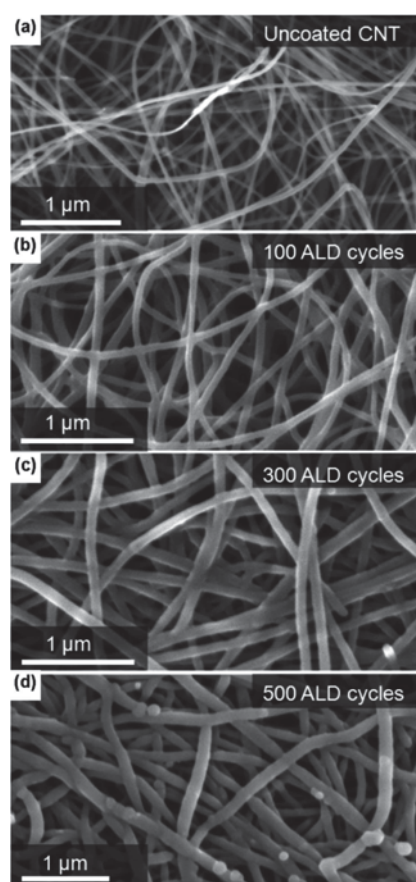


Figure 2-41 SEM images of (a) uncoated samples, and samples coated with VO_x for (b) 100 ALD cycles, (c) 300 ALD cycles, and (d) 500 ALD cycles.⁷¹

with interconnected CNT network is very low, just ranging from 0.025–0.4 Ω cm². The ALD method depositing metal oxide on CNT network has the benefits of binder-free electrode, controllable pore size and specific capacitance.

Yang *et al.*⁸⁰ proposed a novel method to fabricate the vertically aligned V₂O₅ nanotubes

for supercapacitors. Due to the insufficient stability of the vanadium oxide in common anodization electrolytes, the aligned pure V_2O_5 nanotube cannot be achieved by anodization. Therefore, in Yang's work, the "active" V_2O_5 was integrated into the stable nanotube structure of TiO_2 and grow mixed $V_2O_5-TiO_2$ nanotube arrays by anodization of Ti-V alloys, as shown in Figure 2-42. Through the anodization growing, highly ordered nanotubes with average length of 4–5 μm and tube diameter of 150–160 nm were successfully fabricated. The produced electrode possesses a highly ordered three-dimensional TiO_2 -stabilized V_2O_5 vertical nanotube structure. The specific capacitance of the nanotube can reach up to 220 $F g^{-1}$ and the energy density can be up to 19.56 $Wh kg^{-1}$.

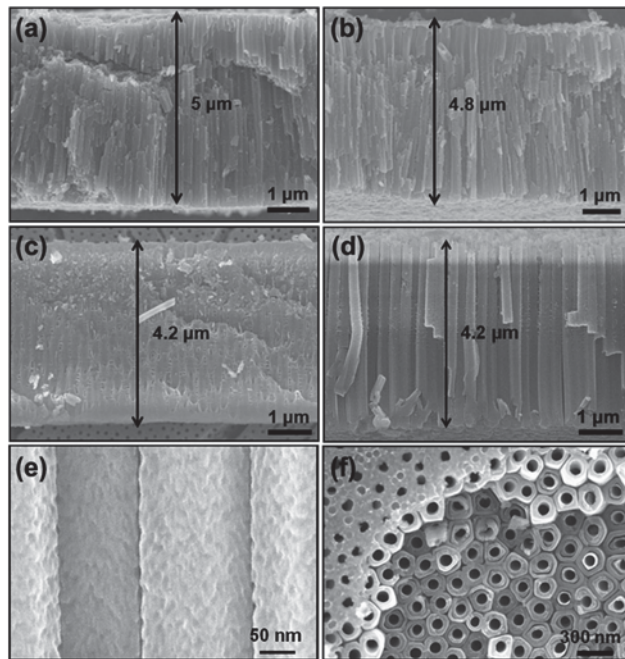


Figure 2-42 Cross-section SEM images of ordered nanotube arrays on different substrates: (a) Ti, (b) $Ti_{0.2}V$, (c) Ti_3V , and (d) $Ti_{18}V$ by anodization in an electrolyte composed of ethylene glycol with 0.2 M HF at 120 V for 30 minutes. (e) and (f) High magnification cross-section and top-view SEM images of the $Ti_{18}V$ Ti-V oxide nanotubes.⁸⁰

2.4.5. Ruthenium Dioxide

Nanocrystalline hydrous ruthenium dioxide ($RuO_2 \cdot xH_2O$) is promising electrode material

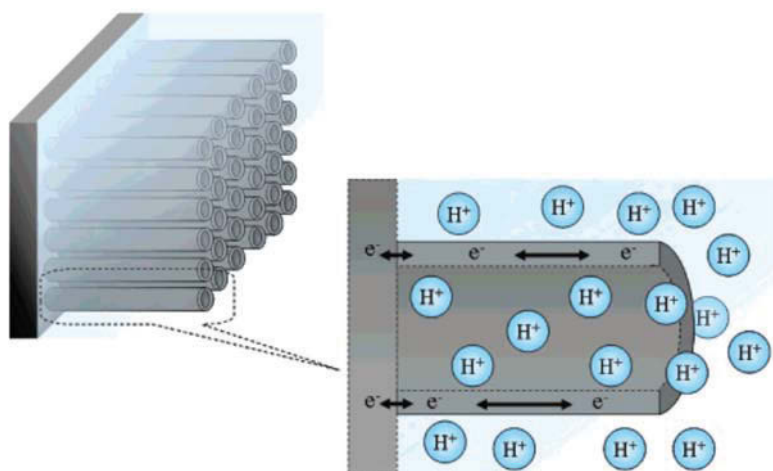


Figure 2-43 An ideal design of the electrode material for next generation supercapacitors, $\text{RuO}_2 \cdot x\text{H}_2\text{O}$ nanotubular arrayed electrode. The mesoporous architecture, hydrous nature, and metallic conductivity provide the proton and electron “superhighways” for the extremely rapid charge/discharge processes.⁷⁴

for supercapacitors.^{75, 153} It has good electronic conductivity,¹⁵⁴ ultrahigh pseudocapacitance,⁹² intrinsic reversibility of superficial redox couples,¹⁵⁵ and appropriate long cycle life. Electrical conductivity of RuO_2 is far greater than carbon and leads to higher inherent power densities or lower resistance-capacitance (RC) time constants.⁹² Nanocrystalline $\text{RuO}_2 \cdot x\text{H}_2\text{O}$ also promotes the rate of proton exchange/diffusion for high-power application due to the proton–electron double injecting/expelling mechanism for the charge storage process.⁷⁴

Nanotubular arrayed architecture of hydrous RuO_2 was fabricated by the use of the membrane-templated synthesis route, as shown in Figure 2-43.⁷⁴ The three-dimensional mesoporous architecture of $\text{RuO}_2 \cdot x\text{H}_2\text{O}$ nanotubular arrayed electrodes not only provide the pathways for the electron, but also promote the rate of proton exchange. In addition, the equivalent series resistance (ESR) was reduced by the 3D mesoporous architecture which simultaneously maintaining the facile electrolyte penetration, fast proton exchange, and the metallic conductivity. The specific power and specific energy of the prepared $\text{RuO}_2 \cdot x\text{H}_2\text{O}$ nanotubes reach to 4320 kW kg^{-1} and 7.5 Wh kg^{-1} , respectively,

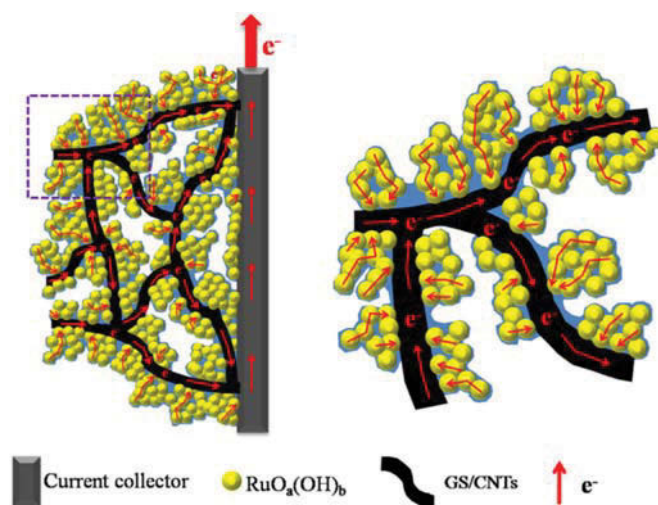


Figure 2-44 The scheme represents the enhanced charge storage process of the prepared electrode.¹⁵⁶

demonstrating the good performance as supercapacitor electrode.

A binder-free onestep process was designed by Chi-Chang Hu *et al.*¹⁵⁶ to fabricate a ternary ruthenium dioxide/reduced graphene oxide/carbon nanotube (Figure 2-44). In the composite, the rGO/CNT acts as a conductive backbone to facilitate the electron transport between current collector and $\text{RuO}_2 \cdot x\text{H}_2\text{O}$ nanoparticles which contributes to improvement of the electrode material conductivity. The specific capacitance of $\text{RuO}_2 \cdot x\text{H}_2\text{O}$ reaches to 1200 F g^{-1} , the unique microstructure builds up the smooth pathways of both proton and electron to access the active oxy-ruthenium species. And the specific energy and power of reaches 135 Wh kg^{-1} and 12 kW kg^{-1} respectively with a good capacitance retention.

2.4.6. Manganese Dioxide

Manganese dioxide (MnO_2) is another transitional metal oxide which received wide attention for supercapacitor application because of its intrinsic characteristics, such as low cost, availability in abundance, nontoxicity, abundance and more environmentally friendly and possessing a high theoretical specific capacitance.^{157, 158} However, the

electrical conductivity of MnO₂ is too poor to be practical use for supercapacitor. In addition to the poor electrical conductivity, the low structural stability and flexibility lead to the degradation of cycle life. Fabrication of the nanostructured MnO₂ or composites with conductive materials like CNT, graphene is widely used because of the improved electrical conductivity, short ion diffusion pathway, fully utilization of active materials.

Number of methods have been reported for the synthesis of MnO₂ nanostructures, such as the hydrothermal method,¹⁵⁹ sol-gel method,¹⁶⁰ electrostatic self-assembly technique.¹⁶¹ Different morphologies of MnO₂ including hollow spheres and hollow urchins, particles, platelets, nanosheets and nanowire were prepared by these methods. Among these fabrication technologies, electrochemical deposition is one of the most common methods because of simply, no polymer binder and modest reaction condition. Plenty of MnO₂ nanostructures have been fabricated using electrochemical deposition.^{158, 162, 163}

MnO₂ nanowires and mesoporous structures were synthesized by employing the electrodeposition technique with the association of porous anodic aluminium oxide.¹⁶⁴ MnO₂ nanowires with a uniform diameter of 60 nm on the Si substrates exhibit a loosely-arranged assembly after removing the template. The aligned structures provides an optimized path for the transfusion of electrolytes and reactants into the whole electrode matrix, even the deep area of the electrode. The enhanced electrochemical properties of the mesoporous MnO₂ nanowire array electrode achieved a high specific capacitance of 493 F g⁻¹ at discharging current of 4 A g⁻¹. However, the template-assisted methods are always complex and need much more time to remove the template. Peng-Yi Tang et al. prepared 3D MnO₂ onto nickel foam by double-pulse polarization and potentiostatic deposition technologies.¹⁵⁸ Nickel foam possesses a highly porous structure, providing

3D scaffold for the growth of MnO₂. The continuous conductive nickel foam therefore is

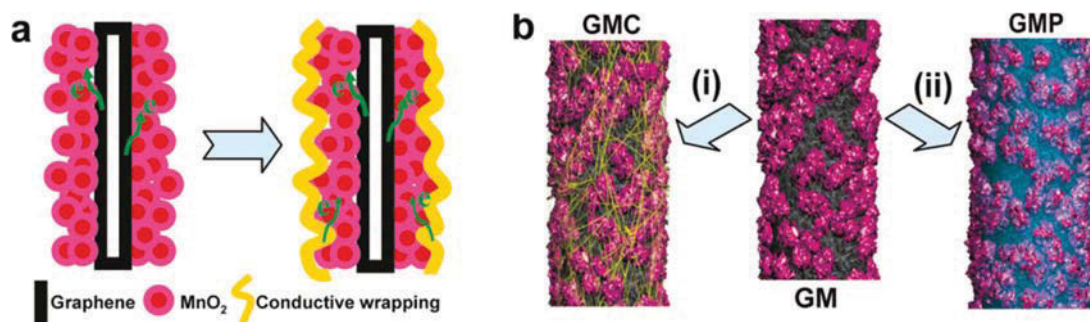


Figure 2-45 (a) Schematic illustration showing conductive wrapping of graphene/MnO₂ to introduce an additional electron transport path (in a discharge cycle). (b) Schematic of graphene/MnO₂/CNT and graphene/MnO₂/conducting polymer systems formed by wrapping of GM nanostructures with CNTs or conducting polymers (black, graphene; rose, MnO₂; yellow, CNTs; blue, conducting polymer).⁸²

a promising current collector to enhance the electrical conductivity and support the formation of ordered MnO₂ nanostructures. The 3D MnO₂ nickel foam show a significant improvement in the specific capacitance of 1222 F g⁻¹ at 5 A g and 600 F g⁻¹ even at a high current density of 100 A g⁻¹.

Due to the poor electronic and ionic conductivities, MnO₂ limits in the performance of power density and cycling. Deposition of MnO₂ onto 3D conductive substrates have been widely utilized in recent years to improve the electrical conductivity and charge-storage capability of MnO₂. As shown in Figure 2-45, a conductive wrapping method was developed by Guihua Yu *et al.*⁸² to improve the electronic and ionic conductivities of MnO₂, then enhancing the supercapacitor performance. The specific capacitance of the 3D conductive wrapping of graphene/MnO₂ nanostructures with carbon nanotubes was increased by 20% with a high value of 380 F g⁻¹. What's more important is that the 3D composite exhibited excellent cycling performance with >95% capacitance retention over 3000 cycles.

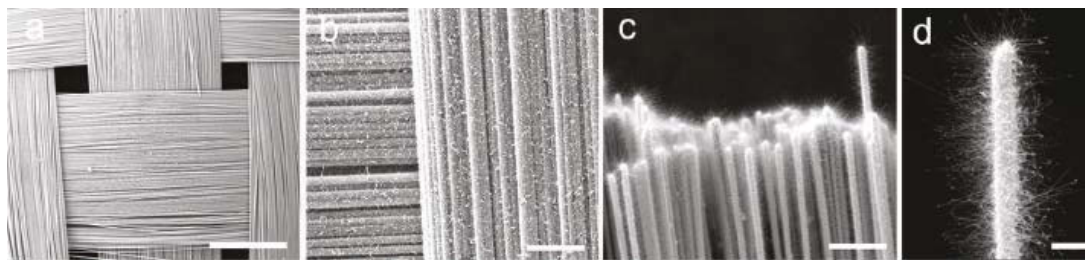


Figure 2-46 Structural characterization of MnO₂/Zn₂SnO₄/ carbon microfibers hybrid composite. (a-d) SEM images of Zn₂SnO₄ nanowires grown radially on the woven carbon microfibers.¹⁶⁵

Lihong Bao et al.¹⁶⁵ designed a facile method to coat MnO₂ film to highly electrical conductive Zn₂SnO₄ nanowires. Vapor transport method in a horizontal tube furnace was used to grow high-density Zn₂SnO₄ nanowires on commercial woven carbon microfibers. The crystalline Zn₂SnO₄ nanowires grown on carbon microfibers supported a highly conductive cores to fully utilize the surface area of redox active MnO₂, as shown in Figure 2-46. The composites achieved high specific capacitance of 621.6 F g⁻¹ at a scan rate of 2 mV s⁻¹, and 642.4 F g⁻¹ by chronopotentiometry at a current density of 1 A g⁻¹, a high-energy density of of 36.8 Wh kg⁻¹, high-power density of 32 kW kg⁻¹ at current density of 40 A g⁻¹, and long-term life that only 1.2% its initial specific capacitance was lost after 1000 cycles for supercapacitor electrode applications.

2.5. Summary

In this chapter, different energy storage technologies were firstly discussed, and then the advantages and disadvantages of each type of technology was comprehensively compared. After that, the metrics of a supercapacitor were summarized and explained. The supercapacitor modellings which play a critical role in the understanding of the energy storage mechanism were presented. In the latter part of this chapter, the electrode materials for supercapacitor and the fabrication methods were reviewed.

Chapter 3. Experimental Methods

The researches undertaken in the project involved synthesis of active materials, followed by characterizations of the as-prepared materials and evaluation of their electrochemical properties for supercapacitor. In this chapter, the materials, synthesis methods, materials characterization techniques, electrode fabrication and electrochemical testing were presented. Various fabrications technologies were used in the project, including hydrothermal method, revised vacuum filtration method and static electric field. The morphologies, crystal structures, surface area and mechanical properties were characterized by scanning electron microscopy (SEM), transmission electron microscopy (TEM), and energy dispersive spectroscopy (EDS), N₂ sorption (BET) and thermogravimetric and differential thermal analysis (TGA-DTA).

3.1. Materials synthesis

A number of materials synthesis techniques have been designed and utilized to prepare graphene-related nanocomposites and metal oxides. The methods used in this project were discussed in the part below in this chapter.

3.1.1. Hydrothermal method

Hydrothermal synthesis is a promising method to prepare large scale, well crystallized and morphology controllable materials. The growth of crystals occur in an autoclave consisting of a steel vessel, in which the precursor is crystallized under high temperature and high vapour pressure. The temperature of the autoclave and the heating time are controlled by a heating oven. Hydrothermal method allows the fabrication of the materials which are not stable at the melting point and have a high vapour pressure near their

melting points.

The morphologies and structures of the as-prepared materials depend on the concentration of the precursors in the solution, the volume of the solvent which determines the vapour pressure in the autoclave, temperature and the experimental duration time. Some surfactants will be used to modify the reaction to fabricate materials with different structures.

Hydrothermal synthesis was usually utilized to fabricate metal oxide or to deposit metal oxide on conductive materials like graphene and carbon nanotube. Homogenous hexagonal starfruit-like vanadium oxide was prepared by the revised hydrothermal method.¹⁶⁶ Various hierarchical three-dimensional (3D) vanadium oxide microstructures, including urchin-like microflowers, nanoborn-structured microspheres, nanosheet-assembled microflowers, and nanosheets bundles, were synthesized by a versatile hydrothermal method. It was found that the morphologies of the as-prepared products significantly depended on the concentration of the precursor.¹⁶⁷ A continuous hydrothermal synthesis method was employed to fabricate nanosized NiCo₂O₄ spinel compounds. A series of crystalline homometallic and heterometallic cobalt and nickel hydroxides and oxides were obtained by using this revised hydrothermal method.¹⁶⁸ Hydrothermal process and chemical bath deposition were combined to fabricate hierarchical NiCo₂O₄@NiCo₂O₄ core/shell nanoflake arrays on nickel foam for high-performance supercapacitor.¹⁶⁹ The core/shell NiCo₂O₄ achieved better electrochemical performance than conventional NiCo₂O₄ nanostructure materials.

The hydrothermal method is able to enable uniform growth of metal oxides on conductive materials. Even though metal oxides possess higher specific energy density than carbon materials, they suffer lower conductivity and worse cyclability. The materials consisting

of metal oxides and conductive materials like carbon nanotube, graphene and conductive polymer are able to achieve high charging and discharging rate, long cycle life and high energy and power density. Satyajit Ratha *et al.* proposed a facile hydrothermal method to synthesize layer structured WS₂ on reduced graphene oxide (RGO) for supercapacitor materials.¹⁷⁰ Because of the unique microstructure with a combination of two layered materials, WS₂/RGO hybrids serving as the supercapacitor electrode material achieved high specific capacitance, energy density, and excellent cycling stability. Two one-dimensional hierarchical hybrid nanostructures composed of NiCo₂O₄ nanorods and ultrathin nanosheets were grown on carbon nanofibers (CNFs) through a facile solution method combined with a simple thermal treatment.⁸⁹ By controlling different additives in the synthesis, NiCo₂O₄ nanorods and nanosheets were obtained. These two structures have high electroactive surface area, ultrathin and porous features, robust mechanical strength, shorter ion and electron transport path.

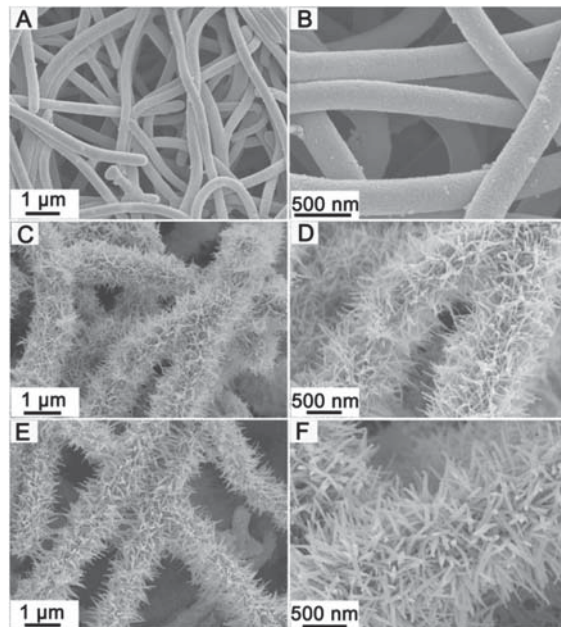


Figure 3-1 Typical FESEM images of (A, B) bare carbon nanofibers after Te nanowire core removal; (C, D) NiCo-precursor nanorod arrays/ carbon nanofibers hybrid nanostructure; and (E, F) crystalline NiCo₂O₄ nanorod arrays/carbon nanofibers hybrid structure obtained by annealing the NiCo-precursor nanorods/carbon nanofibers at 300 °C for 2 h with a slow heating rate of 0.5 °C min⁻¹.⁸⁹

3.1.2. Freeze drying



Figure 3-2 Benchtop Manifold Freeze-Dryer marketed by Millrock Technology.

Freeze drying technology is a dehydration process which is usually used in medicine research or industry. The freeze dryer (Figure 3-2) is usually used to freeze-drying biological materials, pharmaceuticals, biochemical products and foodstuffs which cannot be heated at moderate or high temperatures. The structures or nutrition of the materials can be preserved by freeze drying. It involves in freezing the material and sublimating the ice directly from the solid phase to the gas phase.

Figure 3-3 is the three phase diagram of water representing the phases of water as a function of temperature and pressure. The material is usually placed in a freeze-drying flask or container which is cooled by dry ice or liquid nitrogen. When the temperature is cooled below the triple point of water, the liquid water is totally frozen to solid ice which avoids the melting of water during sublimation. Slow freezing will lead to the production of larger ice crystals. Therefore, people have tried to control the freezing speed to control

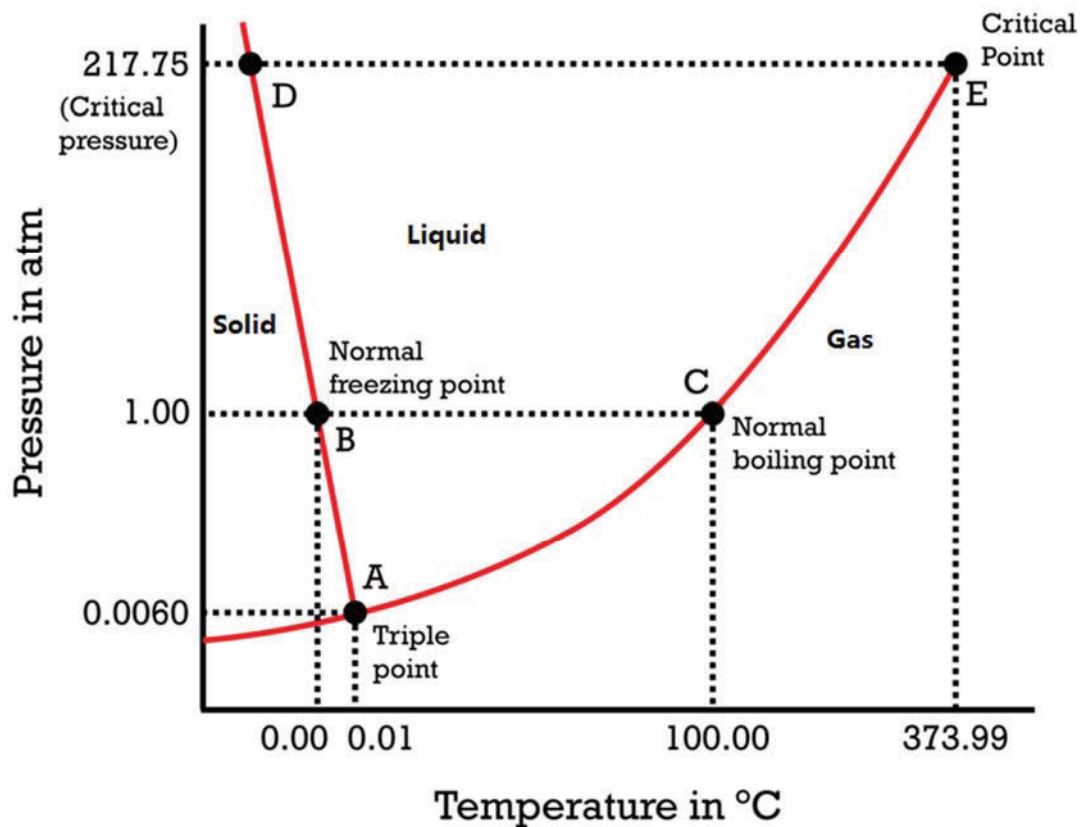


Figure 3-3 The three phase diagram of water.

the size of crystals then control the pore size in the materials. In contrast to slow freezing speed, rapid freezing will be adopted which will generate smaller ice crystals. Small ice crystals will be better for maintaining the structure of the cell wall, resulting in good texture and preventing structural collapse of the materials. After freezing, the materials are introduced into a freeze dryer to sublimate water directly from solid phase to gas phase rather than liquid phase. During the primary drying phase, the pressure is decreased to a few millibars. When the pressure reaches the specific value, enough heat is added to the material for the ice to sublime. The primary drying will be slow and cost several days to avoid damage to the material's structure. In addition, the pressure will be controlled to partial vacuum which is able to speed up the sublimation. 95% of the water in the material will be sublimated. The rest of the water will be dried in the final drying phase. The

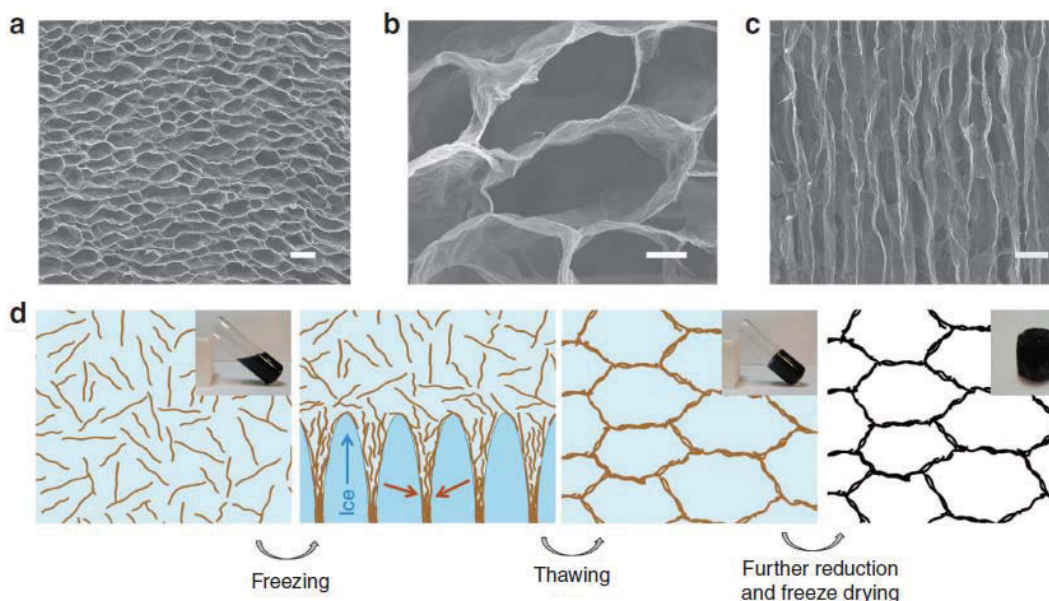


Figure 3-4 (a-c) Typical top-view (a,b) and side-view (c) SEM images of graphene monolith of 5.10 mg cm^{-3} . (d) Schematic showing the formation mechanism of the cork-like monolith by freeze casting. When a well-dispersed pr-GO dispersion (the first scheme) is frozen, pr-GO sheets are concentrated at the boundary of ice crystals and then aligned along the growth direction of ice due to the squeezing effect (the second scheme, side-view). As a result, a continuous honeycomb-like network is formed. The network retains its connectivity when the ice is thawed (the third scheme, top-view). The pr-GO sheets are illustrated as slightly corrugated lines in the scheme with the brown representing partially reduced, whereas the black for fully reduced. Photos of the corresponding samples are presented in the insets. Scale bars, 50 mm (a,c) and 10 mm (b).¹⁵⁶

temperature will be raised higher than in the primary drying phase which breaks the physico-chemical interactions that have formed between the water molecules and the frozen material.

Freeze drying is a useful technique to remove the water in the materials by sublimating frozen water directly from the solid phase to the gas phase while keeping the structure of the materials. Numerous 3D graphene foams have been prepared by using freeze-drying technology.

Ultralight and superelastic graphene-based cellular monoliths were prepared by freeze drying partially reduced GO.¹⁷¹ The resulting materials have 3D graphene networks with high elasticity, which are able to sustain their structural integrity under a load of $>50,000$ times their own weight and can rapidly recover from $>80\%$ compression. Qiu *et al.*¹⁷¹

reported that the amount of oxygen-containing groups of GO has a significant effect on the form of the porous structures. Directly freezing of conventional GO solution will lead to a randomly oriented porous structure, which has poor mechanical strength and a few recoverable deformation region. In contrast, a cork-like graphene cellular structure with high elasticity (Figure 3-4) was obtained by controlling the reduced ratio of GO in the solution. During the freezing process, the ice crystals squeezed the pr-GO to wrap at the crystal boundaries, and then a continuous network was formed. The π - π attraction between the pr-GO sheets resulting from the partial reduction which contributes to the stable structure. The further reduction of GO allowed the GO to maximally reduce and stronger intersheet π - π attraction to form the elastic 3D graphene foam.

Based on the freeze drying method, water, the very soft matter, therefore has the opportunity to serve as an effective space matter to prevent the restacking of graphene sheets during the reduction process. Xiaowei Yang *et al.* used water as the spacer material to separate graphene sheet, basing on freeze drying technology. This method enables the separation of graphene sheets without restacking to graphite. The graphene sheets remained significantly separated when combined together in a parallel manner.

The functionalization-lyophilization-microwave treatment combining with freeze-drying¹⁷² was designed by Han Hu *et al.*, who successfully produced ultralight graphene aerogel with excellent elasticity. This method is able to suppress the restacking of the graphene sheets during the reduction process. As shown in Figure 3-5, GOs are controllably functionalized by ethylenediamine (EDA) and then assembled in to monolithic functionalized graphene hydrogel. Ultralight graphene aerogel (ULGA) with excellent elasticity was obtained after freeze drying and microwave irradiation. The results indicated that the density of ULGA can be controlled by varying the EDA/GO

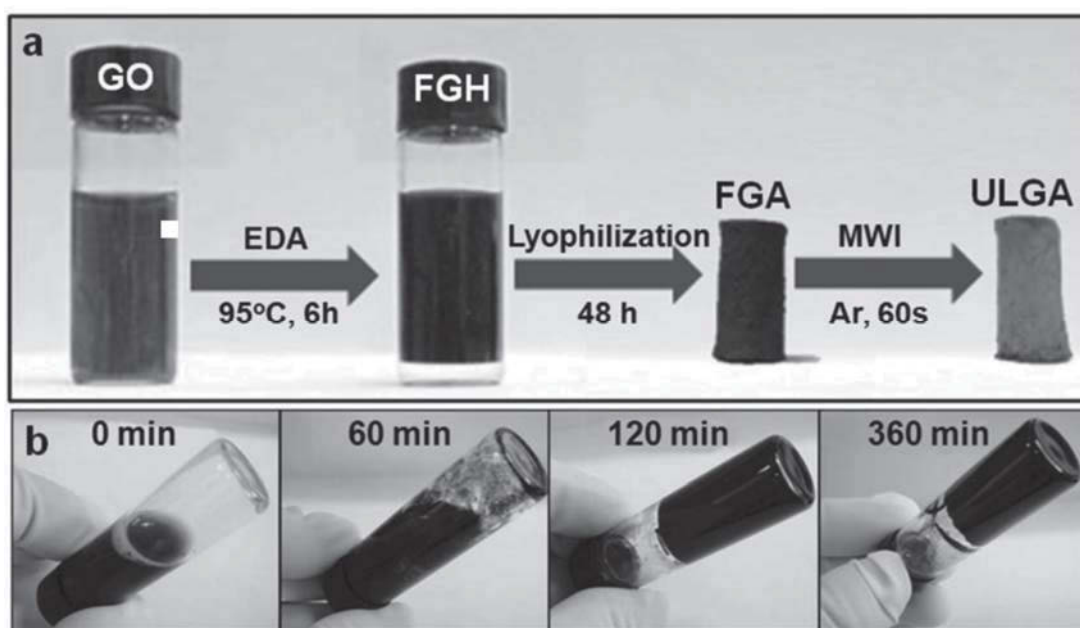


Figure 3-5 (a) Illustration of the fabrication process of the ultralight graphene aerogel (ULGA). (b) Digital images of time-dependent formation process of functionalized graphene hydrogel (FGH).¹⁵⁷

ratio as well as the concentration of GO. The density of ULGA ranges from 3 to 5 mg cm⁻³ and the porosity is as high as 99.7–99.8%. The ultralight ULGA exhibits a strong elastic property, which enable it to recover strain from 90% after being squeezed in to a pellet. A versatile, ultralight and nitrogen doped, three-dimensional (3D) graphene framework was also prepared by the freeze-drying method, which is ultralight with the specific weight of less than 10 mg cm⁻³.¹⁷³ The rich open-pore structures interpenetrating the graphene skeleton contributes to the ultralow weigh density of 2.1 mg cm⁻¹.

Xuetong Zhang *et al.* fabricated a graphene aerogel by combining freeze drying technology and sol-gel chemistry.¹⁷⁴ The resulting graphene aerogels have the density ranging from 12 mg cm⁻¹ to 96 mg cm⁻¹ with large surface area of 512 m² g⁻¹. This graphene aerogel has very strong mechanical properties, which can support more than 14000 times its own weight, nearly twice the amount afforded by the carbon nanotube aerogels. The morphology of the aerogels is quite uniform with a 3D network of randomly oriented sheet-like structures. A flexible solid-state supercapacitor consisting of 3D graphene

hydrogel film was designed by Yuxi Xu *et al.*¹⁷⁵ The 3D graphene film has a highly interconnected 3D network structure with exceptional electrical conductivity and mechanical robustness and flexibility. The thickness of the electrode is up to 120 μm , which exhibited excellent capacitive properties. The supercapacitor based on the electrode achieved a high gravimetric specific capacitance of 186 F g^{-1} , an unprecedented areal specific capacitance of 372 mF cm^{-2} , and good cycling stability.

The freeze-drying technology was also developed to fabricate electrode materials combined with metal oxide and conductive materials. The metal oxides usually have higher capacitance than that of carbon materials. However, they suffer poor conductivity leading to worse cyclability and charging/discharging rate. The combination of metal oxide and conductive materials is able to address these issues by adopting the advantage of both materials. MnO_2 was grown on GO sheets by hydrothermal method, and then introduced into a freeze drying system.¹⁷⁶ A novel method combining freeze-drying and thermal reduction was designed by Xiaoshi Zhou to synthesize silicon nanoparticles inserted into graphene sheets.¹⁷⁷ The as-prepared Si/graphene nanocomposite exhibits remarkably enhanced cycling performance and rate performance compared with bare Si nanoparticles. An *in-situ* chemical synthesis approach combined with freeze drying developed by Kim *et al.* to prepare ruthenium oxide/RGO nanocomposites.¹⁷⁸

3.1.3. Vacuum filtration

Vacuum filtration is usually used to separate solids materials from liquid materials. As shown in Figure 3-7, the moistened filter paper is able to retain the oversize solids and pass the fluid. During the filtration, the solid material is used to block the pores of the filter paper. The vacuum created by the aspirator therefore enhances the filtration speed. Vacuum filtration has been widely used to prepare graphene by filtering the graphene or

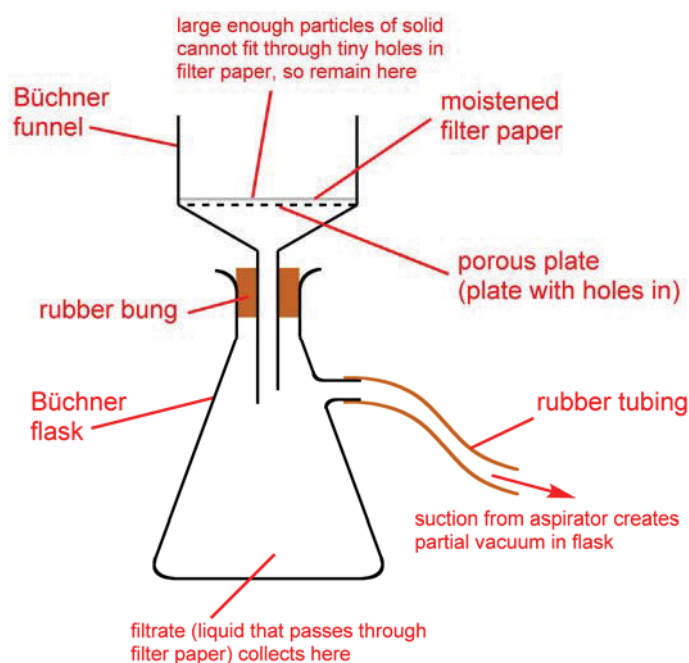


Figure 3-6 Diagram of vacuum filtration.

GO solution. Vacuum-assisted self-assembly method is able to fabricate high-density graphene paper or film, which increases the electrode density. The binder is excluded during the electrode fabrication, leading to high conductivity of the free-standing electrode.

A Vacuum-assisted method was used to densify an activated exfoliated graphite oxide (aMEGO).¹⁷⁹ The density of electrode is increased to 1.15 g cm^{-3} , which is significantly higher than that fabricated by conventional compression. Unlike the electrodes fabricated by conventional methods (Figure 3-7 a and b), the high density of electrode achieved an aligned nano-porous structure (Figure 3-7 c and d). The aligned aMEGO demonstrated a very high volumetric capacitance of 158 F cm^{-3} and 177 F cm^{-3} . A large areal mass, flexible and free-standing RGO/MnO₂ paper was prepared by using vacuum filtration, in which a template was not involved.¹⁸⁰ The large areal mass paper electrodes exhibit remarkable flexibility which can be bent into any desired structure.

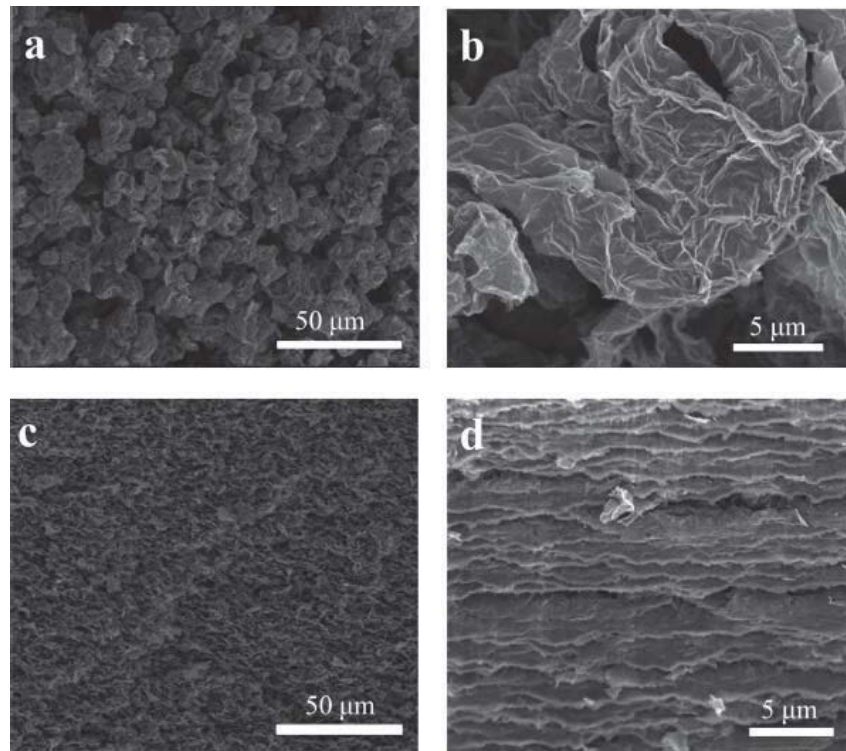


Figure 3-7 Low and high magnification SEM images of (a) and (b) mechanically densified aMEO and (c) and (d) aligned aMEO.¹⁶⁴

Zhiqiang Niu *et al.*¹⁸¹ designed a leavening strategy to prepare RGO foam based on the vacuum filtration method (Figure 3-8). The foam showed an open porous network with pore sizes in the range of sub-micrometer to several micrometers which can be directly

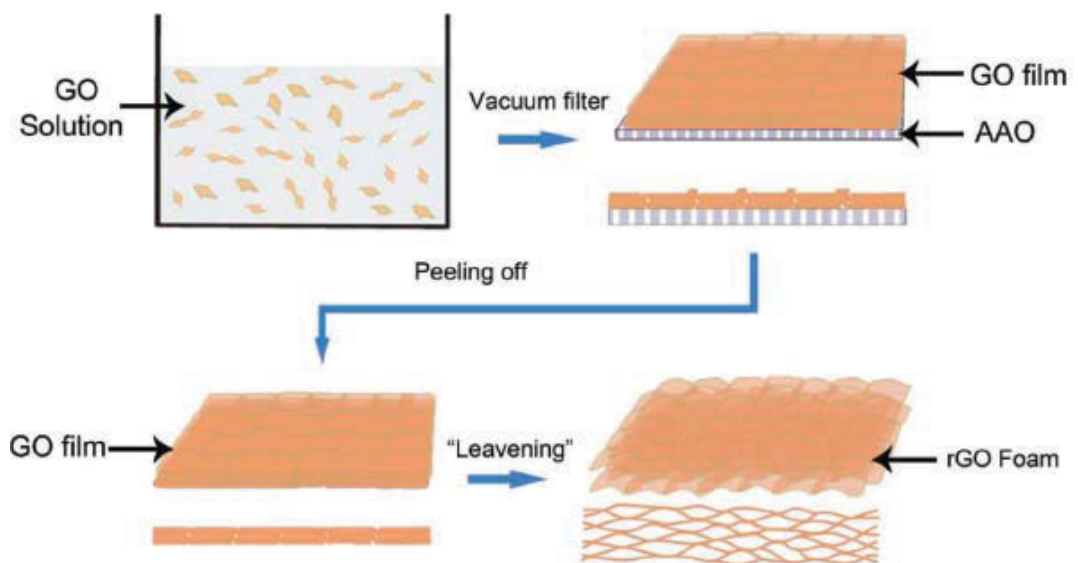


Figure 3-8 Schematic drawings illustrating the leavening process to prepare rGO foams.¹⁶⁶

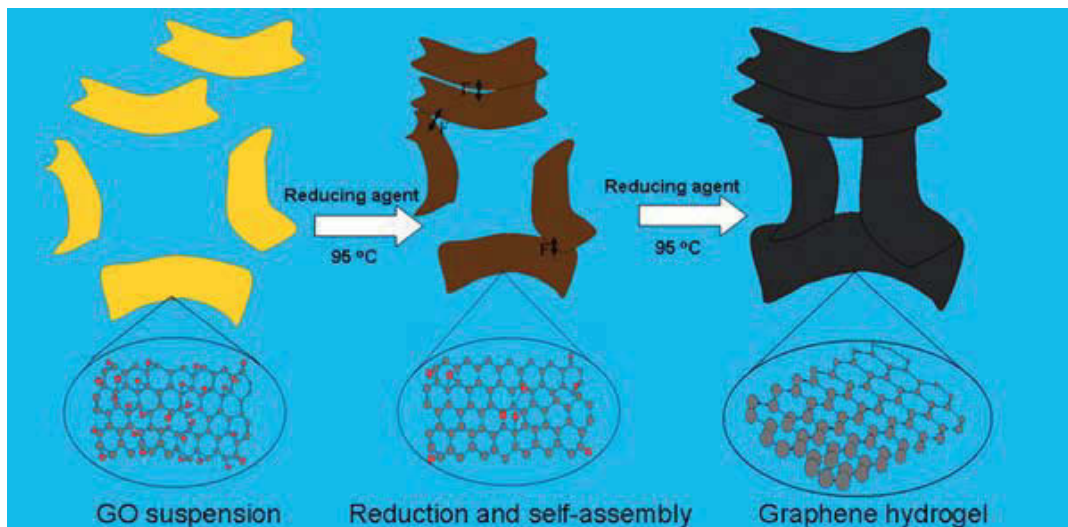


Figure 3-9 The proposed self-assembly mechanism for graphene hydrogel formation during the chemical reduction of GO in an aqueous suspension.¹⁶⁷

used as the electrode of supercapacitor. The walls of the pores in the foam are continuously crosslinked, rather than simply separated between different layers. Such continuously crosslinked structures of RGO not only effectively overcome the restacking of graphene sheets, but also achieve high conductivity of less than $100 \Omega \text{ sq}^{-1}$.

3.1.4. *In-situ* self-assembly

The in-situ self-assembly method usually uses chemical methods to partially or completely reduce GO, and the reduced GO will assemble together by itself to form 3D architectures of graphene.¹⁸² NaHSO_3 , Na_2S , Vitamin C, HI, and hydroquinone can serve as the reducing agents (Figure 3-9). The structures and pore size of the 3D architectures can be controlled by changing the type of reactor and the reducing time. The 3D architectures of graphene have a low density of 18 mg cm^{-3} , high electrical conductivity of 87 S m^{-1} , high mechanical properties, thermal stability and high specific capacitance of 166 F g^{-1} . However, the pore sizes of the 3D graphene architectures fabricated by the simple self-assembly methods is too large to be the electrodes for supercapacitors. A microwave assisted self-assembly method was designed by Han Hu *et al.* which was used

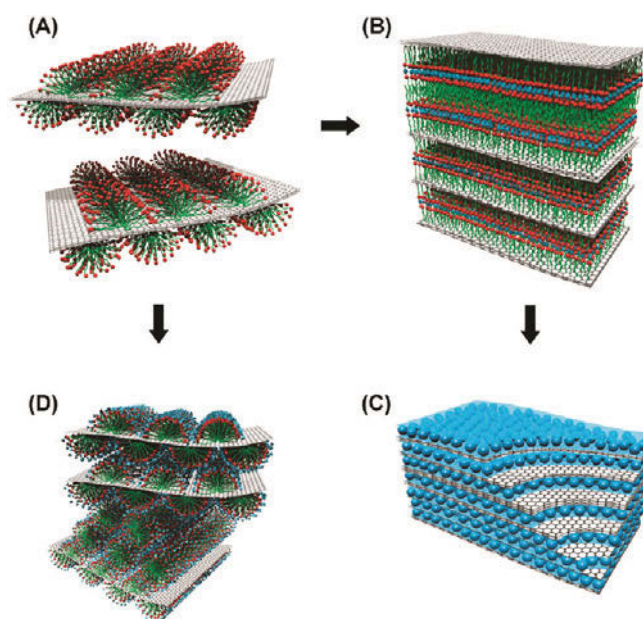


Figure 3-10 Schematic illustrations of the ternary self-assembly approach to ordered metal oxide graphene nanocomposites.¹⁶⁸

to increase the density of the graphene foam.¹⁷² The compressed graphene aerogels were obtained by using a weak reducing agent ethylenediamine (EDA) to functionalize the GO sheets and initiate their assembly into partially reduced graphene hydrogel. The compressed graphene aerogels were obtained after the further microwave irradiation of the graphene hydrogel.

Donghai Wang *et al.* developed a ternary self-assembly approach to construct aligned SnO₂-graphene nanocomposites by using graphene as fundamental building blocks.¹⁸³ The anionic surfactant was introduced onto functionalized graphene sheets (FGSs) which enabled the graphene materials to be dispersed in the hydrophobic of surfactant micelles. The surfactant micelles with the FGSs then become the fundamental building blocks for self-assembly. The surfactants assembled onto the FGSs contribute to absorption and deposition of metal cations, leading to forming an ordered nanocomposite.

3.2. Physical and morphological characterization

The as-prepared materials were introduced to experimental works for characterizing the physical, morphological and electrochemical properties after fabricating by the designed methods. The experimental works involved in various characterizing techniques including X-ray diffractometry, scanning electron microscopy, transmission electron microscopy, thermogravimetric analysis and Brunauer-Emmett-Teller surface area and Barrett-Joyner-Halenda pore size and volume analysis as discussed below.

3.2.1. X-ray Diffractometry (XRD)

X-ray diffractometry is a characterization method to confirm a materials' crystal phases and structures by using an X-ray beam. When the X-ray beam hits on the atoms of the samples, a sensor of the XRD instrument will record the scattered angle, polarization and the wavelength of the scattered X-ray beam. A particular relative intensity of the X-ray peak represents a certain crystal lattice of the sample. The obtained diffraction curve with



Figure 3-11 An X-ray diffractometer (Siemens D5000 model) in UTS.

relative peaks at particular angles is called an XRD pattern. Each material has its own XRD pattern which has been identified by scientists. In this project, XRD was used to identify and confirm the actual phase of the as-prepared materials by comparing the obtained pattern to the standard XRD in the Joint Committee on Powder Diffraction Standards (JCPDS) database. The XRD instrument used in this doctoral work to identify the phase and crystallographic structure of as-prepared materials was a Siemens D5000 diffractometer equipped by a Cu K α 1 radiation ($\lambda = 1.54056 \text{ \AA}$), as shown in Figure 3-11.

3.2.2. Scanning electron microscopy (SEM)

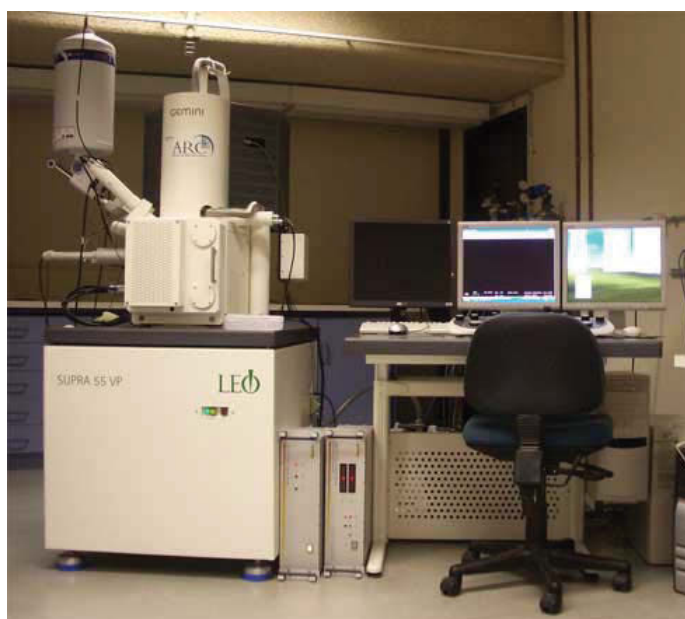


Figure 3-12 An FE-SEM facility (Zeiss Supra 55VP) in UTS.

The morphologies of the materials were observed by high resolution field emission scanning electron microscopes (FESEM, Zeiss Supra 55VP) as shown in Figure 3-12. The SEM images were taken by the microscope at an acceleration voltage of 20 kV. The Energy Dispersive Spectroscopy (EDS) was attached in the Supra 55VP for the elemental mapping and chemical characterization of as-prepared materials.

3.2.3. Transmission Electron Microscopy (TEM)



Figure 3-13 A commercial TEM setup (JEOL 2011 model).

SEMs (FE-SEMs) are used for preliminary analysis to check the structure of the sample. However, TEMs are capable of taking the images of sample at a very high resolution to observe the crystal structures at nanometer scale like lattice planes and d -spacing. The beam of electrons generated in TEM which was operated at 200 kV is able to transmit through the samples deposited on a copper grid, interacting with the sample when the electrons pass through the sample. And then the images of the sample's nanostructure were obtained. In this project, a high-resolution transmission electron microscopy (HRTEM, JEOL JEM-2011) was used to take the TEM images of the samples which worked at an accelerating voltage of 200 kV (Figure 3-13). The bright field image (BF) and selected area electron diffraction (SAED) patterns were recorded by a Gatan CCD camera and then the images were generated. Some atomic resolution TEM images were collected by the transmission electron microscopy (HRTEM) FEGTEM 3000 (JEOL 300KV Atomic Resolution Transmission Electron Microscope (0.192 nm resolution)) worked at an accelerating voltage of 300 kV.

3.2.4. Thermogravimetric Analysis (TGA)



Figure 3-14 A TGA/DTA Analyzer (SDT 2960 model, TA Instruments) in UTS.

Thermogravimetric analysis is used to determine the physical and chemical properties of materials. The changes of samples weight associated with changes in temperature and time. The sensor in the machine accurately records the weight as a function of increasing temperature or as a function of time, drawing a continuous line to identify weight loss processes in relation to the chemical reactions occurring. In the TGA, air is used to reactivate with the samples; or noble gases are employed to prevent the reaction between samples and air. TGA is able to provide the information about the vaporization, sublimation, absorption, adsorption, chemisorptions, desolvation, decomposition and solid-gas reactions. In this project, a TGA instrument (Figure 3-14) was utilized to do the thermogravimetric analysis.

3.2.5. Brunauer-Emmett-Teller (BET) Surface Area and Barrett-Joyner-Halenda (BJH) Pore Size and Volume Analysis

The surface area, pore size and pore volume of the as-prepared materials can be analysed by Brunauer-Emmett-Teller (BET) and Barrett-Joyner-Halenda (BJH). BET analysis measures adsorption of gas molecules on the external area and pore area of the materials



Figure 3-15 A TriStar II Surface Area Analyzer.

to determine the total specific surface area in $\text{m}^2 \text{g}^{-1}$ by nitrogen multilayer adsorption isotherms. The uniform pore size of the electrode material plays a critical role in the electrochemical performance of the electrode. Therefore, researchers employ BJH analysis to characterize pore size distribution of the samples. The nitrogen adsorption and desorption isotherms obtained from a surface area analyzer as shown in Figure 3-15 are able to provide the information about the BET surface area and BJH pore size distribution.

3.3. Electrode fabrication and electrochemical characterization

3.3.1. Electrode fabrication

In this PHD project, there are two major types of electrode materials: free-standing foams and metal oxide/graphene composite powder. If the active materials are graphene-based

nanocomposites, they will be mixed with carbon black and PVdF powders. All of them were pre-weighed before mixing them together. The ratio among active material, carbon black and PVdF are 80:15:5. The three ingredients were mixed together by grinding in a mortar, followed by adding a small volume of NMP to form slurry. The slurry was pasted on platinum foils for a three-electrode test system in an aqueous electrolyte. The three-electrode test system consisted of the working electrode, a counter electrode which was usually platinum foil, and a reference electrode (saturated calomel electrode, SCE or AgCl). After assembling, the three-electrode system was left about one hour before the electrochemical testing.

3.3.2. Electrochemical testing

The as-prepared electrodes were electrochemically tested in the three-electrode system for the studies of the electrochemical properties of the active materials. The electrochemical testing involved cyclic voltammetry, galvanostatic charge/discharge, electrochemical impedance spectroscopy and cycling testing.

3.3.2.1. Cyclic voltammetry (CV)

CV is one of the techniques used to test the performance of prepared materials based on potential dynamic electrochemical measurement. In a CV test a potential ramped linearly versus time is added on the working electrode. When the potential reaches the set value, it is ramped in the opposite direction to return to the initial potential at the same sweep rate. In one CV cycle, the active material will be experienced reduction and oxidization. During the process of reduction and oxidization, a couple of redox peaks will be reveal by the CV curve. The cycle of potential sweeping may be repeated several times to thousands of times. The current which flowed through the working electrode is recorded



Figure 3-16 An electrochemistry workstation (CHI660D model).

and plotted versus the applied voltage. The redox peak potentials shown in CV curves are able to reveal the reaction occurring on the working electrode when the potential changes, which contributes to the further investigation of the energy storage mechanism involved in the reaction. The specific capacitance of the active material can also be calculated based on the CV curves.

The equation represents the area under the current-potential curve which is divided by the sweep rate ν , the mass of the active material of the electrode m , and the potential window V_a-V_b . In the research project, an electrochemistry workstation (CHI660D) (Figure 3-16) was used to conduct the CV tests.

3.3.2.2. Galvanostatic Charge/Discharge (DC)

Galvanostatic Charge/Discharge (DC) is another type of electrochemical measurement for battery and supercapacitor. In the DC testing, a constant current is applied on the working electrode. DC tests are able to provide the electrochemical information through the DC profiles. It also can reveal the columbic efficiency, cycleability and conductivity

of the electrode. All the DC tests of the as-prepared material in this project were conducted on the same electrochemistry workstation (CHI660D).

3.3.2.3. Electrochemical Impedance Spectroscopy

Electrochemical Impedance Spectroscopy (EIS) employs different frequencies to characterize the electrochemical dynamic of an electrode. The use of EIS supercapacitors is able to provide an estimation of the internal resistance (electrolyte resistance and charge-transfer resistance) at an open circuit potential. The supercapacitor has both resistor elements which will consume energy and the capacitor elements which store energy. EIS therefore contributes to the study of the internal electrochemical process.

3.4. Summary

Following Chapter 2, the synthesis methods of supercapacitor were presented. Next the physics and morphologies characterization technologies were introduced. Finally, electrode fabrication and electrochemical characterization which were used in this PhD project were presented.

Chapter 4. Synthesis and Characterization of Vanadium Oxide Nanotubes as Electrode Materials for Electrochemical Capacitors

4.1. Introduction

The supercapacitor with only electrochemical double layer capacitor (EDLC) mechanism is limited by its energy density. There is an urgent need to develop novel supercapacitor electrodes with improved high-energy and remained high-power properties. The transition metal oxide nanomaterials may offer unique benefits for such applications. Among broadly available transition metal oxides, vanadium oxide is one of the most promising ion insertion materials. Vanadium oxide is abundant, relatively inexpensive (\$12 per kg), and exhibits a layered structure and offers a broad range of oxidation states enabling redox reactions suitable for supercapacitor operation.⁷¹ V^{5+} can be easily reduced leading to mixed valence vanadium oxides in which both V^{5+} and V^{4+} and even V^{3+} ions are observed.⁸¹ Currently, a few vanadium oxide nanostructures have been investigated; for example, vanadium oxide nanotubes,^{81, 147, 184-186} nanofibre sheet,¹⁴² porous vanadium pentoxide,¹⁴⁴ powders,¹⁸⁷ mesoporous vanadium oxide,¹⁸⁸ macroporous vanadium foam,^{189, 190} porous nanobelt.¹⁹¹ However, few investigations related to using vanadium oxide as the electrode for electrochemical capacitors have been undertaken recently.^{144, 187, 192} For example, amorphous $V_2O_5 \cdot H_2O$ ¹⁹² was prepared by the reaction of metallic vanadium with a hydrogen peroxide solution, which achieved a high rate of discharge. Ravinder *et al.* synthesized porous structured vanadium oxide by the sol-gel method.¹⁴⁴ The materials showed a good capacitance curve of CV in an aqueous KCl electrolyte. They reported a high specific capacitance at a scan rate of 5 mV s⁻¹ in 2 M

KCl electrolyte. However, specific capacitance faded rapidly over in 2 M KCl at a 50 mV s⁻¹ scan rate. With a different precursor, Lao *et al.* fabricated vanadium pentoxide powders with enhanced surface area which is 41 m² g⁻¹.¹⁸⁷

In this project, we report an effective hydrothermal method to prepare vanadium oxide nanotubes. The preparation involved dissolution of V₂O₅ into H₂O₂ and high-speed stirring (10000 r min⁻¹) with hexadecylamine. The product was characterized by scanning electron microscopy, transmission electron microscope, X-ray diffraction and thermogravimetric analysis. Its physical and electrochemical properties used as the electrode materials for electrochemical capacitors are systematically investigated. The electrochemical properties of the materials as electrodes for electrochemical capacitors were evaluated by cyclic voltammetry in a three electrode system consisting of a saturated calomel electrode as reference electrode, platinum as a counter electrode and the active materials as the working electrode. A high capacitance of 148.5 F g⁻¹ was obtained at a scan rate of 2 mV s⁻¹ in 2 M KCl. The electrode maintained a high capacitance of 105 F g⁻¹ at a higher scan rate of 50 mV s⁻¹ in 2 M KCl electrolyte.

The results demonstrate that the as-prepared materials with nanotubes morphology can utilized the electrolyte effectively which is of benefit to quick charging and discharging.

4.2. Experimental

Commercial vanadium pentoxide (V₂O₅) and hydrogen peroxide (H₂O₂) were used as the starting materials to prepare the vanadium oxide nanotubes. Unlike the previous methods, 200 mg vanadium oxide was firstly added into 10 ml distilled water with vigorous stirring. After 6 hours vigorous stirring, 10 ml 30% hydrogen peroxide was added into the orange solution. The hydrogen peroxide should be slowly mixed with the vanadium oxide

solution due to the highly exothermic reaction. With the decomposition of hydrogen peroxide, the oxygen gas bubbles can be observed during the process. After approximately 2 hours, the color of the solution changed to dark red with slow release of oxygen. It was left to stir for 24 hours and followed by a vigorous stirring at 11000 rpm for 30 minutes. Next 270 mg hexadecylamine was added into the solution with stirring at 11000 rpm for 30mins. Finally, all the solution was transferred to a Teflon-lined autoclave and kept at 180°C for 6 days. After the hydrothermal treatment, the color of the materials changed to black which resulted from a slight reduction of vanadium(V) to vanadium(IV) during the hydrothermal reaction.¹⁹³ The black materials were washed with distilled water and ethanol several times, and dried under vacuum condition at 80°C for 12 hours.

The as-prepared materials were characterized by X-ray diffraction by using a Siemens D5000 X-ray diffractionmeter with Cu K α radiation with 2θ ranging from 10° to 80°. The morphology and crystal structures were characterized by field-emission scanning electron microscopy (FE-SEM, JSM-6700F), and transmission electron microscopy/selected area electron diffraction (TEM/SAED, JEOL JEM-200CX) equipped with an energy-dispersive X-ray spectrometer (EDX). The electrodes were fabricated by mixing the 80 wt% as-prepared materials, 15 wt% acetylene carbon black and 5 wt% polyvinylidene difluoride (PVDF) in the presence of N-methyl pyrrolidinone (NMP). The resulting slurry mixture was pasted onto platinum foil substrates, and then heated at 80°C under vacuum for 12 hours. Electrochemical measurements were carried out using three-electrode cells with platinum as the counter electrode and a saturated calomel electrode (SCE) as the reference electrode. Cyclic voltammetry (CV) measurements were carried out on a CHI 660C electrochemistry workstation in 2 M KCl, 2 M LiCl and 2 M NaCl electrolyte with the scan rates of 2 mV s⁻¹, 5 mV s⁻¹, 10 mV s⁻¹, 20 mV s⁻¹, and 50 mV s⁻¹, respectively.

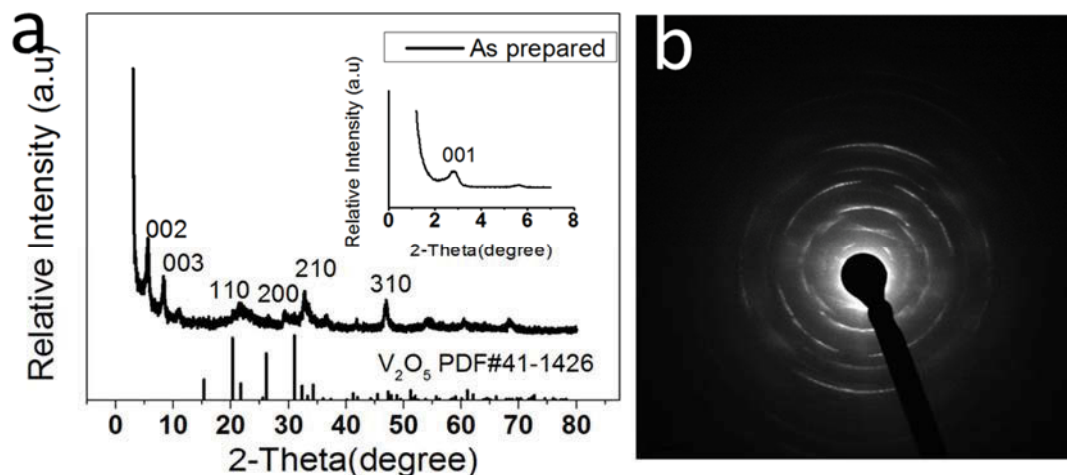


Figure 4-1 XRD pattern of the as-prepared nanotube with the standard V_2O_5 pattern, (b) Schematic depiction of the nanoribbon structure.

4.3. Results and discussion

As shown in Figure 4-1 (a), the XRD pattern of the as-prepared materials after heating at 80 °C under vacuum condition exhibited three peaks with $00l$ series at the low scan angle. The $00l$ series of peaks reflect the layered structure with a preferred orientation of the materials.¹⁸⁹ In the inset figure of Figure 4-1 (a), the first $00l$ peak at around 2.8 degree indicated a basal distance $d_{001}=3.2$ nm which implies that the long chain alkylamines have intercalated into the vanadium oxide layers. In the layered structure of vanadium oxide, the alkylammonium ions are perpendicular to V_2O_5 layers.¹⁹⁴ Also, the $hk0$ series of peaks with lower intensity correspond to the two dimensional structure of the layered vanadium oxide.¹⁸⁴ Compared with Wörle's results,¹⁹⁵ we obtained the similar XRD pattern, as shown in Figure 4-1 (a) and selective area electron diffraction (SAED) Figure 4-1 (b). It indicates the as-prepared materials have parallel sheets of VO_5 square pyramids connecting via VO_4 tetrahedra. The amine molecules intercalate into the space of the vanadate layers.

The morphological features are revealed by the SEM images of the as-fabricated materials.

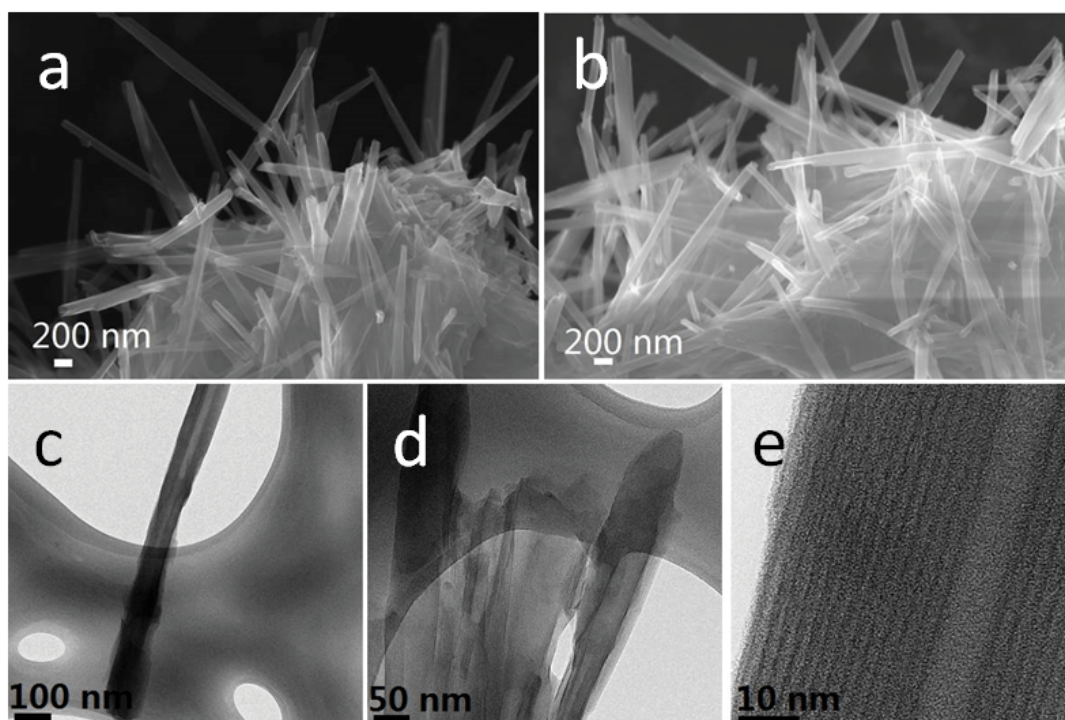


Figure 4-2 The uniform vanadium oxide nanotubes was demonstrated by SEM images (a and b); The detailed information about the nanotubes were shown in the TEM images (c-e).

Figure 4-2 (a) clearly shows that the materials consist of uniform vanadium oxide nanotubes. The vanadium oxide nanotubes have a length of from 5 micrometers to several tens of micrometres. Some of the nanotubes are isolated, and others grow together as is also revealed by the Figure 4-2 (b). In addition, the TEM image (Figure 4-2 (c)) confirms that the nanotubes have an open-ended cylindrical shape. As shown by Figure 4-2 (d), some of the nanotubes stack together, but they still maintain the nanotube morphology with open-ended structure. The TEM image in Figure 4-2 (e) illustrates the nanotubes have internal diameters between 6 to 10 nm and the external tube diameters are from 60 to 100 nm, with the tube wall thickness around 10 to 30 nm.

The electrochemical properties of the vanadium oxide nanotubes were evaluated by cyclic voltammogram (CV) measurements at various scan rates in different electrolytes. Figure 4-3 (a) depicts the CV profiles of the vanadium oxide nanotubes at scan rate of 2 mV s^{-1} ,

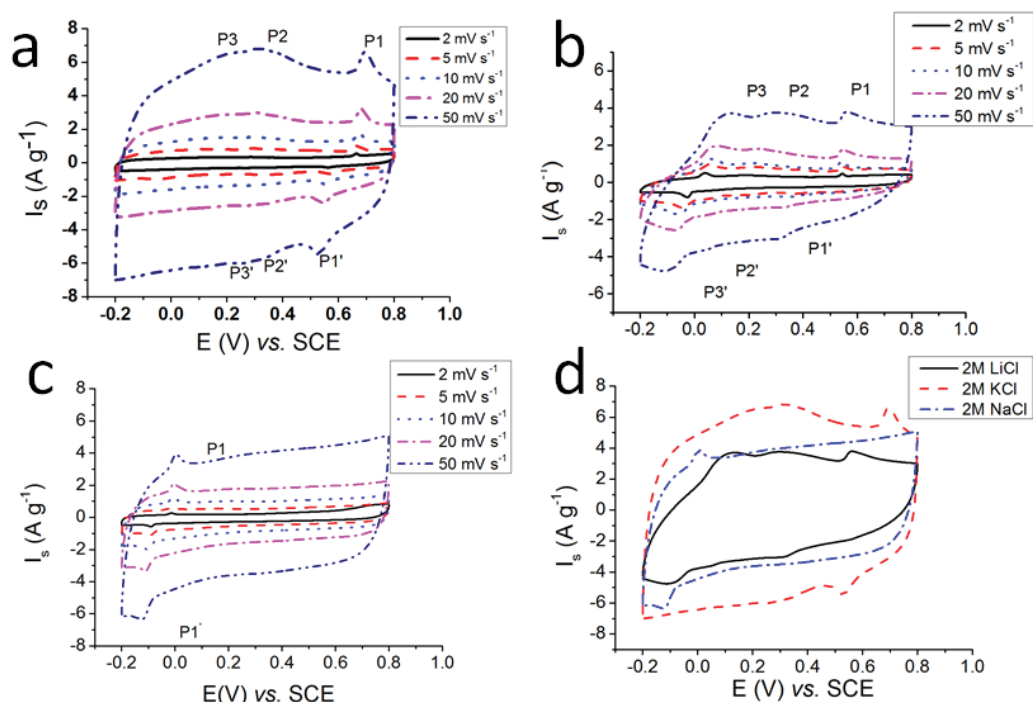


Figure 4-3 Cyclic voltametric curves of the vanadium oxide nanotubes (a) in 2 M KCl, (b) in 2 M LiCl and (c) in 2 M NaCl at the scan rates of 2 mV s⁻¹, 5 mV s⁻¹, 10 mV s⁻¹, 20 mV s⁻¹, and 50 mV s⁻¹. (d) Comparison of CV curves in 2 M KCl, 2 M LiCl and 2 M NaCl at the scan rate of 50 mV s⁻¹.

5

mV s⁻¹, 10 mV s⁻¹, 20 mV s⁻¹ and 50 mV s⁻¹ in 2 M KCl electrolyte. The CV curves show a nearly rectangular shape which means the nanotube materials have good conductivity and good charge propagation within the electrodes.¹²⁵ The as-prepared vanadium oxide nanotubes, even at scan rate of 50 mV s⁻¹, still maintained the rectangular shape with a few variances in the specific capacitance. The intercalation process of the ions (Li⁺, Na⁺ and K⁺) into vanadium oxide can be expressed as



where M stands for the ions of Li⁺, Na⁺ or K⁺), and the x is the mole fraction of intercalated Ions.^{196, 197} As shown in Fig.3a, two pair of obvious oxidation/reduction peaks (P1/P1' and P2/P2') and a pair of small oxidation/reduction peaks (P3/P3') are observed in the CV curves at the five different scan rates, indicating the ion insertion/deinsertion kinetics.¹⁹⁷

The CV curves of the vanadium oxide nanotubes in 2 M LiCl electrolyte are presented in Figure 4-3 (b). The curves also exhibits three pairs of oxidation/reduction peaks as shown in Figure 4-3 (b). However, LiCl electrolyte obviously has degraded the CV rectangle shape and the electrode exhibits less conductivity than that of electrodes in 2 M KCl. In 2 M NaCl electrolyte, the materials have different CV curves (Figure 4-3 (c)). It has better rectangle CV shape than the electrolytes of 2 M LiCl, but worse than that of 2 M KCl. The CV curves of vanadium oxide nanotubes in 2 M KCl, 2 M NaCl and 2 M LiCl at 50 mV s⁻¹ are given in Figure 4-3 (d). In contrast to 2 M KCl electrolyte, the curves shape of the materials in 2 M NaCl and 2 M LiCl are not an ideal rectangle. It means lithium ion has lower diffusion speed into the electrode than the potassium ion, although the size of the potassium ion is larger than that of the lithium ion.

According to the CV testing, the specific capacitances of the electrodes were reported by integrating over the full CV curves to determine voltammetric charge. The specific capacitances were calculated on the basis of equation

$$C = Q / 2vm\Delta E \quad (5-2)$$

where Q is the voltammetric charge obtained by integrating the CV curve, v is the scan rate, m is the active mass of the electrode materials and ΔE is the width of the potential window. The specific capacitances of the vanadium oxide nanotubes in 2 M KCl and 2 M NaCl at different scan rates are presented in Figure 4-4. As is evident from the data, vanadium oxide nanotubes yield the highest specific capacitance in 2 M KCl electrolyte. A high specific capacitance of 148.5 F g⁻¹ was achieved for the vanadium oxide nanotubes at a 2 mV s⁻¹ scan rate in 2 M KCl electrolyte. Even though the vanadium oxide nanotubes achieved a higher specific capacitance of 152 F g⁻¹ in 2 M LiCl electrolyte, the specific capacitance and the shape of the CV curves degraded significantly

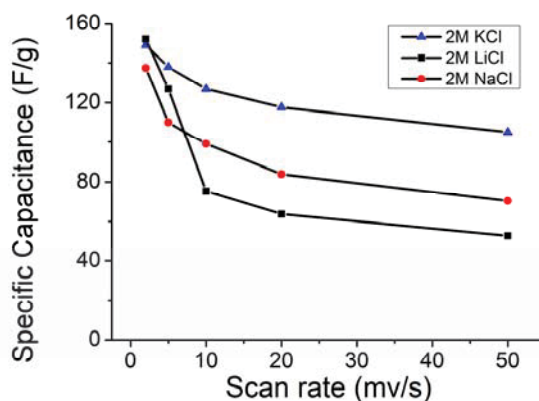


Figure 4-4 Measured capacitance of vanadium oxide nanotubes in 2 M KCl, 2 M LiCl and 2 M NaCl at the scan rates of 2 mV s⁻¹, 5 mV s⁻¹, 10 mV s⁻¹, 20 mV s⁻¹, and 50 mV s⁻¹.

with the increase of the scan rates. When the voltage scan rate reaches to 50 mV s⁻¹ from 2 mV s⁻¹, the specific capacitance dropped by around 100 F g⁻¹. In contrast to 2 M LiCl, there was just only a drop of 43 F g⁻¹ in 2 M KCl electrolyte. It still remained a specific capacitance of 105 F g⁻¹ and an ideally rectangle shape, even at a scan rate of 50 mV s⁻¹. It indicates a better charge propagation in KCl electrolyte than LiCl electrolyte.

4.4. Summary

Vanadium oxide nanotubes were prepared using a hydrothermal method with the assistance of high-speed stirring. The materials show a nearly rectangular shape of CV curve, indicating good conductivity and good charge propagation within the electrodes. It also demonstrated three pairs of redox peaks in the CV curves. A high specific capacitance of 148.5 F g⁻¹ at scan rate of 2 mV s⁻¹ and the minor decreases of specific capacitance with the increase of scan rates were achieved in 2 M KCl electrolyte. The higher specific capacitances of the as-prepared vanadium oxide nanotubes can be explained in term of the nanotubes structure and the redox property of the fabricated materials.

Chapter 5. High-Specific-Capacitance Supercapacitor Based on Vanadium Oxide Nanoribbon

5.1. Introduction

With increased climate change like global warming, more research concerns have been focused on minimizing the exhaust of carbon dioxide. These concerns have led to the proliferation of electricity generation using both smart grid and distributed renewable energy resources, such as wind, solar, and tidal. However, the intermittent nature of these renewable resources raises issues with system stability, power efficiency, and electricity quality. Energy storage systems with high energy density, fast response and high power capacity are needed for compensation of fluctuating output from renewable energy.^{198, 199} Flywheel energy storage systems,^{200, 201} superconducting magnetic energy systems^{202, 203} and compressed air energy storage^{204, 205} are able to provide high energy capacity for the storage of renewable energy resources. However, there are some drawbacks in these energy storage systems. One of them is the large scale that requires large space to set up the facilities. The complex structure also means a long construction period and high capital cost. On the other hand, supercapacitors, also known as electrochemical capacitors, have a longer life time and higher power density than traditional batteries.²⁰⁶ It can be easily assembled to construct a large scale energy storage system with low maintain cost. There are two types of supercapacitors: electrical double layer capacitors (EDLC) and pseudocapacitors.⁴¹ The supercapacitor with only EDLC mechanism is limited by its energy density. Pseudocapacitors have transition metal-oxides electrodes possessing multiple oxidation states/structures that enable rich redox reactions for pseudocapacitance generation.^{86, 207} Among broadly available transition metal oxides, RuO₂ is able to achieve

a specific capacitance as high as 1580 F g^{-1} .⁷⁵ However, the application of a pseudocapacitor based on RuO_2 is limited by the high cost and rareness of Ru resource. Vanadium oxide is relatively inexpensive (about \$12 per kg) because of the abundant resource. It exhibits layered structure and possesses a broad range of oxidation states to enable redox reactions suitable for energy storage.⁷¹ Most of the previous studies just focused on the structures of the vanadium oxide and maximizing the electrolyte contact area.^{144, 187}

In this project, we fabricated vanadium oxide nanoribbon that optimized the ion diffusion path and maintained the electrolyte contact area due to significant length with large contact area. Vanadium oxide nanoribbon was synthesized by a facile and effective hydrothermal treatment with control of the condensation speeds of precursors in the solution along the $\langle 010 \rangle$, $\langle 100 \rangle$ and $\langle 001 \rangle$ directions. The synthesis involved dissolution of V_2O_5 into H_2O_2 , and investigation of the precursor weight ratio and the hydrothermal time. The product was characterized by using scanning electron microscopy, transmission electron microscope and X-ray. The electrochemical properties of the material as the electrode of the electrochemical capacitor were evaluated by cyclic voltammetry in a three electrode system consisting of a saturated calomel electrode as reference electrode, platinum as a counter electrode and the active material as the working electrode. As far as we know, it is for the first time that the fabrication of vanadium oxide nanoribbon by using the hydrothermal method has been reported. The prepared nanoribbon structure possesses relative short width and significant length. The narrow nanoribbon with ultra-length optimizes the ion diffusion path thereby enhancing the specific capacitance. A high capacitance of 453 F g^{-1} was obtained at the scan rate of 2 mV s^{-1} in 2 M NaCl electrolyte; it still maintained a high capacitance of 201 F g^{-1} at a higher scan rate of 50 mV s^{-1} . Also the nanoribbon exhibits faster ion propagation and better

conductivity than the nanotube as revealed by the immediate current response to the potentials applied on the electrode. The electrochemical performances of the vanadium oxide were found to strongly depend on the nanostructures and electrolytes.

As is known, the fabrication of vanadium oxide nanostructure involves the condensation of vanadium species in the aqueous solution. There are two main reactions in the condensation process: olation and oxolation. Both involve the nucleophilic addition of negatively charged OH^- groups onto positive charged vanadium cations V^{3+} . Consequently, it requires the condensation of V-OH groups. During the condensation, the olation reaction is kinetically faster than that of oxolation because the labile water molecules are already formed in the olation process.⁸¹ Therefore, the $\langle 010 \rangle$ is the fastest growth direction and $\langle 001 \rangle$ the slowest due to the weak c-axis bonding.²⁰⁸ In this project, we try to fabricate the ultralong vanadium oxide nanoribbon with a relative narrow width by this formation mechanism. The hydrothermal reaction time and the weight ratio relative to which as used in the fabrication of vanadium oxide nanotube were reduced to synthesize the ultralong vanadium oxide nanoribbon with controlled width. The nanoribbon structure of vanadium oxide achieved higher specific capacitance attributing to the easy ion insertion and electronic transport along the a-b plane rather through the layers of the c-axis.^{208, 209} As far as we know, it is the first time to report the fabrication of vanadium oxide nanoribbon by using the hydrothermal method which is facile and effective.

5.2. Experimental

To prepare the vanadium oxide nanoribbon, commercial vanadium pentoxide (V_2O_5) was dissolved in the hydrogen peroxide (H_2O_2). First of all, 10 ml distilled water was slowly added in to 200 mg V_2O_5 with stirring. A solution with orange color, in which the

vanadium pentoxide was slightly dissolved and uniformly dispersed, was obtained after 6 hour vigorous stirring. Then, 10ml 30% hydrogen peroxide was added into the orange solution. There was a highly exothermic reaction. After approximately 2 hours, the color of the solution changed to dark red. It was left to stir for 1 day and followed by a vigorous stirring at 11000 rpm for 30 minutes. Then, 200 mg hexadecylamine was added into the solution with stirring at 11000 rpm for 30 minutes. Finally, the solution was transferred to the Teflon-lined autoclave and heated under hydrothermal condition at 180 °C for 4 days. Due to the slight reduction of vanadium (V) to vanadium (IV) during the hydrothermal reaction,¹⁹³ the color of the two materials after hydrothermal treatment changed to be black. The as-prepared black materials were washed with distilled water and ethanol several times, and dried under vacuum condition at 80 °C for 12 hours.

The as-prepared materials were characterized by X-ray diffraction by using a Siemens D5000 X-ray diffractionmeter with Cu K α radiation with 2θ ranging from 10° to 80°. The morphology and crystal structures were characterized by field-emission scanning electron microscopy (FE-SEM, JSM-6700F), and transmission electron microscopy/selected area electron diffraction (TEM/SAED, JEOL JEM-200CX) equipped with an energy-dispersive X-ray spectrometer (EDX). Electrodes for electrochemical measurement were fabricated by mixing the 80 wt% prepared materials, 15 wt% acetylene carbon black and 5 wt% polyvinylidene difluoride (PVDF) in the presence of N-methyl pyrrolidinone (NMP). The resulting slurry mixture was pasted onto platinum foil substrates for three-electrode cell measurement, and then heated at 80 °C under vacuum for 12 hours. The cyclic voltammograms (CV) measurement was performed over the potential voltage from -0.2 V to 0.8 V in 2 M KCl and 2 M NaCl electrolyte with the scan rates of 2 mV s⁻¹, 5 mV s⁻¹, 10 mV s⁻¹, 20 mV s⁻¹, and 50 mV s⁻¹, respectively.

5.3. Results and discussion

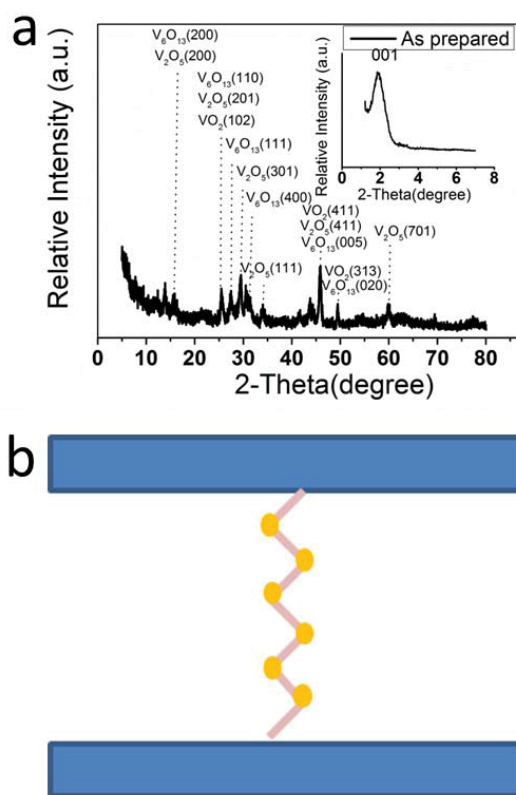


Figure 5-1 (a) XRD pattern of the as-prepared nanoribbon with the standard V₂O₅ pattern, (b) Schematic depiction of the nanoribbon structure.

XRD pattern of the vanadium oxide nanoribbon were shown in Figure 5-1 (a). In the inset figure, an intensive peak located at the low scanning angle around 2 degree is related to space between the vanadium layers. The *00l* peak indicated a basal distance around $d_{00l}=4.5$ nm which is approximately equal to the length of the long chain alkylamines. It means the alkylamines chain has intercalated into the vanadium oxide layers which is almost perpendicular to layers.¹⁹⁴ And the *hk0* series of peaks with lower intensity correspond to the two dimensional structure of the layered vanadium oxide.¹⁸⁴ It indicates the as-prepared material has the nanoribbon structure as shown in Figure 5-1 (b). The nanoribbon consists of parallel sheets of vanadium oxide. The amine molecules intercalate into the space of the vanadate layers. The XRD measurements of the as-

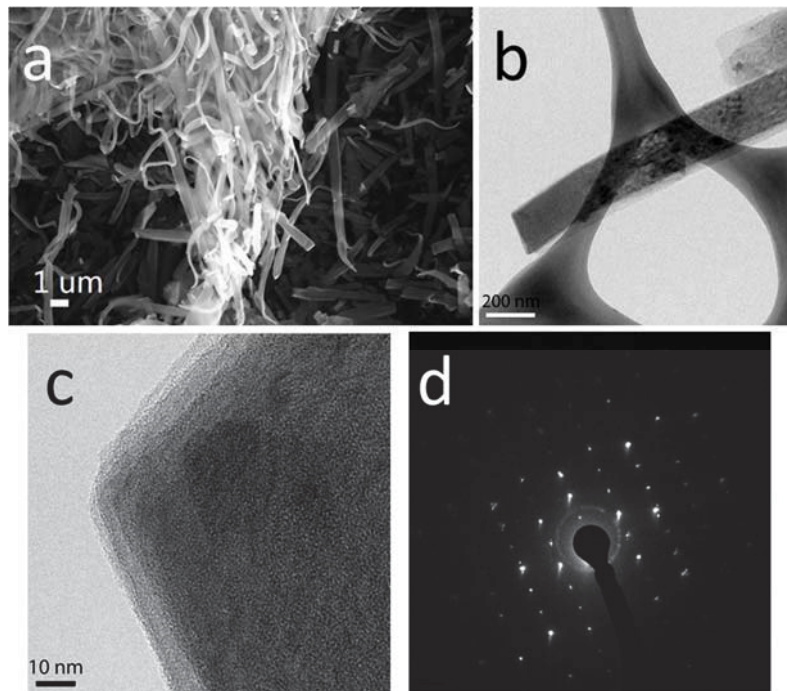


Figure 5-2 (a) SEM images of nanoribbon, (b, c) low- and high-magnification TEM images, respectively. (d) selected area electron diffraction (SAED).

prepared materials shows nano-crystalline feature, but the spectral positions of the reflections correspond to different phases as shown in the Figure 5-1 (a). Mixed valence vanadium oxides with V^{5+} , V^{4+} and V^{3+} even V^{2+} were usually observed in the vanadium materials, leading to different phases.⁷¹ The XRD pattern of the as-prepared materials suggests the presence of the common vanadium phases VO, V_2O_3 , VO_2 , V_2O_5 and V_6O_{13} as shown in the Figure 5-1 (a).

The surface morphological feature of the as-fabricated materials is revealed by the SEM and TEM images. Figure 5-2 (a) clearly demonstrates that the material consists of uniform nanoribbon structure. The low-magnification SEM of the material shows the nanoribbons entangle with each other with a paper-like feature indicating a flexible character of the materials. The TEM image in Figure 5-2 (b) illustrates these nanoribbons are 150 nm to 200 nm in width, and with lengths up to 50 μm (Figure 5-2 (a)). The layered structure of the nanoribbon is revealed by the high-magnificent TEM image (Figure 5-2 (c)). It has

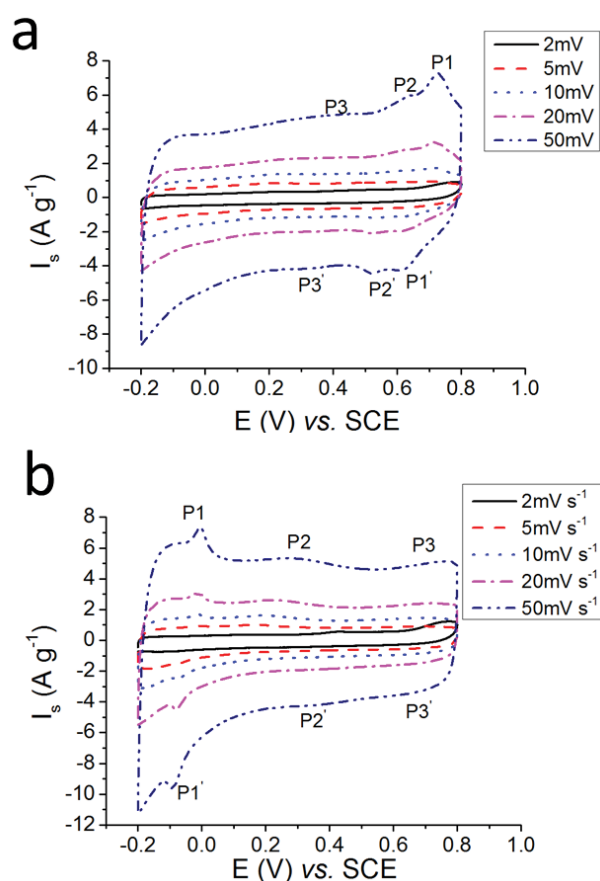


Figure 5-3 Cyclic voltametric curves of the vanadium oxide nanoribbon (a) in 2M KCl (b) in 2M NaCl, nanotube at the scan rates of 2 mV s^{-1} , 5 mV s^{-1} , 10 mV s^{-1} , 20 mV s^{-1} , and 50 mV s^{-1} .

several layers consisting of the vanadium oxide layer. The edge of some of the nanoribbons shows one-layer structure. The selected area electron diffraction (SAED) (Figure 5-2(d)) also confirms that the nanoribbons have nano-crystalline property.

The electrochemical properties of the vanadium oxide nanoribbon were evaluated by CV measurements at various scan rates in different electrolytes. Figure 5-3 (a) depicts the CV profiles of the vanadium oxide nanoribbon at scan rate of 2 mV s^{-1} , 5 mV s^{-1} , 10 mV s^{-1} , 20 mV s^{-1} , and 50 mV s^{-1} in 2M KCl electrolyte. The CV curve shows a nearly rectangular shape which indicates good conductivity and good charge propagation within the electrodes.¹²⁵ The vanadium oxide nanoribbon maintained the rectangular shape with a few variances in the specific capacitance at a high scan rate of 50 mV s^{-1} . The good

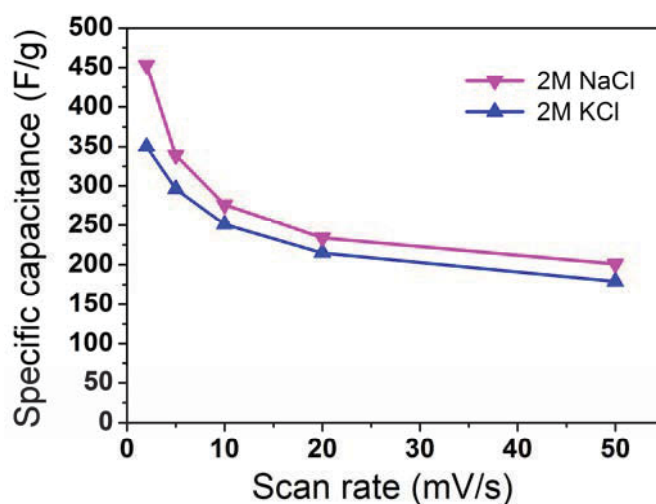


Figure 5-4 The specific capacitance of vanadium oxide nanoribbon in 2M KCl, 2M NaCl at the scan rates of 2 mV s⁻¹, 5 mV s⁻¹, 10 mV s⁻¹, 20 mV s⁻¹, 50 mV s⁻¹.

electrochemical performance is attributed to the nanoribbon structure and high reactivity of vanadium oxide for the energy storage of the as-prepared material. As shown in Figure 5-3 (a), two pairs of obvious oxidation/reduction peaks (P1/P1' and P2/P2') and a pair of small oxidation/reduction peaks (P3/P3') were observed in the CV curve at five different scan rates. The CV curves of the vanadium oxide nanoribbon in 2M NaCl electrolyte are presented in Figure 5-3 (b). In 2M NaCl electrolyte, the material shows different CV curves, indicating faster ion diffusion. The CV curves display nearly rectangular shape with three pairs of redox peaks even at very high scan rates. It indicates supercapacitor features of fast charging and discharging.

The specific capacitances of the vanadium oxide nanoribbon in 2M KCl and 2M NaCl at different scan rates are presented in Figure 5-4. As is evident from the data, vanadium oxide nanoribbon yields the higher specific capacitance in 2 M NaCl electrolyte. It achieved a very high specific capacitance of 453 F g⁻¹ at the scan rate of 2 mV s⁻¹ in 2 M NaCl electrolyte. In addition, a specific capacitance of 350 F g⁻¹ was obtained in 2M KCl electrolyte at the scan rate of 2 mV s⁻¹. The specific capacitances of vanadium oxide

Table 5-1 Comparison of the specific capacitance value of as-prepared vanadium oxide nanoribbon with the reported studies in different electrolyte at the scan rate of 5 mV s⁻¹

Nanostructures	Electrolyte	Specific capacitance(F/g)
Nanoribbon	2M NaCl	339
Nanoribbon	2M KCl	296
Porous structure [15]	2M KCl	214
Porous structure [15]	2M LiCl	122
Porous structure [15]	2M NaCl	114
Powder [16]	2M KCl	262
Powder [16]	2M NaCl	166
Powder [16]	2M LiCl	160

nanostructures in different electrolytes are compared in Table 5-1 with the value of the previous studies. Our material achieved the highest specific capacitance of 339 F g⁻¹ at scan rate of 5 mV s⁻¹ in 2M NaCl electrolyte. It is confirmed that the nanoribbon structure of vanadium oxide achieved higher specific capacitance which is attributed to the easy ion insertion and electronic transport along *a-b* plane rather through the layers of the *c*-axis. The nanoribbon structure shortens the ion diffusion path and exploits efficiently the electrode for energy storage.

5.4. Summary

The synthesis mechanism, morphologies and electrochemical features of vanadium oxide nanoribbon were investigated. The weight ratio of the precursor and the hydrothermal reaction time have a straight correlation between the molecular types in the solution and the solid structure. Both of them play a crucial role in condensation speed of precursors along the <010>, <100> and <001> directions. Through investigating the weight ratio of the precursor and the hydrothermal reaction time, we achieved the controlling of the growth speed in three dimensions: fastest growth in <010> direction, relative slow growth

in $\langle 100 \rangle$ and $\langle 001 \rangle$ directions, resulting in the nanoribbon structure possessing a relative short width and significant length. The narrow ribbon with ultra-length optimizes the ion diffusion path thereby enhancing the specific capacitance. The nanoribbon exhibits faster ion propagation than nanotube revealed by the immediate current response to the potentials applied on the electrode. It even has faster charging speed than the carbon-based electrodes. The measured results confirmed that the higher capacitance of 453 F g^{-1} was achieved by the nanoribbon than that of nanotube.

Chapter 6. 3D Mesoporous Hybrid NiCo₂O₄@graphene Nanoarchitectures as Electrode Materials for Supercapacitors with Enhanced Performances

6.1. Introduction

Supercapacitor, also known as ultracapacitor, is a prevailing energy storage device, which has been intensively investigated. It possesses higher energy density than traditional electrolytic capacitors, and has much higher power density than rechargeable batteries. There are two types of supercapacitors, with each using different energy storage mechanisms: electrochemical double layer capacitors (EDLC) ^{64, 128, 210-212} and pseudocapacitors.²¹³⁻²¹⁷ The EDLCs store energy in the electrostatic field, which is between electrode active materials and the electrolyte. Pseudocapacitors mainly rely on fast and reversible redox reactions. Transition metal oxides are usually employed as electrode materials for pseudocapacitors. However, pure transition metal oxides always suffer from low conductivity, resulting in unsatisfactory performances.

It is well recognized that combining conductive materials and transition metal oxides as composites is an effective method to improve the performance of supercapacitors. Graphene, a 2D monolayer of sp²-hybridized carbon atoms, possesses high conductivity, good mechanical strength, and ultra-large specific surface area, making it a suitable candidate as the conductive material.^{64, 135, 218-222} Many transition metal oxides ^{73-75, 77, 99, 223-225} have been investigated as electrode materials for supercapacitors. NiCo₂O₄ is one of the most promising transition metal oxides for pseudocapacitors owing to its intriguing electronic conductivity, low diffusion resistance to protons/cations, and easy electrolyte penetration.⁸⁴⁻⁸⁷ In the crystal structure of NiCo₂O₄, nickel occupies the octahedral sites

and cobalt distributes over both octahedral and tetrahedral sites, in which the solid-state redox couples $\text{Co}^{3+}/\text{Co}^{2+}$ and $\text{Ni}^{3+}/\text{Ni}^{2+}$ are presented.⁸⁴

Many studies focused on the optimization of morphology and incorporating NiCo_2O_4 with conductive materials to obtain high specific capacitance. Wei *et al.* synthesized spinel nickel cobaltite aerogels with a high specific capacitance at the sweep rate of 25 mV s^{-1} .⁸⁶ Yuan *et al.* demonstrated ultrathin mesoporous NiCo_2O_4 nanosheets growing on Ni foam by co-electro-deposition of Ni and Co.⁸⁷ Furthermore, Zhang *et al.* prepared mesoporous NiCo_2O_4 nanosheets on Ni foam, Ti foil, stainless-steel foil and flexible graphite paper,^{88, 89} and nanoneedle arrays on carbon nanofiber,⁸⁵ exhibiting high capacitance and cycling stability. However, most of these are plagued by poor high-rate performances.

In this project, 3D mesoporous hybrid $\text{NiCo}_2\text{O}_4@\text{graphene}$ nanoarchitectures were successfully synthesized by a combination of freeze drying and hydrothermal reaction. Field-emission scanning electron microscopy (FESEM) and TEM analyses revealed that $\text{NiCo}_2\text{O}_4@\text{graphene}$ nanostructures consist of a hierarchical mesoporous sheet-on-sheet nanoarchitecture with a high specific surface area of $194 \text{ m}^2 \text{ g}^{-1}$. Ultrathin NiCo_2O_4 nanosheets, with a thickness of a few nanometers and mesopores ranging from 2 to 5 nm, were wrapped in graphene nanosheets and formed hybrid nanoarchitectures. When applied as electrode materials in supercapacitors, these novel 3D hierarchical porous nanoarchitectures exhibited high specific capacitances and excellent cycling stabilities at high current densities. It exhibited a high capacitance of 778 F g^{-1} at the current density of 1 A g^{-1} , and an excellent cycling performance extending to 10000 cycles at the high current density of 10 A g^{-1} .

6.2. Experimental

6.2.1. Fabrication of graphene – polyurethane (PU) sponges

Graphene oxide (GO) was prepared from natural graphite flakes by a modified Hummers method,²²⁶ and the GO nanosheets were dispersed in 20 mL DI water at the concentration of 2 mg mL⁻¹ by stirring for 12 hours and ultrasonication (Branson 2510) for 2 hours at room temperature. After dispersion, the homogeneous solution in the vial was transferred to a beaker for stable dispersion. This involved adding 80 mg sodium cholate hydrate (SCH) to the mixture and stirring for 2 hours. Hydrazine solution (35 wt% in water, Aldrich) at the weight ratio of 1:7 was subsequently added to the beaker to obtain the reduced graphene oxide (RGO) solution.²²⁷ The polyurethane (PU)-sponge was cleaned several times using distilled water and acetone, completely dried in a vacuum, and then cut into small pieces, with a thickness of 1 mm and a width by length of 2×2 cm². In a glass tube, three PU-sponge pieces were immersed in 20 ml of the mixture solution, under microwave irradiation at 90 °C for 30 mins (pressure: ~8 Bar) in a single mode microwave reactor (Nova, EU Microwave Chemistry). After freeze-drying for 48 hours, the solvent within the material was completely removed, and the RGO-PU-sponges were obtained.

6.2.2. Preparation of NiCo₂O₄ @graphene nanoarchitectures

1 mmol of Ni(NO₃)₂·6H₂O, 2 mmol of Co(NO₃)₂·6H₂O and 4.5 mmol of hexamethylenetetramine were dissolved in 40 mL of DI water to form a transparent pink solution. 10 ml solution was transferred to a Teflon-lined Autoclave, with one piece of graphene-PU-sponge, and then heated under a hydrothermal condition of 90 °C for 12 hours. The as-prepared black materials were washed several times with distilled water and ethanol, and dried under vacuum condition of 80 °C for 12 hours. This was followed

by annealing at 350 °C for 2 hours with a slow heating rate of 1 °C min⁻¹, in order to achieve 3D mesoporous NiCo₂O₄ on large-size graphene hybrid nanostructures. Using the same procedure, the bare NiCo₂O₄ without graphene was also prepared.

6.2.3. Materials characterization

The crystal structure and phase of the as-prepared materials were characterized by X-ray diffraction (XRD) (Siemens D5000 X-ray diffractionmeter) using Cu K α radiation with 2θ ranging from 10° to 80°. The morphology and crystal structures were characterized by field-emission scanning electron microscopy (FE-SEM, JSM-6700F), and transmission electron microscopy/selected area electron diffraction (TEM/SAED, JEOL JEM-200CX) equipped with an energy-dispersive X-ray spectrometer (EDX). N₂ adsorption-desorption measurements were conducted using a 3 Flex surface characterization analyser at 77 K.

6.2.4. Electrochemical testing

To prepare the working electrode, the as-prepared materials (80 wt %), acetylene black (15 wt %), and poly (vinylidene fluoride) (PVDF, 5 wt %) were mixed in N-methyl-2-pyrrolidone (NMP) to form a slurry. The resultant slurry was pasted onto Ni foam (washed by 10 wt% HCl) with a blade, and then dried at 80 °C for 12 hours under vacuum. The nickel foam was cleaned before using as the current collector. It was immersed into acetone for 10 minutes followed by ultra-sonication for 5 minutes. The nickel foam was then cleaned by 0.1 M hydrochloric acid. And then it was washed by plenty of distilled water with ultra-sonication for 5 minutes. Electrochemical measurements were carried out using three-electrode cells, with platinum as the counter electrode and a saturated calomel electrode (SCE) as the reference electrode. Cyclic voltammetry (CV) and galvanostatic

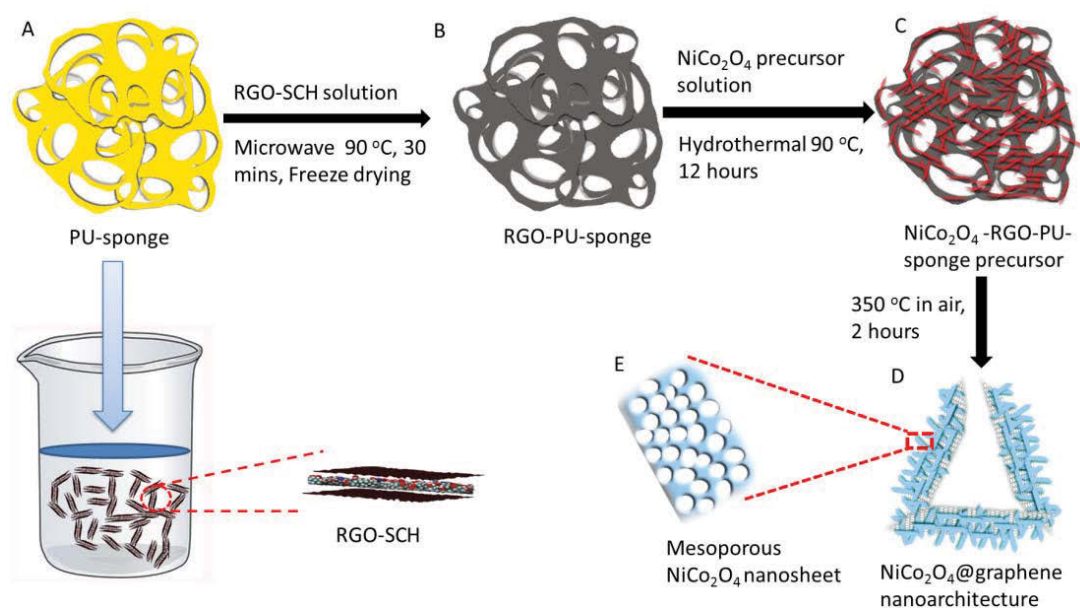


Figure 6-1 Synthesis process of NiCo₂O₄@graphene nanoarchitectures: (A) a piece of PU-sponge and the solution with RGO stabilized using sodium cholate hydrate (SCH); (B) The RGO was coated and anchored onto the PU-sponge assisted by microwave and freeze drying; (C) NiCo₂O₄ precursor nanosheets grown on RGO-PU-sponges; (D) 3D mesoporous hybrid NiCo₂O₄@graphene nanoarchitectures. (E) Crystallized NiCo₂O₄ nanosheets with mesopores.

charge-discharge (CD) was carried out on a CHI 660C electrochemistry workstation using 2.0 M KOH electrolyte. Electrochemical impedance spectroscopy (EIS) measurements were conducted by applying an AC voltage with 1 mV amplitude in a frequency range of 0.01 Hz to 100 kHz at the open circuit potential.

6.3. Results and Discussion

Figure 6-1 illustrates the preparation process for the synthesis of hybrid NiCo₂O₄@graphene nanoarchitectures. In the first step, the commercial PU-sponge was cut into ribbons (Figure 6-1 (A)). The planar amphiphilic surfactant SCH enables the formation of a stable encapsulation layer on each side of the suspended graphene sheets, leading to stable dispersion of graphene in deionized water.^{73, 228-230} Owing to the planar nanosheet structure of graphene and the strong van der Waals force between the PU-sponge and RGO-SCH, the dispersed graphene can be easily and uniformly coated

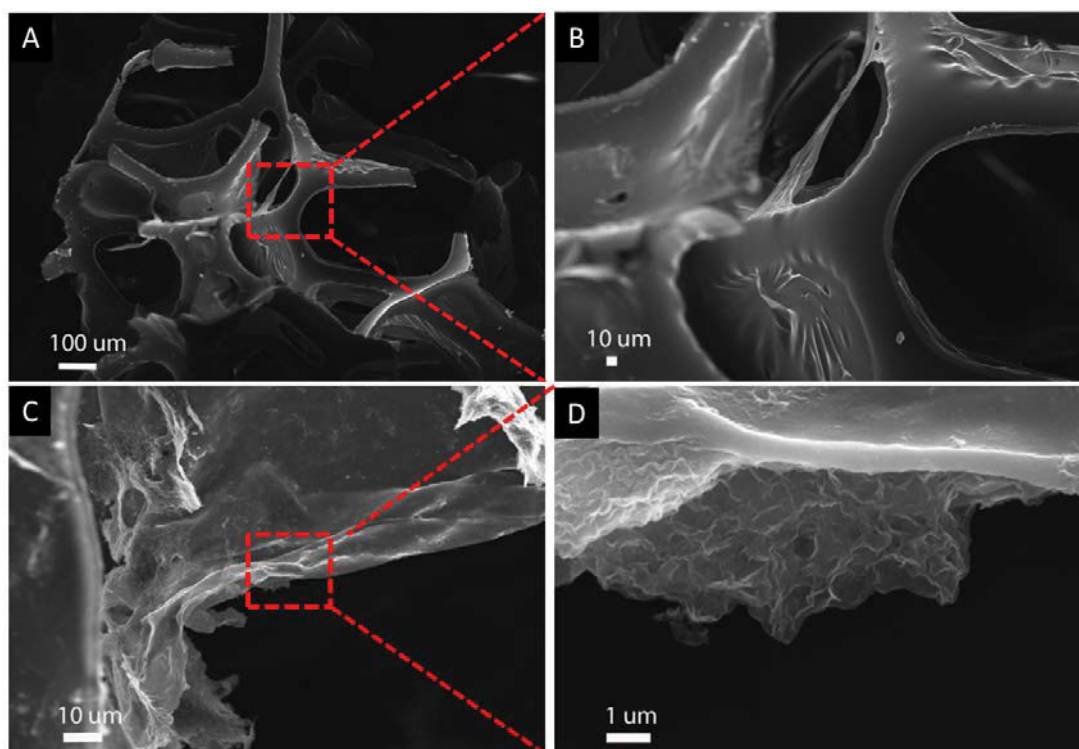


Figure 6-2 The SEM images of the (A, B) PU-sponge, showing macroporous structure; (C, D) RGO-PU-sponge, indicating RGO was coated onto PU-sponge.

onto the surface of the PU-sponge's skeleton by using a microwave-assisted method and a further treatment of freeze drying (Figure 6-1 (B)). The next step was to grow a NiCo_2O_4 precursor onto the RGO-PU-sponge skeleton by the hydrothermal method as shown in Figure 6-1 (C). Hexamethylenetetramine, nickel (II) nitrate hexahydrate crystalline and cobalt (II) nitrate hexahydrate were used to hydrothermally grow NiCo_2O_4 nanosheet precursors on RGO-PU-sponges. The NiCo_2O_4 nanosheet precursors consist of bimetallic (Ni, Co) hydroxide. Upon the annealing treatment (Figure 6-1 (D)), crystallized NiCo_2O_4 nanosheets with mesopores (Figure 6-1 (E)) on large-size graphene sheets were obtained.

The SEM observation identified that the PU-sponge has pore size ranging from 50 μm to 500 μm (Figure 6-2(A) and (B)). After coating with graphene, the PU-sponges preserved the hierarchical macroporous structure. It allows for the flow of the precursor solution into the pores of RGO-PU-sponge, and NiCo_2O_4 nanosheet precursors to grow on the

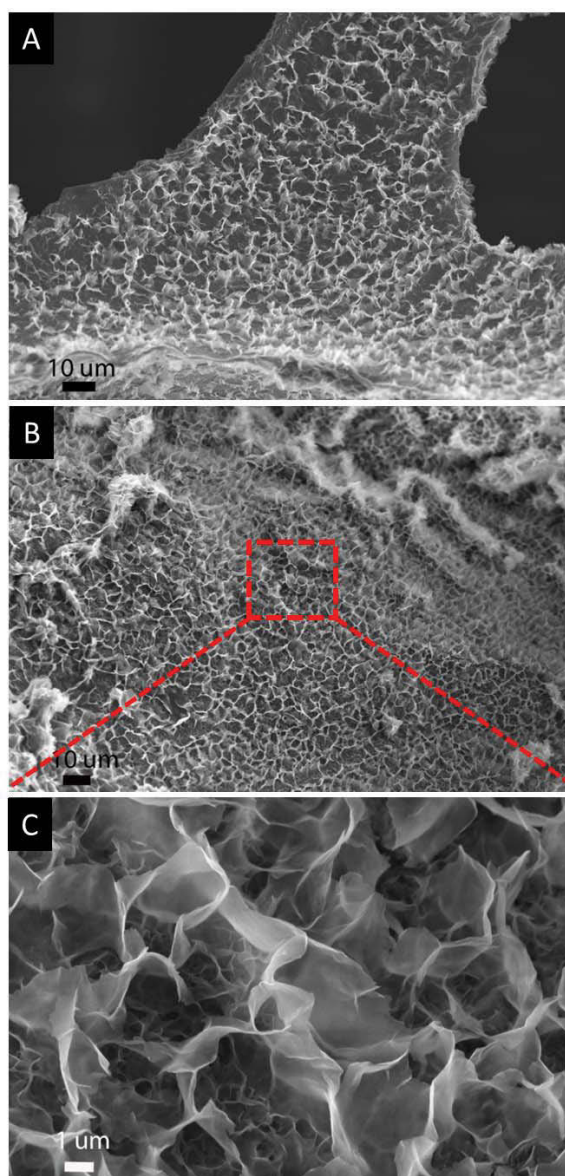


Figure 6-3 SEM images of (A, B) NiCo_2O_4 precursor sheets that grew on the skeleton of RGO-PU-sponge; (C) high magnification SEM image of NiCo_2O_4 precursor with macropores.

surface of the skeleton. The surface of PU-sponges changed from smooth to corrugated after being coated with the RGO (Figure 6-2 (C) and (D)). The SEM observation clearly confirmed that graphene nanosheets have been successfully coated onto the surface of PU-sponges.

SEM images of NiCo_2O_4 -RGO-PU-sponge precursors clearly show a 3D hierarchical porous structure. Figure 6-3 (A) and (B) illustrate that NiCo_2O_4 precursor nanosheets

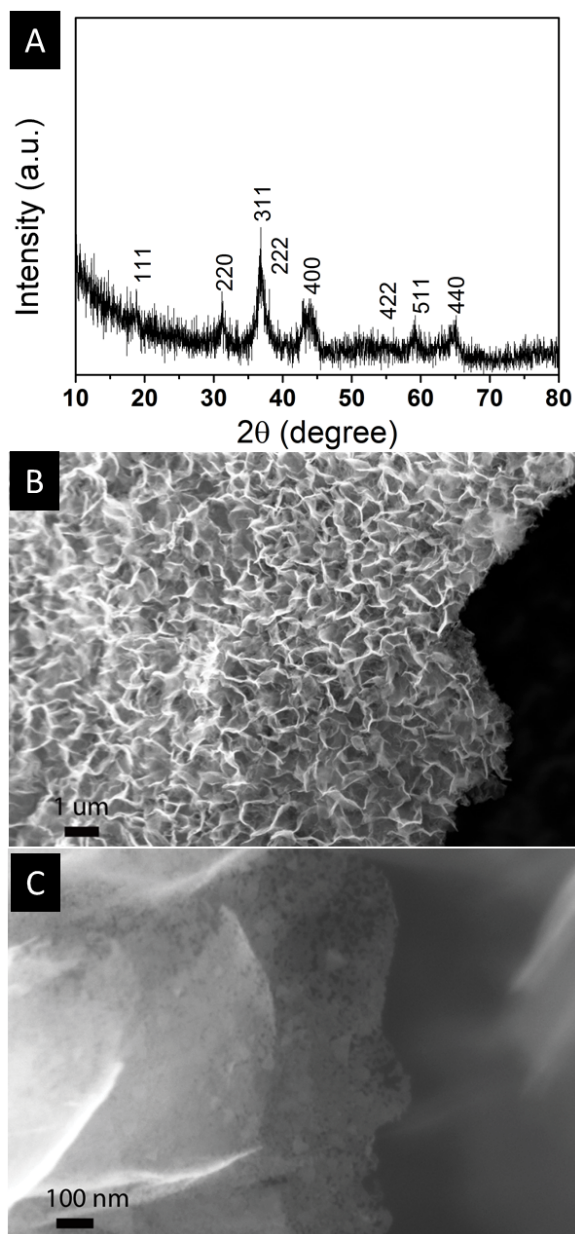


Figure 6-4 (A) XRD pattern of NiCo₂O₄@graphene nanoarchitectures. (B) SEM image of foam-like hybrid NiCo₂O₄@graphene nanoarchitectures with hierarchical pores. (C) SEM image of NiCo₂O₄ nanosheets.

grew on the conductive RGO-PU-sponges. In the inner region (Figure 6-3 (C)), the NiCo₂O₄ precursor nanosheets are interconnected with each other to form the macroporous structure. It should be noted that NiCo₂O₄ precursor nanosheets grew vertically to the graphene nanosheet substrates.

After having been annealed at 350 °C in air for 2 hours, the final product materials were

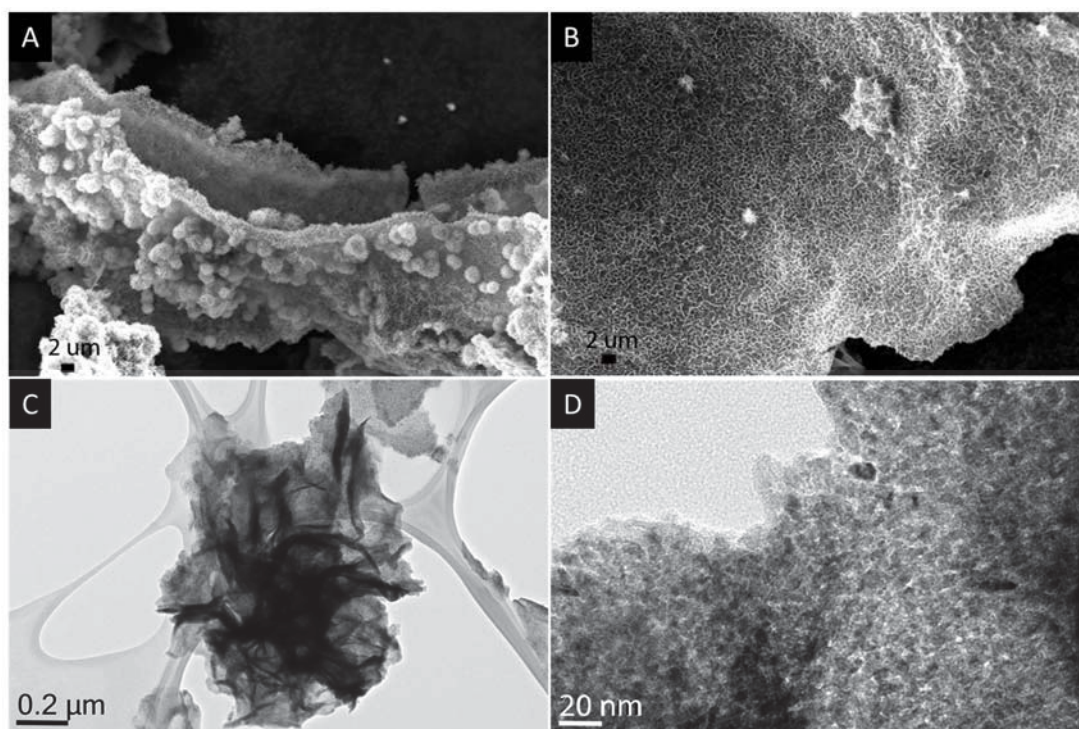


Figure 6-5 The SEM images of (A, B) large-size NiCo₂O₄@graphene obtained by annealing the precursor at 350 °C in air for 2 hours; TEM images of (C) NiCo₂O₄@graphene nanoarchitectures with macropores, (D) mesopores ranging from 2-5nm.

characterized by XRD, SEM and TEM. Figure 6-4 (A) shows the XRD pattern of the 3D mesoporous NiCo₂O₄@graphene nanoarchitectures. Seven diffraction peaks were observed at the 2θ of 18.9°, 31.1°, 36.6°, 44.6°, 59.1°, 64.9° and 68.3°. All the peaks can be indexed to the standard spinel NiCo₂O₄ crystalline structure, with the indices of (111), (220), (311), (400), (422), (511) and (440) (JCPDF-20-0781). After annealing, the morphologies of the 3D porous structure were well preserved. PU-sponges were completely burnt out at 350 °C in air. The NiCo₂O₄@graphene nanosheets retained the 3D shape of the PU-sponge (Figure 6-5 (A)). A foam-like nanoarchitecture consisting of hierarchical pores was obtained (as shown in Figure 6-5 (A) and (B)). From the magnified view (Figure 6-4 (B)), porous NiCo₂O₄ nanosheets can be observed. Furthermore, the highly magnified SEM image of the crystalline NiCo₂O₄ nanosheets (Figure 6-4 (C)) clearly shows the presence of the mesoporous structure of the ultra-thin NiCo₂O₄

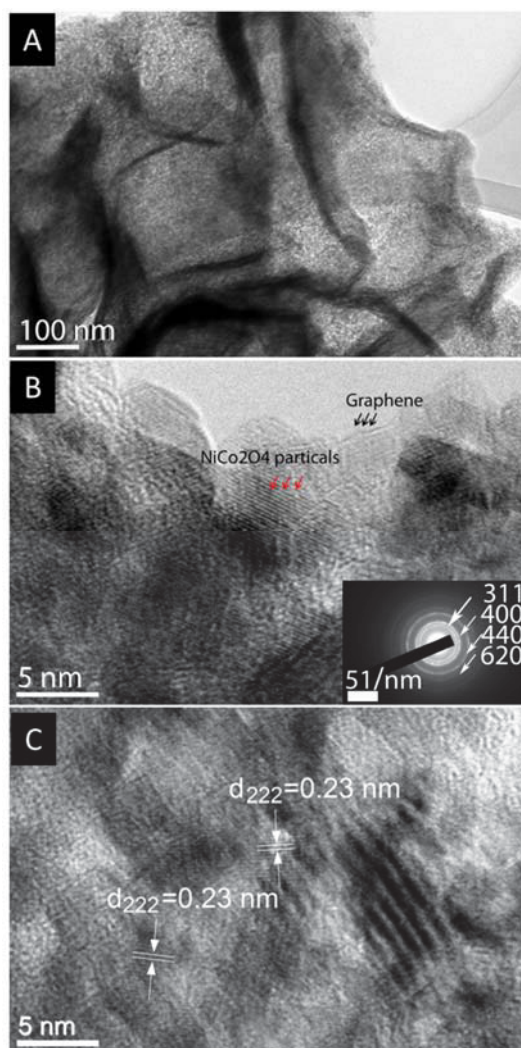


Figure 6-6 (A) TEM image of NiCo₂O₄@graphene nanosheets, showing the porous architecture. (B) HRTEM images of NiCo₂O₄@graphene nanosheets. The inset SAED pattern can be fully indexed to polycrystalline NiCo₂O₄. (C) Lattice resolved HRTEM image of NiCo₂O₄ nanosheets.

nanosheets.

TEM images also revealed that NiCo₂O₄@graphene nanosheets contain porous 3D architectures with mesopores and macropores. The macropores (50 – 200 nm) are formed by the interconnection of NiCo₂O₄ nanosheets, which are clearly visible in Figure 6-5 (C) Figure 6-6 (A). The mesopores, ranging from 2 to 5 nm, are uniformly distributed on the NiCo₂O₄ nanosheets, which grew on large-size graphene sheets (as shown in Figure 6-5 (D) and Figure 6-6 (B)). As shown in the inset image of Figure 6-6 (B), the corresponding

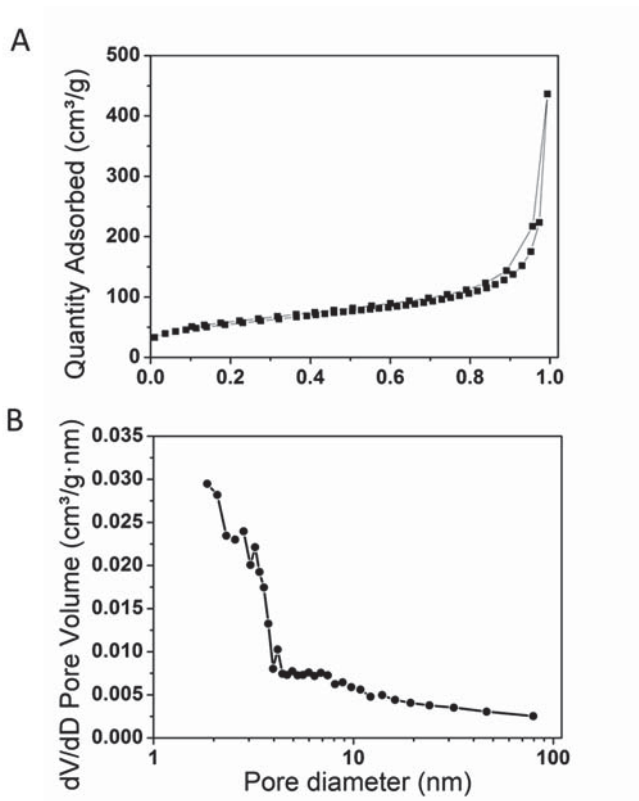


Figure 6-7 (A) Nitrogen adsorption/desorption isotherms; (B) pore size distribution of NiCo₂O₄@graphene nanoarchitectures.

crystalline diffraction rings of (311), (400), (440) and (620) in the selected area electron diffraction (SAED) pattern confirmed the polycrystalline NiCo₂O₄. Furthermore, HRTEM image (Figure 6-6 (C)) demonstrates that the NiCo₂O₄ nanosheets are well-crystallized with an interplanar (022) space of 0.23 nm.

The pore-size features of the 3D mesoporous hybrid NiCo₂O₄ @graphene nanoarchitectures were further measured by nitrogen adsorption/desorption isotherms. The Brunauer–Emmett–Teller (BET) surface area is determined by the nitrogen adsorption/desorption at 77 K. The isotherm of the material exhibits the characteristics of type II and VI isotherms, which indicates the combination of macropores and mesopores²³¹ (Figure 6-7 (A)). Because of the 3D hierarchical porous structure, a large surface area of 195.4 m² g⁻¹ and the total pore volume ratio of 0.27 cm³ g⁻¹ were achieved.

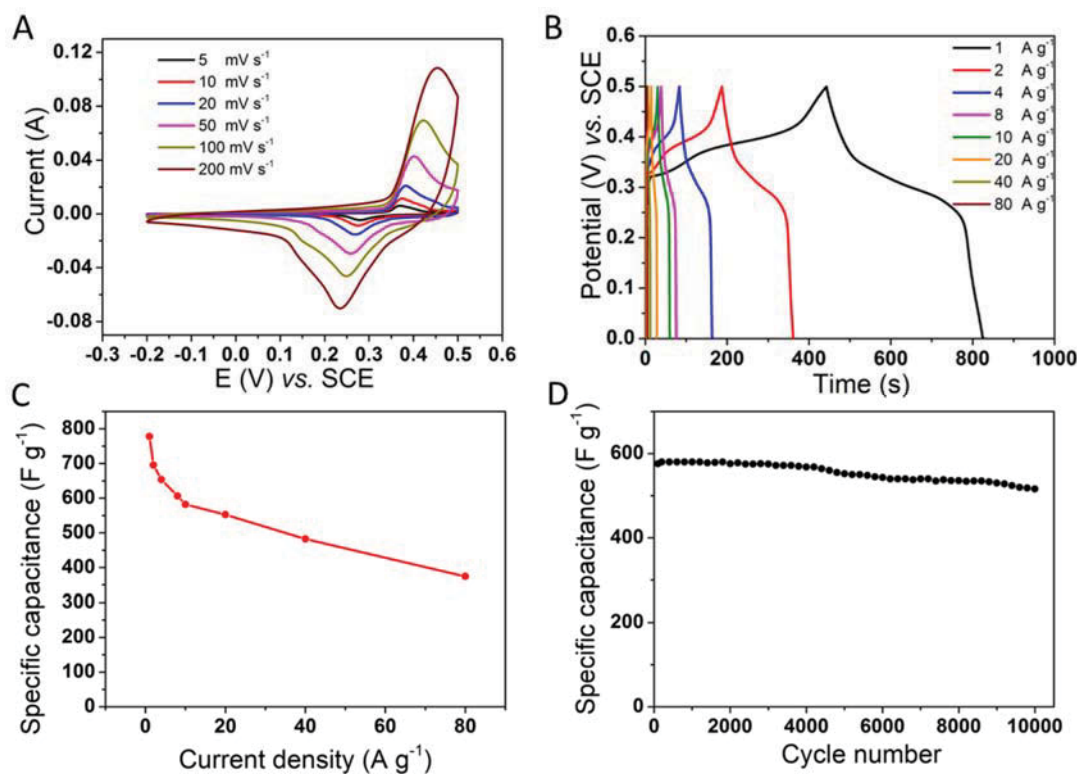


Figure 6-8 Electrochemical performance of the NiCo₂O₄@graphene nanoarchitectures. (A) CV curves at the scan rate of 5 mV s⁻¹ to 200 mV s⁻¹; (B) constant-current charge/discharge profile at the current densities of 1 A g⁻¹ to 80 A g⁻¹; (C) specific capacitance vs current density; (D) capacity retention vs cycle number up to 10,000 cycles at 10 A g⁻¹. All the data are taken in 2.0 M KOH electrolyte.

The corresponding pore size distribution (Figure 6-7 (B)) indicates a pore size range of 2–5 nm, which is consistent with the SEM and TEM observations.

The electrochemical performances of the 3D porous hybrid NiCo₂O₄@graphene nanoarchitectures were tested as the electrodes for supercapacitors. As shown in Figure 6-8 (A) and (B), the electrodes are able to function in a wide range of scan rates, ranging from 5 mV s⁻¹ up to 200 mV s⁻¹. The shape of the CV curves clearly reveals the characteristic of pseudocapacitors with a pair of redox peaks existing in the potential range of -0.2 to 0.5 V vs. SCE at all scan rates, even at a high scan rate of 200 mV s⁻¹. The oxidation peak locates at 0.37 V and the reduction peak is at 0.28 V. The NiCo₂O₄@graphene electrodes are tolerant to a high scan rate, which indicates good conductivity and good charge propagation within the electrodes.¹²⁵ For the carbon-

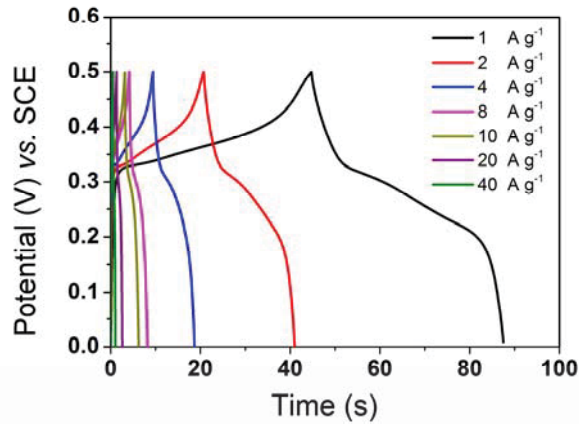


Figure 6-9 Charging/discharging profile of pure Ni foam at the same current rates of the active material, ranging from 1 to 40 A g⁻¹.

based electrode, the shape of the CV curve degrades significantly with the increase of the scan rate. On the contrary, the 3D NiCo₂O₄@graphene electrodes maintain the shape of the pseudocapacitance curve, even at high scan rates. The 3D porous nanoarchitectures, highly conductive graphene and high reactivity of NiCo₂O₄ jointly contribute to such a high rate performance. With the increase of the scan rate, there is a little shift of the redox peaks, suggesting low polarization.⁸⁷ To further investigate the electrochemical characteristics of the as-prepared materials, galvanostatic charge-discharge measurements were carried out in 2M KOH electrolyte at various current densities. As shown in Figure 6-8 (B), the supercapacitor operates well within a wide range of current densities, from 1 A g⁻¹ to 80 A g⁻¹. This clearly demonstrates the excellent electrochemical performances of the 3D porous hybrid NiCo₂O₄@graphene nanoarchitectures.

Based on the charging/discharging curves, and the equation:

$$C = (I \times \Delta t) / (m \times \Delta v)$$

where I is the discharge current, Δt is the discharge time, Δv is the voltage range and m is the mass of the active material, the calculated specific capacitance as the function

of discharging current density was plotted in Figure 6-8 (C). The nickel foam will contribute to the capacitance in KOH electrolyte when it was used as the current collector.²³² The specific capacitance of bare nickel foam was measured (Figure 6-9) and subtracted from the capacitance value of the material. NiCo₂O₄@graphene electrodes show excellent specific capacitance of 778, 696, 653, 606, 582, 552, 482 and 374 F g⁻¹, at current densities of 1, 2, 4, 8, 10, 20, 40 and 80 A g⁻¹, respectively. The electrode still maintains a high specific capacitance of 374 F g⁻¹ at the high current density of 80 A g⁻¹. This outstanding pseudocapacitor performance could be ascribed to good conductivity and the 3D porous structure of the materials. Large-size graphene nanosheets were formed by using freeze drying, which provided the high electrical conductive medium for the electron transport. The ultrathin NiCo₂O₄ sheets lead to the high specific area to react with ions in the electrolyte. The uniform mesoporous and macroporous structure optimizes the ion diffusion path, and facilitates the adsorption/desorption of K⁺ and the transportation of ions. This allows for the complete distribution of electrolyte into the electrode, and for maximizing the utilization of the NiCo₂O₄. It ensures that there are efficient reactive sites between the NiCo₂O₄ electrode and the electrolyte. In order to investigate the long-time cyclability, charge-discharge cycling up to 10,000 cycles has been conducted at the current density of 10 A g⁻¹ (as shown in Figure 6-8 (D)). Approximately 90% of the initial capacitance is retained after 10,000 cycles, demonstrating good cycling stability at high charge/discharge current density.

In order to further illustrate the advantages of porous NiCo₂O₄@graphene nanoarchitectures as electrode materials for supercapacitors, the electrochemical performances of the bare NiCo₂O₄ were also evaluated. As shown in Figure 6-10, the bare NiCo₂O₄ electrodes exhibited many poor performances at different current densities, compared with porous NiCo₂O₄@graphene electrodes. Figure 6-11 shows the Nyquist

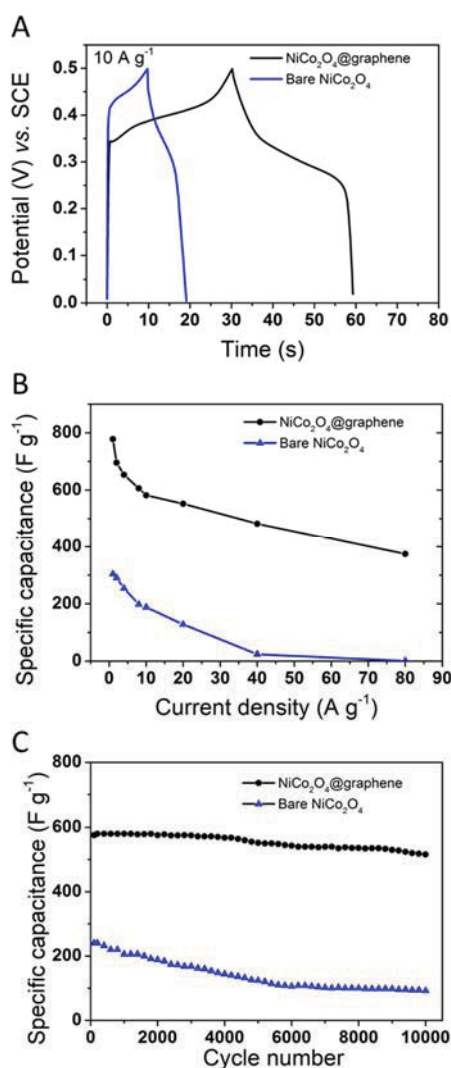


Figure 6-10 Electrochemical performance of NiCo₂O₄@graphene nanoarchitectures and bare NiCo₂O₄ (A) charging/discharging curves at a current density of 10 A g⁻¹; (B) specific capacitances at current densities of 1 to 80 A g⁻¹; (C) capacities retention up to 10000 cycles at 10 A g⁻¹;

plots of the a.c. impedance spectra of both the porous NiCo₂O₄@graphene electrode and the bare NiCo₂O₄ electrode. It can be seen that the charge transfer resistance of the porous NiCo₂O₄@graphene electrode is much lower than that of the bare NiCo₂O₄ electrode. Therefore, the unique porous NiCo₂O₄@graphene nanosheet architectures can significantly reduce the internal resistance (including solution resistance, charge transfer resistance and other resistances).²¹³ As shown in Table 6-1, compared to previous reports, the as-prepared materials achieved good cycleability at high current densities.

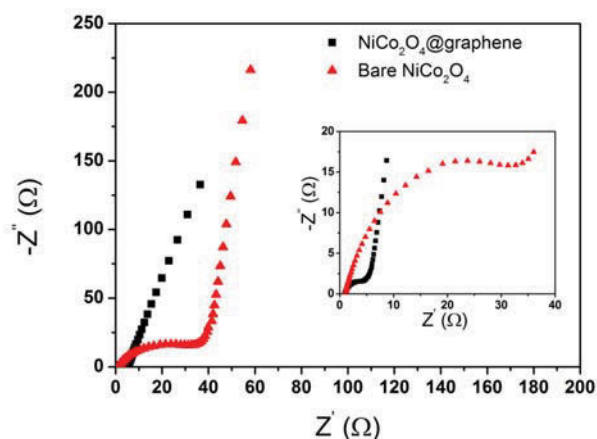


Figure 6-11 Nyquist plots of the a.c. impedance spectra of the porous NiCo₂O₄@graphene electrode and the bare NiCo₂O₄ electrode in the frequency range from of 100 kHz to 0.01 Hz.

6.4. Summary

In summary, we have successfully developed a novel synthetic method to prepare 3D porous NiCo₂O₄@graphene nanoarchitectures. The synthesis process involves coating of hydrazine-reduced graphene oxide onto the PU-sponge, and growing bimetallic (Ni, Co)

Table 6-1 Comparison of the electrochemical performance of as-prepared NiCo₂O₄@graphene with the materials reported in the literatures

References	Mass loading	2 or 3 electrode configuration	Specific Capacitance (F g ⁻¹) at 1 A g ⁻¹	Maximum Current Densities (A g ⁻¹)	Capacity Retention Cycle&Current Densities	Cycles
As-prepared NiCo ₂ O ₄ @graphene	1 mg cm ⁻¹	3	778	80	90% at 10 A g ⁻¹	10000
W. Chen et. al ¹	----	3	743	40	93.8% at 1 A g ⁻¹	3000
Te-Yu Wei et. al ²	0.4 mg cm ⁻¹	3	719 (at 25mV s ⁻¹)	25mV s ⁻¹	91% at 25mV s ⁻¹	2000
H. Wang et. al ³	1 mg cm ⁻¹	3	722	20	80% at 10 A g ⁻¹	3000
H. W. Wang et. al ⁴	2 mg cm ⁻¹	3	835	16	----	4000

ultrathin nanosheets. The final products consist of ultrathin NiCo₂O₄ sheets with mesopores ranging from 2 to 5 nm. The mesoporous ultrathin NiCo₂O₄ nanosheets also form the 3D macropores with the size in the range of 50 to 100 nm. Owing to the 3D hierarchical porous structure, the NiCo₂O₄@graphene nanoarchitectures exhibit high specific capacitance, an ultrafast charge/discharge rate, and excellent cycling stability. In particular, NiCo₂O₄@graphene nanoarchitectures delivered a high specific capacitance of 778 F g⁻¹ and 374 F g⁻¹ at the current densities of 1 A g⁻¹ and 80 A g⁻¹, respectively.

Chapter 7. A High-Rigid Binder-Free 3D Free-Standing NiCo₂O₄@graphene Foam Fabricated by Controllable Freeze Casting for High-performance Supercapacitors

7.1. Introduction

With the growing demand for energy storage in renewable energy and electric vehicles, there has been a desire to design and fabricate energy storage devices that can simultaneously deliver high energy and high power, and that possess a long life cycle and a wide operation temperature. Supercapacitors have higher energy density than conventional dielectric capacitors, and much higher power density than rechargeable batteries.²³³ They have attracted much attention in recent years for a variety of energy storage applications ranging from memory back-up for portable devices to industrial energy storage. The Electrochemical double layer capacitor (EDLC) is a kind of supercapacitor. It stores electrical energy in a double layer interface between the electrode material and aqueous or organic electrolyte. The electrode is usually composed of conductive materials such as activated carbon, carbon nanotube and graphene with a large surface area. The higher specific surface area contributes to a larger charge storage in the double layer for a given weight and volume of the electrode, which leads to an increase in energy storage, maintaining high power density of supercapacitors. Pseudocapacitor is another type of supercapacitors which rely on fast and reversible redox reactions, in which transition metal oxides are usually employed as electrode materials.

Graphene, a one-atom-thick two-dimensional sheet of sp²-hybridized carbon atoms,^{65, 66} is considered to be one of the outstanding electrode materials for electrochemical double layer capacitors.^{42, 64, 66-68} Due to its intriguing single layer structure of carbon,⁶⁹

graphene possesses high electric conductivity and mechanical strength, charge carrier mobility,⁴² and high specific surface area of up to $2675 \text{ m}^2 \text{ g}^{-1}$,^{64, 68} which is much larger than that of activated carbon and carbon nanotubes. Moreover, the specific capacitance of graphene is able to reach to 21 uF cm^{-2} , and graphene has the largest theoretical electrochemical double layer capacitance at around 526 F g^{-1} .⁶⁴ It can also provide conduction pathways to a greater area per unit mass than CNTs, which should translate into improved conductivity.⁶⁹ However, graphene usually agglomerates to form the graphite through the van der Waals interactions during the drying process and fails to maintain its intrinsic properties especially the large surface area.²³⁴ Consequently, the ions of electrolyte, especially organic electrolyte with large-size ions, have difficulty accessing the electrode, especially the inner parts.

To effectively utilize the high surface area of graphene and optimize the ion diffusion paths, many researchers have focused on fabricating macroscopic architectures by using graphene sheets as building blocks. 2D and 3D graphene macro-structure materials have been fabricated by various methods. One of the methods is vacuum filtration, which filters the aqueous graphene or GO dispersions in order to prepare graphene paper.^{179, 181, 227, 235, 236} The vacuum-assisted self-assembly method is able to densify the graphene, which increases the electrode density. The graphene paper has the free-standing feature which avoids the usage of binder material. This means that the conductivity of the electrode based on this graphene paper is substantial improvement on conventional graphene powders. Even though the vacuum filtration assists in preparing the free-standing paper, the graphene agglomerates together easily, which will inevitably increase the ion diffusion resistance. Chemical vapour deposition (CVD) based on a metal substrate is another promising technique for fabricating 3D graphene foams.²³⁷⁻²⁴² The 3D foam-like graphene macrostructures consist of an interconnected flexible network of graphene,

which have fast transport channels of charge carriers for high electrical conductivity. In situ self-assembly of graphene prepared by mild chemical reduction was developed by Chen *et al.* to fabricate 3D architectures of graphene.¹⁸² The water absorbed in the as-prepared graphene hydrogel was removed by using freeze drying. The aerogels that were subsequently obtained were ultralight and highly porous with a density of 18 mg cm⁻³. Marcus *et al.*²⁴³ reported on the use of organic sol-gel chemistry to synthesize graphene aerogels. The as-prepared graphene gels with density of a 10 mg cm⁻³ exhibit high electrical conductivities and large internal surface areas. The aerogels also possess large surface areas (584 m² g⁻¹) and pore volumes (2.96 cm³ g⁻¹). Freeze drying is a useful technique to remove the water in the materials by sublimating frozen water directly from the solid phase to the gas phase, thereby keeping the structure of the materials. Numerous researchers have reported fabrication of 3D graphene foam by using freeze-drying technology.^{173, 244-248} Ling Qiu *et al.* prepared ultralight and superelastic graphene-based cellular monoliths by freeze drying.¹⁷¹ The functionalization-lyophilization-microwave treatment combined with freeze-drying was designed by Han Hu *et al.*, which successfully produced ultralight graphene aerogel with excellent elasticity.¹⁷² A versatile, ultralight and nitrogen doped, three-dimensional (3D) graphene framework was also prepared using freeze-drying method.¹⁷³ The rich open-pore structures interpenetrating the graphene skeleton contributes to the ultra-low weight density of 2.1 mg cm⁻³. The freeze-drying technology was used to dry the graphene oxide and carbon nanotubes aerogel, leading to an ultra-flyweight 3D graphene and carbon nanotubes foam with a density of less than 1 mg cm⁻³.²⁴⁷

Due to the low specific capacitance (SC) of EDLCs, they are unable to meet the ever-growing need for peak-power assistance in most applications, and thus many transition metal oxides, including MnO₂,^{95, 97, 98, 249-252} RuO₂,^{74, 253, 254} NiO²⁵⁵⁻²⁵⁹ and Co₃O₄^{240, 260-}

²⁶² *et al.*, have been investigated as electrode materials for supercapacitors. NiCo₂O₄ possesses intriguing electronic conductivity, low diffusion resistance to protons/cations, and easy electrolyte penetration, and therefore is one of the most promising transition metal oxides for pseudocapacitors.⁸⁴⁻⁸⁶ Yuan *et al.* fabricated ultrathin mesoporous NiCo₂O₄ nanosheets by co-electrodeposition of Ni and Co on to bimetallic (Ni, Co) hydroxide precursor on a Ni foam.⁸⁷ The as-prepared ultrathin NiCo₂O₄ nanosheets, with a thickness of a few nanometers and many interparticle mesopores with sizes ranging from 2 to 5 nm, contribute to the high supercapacitor performance. Furthermore, Zhang *et al.* developed a facile solution method to synthesize NiCo₂O₄ nanoneedle arrays directly onto conductive metallic substrates and carbon nanofibers, which possess an enhanced electrochemical performance for supercapacitors.⁸⁵

The 2D and 3D graphene macro-structure materials contribute to a large specific surface area of electroactive materials, which are able to accommodate a sizeable amount of electroactive species for participation in the faradaic redox reactions, and consequently advance specific capacitance. Because of the van der Waals attractions between two graphene sheets, aggregation or restacking inevitably occurs in the graphene assembly process by using a simple vacuum-assisted self-assembly method. Consequently, most of the unique properties of graphene sheets, such as high specific surface area and high electrical conductivity, deteriorate significantly or are even unavailable. In fabrication methods based on freeze-drying technology, water is able to serve as the effective spacer that prevents the aggregation of the chemically reduced graphene sheets. Another function of water in the freeze-drying assisted method is that it serves as the template to fabricate porous graphene foam. After sublimating frozen water directly from the solid phase to the gas phase, the structure of the materials is maintained and the pores are formed by the solid ice residue in the materials. However, the pore size of the materials

fabricated by the conventional freeze-drying is too big to be used as the electrode, and the resulting graphene foams are generally brittle. Therefore, the materials have to be ground and mixed with binder to form a slurry, which is then passed onto the current collector, resulting in the collapse of the structure. In-situ self-assembly of graphene or graphene oxide is a good method for shrinking the size of pores of the graphene aerogels. The graphene oxide sheets in the solution, which are partially reduced by the reducing agents, tend to form cork-like monoliths with a smaller pore-size structure. Even though these materials are able to sustain their structural integrity under a weight load, the volumetric density is too small to serve as the electrode because practical applications require the design and fabrication of small scale energy storage devices.

In the present work, a vacuum-and-pressure-assisted assembly method was designed to fabricate 3D NiCo₂O₄@graphene foam, in which RGO sheets are interconnected, forming free-standing nanoarchitectures with a high surface area of 252.4 m² g⁻¹. Unlike the conventional stacked geometry of graphene foam, wherein the pores formed by interconnected RGO sheets are either too large or too small to serve as the supercapacitor electrode, in the new method, the pore size of graphene foam is controllable and is compressed to be directly used as the electrode for the supercapacitor. The pore size and thickness of the material are easily controlled by regulating the amount of water in the precursor solution. As is well known, it is difficult to prepare a high concentration of graphene oxide (GO) aqueous solution with uniform dispersions. The hydrophilous bimetallic (Ni, Co) hydroxides are introduced onto GO sheets, which contribute to the uniform dispersion of GO in water, even when the concentration of GO is very high during filtration. The external air pressure added to the solution in the container allows the uniform distribution of water in the bulk. Consequently, uniform-size pores are formed in the foam after removing the water by using freeze drying. Our new method

should facilitate large-scale fabrication of free-standing graphene foam, and open the way for building high conductive and high-surface-area skeletons to support the metal oxide deposition. It also offers opportunities for fabricating thick electrode materials, thereby improving the electrode density and energy density.

7.2. Experimental

7.2.1. Fabrication of 3D NiCo₂O₄@graphene Precursor

GO was prepared from natural graphite flakes by a modified Hummers method,²²⁶ and the GO nanosheets were dispersed in 30 mL of distilled water at a concentration of 5 mg mL⁻¹ by stirring for 12 hours and ultrasonication (Branson 2510) for 2 hours at room temperature. After dispersion, 1 mmol of Ni(NO₃)₂·6H₂O, 2 mmol of Co(NO₃)₂·6H₂O and 4.5 mmol of urea were added to the 30 mL of GO aqueous solution. The solution was transferred to a Teflon-lined autoclave and then heated under hydrothermal conditions at 95 °C for 6 hours. The precursor prepared by hydrothermal method was washed several times using distilled water and filtration, followed by redissolving in distilled water to form NiCo₂O₄@graphene precursor aqueous suspension.

7.2.2. Fabrication of 3D NiCo₂O₄@graphene Foam

A filter paper with a diameter of 14 mm was placed at the bottom of a cylindrical tube. 1 mL of volume of the precursor solution was taken in by a 10 mL plastic syringe and expelled into the cylindrical tube of the designed device. The device was then introduced to the vacuum filtration system. The plunger was then inserted into the cylindrical tube. With the pressure added by the plunger, air pressure was generated in the cylindrical tube, and pushed the water through the bulk filtering it. The amount of water in the bulk depended on the volume of the material in the cylindrical tube, and was indicated by

graduated marks. The device with the filtered bulk was then immersed into liquid nitrogen for 20 mins. After freeze-drying for 48 hours, the water within the material was completely removed. The as-prepared black materials were further dried under vacuum at 80 °C for 12 hours. This was followed by annealing at 600 °C for 2 hours in pure argon with a slow heating rate of 1 °C min⁻¹, in order to obtain RGO. Finally, the bulk materials were annealed at 250 °C for 2 hours in air to obtain 3D NiCo₂O₄@graphene foam.

7.2.3. Material Characterization

The crystal structure and phase of the as-prepared materials were characterized by X-ray diffraction (XRD) (Siemens D5000 X-ray diffractometer) using Cu K α radiation with 2θ ranging from 10° to 80°. The morphology and crystal structures were characterized by field-emission scanning electron microscopy (FE-SEM, JSM-6700F), and transmission electron microscopy/selected area electron diffraction (TEM/SAED, JEOL JEM-200CX) equipped with an energy-dispersive X-ray spectrometer (EDX). N₂ adsorption–desorption measurements were conducted using a 3 Flex surface characterization analyser at 77 K.

7.2.4. Electrochemical testing

The as-prepared foam was directly used as the electrode without binder. A nickel wire with a diameter of 0.5 mm was employed to wire the foam with a nickel current collector, leading to good conductive contact between the active material and current collector. The nickel foam and wire were initially cleaned before use as the current collector. They were

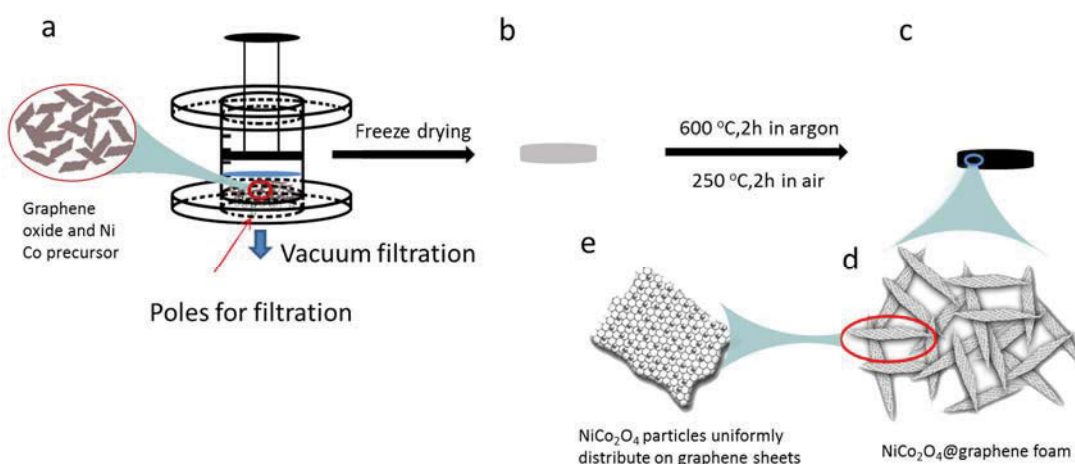


Figure 7-1 Schematic illustration showing the experimental steps of fabricating NiCo₂O₄@graphene foam.

immersed in acetone for 10 minutes followed by ultrasonication for 5 minutes. The nickel foam was then cleaned with 0.1 M hydrochloric acid. After that, it was washed with distilled water using ultrasonication for 5 minutes. Electrochemical measurements were carried out using three-electrode cells, with platinum as the counter electrode and a saturated calomel electrode (SCE) as the reference electrode. Cyclic voltammetry (CV) and galvanostatic charge–discharge (CD) was carried out on a CHI 660C electrochemistry workstation using 2.0 M KOH electrolyte.

7.3. Results and Discussion

Figure 7-1 illustrates the process for the preparation of the 3D NiCo₂O₄@graphene foam by using CFC. The first step was to fabricate NiCo₂O₄ precursors on the GO sheets by using a hydrothermal method. NiCo₂O₄ precursors were able to be uniformly synthesized on to GO sheets under hydrothermal conditions. After being washed several times using distilled water and filtration, the as-prepared precursor was redissolved in distilled water to form NiCo₂O₄@graphene precursor aqueous suspension. A syringe with the volume of

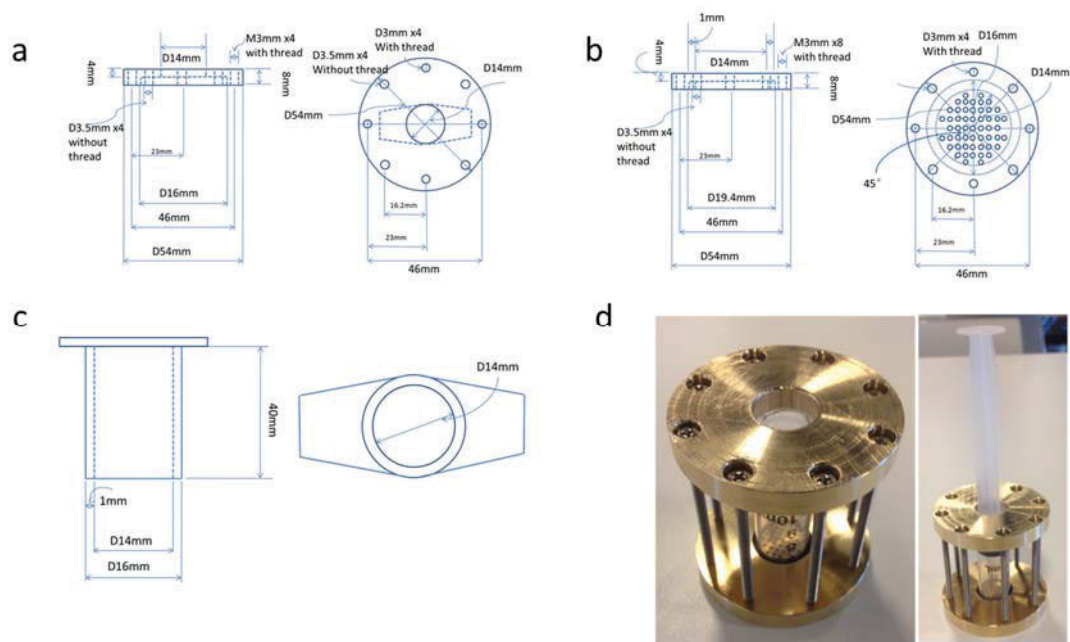


Figure 7-2 The schematics of the (a) upper base, (b) bottom base and (c) cylinder tube of the as-designed device. (d) The images of the device (left image), after inserting the plunger (right image).

10 mL was used to transfer a specific volume of solution into the as-designed device. As shown in Figure 7-2 (a), the base of the as-manufactured device has a diameter of 54 mm, which was matched to the diameter of the base of the vacuum filter. Copious holes (Figure 7-2 (b)) in the base of the device provided a path for water to exit. The surface of the bottom of the device is very smooth, leading to good contact between the device and the vacuum base, and consequently good vacuum filtration was achieved. A cylindrical plastic tube (Figure 7-2 (c)) with a height of 40 mm cut from a syringe was sandwiched between the two bases. After injecting a specific volume of precursor solution, the device was placed on vacuum base. The plunger was immediately added into the cylindrical tube with an external push (Figure 7-2 (d)). Because the volume of the solution was much less than that of the cylindrical tube, air space in the cylindrical tube was present. When the plunger was pushed, air pressure was generated in the plastic cylinder. The air pressure generated in the cylindrical tube pushed the water through the bulk filtering it. The air pressure therefore has two functions. The first is that it contributes to quick vacuum

filtration. Due to the planar nature of GO, it blocks the pores of the filter paper, leading to lengthy filtration of the GO aqueous solution. With the assistance of the extra air pressure, the water in the GO aqueous solution is more easily removed by the vacuum filtration system. As shown in the video in the supported information, it takes less than one minute to fabricate one such electrode. Another significant function is that the air pressure contributes to uniform distribution of water in the bulk. As is well known, the planar GO will block the pores of the filter paper. If no extra air pressure is added to the top of the solution, with the regularly decreasing amount of water during filtration, there will be less water in the bottom area of the bulk and more water in the upper region of the bulk. However, the extra air pressure pushed the water through the bulk, forming a uniform water distribution. When the bulk was introduced to liquid nitrogen, uniform distribution of ice crystals was generated. Consequently, aligned and uniform pores were retained after removing the ice by using freeze drying. The next step was to filter the solution to a specific volume. With the assistance of air pressure, the solution was gradually filtered without adhering to the inner surface of the cylindrical tube. There were graduated marks indicating the volume of the solution in the tube. When the solution reached a specific mark (specific volume), the bulk, together with the device, was immediately immersed in liquid nitrogen. The device should be immersed into liquid nitrogen gradually. If the device is totally immersed into the liquid nitrogen too quickly, the boiling liquid nitrogen will enter through the holes in the base and damage the structure of the material. Therefore, the base of the device must first be cooled down by the liquid nitrogen. Then, the device can be immersed into liquid nitrogen a little bit deeper. Through this procedure, the whole device was immersed into liquid nitrogen for 20 minutes, followed by the transferral of the device into the freeze-drying system (Scheme. 1b). After drying, the material was annealed in argon at 600 °C for 4 hours, followed by 250 °C for 2 hours in air, leading to

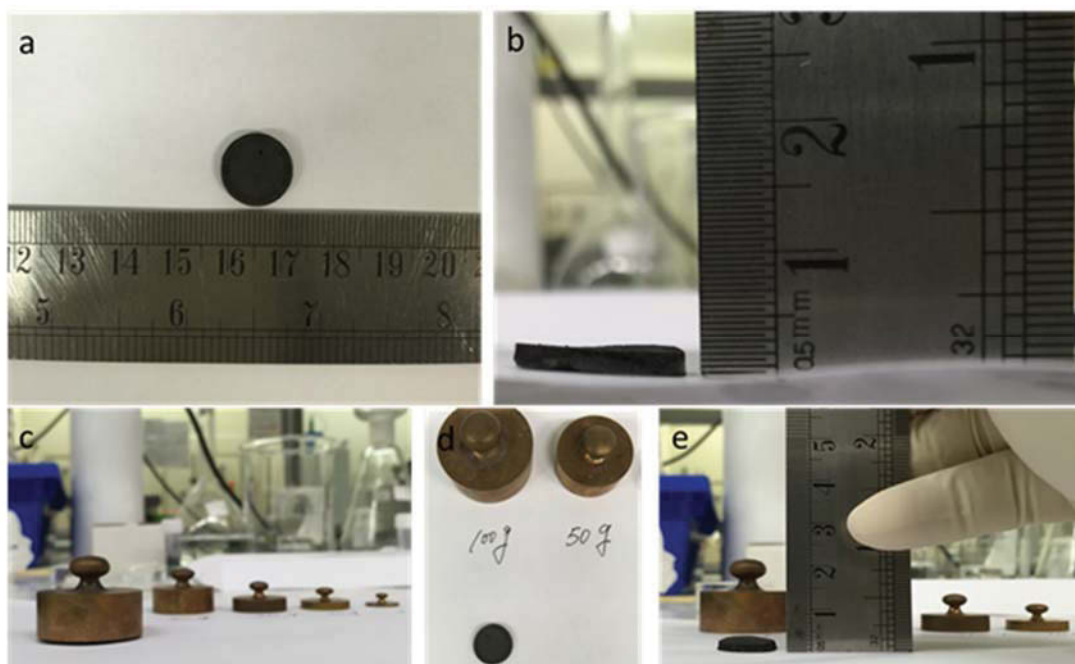


Figure 7-3 The compression test shows that the as-prepared foam has a high-rigid mechanical property. The foam has (a) a diameter of 14 mm and (b) a thickness of about 2 mm. (c) The real-time image of the compressed sample loading with the balance of 100 g. (d) the images of the sample after loading the weights, shows that the foam retained the original structure without collapsing. (e) There is no change in the thickness of the foam after loading the related balance weight.

a reduction of graphene oxide (Figure 7-1 (c)). Upon the annealing treatment, reduced graphene oxide sheets served as the building block for fabricating the 3D foam structure (Figure 7-1 (d)), and the crystallized NiCo₂O₄ nanoparticles uniformly distributed on RGO sheets (Figure 7-1 (e)).

The mechanical properties of the 3D NiCo₂O₄@graphene foam were characterized by a compression test. The test, which loads different balancing weights onto the foam, revealed that the 3D NiCo₂O₄@graphene foam exhibited strong mechanical properties. As with most of the existing porous carbon materials, the conventional RGO foams are generally brittle and have small recoverable deformation when loads are added onto the materials.^{171, 172} Even though elastomeric polymers²⁶³ can be used to achieve elastic 3D graphene materials, they are not suitable to serve as the supercapacitor electrodes owing to the large pore size and structure distortion. As shown in Figure 7-3

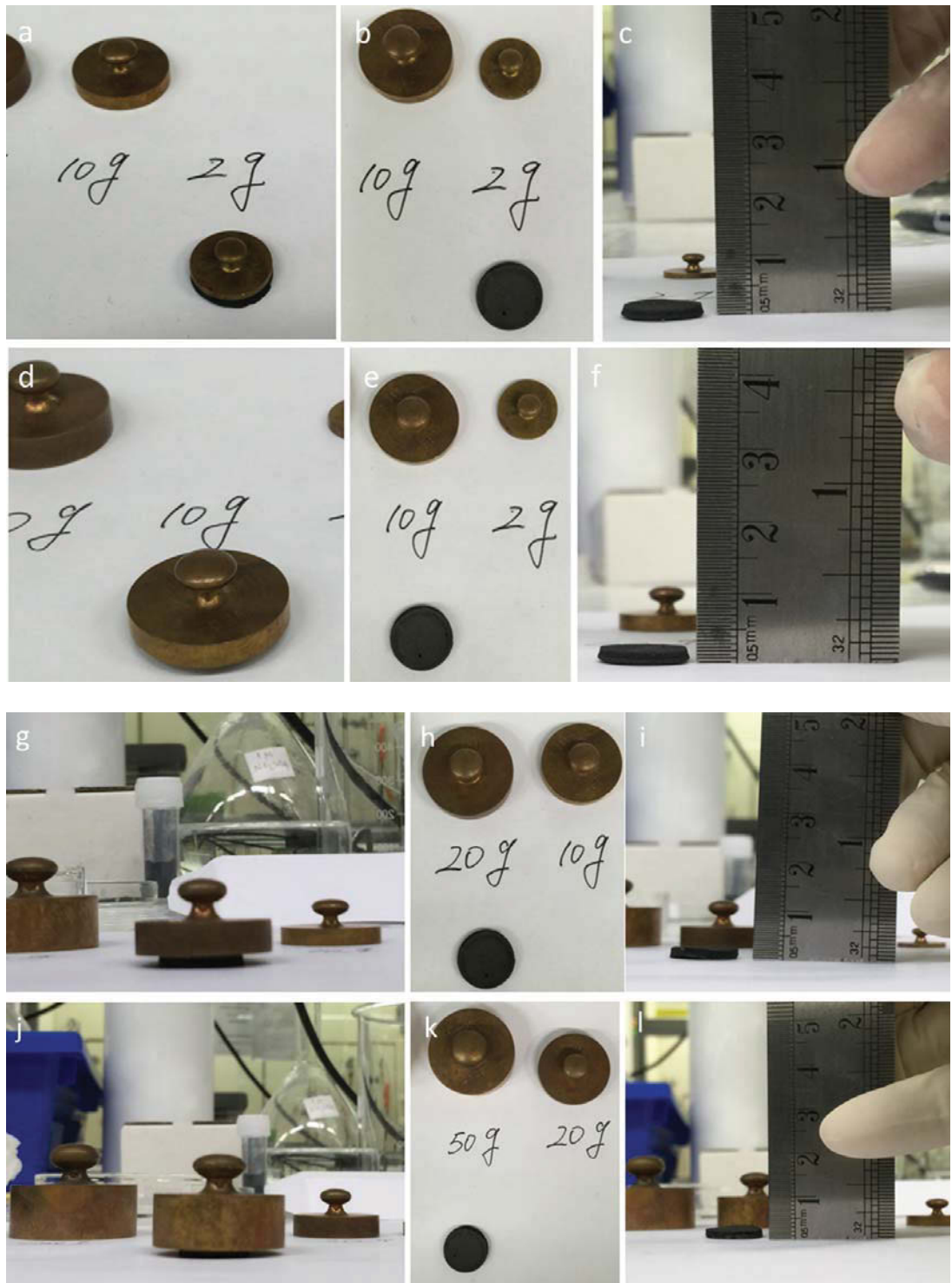


Figure 7-4 The real-time images of the compressed sample loading with the balance of (a) 2 g, (d) 10 g, (g) 20 g and (j) 50 g. (b), (e), (h) and (k) the images of the sample after loading these weights, showing the foam retained the original structure without collapsing. (c), (f), (i) and (l) there is no change in the thickness of the foam after loading the related balance weight.

(a) and (b), the as-fabricated $\text{NiCo}_2\text{O}_4@\text{graphene}$ foam has a diameter of 14 mm and a

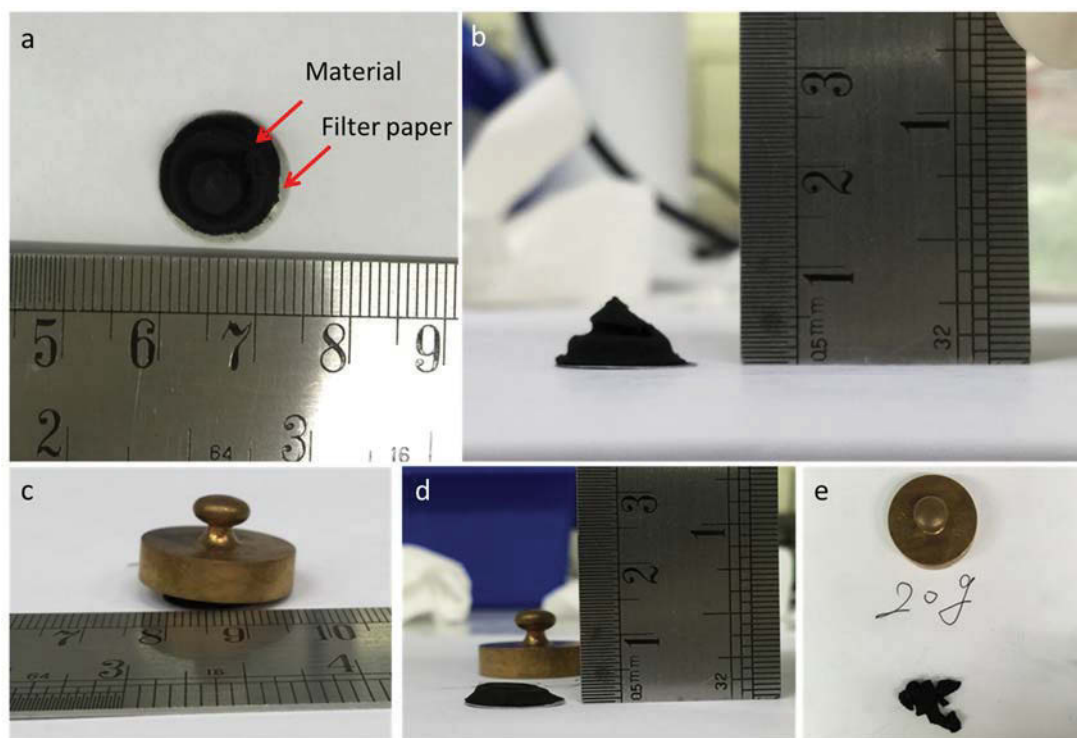


Figure 7-5 The compression test of the material fabricated without using extra air compress pressure. (a) The size of the foam is smaller than that of filter paper due to the shrink during the freeze drying process. (b) Cross-sectional image of the foam, showing cone-like structure. (c) The foam was loaded with the balance of 20g. (d) and (e) The image of sample after loading the weight, showing the foam suffered structure collapsing.

thickness of about 2 mm. The balancing weights of 2 g, 10 g, 20 g, 50 g (Figure 7-4) and 100 g (Figure 7-3 (c)) were left on the foam, respectively. The foam did not suffer structure collapse (as shown in Figure 7-3 (d), Figure 7-4 (b), (e), (h) and (k)) and its thickness remained the same as the original (Figure 7-3 (e), Figure 7-4 (c), (f), (i) and (l)). Even though the balance weight increased to 100g (Figure 7-3 (c)), there was no structure damage (Figure 7-3 (d)) or thickness change of the foam (Figure 7-3 (e)). This means that the foam is able to support over 20,000 times of its own weight without structure collapse. This is equal to 0.64 Mpa, which has rarely been reported in other foam-like materials.

In order to illustrate the advantage of our designed fabrication methods, the material fabricated by the traditional freeze drying method and complete filtration was also investigated. In contrast to our designed method, the device with the 1 mL precursor was

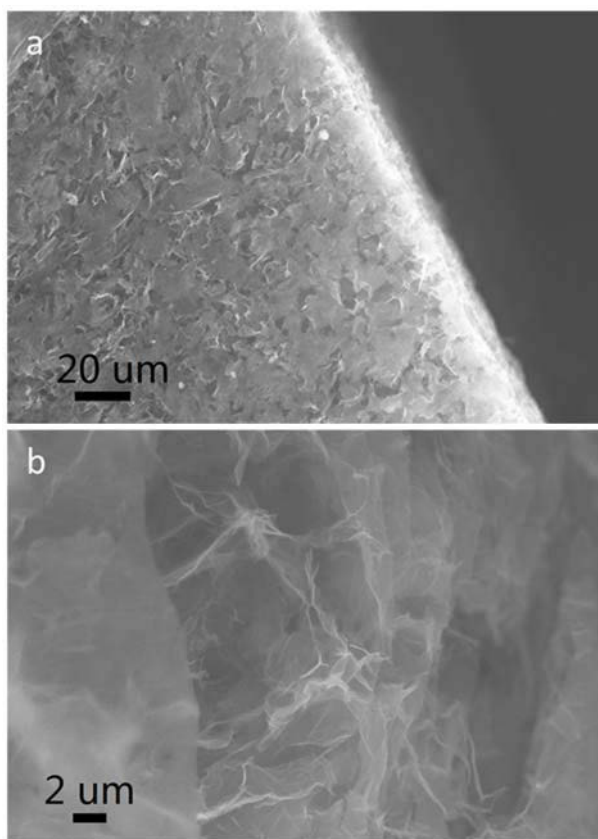


Figure 7-6 (a) SEM images of NiCo₂O₄ precursor foam after freeze drying. (b) Magnified SEM image showing NiCo₂O₄ precursor grown on GO sheets.

gradually immersed into the liquid nitrogen without adding the extra gas pressure. After freeze drying, the as-prepared foam suffered shrinkage. As shown in Figure 7-5 (a), the size of the as-prepared foam is smaller than that of the filter paper. The cross-section image (Figure 7-5 (b)) indicates that the foam has a cone-like structure. It implies that the top of the suspended solution precursor has lower density than that of the solution at the bottom. It also confirms that our method enable the uniform distribution of the suspended precursor in the solution. After adding the 20 g balancing weight (Figure 7-5 (c)), the thickness of the foam was reduced as shown in Figure 7-5 (d), and the foam structure was totally destroyed Figure 7-5 (e). It revealed the fragile nature of the foam fabricated by conventional freeze drying method.

A 3D hierarchical foam structure was clearly revealed by the SEM images of the

NiCo₂O₄@graphene precursors (Figure 7-6 (a)). As shown in Figure 7-6 (b), NiCo₂O₄ sheet precursors had grown on GO sheets. NiCo₂O₄@graphene precursors were interconnected and compressed together to form a foam structure. GO sheets served as the skeleton which supported the NiCo₂O₄ nanosheets precursors.

After annealing, the final products were characterized by XRD. Figure 7-7 (a) shows the XRD pattern of the 3D NiCo₂O₄@graphene foam. There was a characteristic peak of reduced graphene oxide at 24.8°, indicating that the interplanar spacing of d₀₀₂ is around 0.358 nm, which is slightly larger than that of standard graphite (0.335 nm). Another seven diffraction peaks were observed at 2θ of 18.9°, 31.1°, 36.6°, 44.6°, 59.1°, 64.9° and 68.3°. All the peaks can be indexed to the standard spinel NiCo₂O₄ crystalline structure, with indices of (111), (220), (311), (400), (422), (511) and (440) (JCPDF-20-0781).

After annealing, the materials retained the structure of 3D foam without any collapse (Figure 7-8 (a)). It means that the skeleton of the foam consisting of RGO sheets was not

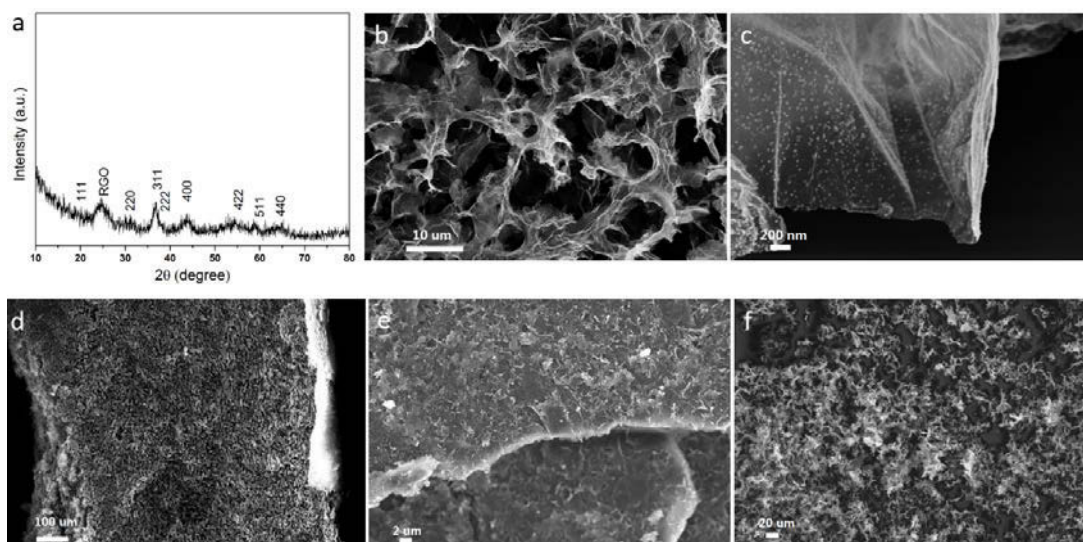


Figure 7-7 (a) XRD pattern of the NiCo₂O₄@graphene nanoarchitectures. (b) SEM images of the foam indicating a compressed structure with small-size pores, ranging from 1-10 μm. (c) The magnified SEM image of ROG sheets. (d) Cross-sectional SEM image of the foam which shows plenty of horizontal channels built by NiCo₂O₄@graphene sheets. (e) SEM image of the fully filtered NiCo₂O₄@graphene, indicating the NiCo₂O₄@graphene sheets stacked together without the porous structure and vertical channels. (f) SEM image of the 1 ml NiCo₂O₄@graphene precursor directly freeze dried without filtration, showing random structure and fragile property.

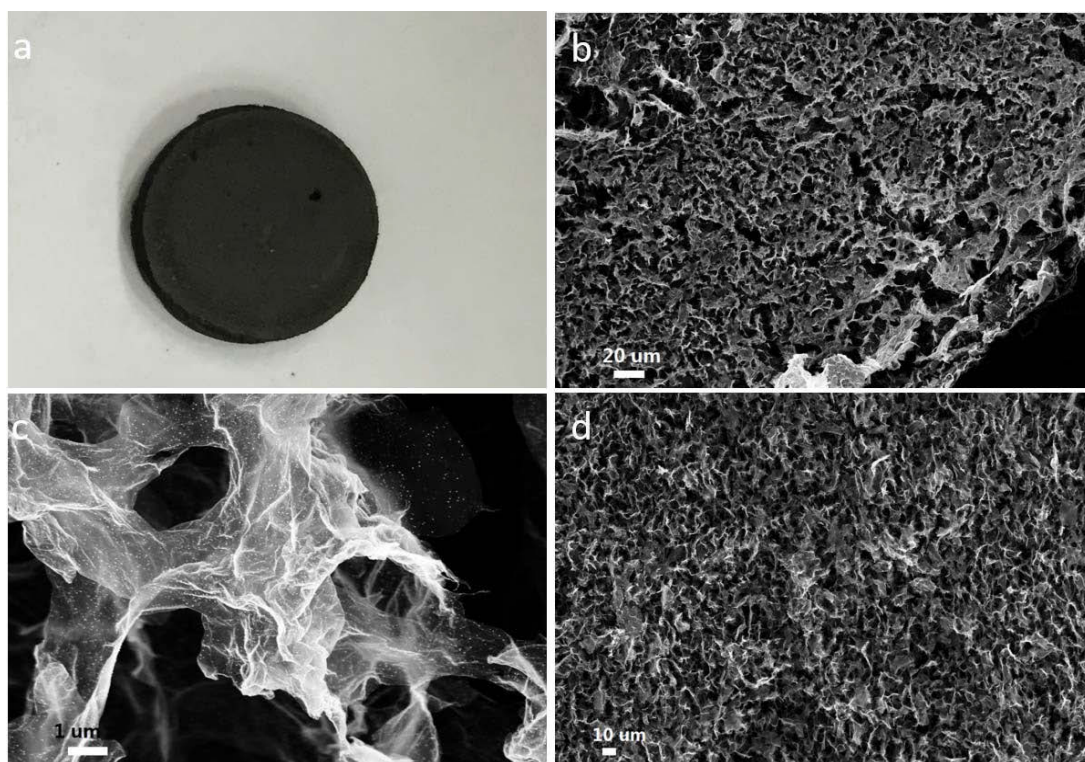


Figure 7-8 (a) Image of the material after annealing at 600 °C for 2 hours in pure argon and then 250 °C for 2 hours in air. (b) The SEM images of the foam with vertical channels with respect to the current collector. (c) Magnified SEM image of the foam showing the pore size from 1 μm to 10 μm. (d) Magnified cross-sectional SEM images (Figure 3d) of the foam.

damaged during the annealing process. The morphologies of the 3D compressed structures were well observed by scanning electron microscope (SEM). Figure 7-8 (b) clearly shows that a foam-like architecture was formed in the as-prepared material with a density of 16.7 mg cm^{-3} . In contrast to other foam materials prepared by conventional freeze casting method, our materials exhibit a compressed structure with small-size pores, ranging from 1-10 μm (Figure 7-7 (b) and Figure 7-8 (c)). The highly magnified SEM image of the material (Figure 7-7 (c) and Figure 7-8(c)) clearly shows that crystalline NiCo_2O_4 nanoparticles were uniformly distributed on RGO sheets. It is noteworthy that the foam has both vertical channels (Figure 7-7 (b) and Figure 7-8 (b)) and horizontal channels (Figure 7-7 (d) and Figure 7-8 (d)) with respect to the current collector, which were built by the RGO sheets. There are few perpendicular channels in the materials

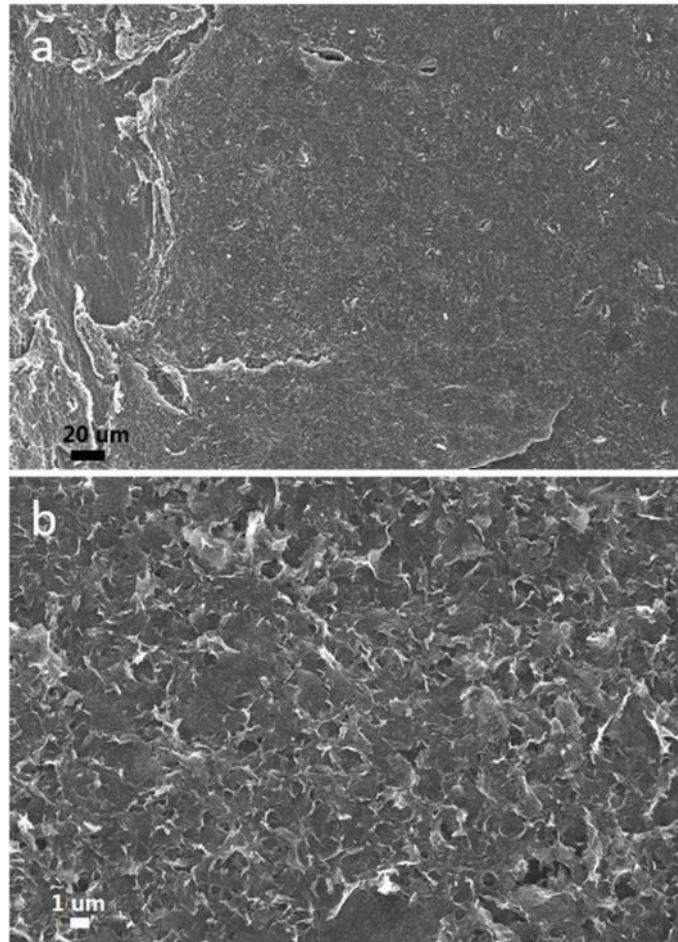


Figure 7-9 (a) Low-magnified and (b) high-magnified SEM images of the fully filtered $\text{NiCo}_2\text{O}_4@\text{graphene}$.

fabricated by the previous vacuum-assisted self-assembly method, leading to longer ion diffusion path and less power performance. The open perpendicular and horizontal channels of our materials, we believe, benefit by less impendence of ion diffusion, and the ability of the electrolyte to percolate into the inner regions of the electrode to allow for full utilization of the electrochemical surface area. The magnified cross-sectional SEM image (Figure 7-8 (d)) of the foam indicates uniform pore size distribution from the top to the bottom of the materials, which confirmed that the air pressure contributes to uniform distribution of water in the bulk. However, the fully filtered $\text{NiCo}_2\text{O}_4@\text{graphene}$ material suffered agglomeration (Figure 7-9 (a) and (b)), leading to a paper-like structure

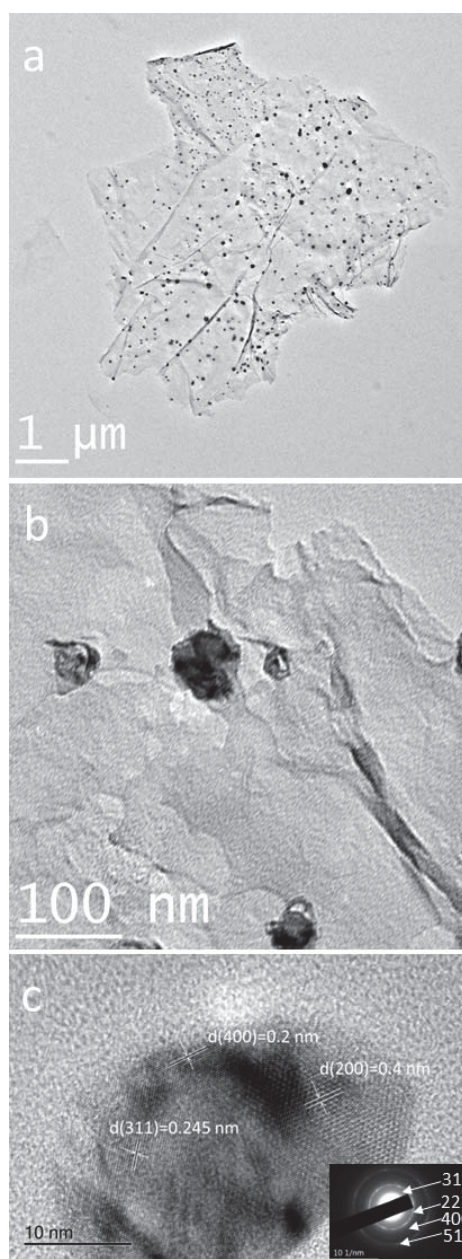


Figure 7-10 (a) TEM image of the NiCo₂O₄@graphene nanosheets of the foam, showing uniform distribution of NiCo₂O₄ on RGO sheet. (b) Magnified TEM image of the NiCo₂O₄ nanoparticles, ranging from 20 - 50 nm. (c) HRTEM image of the NiCo₂O₄ nanoparticle. The lattice spacing of 0.2 nm corresponds to the (4 0 0) lattice planes, the lattice spacing of 0.245 nm corresponds to the (3 1 1) lattice planes and the lattice spacing of 0.4 nm corresponds to the (2 0 0) lattice planes. The inset SAED pattern can be indexed to the diffraction planes of the spinel phase of NiCo₂O₄.

without the porous structure and vertical channels (Figure 7-7 (e)). By comparison, the same volume of NiCo₂O₄@graphene precursor solution was directly introduced into the freeze drying system without filtration. The SEM image (Figure 7-7 (f)) indicated that there is no aligned structure with large pore size which means the structure of this material

is fragile.

TEM images further reveal the nanostructure of the 3D NiCo₂O₄@graphene foam. RGO sheets do not stack together and NiCo₂O₄ nanoparticles are uniformly distributed on these RGO sheets (Figure 7-10 (a)). The size of NiCo₂O₄ ranges from 20 nm to 50 nm (Figure 7-10 (b)). The HRTEM image (Figure 7-10 (c)) demonstrates that the NiCo₂O₄ nanosheets are well-crystallized with the lattice spacing of 0.2 nm, 0.245nm and 0.4 nm corresponding to the lattice planes (4 0 0), (3 1 1) and (2 0 0), respectively. As shown in the inset image of Figure 7-10 (c), the corresponding crystalline diffraction rings of (3 1 1), (2 2 2), (4 0 0) and (5 1 1) in the selected area electron diffraction (SAED) pattern confirm the polycrystalline nature of the NiCo₂O₄.

The relevant elemental (Ni, Co, O and C) distribution was mapped out by using energy dispersive X-ray spectroscopy (EDS) in SEM. Figure 7-11 (a) shows an SEM image of the mapped electrode surface. As shown in Figure 7-12, the characteristic peaks of Ni, Co, O and C elements are detected. EDS spectra in Figure 5b to 5f further confirm that

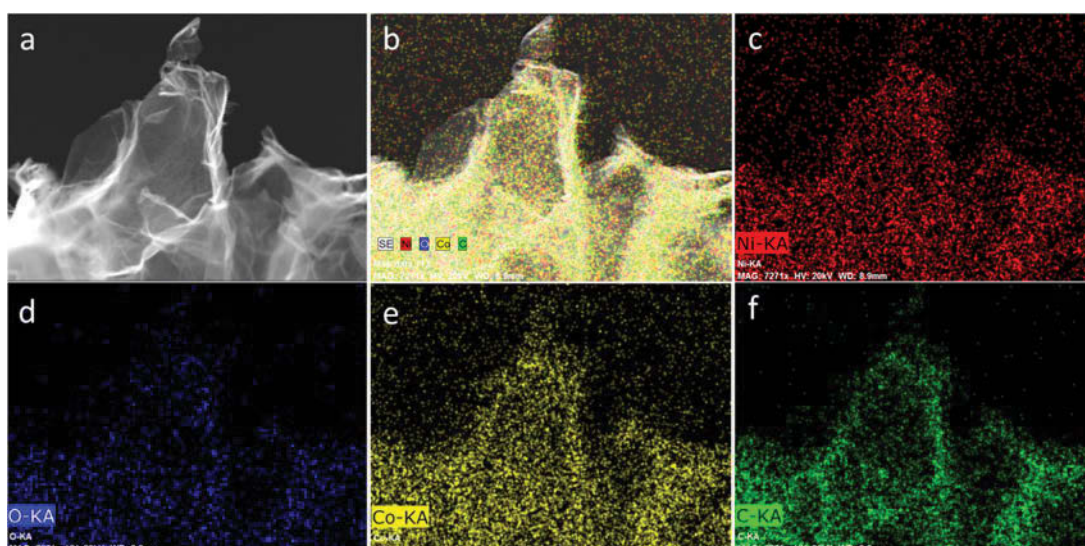


Figure 7-11 Energy dispersive X-ray spectroscopy (EDS) characterization of the 3D free-standing NiCo₂O₄@graphene foam. (a) SEM image of part of the foam; (b) elemental mapping image of the foam; (c-f) EDS Ni, O, Co and C mapping of the region as show in (a).

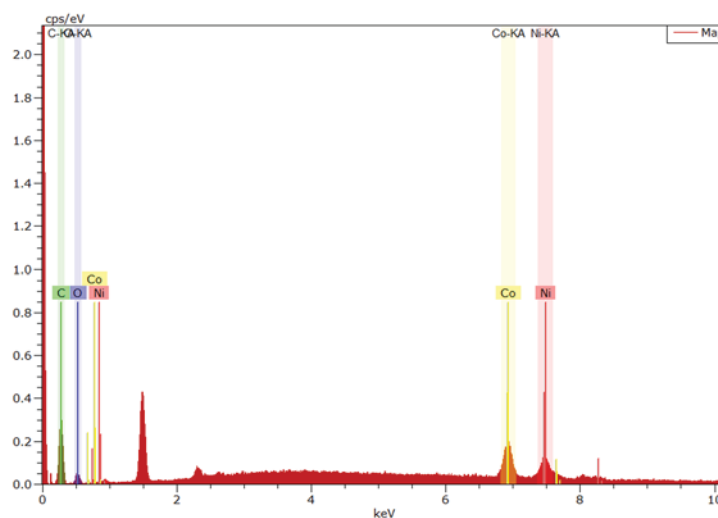


Figure 7-12 EDS spectrum captured for the region shown in Figure 6-11 (a).

NiCo₂O₄ nanoparticles are uniformly distributed on RGO sheets.

The pore-size features of the 3D NiCo₂O₄@graphene foam are further measured by nitrogen adsorption/desorption isotherms. The Brunauer–Emmett–Teller (BET) surface area is determined by the nitrogen adsorption/desorption at 77 K. Because of the 3D hierarchical porous structure, a large surface area of 252.4 m² g⁻¹ is achieved. The

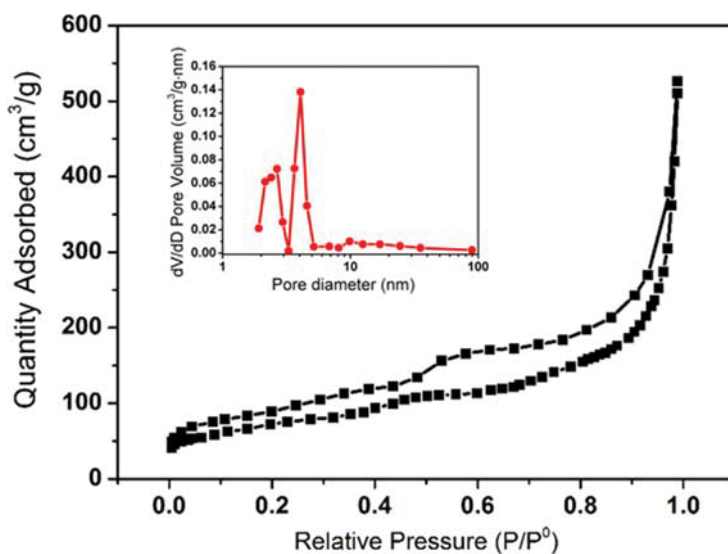


Figure 7-13 N₂ adsorption–desorption isotherms of the 3D NiCo₂O₄@graphene foam. The inset shows the pore size distribution.

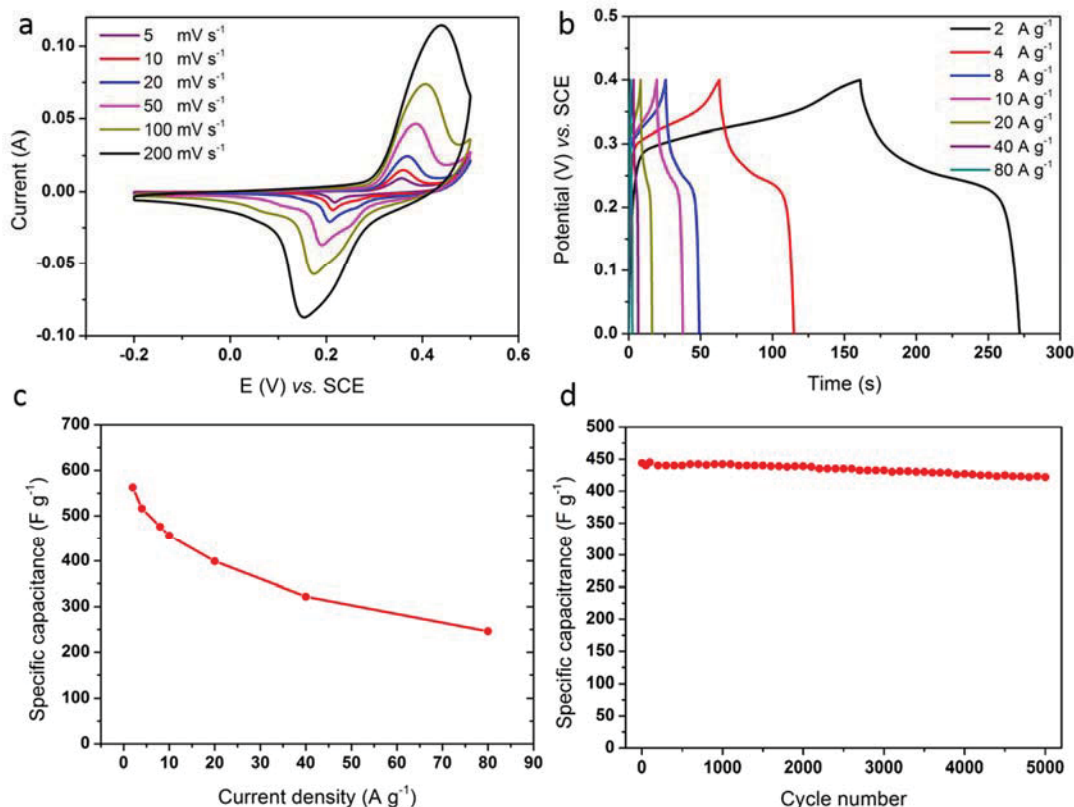


Figure 7-14 Electrochemical performance of the NiCo₂O₄@graphene foam. (a) CV curves at a scan rate of 5 mV s⁻¹ to 200 mV s⁻¹; (b) constant-current charge/discharge profile at current densities of 2 A g⁻¹ to 80 A g⁻¹; (c) specific capacitance vs. current density; (d) capacity retention vs. cycle number up to 5000 cycles at 10 A g⁻¹. All the data are taken in 2.0 M KOH electrolyte.

corresponding pore size distribution (inset of Figure 7-13) indicates a major pore size range of 2.7 nm and 3.6 nm.

The electrochemical performance of the high-rigid 3D free-standing NiCo₂O₄@graphene foam is studied as electrodes for SCs. These supercapacitors are able operated over a wide range of scan rates from 5 to 200 mV s⁻¹. The shape of the CV curves (Figure 7-14 (a)) clearly reveals the electrodes have the characteristics of pseudocapacitors. Every CV curve has a pair of redox peaks existing in the potential range from -0.2 v to 0.5 V vs. SCE at all scan rates. It still retain the good redox behaviour even at a high scan rate of 200 mV s⁻¹. The good conductivity and good ion diffusion within the electrodes was revealed by the good operation of the foam at the high scan rate. The

electrochemical characteristics of the as-prepared materials were further investigated by galvanostatic discharge-charge (DC) measurements which were carried out in 2M KOH electrolyte at various current densities. Figure 7-14 (b) shows the constant current discharge profiles at different current densities from 2 to 80 A g⁻¹. The DC testing clearly demonstrates the excellent electrochemical performance of the high-rigid 3D free-standing NiCo₂O₄@graphene foam. The specific capacitance is calculated by the formula, $C = I\Delta t/m\Delta V$, where I is the discharge current, Δt is the discharge time, ΔV is the voltage range and m is the mass of the active material. The calculated specific capacitance as a function of the discharging current density is plotted in Figure 7-14 (c). The NiCo₂O₄@graphene electrodes achieve excellent specific capacitances of 562, 516, 476, 456, 399, 322, 245 F g⁻¹, at current densities of 2, 4, 8, 10, 20, 40 and 80 A g⁻¹, respectively. The electrode is still able to maintain a high specific capacitance of 245 F g⁻¹ at the high current density of 80 A g⁻¹. This outstanding pseudocapacitor performance could be ascribed to good conductivity of the RGO skeletons and the 3D porous structure of the materials. The conductive RGO skeleton was formed by using freeze drying, which provided the high electrical conductivity medium for the electron transport. In contrast to previous free-standing materials that possess few perpendicular channels, the vertical channels and horizontal channels of our materials, which were built by the RGO sheets, optimized the ions diffusion paths. Less impedance for ion diffusion, and increased electrolyte permeability into the inner regions of the electrode were achieved by the open perpendicular and horizontal channels. The compressed 3D RGO skeleton not only avoids the aggregation of RGO sheets to allow for full utilization of the electrochemical surface area, but also achieves the controllable pore size which is suitable to serve as the electrode for SCs. The NiCo₂O₄ nanoparticles uniformly distributed on RGO sheets with a large surface area facilitates the transportation of ions in the electrode and maximizes the

utilization of NiCo₂O₄, consequently enabling the adsorption/desorption of K⁺. In order to investigate the long-term cyclability, charge–discharge cycling up to 5000 cycles was conducted at a current density of 10 A g⁻¹ (Figure 7-14 (d)). Approximately 95% of the initial capacitance is retained after 5000 cycles, demonstrating good cycling stability at high charge/discharge current density.

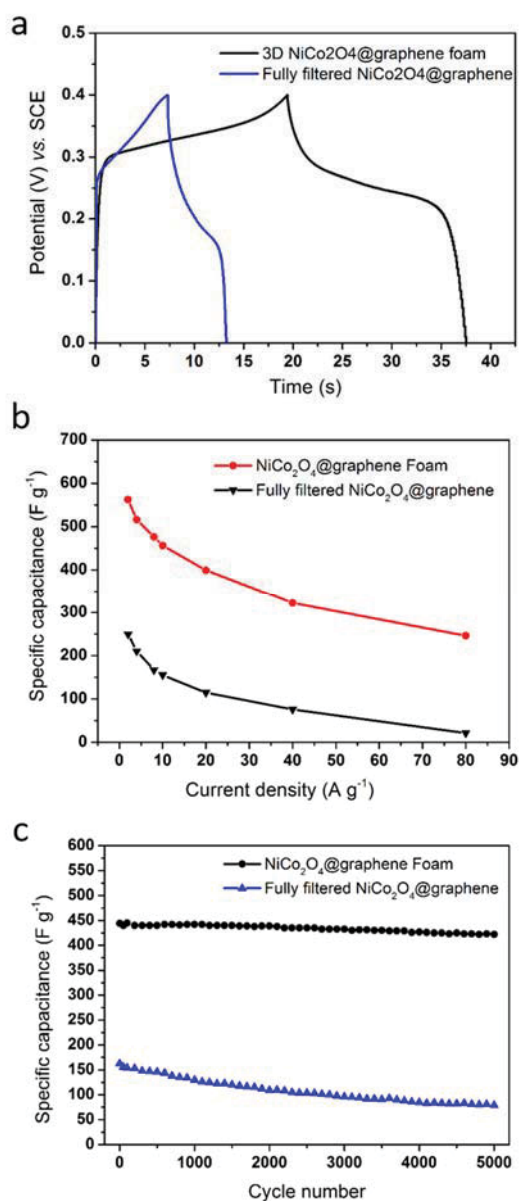


Figure 7-15 Electrochemical performance of 3D NiCo₂O₄@graphene foam and the fully filtered NiCo₂O₄@graphene (a) Charging/discharging curves at a current density of 10 A g⁻¹; (b) Specific capacitances at current densities of 2 to 80 A g⁻¹; (c) Capacities retention up to 5000 cycles at 10 A g⁻¹.

In order to further illustrate the good electrochemical performance of the 3D porous NiCo₂O₄@graphene foam as electrode materials for supercapacitors, the fully filtered NiCo₂O₄@graphene was also evaluated as the supercapacitor electrode. As shown in Figure S7, the fully filtered NiCo₂O₄@graphene electrodes exhibited poor performances at different current densities, compared with the 3D porous NiCo₂O₄@graphene foam. The specific capacity of fully filtered NiCo₂O₄@graphene also declines much further, and much faster than that of the 3D porous NiCo₂O₄@graphene foam (Figure 7-15).

7.4. Summary

In summary, we have successfully developed a novel, simple and lower cost synthetic method to prepare rigid free-standing 3D porous NiCo₂O₄@graphene foams. The synthesis process involves utilizing water as the template to form aligned pores in the foam. The external air pressure is able to control the amount and uniform distribution of water in the bulk. The hydrophilous bimetallic (Ni, Co) hydroxides introduced onto GO sheets contribute to the uniform dispersion of GO in the water during filtration. Even more importantly, that the binder was not used in the process, but a high rigid property was achieved. It is able to support over 20,000 times its own weight without the structure collapse, which is rare in previously reported foam-like materials. In contrast to other foam materials prepared by conventional freeze drying method, our materials exhibit a compressed structure with small-size pores, ranging from 1-10 μm , which effectively utilize the volume of the electrode. In the materials, the vertical and horizontal channels with respect to the current collectors, built by high conductive RGO sheets, contribute to high specific capacitance, an ultrafast charge/discharge rate, and excellent cycling stability. In particular, the rigid free-standing 3D NiCo₂O₄@graphene nanoarchitectures delivered high specific capacitances of 562 F g⁻¹ and 245 F g⁻¹ at current densities of 2 A

g^{-1} and 80 A g^{-1} , respectively.

Chapter 8. Conclusion and Future Work

8.1. General Conclusion

In this PhD thesis, the energy storage mechanism of supercapacitor has been intensively studied. Based on the studies of the energy storage mechanism, various metal oxides and the graphene-based composites were fabricated and investigated for the supercapacitor application. The specific surface area, conductivity, ion diffusion path, theoretical capacitance of the precursor materials and electrolytes play critical roles in the performance of the fabricated supercapacitors. All the factors were evaluated in this thesis for the supercapacitor applications.

RuO_2 is able to achieve a specific capacitance as high as 1580 F g^{-1} . However, RuO_2 is too expensive and too rare Ru resource to be used in industry with large-scale fabrication. Vanadium oxide is relatively inexpensive because of abundant resource, and possesses a broad range of oxidation states to enable redox reactions suitable for energy storage. Most of the previous studies just focused on the structures of the vanadium oxide and maximizing the electrolyte contact area. In order to optimize the ion diffusion path and maintained the electrolyte contact area, vanadium oxide nanoribbon was fabricated by using revised synthesis method. The as-prepared vanadium oxide nanoribbon has significant length with large contact area. A high capacitance of 453 F g^{-1} was obtained at the scan rate of 2 mV s^{-1} in 2 M NaCl electrolyte, and it still maintained a high capacitance of 201 F g^{-1} at a higher scan rate of 50 mV s^{-1} . The electrochemical performances of the vanadium oxide were found to strongly depend on the nanostructures and electrolytes.

A revised hydrothermal method assisted by high-speed stirring was used to fabricate vanadium oxide nanotube. A high capacitance of 148.5 F/g was obtained at a scan rate of

2 mV/s in 2M KCl. The electrode maintained a high capacitance of 105 F/g at a higher scan rate of 50 mV/s in 2M KCl electrolyte. The results demonstrate that the as-prepared materials with nanotubes morphology can utilize the electrolyte effectively which is of benefit to quick charging and discharging.

3D mesoporous hybrid NiCo₂O₄@graphene nanoarchitectures were successfully synthesized by a combination of freeze drying and hydrothermal reaction. Field-emission scanning electron microscopy (FESEM) and TEM analyses revealed that NiCo₂O₄@graphene nanostructures consist of a hierarchical mesoporous sheet-on-sheet nanoarchitecture with a high specific surface area of 194 m² g⁻¹. Ultrathin NiCo₂O₄ nanosheets, with a thickness of a few nanometers and mesopores ranging from 2 to 5 nm, were wrapped in graphene nanosheets and formed hybrid nanoarchitectures. When applied as electrode materials in supercapacitors, these novel 3D hierarchical porous nanoarchitectures exhibited high specific capacitances and excellent cycling stabilities at high current densities. It exhibited a high capacitance of 778 F g⁻¹ at the current density of 1 A g⁻¹, and an excellent cycling performance extending to 10000 cycles at the high current density of 10 A g⁻¹.

A high-densely assembled and aligned free-standing NiCo₂O₄@graphene 3D foam was prepared by using vacuum filtration and air compress assembly method. The controllable pore size and aligned structures were obtained by controlling the amount of water in the bulk. This free-standing foam retains the intrinsic properties of graphene sheet, such as high surface area and high electrical conductivity. Also, NiCo₂O₄ nanoparticles were uniformly distributed on the graphene sheets which built the skeletons with high surface areas. By controlling the amount of water in the precursor, it is possible to fabricate 3D NiCo₂O₄@graphene foams with a wide range of thickness and pore size. The pore size of

graphene foam is controllable and compressed to be directly used as the electrode for supercapacitor without adding binder. The external air pressure added to the solution in the container achieved the uniform distribution of water in the bulk; consequently uniform-size pores formed in the foam after removing the water by using freeze drying. This dense NiCo₂O₄@graphene material exhibited a high capacitance of 790 F g⁻¹ at a current density of 2 A g⁻¹, and an excellent cycling performance at a high current density of 10 A g⁻¹. The compression test revealed that the 3D NiCo₂O₄@graphene foam exhibited strong mechanical property which is able to support 20,000 times its own weight without the structural collapse. The novel synthesis method of such 3D foam with excellent properties paves the way to explore the application of lamellar materials like graphene in a self-supporting, metal oxide deposition and 3D form.

8.2. Future Work

The energy storage mechanism of supercapacitor can be further studied, which will guide the fabrication of the electrode materials. Due to the time limitation, the factors that determine the electrochemical performances of the as-prepared materials were not completely investigated. The electrolytes are need to be further analyzed; these play a critical role in improving the specific energy density of supercapacitors. The studies about the relationship between the conductivity and the structure of materials should be studied based on additional experiments and analysis.

Although a few metal oxide have been prepared to be used as the electrodes of supercapacitor, it is not enough to confirm which one is the best candidate electrode material. The conductivity of metal oxide is still one of the most challenging problems, which needs to be solved in the future. The cost and the process for producing these materials have not been studied in detail. Therefore, low cost and large scale fabrication

is critical for the commercialization of these materials.

Graphene is one of the outstanding electrode materials for electrochemical double layer capacitors, due to its high electric conductivity and mechanical strength, charge carrier mobility and high specific surface area. The specific capacitance of graphene has the largest theoretical electrochemical double layer capacitance of about 526 F g^{-1} . It can also provide conduction pathways to a greater area per unit mass than CNTs, which should translate into improved conductivity. However, graphene usually agglomerates together to form graphite and fails to maintain its intrinsic properties especially the large surface area. The spacer materials and related synthesis strategies will be investigated to allow the effective utilization of the high surface area of graphene.

In addition, the 2D and 3D graphene macro-structure materials contribute to the large specific surface area of electroactive materials. They contribute to the accommodation of a large amount of electroactive species for participation in the faradaic redox reactions. In this project, a new fabrication method was proposed. A compressed 3D graphene foam was successfully prepared by the as-designed method. It will be used to fabricate other 3D materials, and their electrochemical properties will also be investigated.

REFERENCES

- [1] Dhameja, S. *Newnes* **2001**.
- [2] Vazquez, S.; Lukic, S. M.; Galvan, E.; Franquelo, L. G.; Carrasco, J. M. *Industrial Electronics, IEEE Transactions on* **2010**, 57, (12), 3881-3895.
- [3] Jinrui, N.; Zhifu, W.; Qinglian, R. In *Simulation and Analysis of Performance of a Pure Electric Vehicle with a Super-capacitor*, Vehicle Power and Propulsion Conference, 2006. VPPC '06. IEEE, 6-8 Sept. 2006, 2006; pp 1-6.
- [4] Amrhein, M.; Krein, P. T. *Vehicular Technology, IEEE Transactions on* **2005**, 54, (3), 825-836.
- [5] Burke, A. F. *Proceedings of the IEEE* **2007**, 95, (4), 806-820.
- [6] Ehsani, M.; Yimin, G.; Miller, J. M. *Proceedings of the IEEE* **2007**, 95, (4), 719-728.
- [7] Fiengo, G.; Glielmo, L.; Vasca, F. *Control Systems Technology, IEEE Transactions on* **2007**, 15, (6), 1122-1130.
- [8] Jian, C.; Emadi, A. *Power Electronics, IEEE Transactions on* **2012**, 27, (1), 122-132.
- [9] Khaligh, A.; Zhihao, L. *Vehicular Technology, IEEE Transactions on* **2010**, 59, (6), 2806-2814.
- [10] Lukic, S. M.; Emadi, A. *Vehicular Technology, IEEE Transactions on* **2004**, 53, (2), 385-389.
- [11] Miller, J. M. *Power Electronics, IEEE Transactions on* **2006**, 21, (3), 756-767.
- [12] Qiuming, G.; Yaoyu, L.; Zhong-Ren, P. *Vehicular Technology, IEEE Transactions on* **2008**, 57, (6), 3393-3401.
- [13] Sulaiman, E.; Kosaka, T.; Matsui, N. *Magnetics, IEEE Transactions on* **2011**,

47, (10), 4453-4456.

[14]Sung Chul, O.; Emadi, A. *Vehicular Technology, IEEE Transactions on* **2004**, 53, (3), 912-919.

[15]Tyrus, J. M.; Long, R. M.; Kramskaya, M.; Fertman, Y.; Emadi, A. *Vehicular Technology, IEEE Transactions on* **2004**, 53, (5), 1607-1622.

[16]Salisa, A. R.; Zhang, N.; Zhu, J. G. *Vehicular Technology, IEEE Transactions on* **2011**, 60, (1), 44-54.

[17]Amjadi, Z.; Williamson, S. S. *Industrial Electronics, IEEE Transactions on* **2010**, 57, (2), 608-616.

[18]Bai, H.; Zhang, Y.; Semanson, C.; Luo, C.; Mi, C. C. *Electrical Systems in Transportation, IET* **2011**, 1, (1), 3-10.

[19]Bingzhan, Z.; Mi, C. C.; Mengyang, Z. *Vehicular Technology, IEEE Transactions on* **2011**, 60, (4), 1516-1525.

[20]Bo, G.; Mills, J. K.; Dong, S. *Vehicular Technology, IEEE Transactions on* **2011**, 60, (9), 4238-4248.

[21]Cassani, P. A.; Williamson, S. S. *Vehicular Technology, IEEE Transactions on* **2009**, 58, (8), 3938-3946.

[22]Darabi, Z.; Ferdowsi, M. *Sustainable Energy, IEEE Transactions on* **2011**, 2, (4), 501-508.

[23]Ghorbani, R.; Bibeau, E.; Filizadeh, S. *Vehicular Technology, IEEE Transactions on* **2010**, 59, (4), 2016-2020.

[24]Hajimiragha, A. H.; Canizares, C. A.; Fowler, M. W.; Moazeni, S.; Elkamel, A. *Power Systems, IEEE Transactions on* **2011**, 26, (4), 2264-2274.

[25]Mapelli, F. L.; Tarsitano, D.; Mauri, M. *Industrial Electronics, IEEE Transactions on* **2010**, 57, (2), 598-607.

- [26]Moura, S. J.; Fathy, H. K.; Callaway, D. S.; Stein, J. L. *Control Systems Technology, IEEE Transactions on* **2011**, 19, (3), 545-555.
- [27]Rotering, N.; Ilic, M. *Power Systems, IEEE Transactions on* **2011**, 26, (3), 1021-1029.
- [28]Stockar, S.; Marano, V.; Canova, M.; Rizzoni, G.; Guzzella, L. *Vehicular Technology, IEEE Transactions on* **2011**, 60, (7), 2949-2962.
- [29]Tara, E.; Shahidinejad, S.; Filizadeh, S.; Bibeau, E. *Vehicular Technology, IEEE Transactions on* **2010**, 59, (6), 2786-2794.
- [30]Xuesong, W.; Hua, B.; Zhengming, Z.; Liqiang, Y. *Vehicular Technology, IEEE Transactions on* **2011**, 60, (9), 4288-4298.
- [31]Yimin, G.; Ehsani, M. *Industrial Electronics, IEEE Transactions on* **2010**, 57, (2), 633-640.
- [32]Young-Joo, L.; Khaligh, A.; Emadi, A. *Vehicular Technology, IEEE Transactions on* **2009**, 58, (8), 3970-3980.
- [33]Jacobson, M. Z.; Colella, W. G.; Golden, D. M. *Science* **2005**, 308, (5730), 1901-1905.
- [34]Chan, C. C. *Proceedings of the IEEE* **2007**, 95, (4), 704-718.
- [35]Signorelli, R.; Ku, D. C.; Kassakian, J. G.; Schindall, J. E. *Proceedings of the IEEE* **2009**, 97, (11), 1837-1847.
- [36]Lv, Y.; Zhang, F.; Dou, Y.; Zhai, Y.; Wang, J.; Liu, H.; Xia, Y.; Tu, B.; Zhao, D. *Journal of Materials Chemistry* **2012**, 22, (1).
- [37]Li, L.; Liu, E.; Li, J.; Yang, Y.; Shen, H.; Huang, Z.; Xiang, X.; Li, W. *Journal of Power Sources* **2010**, 195, (5), 1516-1521.
- [38]Saliger, R.; Fischer, U.; Herta, C.; Fricke, J. *Journal of Non-Crystalline Solids* **1998**, 225, (0), 81-85.

- [39] Frackowiak, E.; Béguin, F. *Carbon* **2001**, 39, (6), 937-950.
- [40] Frackowiak, E.; Béguin, F. *Carbon* **2002**, 40, (10), 1775-1787.
- [41] Conway, B. E. *Kluwer Academic/Plenum Publishers, New York* **1999**.
- [42] Sun, Y.; Wu, Q.; Shi, G. *Energy & Environmental Science* **2011**, 4, (4), 1113-1132.
- [43] Gamby, J.; Taberna, P. L.; Simon, P.; Fauvarque, J. F.; Chesneau, M. *Journal of Power Sources* **2001**, 101, (1), 109-116.
- [44] Niu, C.; Sichel, E. K.; Hoch, R.; Moy, D.; Tennent, H. *Applied Physics Letters* **1997**, 70, (11), 1480-1482.
- [45] Osaka, T.; Liu, X.; Nojima, M.; Momma, T. *Journal of The Electrochemical Society* **1999**, 146, (5), 1724-1729.
- [46] Lewandowski, A.; Zajder, M.; Frackowiak, E.; Béguin, F. *Electrochimica Acta* **2001**, 46, (18), 2777-2780.
- [47] Fang, B.; Binder, L. *Journal of Power Sources* **2006**, 163, (1), 616-622.
- [48] Taberna, P. L.; Simon, P.; Fauvarque, J. F. *Journal of The Electrochemical Society* **2003**, 150, (3), A292-A300.
- [49] Ruiz, V.; Blanco, C.; Santamaría, R.; Ramos-Fernández, J. M.; Martínez-Escandell, M.; Sepúlveda-Escribano, A.; Rodríguez-Reinoso, F. *Carbon* **2009**, 47, (1), 195-200.
- [50] Baughman, R. H.; Zakhidov, A. A.; de Heer, W. A. *Science* **2002**, 297, (5582), 787-792.
- [51] Frank, S.; Poncharal, P.; Wang, Z. L.; Heer, W. A. d. *Science* **1998**, 280, (5370), 1744-1746.
- [52] Liang, W.; Bockrath, M.; Bozovic, D.; Hafner, J. H.; Tinkham, M.; Park, H. *Nature* **2001**, 411, (6838), 665-669.

- [53]Bachtold, A.; Hadley, P.; Nakanishi, T.; Dekker, C. *Science* **2001**, 294, (5545), 1317-1320.
- [54]Lee, C. Y.; Choi, W.; Han, J.-H.; Strano, M. S. *Science* **2010**, 329, (5997), 1320-1324.
- [55]Yu, M.-F.; Files, B. S.; Arepalli, S.; Ruoff, R. S. *Physical Review Letters* **2000**, 84, (24), 5552-5555.
- [56]Treacy, M. M. J.; Ebbesen, T. W.; Gibson, J. M. *Nature* **1996**, 381, (6584), 678-680.
- [57]Hiralal, P.; Wang, H.; Unalan, H. E.; Liu, Y.; Rouvala, M.; Wei, D.; Andrew, P.; Amaratunga, G. A. J. *Journal of Materials Chemistry* **2011**, 21, (44), 17810-17815.
- [58]Futaba, D. N.; Hata, K.; Yamada, T.; Hiraoka, T.; Hayamizu, Y.; Kakudate, Y.; Tanaike, O.; Hatori, H.; Yumura, M.; Iijima, S. *Nat Mater* **2006**, 5, (12), 987-994.
- [59]Yoon, B.-J.; Jeong, S.-H.; Lee, K.-H.; Seok Kim, H.; Gyung Park, C.; Hun Han, J. *Chemical Physics Letters* **2004**, 388, (1-3), 170-174.
- [60]Marschilok, A.; Lee, C.-Y.; Subramanian, A.; Takeuchi, K. J.; Takeuchi, E. S. *Energy & Environmental Science* **2011**, 4, (8), 2943-2951.
- [61]An, K. H.; Kim, W. S.; Park, Y. S.; Choi, Y. C.; Lee, S. M.; Chung, D. C.; Bae, D. J.; Lim, S. C.; Lee, Y. H. *Advanced Materials* **2001**, 13, (7), 497-500.
- [62]Du, C.; Pan, N. *Journal of Power Sources* **2006**, 160, (2), 1487-1494.
- [63]An, K. H.; Kim, W. S.; Park, Y. S.; Moon, J. M.; Bae, D. J.; Lim, S. C.; Lee, Y. S.; Lee, Y. H. *Advanced Functional Materials* **2001**, 11, (5), 387-392.
- [64]Cheng, Q.; Tang, J.; Ma, J.; Zhang, H.; Shinya, N.; Qin, L.-C. *Physical Chemistry Chemical Physics* **2011**, 13, (39), 17615-17624.
- [65]Jeong, H. Y.; Lee, D.-S.; Choi, H. K.; Lee, D. H.; Kim, J.-E.; Lee, J. Y.; Lee, W. J.; Kim, S. O.; Choi, S.-Y. *Applied Physics Letters* **2010**, 96, (21), 213105-3.

- [66]Jia, X.; Campos-Delgado, J.; Terrones, M.; Meunier, V.; Dresselhaus, M. S. *Nanoscale* **2011**, 3, (1), 86-95.
- [67]Yu, D.; Dai, L. *The Journal of Physical Chemistry Letters* **2009**, 1, (2), 467-470.
- [68]Zhang, K.; Ang, B. T.; Zhang, L. L.; Zhao, X. S.; Wu, J. *Journal of Materials Chemistry* **2011**, 21, (8).
- [69]Tung, V. C.; Chen, L.-M.; Allen, M. J.; Wassei, J. K.; Nelson, K.; Kaner, R. B.; Yang, Y. *Nano Letters* **2009**, 9, (5), 1949-1955.
- [70]Cote, L. J.; Kim, F.; Huang, J. *Journal of the American Chemical Society* **2009**, 131, (3), 1043-1049.
- [71]Boukhalifa, S.; Evanoff, K.; Yushin, G. *Energy & Environmental Science* **2012**, 5, (5), 6872-6879.
- [72]Lang, X.; Hirata, A.; Fujita, T.; Chen, M. *Nature nanotechnology* **2011**, 6, (4), 232-236.
- [73]Yu, G.; Hu, L.; Vosgueritchian, M.; Wang, H.; Xie, X.; McDonough, J. R.; Cui, X.; Cui, Y.; Bao, Z. *Nano letters* **2011**, 11, (7), 2905-2911.
- [74]Hu, C.-C.; Chang, K.-H.; Lin, M.-C.; Wu, Y.-T. *Nano Letters* **2006**, 6, (12), 2690-2695.
- [75]Hu, C.-C.; Chen, W.-C.; Chang, K.-H. *Journal of The Electrochemical Society* **2004**, 151, (2), A281-A290.
- [76]Park, J. H.; Ko, J. M.; Park, O. O. *Journal of The Electrochemical Society* **2003**, 150, (7), A864-A867.
- [77]Bi, R.-R.; Wu, X.-L.; Cao, F.-F.; Jiang, L.-Y.; Guo, Y.-G.; Wan, L.-J. *The Journal of Physical Chemistry C* **2010**, 114, (6), 2448-2451.
- [78]Min, M.; Machida, K.; Jang, J. H.; Naoi, K. *Journal of The Electrochemical*

Society **2006**, 153, (2), A334-A338.

[79]Zang, J.; Bao, S.-J.; Li, C. M.; Bian, H.; Cui, X.; Bao, Q.; Sun, C. Q.; Guo, J.; Lian, K. *The Journal of Physical Chemistry C* **2008**, 112, (38), 14843-14847.

[80]Yang, Y.; Kim, D.; Yang, M.; Schmuki, P. *Chemical Communications* **2011**, 47, (27), 7746-7748.

[81]Livage, J. *Materials* **2010**, 3, (8), 4175-4195.

[82]Yu, G.; Hu, L.; Liu, N.; Wang, H.; Vosgueritchian, M.; Yang, Y.; Cui, Y.; Bao, Z. *Nano letters* **2011**, 11, (10), 4438-4442.

[83]Li, G.-R.; Feng, Z.-P.; Ou, Y.-N.; Wu, D.; Fu, R.; Tong, Y.-X. *Langmuir* **2010**, 26, (4), 2209-2213.

[84]Cui, B.; Lin, H.; Li, J. B.; Li, X.; Yang, J.; Tao, J. *Advanced Functional Materials* **2008**, 18, (9), 1440-1447.

[85]Zhang, G. Q.; Wu, H. B.; Hoster, H. E.; Chan-Park, M. B.; Lou, X. W. D. *Energy & Environmental Science* **2012**, 5, (11), 9453-9456.

[86]Wei, T. Y.; Chen, C. H.; Chien, H. C.; Lu, S. Y.; Hu, C. C. *Advanced materials* **2010**, 22, (3), 347-351.

[87]Yuan, C.; Li, J.; Hou, L.; Zhang, X.; Shen, L.; Lou, X. W. D. *Advanced Functional Materials* **2012**, 22, (21), 4592-4597.

[88]Zhang, G.; Lou, X. W. D. *Advanced Materials* **2012**.

[89]Zhang, G.; Lou, X. W. D. *Scientific reports* **2013**, 3.

[90]Wu, M.; Snook, G. A.; Chen, G. Z.; Fray, D. J. *Electrochemistry communications* **2004**, 6, (5), 499-504.

[91]Sarangapani, S.; Tilak, B.; Chen, C. P. *Journal of the Electrochemical Society* **1996**, 143, (11), 3791-3799.

[92]Ramani, M.; Haran, B. S.; White, R. E.; Popov, B. N. *Journal of The*

Electrochemical Society **2001**, 148, (4), A374-A380.

[93] Yan, J.; Fan, Z.; Wei, T.; Cheng, J.; Shao, B.; Wang, K.; Song, L.; Zhang, M. *Journal of Power Sources* **2009**, 194, (2), 1202-1207.

[94] Reddy, A. L. M.; Shaijumon, M. M.; Gowda, S. R.; Ajayan, P. M. *The Journal of Physical Chemistry C* **2009**, 114, (1), 658-663.

[95] Kim, J.-H.; Lee, K. H.; Overzet, L. J.; Lee, G. S. *Nano letters* **2011**, 11, (7), 2611-2617.

[96] Amade, R.; Jover, E.; Caglar, B.; Mutlu, T.; Bertran, E. *Journal of Power Sources* **2011**, 196, (13), 5779-5783.

[97] Hou, Y.; Cheng, Y.; Hobson, T.; Liu, J. *Nano letters* **2010**, 10, (7), 2727-2733.

[98] Chen, S.; Zhu, J.; Wu, X.; Han, Q.; Wang, X. *ACS nano* **2010**, 4, (5), 2822-2830.

[99] Peng, L.; Peng, X.; Liu, B.; Wu, C.; Xie, Y.; Yu, G. *Nano Letters* **2013**.

[100] Becker, H. I., Low voltage electrolytic capacitor. Google Patents: 1957.

[101] Boos, D. L., Electrolytic capacitor having carbon paste electrodes. Google Patents: 1970.

[102] Conway, B. E. *Journal of the Electrochemical Society* **1991**, 138, (6), 1539-1548.

[103] Caumont, O.; Le Moigne, P.; Rombaut, C.; Muneret, X.; Lenain, P. *Energy Conversion, IEEE Transactions on* **2000**, 15, (3), 354-360.

[104] Szymborski, J. In *Lead-acid batteries for use in submarine applications*, Autonomous Underwater Vehicles, 2002. Proceedings of the 2002 Workshop on, 2002, 2002; pp 11-17.

[105] Wang, D.; Wu, Z.-h.; Xu, G.; Song, M.; Peng, X.-t. In *Real-time power control of superconducting magnetic energy storage*, Power System Technology

- (POWERCON), 2012 IEEE International Conference on, 2012; IEEE: pp 1-5.
- [106] Louie, H.; Strunz, K. *Applied Superconductivity, IEEE Transactions on* **2007**, 17, (2), 2361-2364.
- [107] Huang, J.; Qiao, R.; Sumpter, B. G.; Meunier, V. *Journal of Materials Research* **2010**, 25, (08), 1469-1475.
- [108] Zhang, L. L.; Zhao, X. S. *Chemical Society Reviews* **2009**, 38, (9), 2520-2531.
- [109] Torrie, G. M.; Valleau, J. P. *The Journal of Physical Chemistry* **1982**, 86, (16), 3251-3257.
- [110] Martynov, G. A. *Berlin ; New York : Springer-Verlag* **1983**.
- [111] Srinivasan, S., Electrode/electrolyte interfaces: Structure and kinetics of charge transfer. In *Fuel Cells*, Springer: 2006; pp 27-92.
- [112] Karden, E.; Buller, S.; De Doncker, R. W. *Electrochimica Acta* **2002**, 47, (13-14), 2347-2356.
- [113] Zubieta, L.; Bonert, R. *Industry Applications, IEEE Transactions on* **2000**, 36, (1), 199-205.
- [114] New, D. A. *MIT Thesis* **2002**.
- [115] Buller, S.; Karden, E.; Kok, D.; De Doncker, R. W. *Industry Applications, IEEE Transactions on* **2002**, 38, (6), 1622-1626.
- [116] R, d. L. *Electrochimica Acta* **1964**, 9, (9), 1231-1245.
- [117] Barcia, O. E.; D'Elia, E.; Frateur, I.; Mattos, O. R.; Pébère, N.; Tribollet, B. *Electrochimica Acta* **2002**, 47, (13-14), 2109-2116.
- [118] Bohlen, O.; Kowal, J.; Sauer, D. U. *Journal of Power Sources* **2007**, 172, (1), 468-475.
- [119] Kötz, R.; Carlen, M. *Electrochimica Acta* **2000**, 45, (15-16), 2483-2498.

- [120] Kim, S.; Choi, W.; Lee, K.; Choi, S. *Power Electronics, IEEE Transactions on* **2011**, 26, (11), 3377-3385.
- [121] Buller, S.; Thele, M.; De Doncker, R. W. A. A.; Karden, E. *Industry Applications, IEEE Transactions on* **2005**, 41, (3), 742-747.
- [122] Buller, S.; Thele, M.; Karden, E.; De Doncker, R. W. *Journal of Power Sources* **2003**, 113, (2), 422-430.
- [123] Buller, S.; Thele, M.; De Doncker, R.; Karden, E. *IEEE Trans. Ind. Appl* **2005**, 41, (3), 742-747.
- [124] Bohlen, O.; Kowal, J.; Dirk Uwe, S. *Journal of Power Sources* **2007**, 173, (1), 626-632.
- [125] Stoller, M. D.; Park, S.; Zhu, Y.; An, J.; Ruoff, R. S. *Nano Letters* **2008**, 8, (10), 3498-3502.
- [126] Wang, Y.; Shi, Z.; Huang, Y.; Ma, Y.; Wang, C.; Chen, M.; Chen, Y. *The Journal of Physical Chemistry C* **2009**, 113, (30), 13103-13107.
- [127] Yang, S.-Y.; Chang, K.-H.; Tien, H.-W.; Lee, Y.-F.; Li, S.-M.; Wang, Y.-S.; Wang, J.-Y.; Ma, C.-C. M.; Hu, C.-C. *Journal of Materials Chemistry* **2011**, 21, (7), 2374-2380.
- [128] Guo, C. X.; Li, C. M. *Energy & Environmental Science* **2011**, 4, (11).
- [129] Si, P.; Ding, S.; Lou, X.-W. D.; Kim, D.-H. *Rsc Advances* **2011**, 1, (7), 1271-1278.
- [130] Cai, D.; Song, M.; Xu, C. *Advanced Materials* **2008**, 20, (9), 1706-1709.
- [131] Kim, Y.-K.; Min, D.-H. *Langmuir* **2009**, 25, (19), 11302-11306.
- [132] Hong, T.-K.; Lee, D. W.; Choi, H. J.; Shin, H. S.; Kim, B.-S. *ACS Nano* **2010**, 4, (7), 3861-3868.
- [133] Li, C.; Li, Z.; Zhu, H.; Wang, K.; Wei, J.; Li, X.; Sun, P.; Zhang, H.; Wu, D.

The Journal of Physical Chemistry C **2010**, 114, (33), 14008-14012.

[134] Campos-Delgado, J.; Romo-Herrera, J. M.; Jia, X.; Cullen, D. A.; Muramatsu, H.; Kim, Y. A.; Hayashi, T.; Ren, Z.; Smith, D. J.; Okuno, Y.; Ohba, T.; Kanoh, H.; Kaneko, K.; Endo, M.; Terrones, H.; Dresselhaus, M. S.; Terrones, M. *Nano Letters* **2008**, 8, (9), 2773-2778.

[135] Yoo, J. J.; Balakrishnan, K.; Huang, J.; Meunier, V.; Sumpter, B. G.; Srivastava, A.; Conway, M.; Mohana Reddy, A. L.; Yu, J.; Vajtai, R.; Ajayan, P. M. *Nano Letters* **2011**, 11, (4), 1423-1427.

[136] Lee, D. H.; Kim, J. E.; Han, T. H.; Hwang, J. W.; Jeon, S.; Choi, S.-Y.; Hong, S. H.; Lee, W. J.; Ruoff, R. S.; Kim, S. O. *Advanced Materials* **2010**, 22, (11), 1247-1252.

[137] Terrones, M. *Nature* **2009**, 458, (7240), 845-846.

[138] Kosynkin, D. V.; Higginbotham, A. L.; Sinitskii, A.; Lomeda, J. R.; Dimiev, A.; Price, B. K.; Tour, J. M. *Nature* **2009**, 458, (7240), 872-876.

[139] Jiao, L.; Zhang, L.; Wang, X.; Diankov, G.; Dai, H. *Nature* **2009**, 458, (7240), 877-880.

[140] Cano-Márquez, A. G.; Rodríguez-Macías, F. J.; Campos-Delgado, J.; Espinosa-González, C. G.; Tristán-López, F.; Ramírez-González, D.; Cullen, D. A.; Smith, D. J.; Terrones, M.; Vega-Cantú, Y. I. *Nano Letters* **2009**, 9, (4), 1527-1533.

[141] Quyet Huu, D.; Changchun, Z.; Chuck, Z.; Ben, W.; Jim, Z. *Nanotechnology* **2011**, 22, (36), 365402.

[142] Gu, G.; Schmid, M.; Chiu, P.-W.; Minett, A.; Fraysse, J.; Kim, G.-T.; Roth, S.; Kozlov, M.; Munoz, E.; Baughman, R. H. *Nat Mater* **2003**, 2, (5), 316-319.

[143] Bonso, J. S.; Rahy, A.; Perera, S. D.; Nour, N.; Seitz, O.; Chabal, Y. J.;

- Balkus Jr, K. J.; Ferraris, J. P.; Yang, D. J. *Journal of Power Sources* **2012**, 203, (0), 227-232.
- [144] Reddy, R. N.; Reddy, R. G. *Journal of Power Sources* **2006**, 156, (2), 700-704.
- [145] Su, Q.; Huang, C. K.; Wang, Y.; Fan, Y. C.; Lu, B. A.; Lan, W.; Wang, Y. Y.; Liu, X. Q. *Journal of Alloys and Compounds* **2009**, 475, (1–2), 518-523.
- [146] FilipeLS Mello, L. C., EduardoPadrón Hernández, AndréaMDuarte de Farias, and Marco A Fraga. *Nanoscale Res Lett.* **2010**, 5(6), 1002–1009.
- [147] Cui, C.-J.; Wu, G.-M.; Yang, H.-Y.; She, S.-F.; Shen, J.; Zhou, B.; Zhang, Z.-H. *Electrochimica Acta* **2010**, 55, (28), 8870-8875.
- [148] Hu, C.-C.; Huang, C.-M.; Chang, K.-H. *Journal of Power Sources* **2008**, 185, (2), 1594-1597.
- [149] Hu, C.-C.; Chang, K.-H.; Huang, C.-M.; Li, J.-M. *Journal of The Electrochemical Society* **2009**, 156, (11), D485-D489.
- [150] Ahmad, A. L.; Koohestani, B.; Bhatia, S.; Ooi, B. S. *Journal of Sol-Gel Science and Technology* **2010**, 56, (3), 327-332.
- [151] Zhou, X.; Wu, G.; Gao, G.; Cui, C.; Yang, H.; Shen, J.; Zhou, B.; Zhang, Z. *Electrochimica Acta* **2012**, 74, (0), 32-38.
- [152] Ghimbeu, C. M.; Raymundo-Pinero, E.; Fioux, P.; Beguin, F.; Vix-Guterl, C. *Journal of Materials Chemistry* **2011**, 21, (35), 13268-13275.
- [153] Xia, H.; Meng, Y. S.; Yuan, G.; Cui, C.; Lu, L. *Electrochemical and Solid-State Letters* **2012**, 15, (4), A60-A63.
- [154] Zheng, J.; Cygan, P.; Jow, T. *Journal of the Electrochemical Society* **1995**, 142, (8), 2699-2703.
- [155] Chang, K.-H.; Hu, C.-C. *Applied physics letters* **2006**, 88, (19), 3102.

- [156] Hu, C.-C.; Wang, C.-W.; Chang, K.-H.; Chen, M.-G. *Nanotechnology* **2015**, 26, (27), 274004.
- [157] Wei, W.; Cui, X.; Chen, W.; Ivey, D. G. *Chemical Society Reviews* **2011**, 40, (3), 1697-1721.
- [158] Tang, P.-Y.; Zhao, Y.-Q.; Wang, Y.-M.; Xu, C.-L. *Nanoscale* **2013**, 5, (17), 8156-8163.
- [159] Xu, M.; Kong, L.; Zhou, W.; Li, H. *The Journal of Physical Chemistry C* **2007**, 111, (51), 19141-19147.
- [160] Reddy, R. N.; Reddy, R. G. *Journal of Power Sources* **2003**, 124, (1), 330-337.
- [161] Wang, L.; Omomo, Y.; Sakai, N.; Fukuda, K.; Nakai, I.; Ebina, Y.; Takada, K.; Watanabe, M.; Sasaki, T. *Chemistry of materials* **2003**, 15, (15), 2873-2878.
- [162] Zhao, Y.-Q.; Zhao, D.-D.; Tang, P.-Y.; Wang, Y.-M.; Xu, C.-L.; Li, H.-L. *Materials Letters* **2012**, 76, 127-130.
- [163] Wang, Y.-L.; Zhao, Y.-Q.; Xu, C.-L. *Journal of Solid State Electrochemistry* **2012**, 16, (3), 829-834.
- [164] Xu, C.; Zhao, Y.; Yang, G.; Li, F.; Li, H. *Chem. Commun.* **2009**, (48), 7575-7577.
- [165] Bao, L.; Zang, J.; Li, X. *Nano letters* **2011**, 11, (3), 1215-1220.
- [166] Shao, J.; Li, X.; Qu, Q.; Zheng, H. *Journal of Power Sources* **2012**, 219, 253-257.
- [167] Pan, A.; Wu, H. B.; Yu, L.; Zhu, T.; Lou, X. W. *ACS applied materials & interfaces* **2012**, 4, (8), 3874-3879.
- [168] Boldrin, P.; Hebb, A. K.; Chaudhry, A. A.; Otley, L.; Thiebaut, B.; Bishop, P.; Darr, J. A. *Industrial & engineering chemistry research* **2007**, 46, (14), 4830-

4838.

[169] Liu, X.; Shi, S.; Xiong, Q.; Li, L.; Zhang, Y.; Tang, H.; Gu, C.; Wang, X.; Tu, J. *ACS applied materials & interfaces* **2013**, 5, (17), 8790-8795.

[170] Ratha, S.; Rout, C. S. *ACS applied materials & interfaces* **2013**, 5, (21), 11427-11433.

[171] Qiu, L.; Liu, J. Z.; Chang, S. L.; Wu, Y.; Li, D. *Nature communications* **2012**, 3, 1241.

[172] Hu, H.; Zhao, Z.; Wan, W.; Gogotsi, Y.; Qiu, J. *Advanced Materials* **2013**.

[173] Zhao, Y.; Hu, C.; Hu, Y.; Cheng, H.; Shi, G.; Qu, L. *Angewandte Chemie* **2012**, 124, (45), 11533-11537.

[174] Zhang, X.; Sui, Z.; Xu, B.; Yue, S.; Luo, Y.; Zhan, W.; Liu, B. *journal of materials chemistry* **2011**, 21, (18), 6494-6497.

[175] Xu, Y.; Lin, Z.; Huang, X.; Liu, Y.; Huang, Y.; Duan, X. *ACS nano* **2013**, 7, (5), 4042-4049.

[176] Li, Z.; Wang, J.; Liu, S.; Liu, X.; Yang, S. *Journal of power sources* **2011**, 196, (19), 8160-8165.

[177] Zhou, X.; Yin, Y.-X.; Wan, L.-J.; Guo, Y.-G. *Chemical Communications* **2012**, 48, (16), 2198-2200.

[178] Wang, X.; Liu, S.; Wang, H.; Tu, F.; Fang, D.; Li, Y. *Journal of Solid State Electrochemistry* **2012**, 16, (11), 3593-3602.

[179] Ghaffari, M.; Zhou, Y.; Xu, H.; Lin, M.; Kim, T. Y.; Ruoff, R. S.; Zhang, Q. *Advanced Materials* **2013**, 25, (35), 4879-4885.

[180] Sumboja, A.; Foo, C. Y.; Wang, X.; Lee, P. S. *Advanced materials* **2013**, 25, (20), 2809-2815.

[181] Niu, Z.; Chen, J.; Hng, H. H.; Ma, J.; Chen, X. *Advanced Materials* **2012**,

24, (30), 4144-4150.

[182] Chen, W.; Yan, L. *Nanoscale* **2011**, 3, (8), 3132-3137.

[183] Wang, D.; Kou, R.; Choi, D.; Yang, Z.; Nie, Z.; Li, J.; Saraf, L. V.; Hu, D.; Zhang, J.; Graff, G. L. *ACS nano* **2010**, 4, (3), 1587-1595.

[184] Chandrappa, G. T.; Steunou, N.; Cassaignon, S.; Bauvais, C.; Livage, J. *Catalysis Today* **2003**, 78, (1–4), 85-89.

[185] FilipeLS Mello, L. C., EduardoPadrón Hernández, AndréaMDuarte de Farias, and Marco A Fraga. *Nanoscale Res Lett.* **2010**, 5(6), 1002–1009.

[186] Petkov, V.; Zavalij, P. Y.; Lutta, S.; Whittingham, M. S.; Parvanov, V.; Shastri, S. *Physical Review B* **2004**, 69, (8), 085410.

[187] Lao, Z. J.; Konstantinov, K.; Tournaire, Y.; Ng, S. H.; Wang, G. X.; Liu, H. K. *Journal of Power Sources* **2006**, 162, (2), 1451-1454.

[188] Liu, P.; Lee, S. H.; Tracy, C. E.; Yan, Y.; Turner, J. A. *Advanced Materials* **2002**, 14, (1), 27-30.

[189] G. T. Chandrappa, N. S. J. L. *Nature* **2002**, 416, 702.

[190] Durupthy, O.; Jaber, M.; Steunou, N.; Maquet, J.; Chandrappa, G. T.; Livage, J. *Chem Mater* **2005**, 17, (25), 6395-6402.

[191] Yun, Y. J.; Kim, B. H.; Hong, W. G.; Kim, C. H.; Kim, Y. Y.; Jeong, E.-j.; Jang, W. I.; Yu, H. Y. *Nanoscale* **2012**, 4, (5), 1636-1640.

[192] Kudo, T.; Ikeda, Y.; Watanabe, T.; Hibino, M.; Miyayama, M.; Abe, H.; Kajita, K. *Solid State Ionics* **2002**, 152–153, (0), 833-841.

[193] Spahr, M. E.; Stoschitzki - Bitterli, P.; Nesper, R.; Haas, O.; Novák, P. *Journal of The Electrochemical Society* **1999**, 146, (8), 2780-2783.

[194] Legendre, J.-J.; Livage, J. *Journal of Colloid and Interface Science* **1983**, 94, (1), 75-83.

- [195] Wörle, M.; Krumeich, F.; Bieri, F.; Muhr, H.-J.; Nesper, R. *Zeitschrift für anorganische und allgemeine Chemie* **2002**, 628, (12), 2778-2784.
- [196] Liu, Y.; DeGroot, D.; Schindler, J.; Kannewurf, C.; Kanatzidis, M. *Chemistry of materials* **1991**, 3, (6), 992-994.
- [197] Chen, Z.; Augustyn, V.; Wen, J.; Zhang, Y.; Shen, M.; Dunn, B.; Lu, Y. *Advanced Materials* **2011**, 23, (6), 791-795.
- [198] Jae Woong, S.; Youngho, C.; Seog-Joo, K.; Sang Won, M.; Kyeon, H. *Applied Superconductivity, IEEE Transactions on* **2013**, 23, (3), 5701205-5701205.
- [199] Ise, T.; Kita, M.; Taguchi, A. *Applied Superconductivity, IEEE Transactions on* **2005**, 15, (2), 1915-1918.
- [200] Jisung, L.; Sangkwon, J.; Young-Hee, H.; Byung-Jun, P. *Applied Superconductivity, IEEE Transactions on* **2011**, 21, (3), 2221-2224.
- [201] Subkhan, M.; Komori, M. *Applied Superconductivity, IEEE Transactions on* **2011**, 21, (3), 1485-1488.
- [202] Zheng, W.; Zhixiang, Z.; Yang, Z. *Applied Superconductivity, IEEE Transactions on* **2013**, 23, (3), 5701505-5701505.
- [203] Padimiti, D. S.; Chowdhury, B. H. In *Superconducting Magnetic Energy Storage System (SMES) for Improved Dynamic System Performance*, Power Engineering Society General Meeting, 2007. IEEE, 24-28 June 2007, 2007; pp 1-6.
- [204] Swider, D. J. *Energy Conversion, IEEE Transactions on* **2007**, 22, (1), 95-102.
- [205] Lemofouet, S.; Rufer, A. *Industrial Electronics, IEEE Transactions on* **2006**, 53, (4), 1105-1115.

- [206] Simon, P.; Gogotsi, Y. *Nature materials* **2008**, 7, (11), 845-854.
- [207] Hall, P. J.; Mirzaeian, M.; Fletcher, S. I.; Sillars, F. B.; Rennie, A. J.; Shitta-Bey, G. O.; Wilson, G.; Cruden, A.; Carter, R. *Energy & Environmental Science* **2010**, 3, (9), 1238-1251.
- [208] Chan, C. K.; Peng, H.; Twisten, R. D.; Jarausch, K.; Zhang, X. F.; Cui, Y. *Nano Letters* **2007**, 7, (2), 490-495.
- [209] Li, W.; Garofalini, S. H. *Journal of The Electrochemical Society* **2005**, 152, (2), A364-A369.
- [210] Zhai, Y.; Dou, Y.; Zhao, D.; Fulvio, P. F.; Mayes, R. T.; Dai, S. *Advanced Materials* **2011**, 23, (42), 4828-4850.
- [211] Huang, X.; Zeng, Z.; Fan, Z.; Liu, J.; Zhang, H. *Advanced Materials* **2012**, 24, (45), 5979-6004.
- [212] Liu, C.; Yu, Z.; Neff, D.; Zhamu, A.; Jang, B. Z. *Nano Letters* **2010**, 10, (12), 4863-4868.
- [213] Chen, W.; Rakhi, R.; Hu, L.; Xie, X.; Cui, Y.; Alshareef, H. *Nano letters* **2011**, 11, (12), 5165-5172.
- [214] Yan, L.; Wu, S.; Chen, W. *Journal of Materials Chemistry A* **2013**.
- [215] Mahmood, N.; Zhang, C.; Yin, H.; Hou, Y. *Journal of Materials Chemistry A* **2014**.
- [216] Zhi, M.; Xiang, C.; Li, J.; Li, M.; Wu, N. *Nanoscale* **2013**, 5, (1), 72-88.
- [217] Su, Z.; Yang, C.; Xu, C.; Wu, H.; Zhang, Z.; Liu, T.; Zhang, C.; Yang, Q.; Li, B.; Kang, F. *Journal of Materials Chemistry A* **2013**, 1, (40), 12432-12440.
- [218] Tan, Y. B.; Lee, J.-M. *Journal of Materials Chemistry A* **2013**, 1, (47), 14814-14843.
- [219] Sawangphruk, M.; Suksomboon, M.; Kongsupornsak, K.; Khuntilo, J.;

- Srimuk, P.; Sanguansak, Y.; Klunbud, P.; Suktha, P.; Chiochan, P. *Journal of Materials Chemistry A* **2013**, 1, (34), 9630-9636.
- [220] Chen, S.; Xing, W.; Duan, J.; Hu, X.; Qiao, S. Z. *Journal of Materials Chemistry A* **2013**, 1, (9), 2941-2954.
- [221] Lee, M.-T.; Fan, C.-Y.; Wang, Y.-C.; Li, H.-Y.; Chang, J.-K.; Tseng, C.-M. *Journal of Materials Chemistry A* **2013**, 1, (10), 3395-3405.
- [222] Wang, S.; Dryfe, R. A. W. *Journal of Materials Chemistry A* **2013**, 1, (17), 5279-5283.
- [223] Perera, S. D.; Patel, B.; Nijem, N.; Roodenko, K.; Seitz, O.; Ferraris, J. P.; Chabal, Y. J.; Balkus, K. J. *Advanced Energy Materials* **2011**, 1, (5), 936-945.
- [224] Zhao, H.; Pan, L.; Xing, S.; Luo, J.; Xu, J. *Journal of Power Sources* **2013**, 222, (0), 21-31.
- [225] Wang, H.; Yi, H.; Chen, X.; Wang, X. *Journal of Materials Chemistry A* **2014**.
- [226] Hummers Jr, W. S.; Offeman, R. E. *Journal of the American Chemical Society* **1958**, 80, (6), 1339-1339.
- [227] Choi, B. G.; Yang, M.; Hong, W. H.; Choi, J. W.; Huh, Y. S. *ACS nano* **2012**, 6, (5), 4020-4028.
- [228] Mukhopadhyay, S.; Maitra, U. *Current Science* **2004**, 87, (12), 1666-1683.
- [229] Green, A. A.; Hersam, M. C. *Nano letters* **2009**, 9, (12), 4031-4036.
- [230] Lin, S.; Shih, C.-J.; Strano, M. S.; Blankschtein, D. *Journal of the American Chemical Society* **2011**, 133, (32), 12810-12823.
- [231] Ryu, Z.; Zheng, J.; Wang, M.; Zhang, B. *Carbon* **1999**, 37, (8), 1257-1264.
- [232] Xing, W.; Qiao, S.; Wu, X.; Gao, X.; Zhou, J.; Zhuo, S.; Hartono, S. B.; Hulicova-Jurcakova, D. *Journal of Power Sources* **2011**, 196, (8), 4123-4127.

- [233] Wei, Y.; Chen, S.; Su, D.; Sun, B.; Zhu, J.; Wang, G. *Journal of Materials Chemistry A* **2014**, 2, (21), 8103-8109.
- [234] Yan, J.; Wei, T.; Shao, B.; Ma, F.; Fan, Z.; Zhang, M.; Zheng, C.; Shang, Y.; Qian, W.; Wei, F. *Carbon* **2010**, 48, (6), 1731-1737.
- [235] Li, D.; Müller, M. B.; Gilje, S.; Kaner, R. B.; Wallace, G. G. *Nature nanotechnology* **2008**, 3, (2), 101-105.
- [236] Zhang, L. L.; Zhao, X.; Stoller, M. D.; Zhu, Y.; Ji, H.; Murali, S.; Wu, Y.; Perales, S.; Clevenger, B.; Ruoff, R. S. *Nano letters* **2012**, 12, (4), 1806-1812.
- [237] Chen, Z.; Ren, W.; Gao, L.; Liu, B.; Pei, S.; Cheng, H.-M. *Nature materials* **2011**, 10, (6), 424-428.
- [238] Bi, H.; Huang, F.; Liang, J.; Tang, Y.; Lü, X.; Xie, X.; Jiang, M. *Journal of Materials Chemistry* **2011**, 21, (43), 17366-17370.
- [239] Gomez De Arco, L.; Zhang, Y.; Schlenker, C. W.; Ryu, K.; Thompson, M. E.; Zhou, C. *ACS nano* **2010**, 4, (5), 2865-2873.
- [240] Dong, X.-C.; Xu, H.; Wang, X.-W.; Huang, Y.-X.; Chan-Park, M. B.; Zhang, H.; Wang, L.-H.; Huang, W.; Chen, P. *ACS nano* **2012**, 6, (4), 3206-3213.
- [241] Chen, Z.; Xu, C.; Ma, C.; Ren, W.; Cheng, H. M. *Advanced Materials* **2013**, 25, (9), 1296-1300.
- [242] Mecklenburg, M.; Schuchardt, A.; Mishra, Y. K.; Kaps, S.; Adelung, R.; Lotnyk, A.; Kienle, L.; Schulte, K. *Advanced Materials* **2012**, 24, (26), 3486-3490.
- [243] Worsley, M. A.; Pauzuskie, P. J.; Olson, T. Y.; Biener, J.; Satcher Jr, J. H.; Baumann, T. F. *Journal of the American Chemical Society* **2010**, 132, (40), 14067-14069.
- [244] Wei, W.; Yang, S.; Zhou, H.; Lieberwirth, I.; Feng, X.; Müllen, K. *Advanced Materials* **2013**, 25, (21), 2909-2914.

- [245] Meng, Y.; Zhao, Y.; Hu, C.; Cheng, H.; Hu, Y.; Zhang, Z.; Shi, G.; Qu, L. *Advanced Materials* **2013**, 25, (16), 2326-2331.
- [246] Huang, X.; Qian, K.; Yang, J.; Zhang, J.; Li, L.; Yu, C.; Zhao, D. *Advanced Materials* **2012**, 24, (32), 4419-4423.
- [247] Sun, H.; Xu, Z.; Gao, C. *Advanced Materials* **2013**, 25, (18), 2554-2560.
- [248] Xu, Z.; Zhang, Y.; Li, P.; Gao, C. *ACS nano* **2012**, 6, (8), 7103-7113.
- [249] He, Y.; Chen, W.; Li, X.; Zhang, Z.; Fu, J.; Zhao, C.; Xie, E. *ACS nano* **2012**.
- [250] Cottineau, T.; Toupin, M.; Delahaye, T.; Brousse, T.; Belanger, D. *Applied Physics A* **2006**, 82, (4), 599-606.
- [251] Fan, Z.; Yan, J.; Wei, T.; Zhi, L.; Ning, G.; Li, T.; Wei, F. *Advanced Functional Materials* **2011**, 21, (12), 2366-2375.
- [252] Lei, Z.; Shi, F.; Lu, L. *ACS Applied Materials & Interfaces* **2012**, 4, (2), 1058-1064.
- [253] Wu, Z. S.; Wang, D. W.; Ren, W.; Zhao, J.; Zhou, G.; Li, F.; Cheng, H. M. *Advanced Functional Materials* **2010**, 20, (20), 3595-3602.
- [254] Ye, J. S.; Cui, H. F.; Liu, X.; Lim, T. M.; Zhang, W. D.; Sheu, F. S. *Small* **2005**, 1, (5), 560-565.
- [255] Kim, S.-I.; Lee, J.-S.; Ahn, H.-J.; Song, H.-K.; Jang, J.-H. *ACS applied materials & interfaces* **2013**, 5, (5), 1596-1603.
- [256] Yuan, C.; Zhang, X.; Su, L.; Gao, B.; Shen, L. *Journal of Materials Chemistry* **2009**, 19, (32), 5772-5777.
- [257] Lang, J.-W.; Kong, L.-B.; Wu, W.-J.; Luo, Y.-C.; Kang, L. *Chemical Communications* **2008**, 35, (35), 4213-4215.
- [258] Lu, Q.; Lattanzi, M. W.; Chen, Y.; Kou, X.; Li, W.; Fan, X.; Unruh, K. M.;

Chen, J. G.; Xiao, J. Q. *Angewandte Chemie* **2011**, 123, (30), 6979-6982.

[259] Cao, C.-Y.; Guo, W.; Cui, Z.-M.; Song, W.-G.; Cai, W. *Journal of Materials Chemistry* **2011**, 21, (9), 3204-3209.

[260] Lou, X. W. D. *Energy & Environmental Science* **2012**, 5, (7), 7883-7887.

[261] Ma, L.; Zhou, H.; Shen, X.; Chen, Q.; Zhu, G.; Ji, Z. *RSC Advances* **2014**, 4, (95), 53180-53187.

[262] Rakhi, R.; Chen, W.; Cha, D.; Alshareef, H. *Nano letters* **2012**, 12, (5), 2559-2567.

[263] Kim, K. H.; Oh, Y.; Islam, M. *Nature Nanotechnology* **2012**.